Fitted and Unfitted Finite Element Methods for Solving the EEG Forward Problem

Inaugural-Dissertation
zur Erlangung des Doktorgrades der Naturwissenschaften
– Dr. rer. nat. –
im Fachbereich Mathematik und Informatik
der Mathematisch-Naturwissenschaftlichen Fakultät
der Westfälischen Wilhelms-Universität Münster

Vorgelegt von:

Andreas Nüßing
aus Warendorf

– 2018 –

Abstract

The aim of this thesis is to develop, implement and validate accurate and efficient strategies for solving the electroencephalography (EEG) forward problem. For this purpose, two types of approaches are considered: fitted and unfitted finite element methods.

For the fitted methods, such as the conforming finite element method or the discontinuous Galerkin method, various discretization schemes of the dipolar source term are derived and evaluated. One of the schemes represents a new framework for the Venant source model. This framework allows for a conforming representation of the discrete source term which is applicable for various numerical methods. In addition, the connection of the Venant approach to the partial integration source model is shown. A new subtraction scheme is mathematically derived and analyzed. This approach maintains the properties of the classical subtraction approach while drastically reducing the computational load. The application of the new subtraction source model is feasible even in highly resolved models.

In the second part of this thesis, two unfitted finite element methods are introduced for the solution of the EEG forward problem: the CutFEM method and the unfitted discontinuous Galerkin method (UDG). These approaches use an implicit representation of the model geometry and lead to a simpler forward modeling pipeline while keeping or exceeding the accuracy of the conforming finite element method. Within this framework, a topology preserving marching cubes algorithm for performing numerical integration over the implicitly defined domains is presented. Finally, the linear system obtained from an unfitted finite element method is solved using algebraic multigrid techniques.

In the last part of this work and in order to transport the modern mathematical methods presented in this thesis into application, the duneuro software toolbox is introduced. It offers extendible interfaces for forward modeling in neuroscience based on the Dune framework.

Acknowledgements

I would like to thank all people who made writing this thesis and my doctoral studies possible. Especially I would like to thank:

Contents

Notations and Abbreviations

u	electric potential.
$\boldsymbol{J}^p$	primary current.
σ	electric conductivity tensor.
x_{dp}	Position of a mathematical dipole.
$\boldsymbol{M}$	Moment of a mathematical dipole.
Ω	The open model domain.
$L^2(\Omega)$	Set of square-integrable functions over Ω.
$\mathcal{D}(\Omega)$	Set of test functions over Ω.
$\mathcal{D}'(\Omega)$	Set of distributions over Ω.
δ_x	Delta distribution centered at $x \in \mathbb{R}^d$.
$D^\alpha u$	Derivative of u with respect to the multi-index α.
$\mathbb{P}_k(E)$	Space spanned by monomials with exponents of $\lvert \cdot \rvert_1$-norm at most k.
$\mathbb{Q}_k(E)$	Space spanned by monomials with exponents of $\lvert \cdot \rvert_\infty$-norm at most k.
$\mathrm{supp}(u)$	Support of a function or distribution u.
$H^k(\Omega)$	Sobolev space of L^2 functions with L^2 derivatives up to order $k \in \mathbb{N}$.
$H^k_*(\Omega)$	Sobolev space of functions with zero mean.
$\mathcal{T}_h(\Omega)$	Tessellation of the domain Ω.
Γ_h^{int}	Internal skeleton of a tessellation.
Γ_h	Full skeleton of a tessellation.
$[\![\cdot]\!]$	jump of a function on a face.
$\{\cdot\}$	average of a function on a face.
η	scalar penalty parameter.
$\tilde{\eta}$	scalar ghost penalty parameter.
u^∞	Singularity potential of the subtraction approach.
$\tilde{u}$	Correction potential of the subtraction approach.
Ω^∞	Patch of the localized subtraction approach.
$\tilde{\Omega}$	Outer domain of the localized subtraction approach $\tilde{\Omega} = \Omega \setminus \Omega^\infty$.

AMG   algebraic multigrid.
CG   continuous Galerkin method or conforming finite element method.
DG   discontinuous Galerkin method.
EEG   electroencephalography.
IQR   inter-quartile range.
MAG   magnitude error.
MEG   magnetoencephalography.
PDE   partial differential equation.
PI   partial integration approach.
RDM   relative difference measure.
TR   total range.
UDG   unfitted discontinuous Galerkin method.

List of Figures

List of Tables

Introduction

The electroencephalography (EEG) is a tool to measure potential differences on the surface of the head that are due to electric activity in the brain. EEG offers a high time resolution and gives insight into the function and dysfunction of the brain. Even though the direct signals can already be used and analyzed, certain investigations require a reconstruction of the origin of the measured signals. This reconstruction can be formulated as an inverse problem, which aims to estimate the electric activity within the brain given the EEG measurements on the head surface. As the solution is in general not unique, the inverse problem is ill-posed. A crucial component for solving the inverse problem for source analysis is the EEG forward problem. Assuming a known source current in the brain, the forward problem simulates the current propagation and the resulting potential differences on the head surface. The accuracy of solving the forward problem strongly influences the overall accuracy of source analysis. In particular, errors in the forward solution deteriorate the estimated reconstruction. The EEG forward problem can be formulated as a partial differential equation (PDE). For simple approximations of the head geometry, such as a set of concentric spheres, formulas are available to solve the PDE quasi-analytically (De Munck and Peters, 1993). However, a set of concentric spheres is only a rough approximation of the human head and large errors in the solution can be expected. To improve the model geometry, individual head models based on imaging data, such as magnetic resonance imaging or computed tomography, can be adopted. For such models, no analytical formulas exist and the PDE has to be solved numerically. Several methods have been proposed for the numerical solution of the EEG forward problem, such as finite difference methods (Montes-Restrepo et al., 2014; Vatta et al., 2009; Wendel et al., 2008), finite volume methods (Cook and Koles, 2006), boundary element methods (Acar and Makeig, 2010; Gramfort et al., 2011; Mosher et al., 1999; Stenroos and Sarvas, 2012) or finite element methods (Gençer and Acar, 2004; Schimpf et al., 2002; Vorwerk et al., 2012; Weinstein et al., 2000) and each of them has specific advantages and disadvantages.

Challenging problems for finite element methods are the discretization of the source term, which is usually modeled as a singular current dipole, and an accurate treatment of the model geometry. In order to include the source term into the numerical model, a discrete representation of the singularity has to be provided. Several approaches have been introduced to construct this discretization,

such as the partial integration approach, the Venant approach (Medani et al., 2015; Vorwerk, 2016; Wolters et al., 2007b), the Whitney approach (Bauer et al., 2015; Pursiainen et al., 2011, 2016) or the subtraction approach (Bertrand et al., 1991; Drechsler et al., 2009; Wolters et al., 2007a). For the Venant approach, the dipole is replaced by a set of monopoles around the source location whose strengths are computed such that specific properties of the dipole are maintained. While this approach offers a way to include the dipole into the numerical model, it uses singularities in the source representation and provides a non-smooth source distribution. A smoother distribution and a way to completely remove the singularity from the mathematical model is provided by the subtraction approach. The complete removal of the singularity comes at the cost of a strong increase in the computational load compared to other discretization approaches, which makes the subtraction approach currently unfeasible for many applications when using highly resolved model geometries. Important for the practical relevance of a source discretization is the combination of accuracy and time consumption. The second challenging problem is the accurate representation of the individual head geometry. For the finite element method the individual head geometry is partitioned into a set of simple elements. Two approaches are currently used: a tetrahedral or a hexahedral geometry-conforming mesh. While a tetrahedral mesh offers a high accuracy in representing the surfaces of the different tissue compartments of the head, its construction is a challenging task which might even involve careful manual interaction and modification of the tissue surfaces (Vorwerk et al., 2014). On the other hand, a hexahedral mesh offers the advantage of an automatic mesh generation based on a voxel segmentation of the imaging data, but it results in a staircase-like representation of the different surfaces (Wolters et al., 2007b). Both approaches have in common that the discrete representation of the geometry is conforming the head geometry. We will refer to such approaches as *fitted finite element methods*.

The contributions of this thesis respond to the two challenges identified above and provide methods towards an automated and accurate simulation pipeline for solving the EEG forward problem. In the first part we address the questions regarding the discretization of the dipolar source term. We provide a framework for the Venant approach which is applicable for various finite element methods and which avoids the introduction of singularities into the numerical model. Using a localization approach we provide a new subtraction approach. On the one hand, it keeps the properties of the original approach but on the other hand it is applicable even when using highly resolved meshes. The representation of the model geometry is considered in the second part, where two new finite element methods for solving the EEG forward problem are introduced: the CutFEM method (Burman et al., 2015; Burman and Hansbo, 2012) and the unfitted discontinuous Galerkin method (Bastian and Engwer, 2009; Engwer, 2009). Both methods use an implicit representation of the geometry which avoids the construction of a geometry-conforming mesh but still offers an accurate forward solution. These methods are also referred to as *unfitted finite element methods*. In this thesis, some implementational aspects related to the practical application of such methods are considered. For example, we need to perform numerical integration over the implicitly defined domains within the numerical model. Furthermore, we need to efficiently solve the resulting linear systems. Another aspect considering the development of modern mathematical methods for solving the EEG forward problem is the transfer of those methods into application. With this purpose in mind, we present *duneuro*, an extendible software framework based on the Dune framework (Bastian et al., 2008a,b) that allows for an accessible usage of the presented methods and that is robust with respect to future

extensions.

The thesis is structured as follows: in Chapter 1 we present the physiological and mathematical background of the EEG forward problem. We introduce the well established conforming finite element method as well as the more recent discontinuous Galerkin method and the mixed finite element method. The focus of Chapter 2 lies on the extension of two approaches for discretizing the dipolar source term. We introduce a conforming formulation of the Venant approach and investigate various properties of the discrete source model. Additionally, we derive and analyze the localized subtraction approach, which modifies the full subtraction approach and uses a local support of the discretized source term. This enables the practical use of the subtraction approach even for high mesh resolutions. In Chapter 3 we introduce two cut-cell methods for solving the EEG forward problem. The CutFEM method uses a conforming function space for each tissue compartment while the UDG method allows for discontinuities within each tissue. The cut-cell methods are validated in multi-layer sphere models as well as in realistically shaped head models. In Chapter 4 we consider implementational aspects of cut-cell methods: the numerical integration over implicitly defined domains and the efficient solution of the linear system using algebraic multigrid techniques. All methods that are presented in this thesis are implemented in the duneuro toolbox which is presented in Chapter 5. An extendible software framework is introduced which enables the transfer of the modern mathematical methods into application. Finally, a summary of the main results of this thesis and an outlook are given in Chapter 6.

Physiological and Mathematical Background

In this chapter we will briefly recall the established physiological and mathematical background of the EEG forward problem. In Section 1.1, the physiological origin of the measured electric signals is described. Based on Maxwell's equations, the derivation of Poisson's equation is presented which forms the basis of electrostatics. Section 1.2 describes the mathematical foundation for describing Poisson's equation and its source term and introduces a conforming finite element method using Lagrangian elements. In order to solve the EEG forward problem numerically, discrete approximations of analytical source terms are presented. In Section 1.3, an alternative approach to the conforming finite element method, the non-conforming discontinuous Galerkin method is introduced. It allows discontinuities within the computational domain and provides conservation properties on the discrete level. Section 1.4 briefly introduces the mixed finite element method. It is based on a first order formulation of Poisson's equation and is able to provide conservation properties. The chapter closes with a summary and conclusion in Section 1.5.

1.1 The EEG Forward Problem

The generators of the electric signals that are measured by EEG devices are groups of neurons in the gray matter of the brain as described, e.g., in (Hämäläinen et al., 1993). These neurons are connected among each other and form a large network to communicate and transport signals through the cortex. The neurons can be separated into two main types, the stellate cells and the pyramidal cells. The pyramidal cells consist of the cell body or soma, the axon and multiple dendrites which form connections via synapses to other neurons. They receive electrical input signals of multiple neighboring neurons and propagate these signals by firing an action potential, if a certain input threshold has been reached. The postsynaptic potential differences of a group of neurons produce a current of dipolar form, which can be modeled as a current dipole. Due to the orientation of the pyramidal cells, the dipole moment is mainly oriented normal to the cortical surface. Figure 1.1 shows an illustration of the neural cells in the cortex.
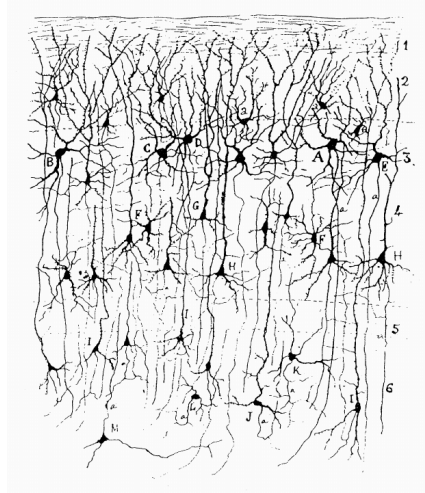
Figure 1.1: Illustration showing a group of neural cells in a rat cortex. Both, stellate cells and pyramidal cells are visible. Drawn by Ramón y Cajal in 1888 and presented in (Hämäläinen et al., 1993).

The basis of the macroscopic model for volume conduction in the head is described by Maxwell's equations, which can be formulated as

$$\nabla \cdot \boldsymbol{E} = \frac{\rho}{\varepsilon_0} \tag{1.1}$$

$$\nabla \times \boldsymbol{E} = -\frac{\partial \boldsymbol{B}}{\partial t} \tag{1.2}$$

$$\nabla \cdot \boldsymbol{B} = 0 \tag{1.3}$$

$$\nabla \times \boldsymbol{B} = \mu_0 \left(\boldsymbol{J} + \varepsilon_0 \frac{\partial \boldsymbol{E}}{\partial t} \right). \tag{1.4}$$

With the electric field E, the electric charge density ρ, the electric constant ε_0, the magnetic field $\boldsymbol{B}$, the magnetic constant μ_0 and the current density $\boldsymbol{J}$. (Hämäläinen et al., 1993) derive, that for the occurring frequencies and spatial scales occurring in neuroelectromagnetism, the quasi-static approximation of Maxwell's equations is valid and the time dependent components $\partial \boldsymbol{B}/\partial t$ and $\partial \boldsymbol{E}/\partial t$ can be neglected when considering the macroscopic behavior. From (1.2) we can see that the rotational component of the electric field is zero and the electric field can be represented as a gradient field, i.e., $E = -\nabla u$ with the electric potential u. We split the current density into two parts $\boldsymbol{J} = \boldsymbol{J}^p + \sigma \boldsymbol{E}$, a primary current $\boldsymbol{J}^p$ and a volume or return current $\sigma \boldsymbol{E}$. Here σ denotes the electric conductivity tensor. The primary current can be seen as the main source of the electric activity which is located in the vicinity of the active neural cells, while the volume current describes the current flow within the remaining portion of the head. Taking the divergence of (1.4), considering that the divergence of the curl is zero and inserting the electric potential, we obtain

$$\nabla \cdot \sigma \nabla u = \nabla \cdot \boldsymbol{J}^p. \tag{1.5}$$

As noted above, the primary current can be modeled as a current dipole, which is defined as

$$J^p := M\delta(x - x_{\mathrm{dp}}),$$

with the moment M at the position x_{dp} and the delta distribution δ.

1.2 A Conforming Finite Element Method

In this section we will describe the mathematical foundation of describing Poisson's equation and its source term and introduce a conforming finite element method to solve the EEG forward problem numerically. This section mainly follows (Braess, 2007), (Brenner and Scott, 2007) and (Friedlander and Joshi, 1998).

A weak formulation The main function space that we consider and that is the basis of the Sobolev spaces is the space $L^2(\Omega)$ over the domain $\Omega \subset \mathbb{R}^d$, $d \in \mathbb{N}$ which consists of the square-integrable functions. In the strict sense, $L^2(\Omega)$ is an equivalence class of functions, where two functions are considered equivalent if they differ only on a set of zero measure. Together with the scalar product

$$\langle u, v \rangle_{L^2(\Omega)} := \int_\Omega u(x)v(x)\,\mathrm{d}x$$

and the associated norm

$$\|u\|_{L^2(\Omega)} := \sqrt{\langle u, u \rangle_{L^2(\Omega)}},$$

the space $L^2(\Omega)$ forms a Hilbert space. If no ambiguities arise, we will omit the subscript of both scalar product and norm. In order to define Poisson's equation for this function space in a weak sense, we introduce the concept of *weak derivatives*, which requires the concept of *distributions*. Distributions also form the basis of defining the source term of the EEG forward problem as motivated in the previous section: the mathematical point dipole. A distribution is a linear form that is described by its effect on a set of *test functions*, which are smooth functions of compact support:

Definition 1.1 (Test functions)**.** *Let $\Omega \subset \mathbb{R}^d$ be a domain. Denote by $\mathcal{D}(\Omega)$ the $C^\infty(\Omega)$ functions with compact support, i.e., $\mathcal{D}(\Omega) := C_0^\infty(\Omega)$. These functions will also be called test functions.*

We will define derivatives with respect to different variables. A useful short hand notation for this multi-dimensional derivative is provided by multi-indices:

Definition 1.2 (Multi-index)**.** *A vector $\alpha \in \mathbb{N}^d$ is called a multi-index. We define the norms*

$$|\alpha|_1 := \sum_{i=0}^{d-1} \alpha_i, \quad |\alpha|_\infty := \max_{i=0}^{d-1} \alpha_i, \tag{1.6}$$

Using this multi-index, we will write

$$D^\alpha u = \frac{\partial^{|\alpha|_1} u}{\partial x_0^{\alpha_0} \partial x_1^{\alpha_1} \dots \partial x_{d-1}^{\alpha_{d-1}}} \tag{1.7}$$

for a multi-index $\alpha \in \mathbb{N}^d$ and $u \in C^{|\alpha|_1}(\Omega)$. Distributions form a generalization of the concept of functions and can be defined as

Definition 1.3 (Distribution (Friedlander and Joshi, 1998, Definition 1.3.1))**.** *Let $\Omega \subset \mathbb{R}^d$ be a domain. A linear form $u : \mathcal{D}(\Omega) \to \mathbb{R}$ is called a distribution if, for every compact set $K \subset \Omega$, there is a $C \in \mathbb{R}$ with $C \geq 0$ and $N \in \mathbb{N}$ such that*

$$|u(\xi)| \leq C \sum_{|\alpha|_1 \leq N} \sup_{x \in K} |D^\alpha \xi(x)|$$

for all $\xi \in \mathcal{D}(\Omega)$ with $\operatorname{supp} \xi \subset K$. The space of distributions on Ω is denoted by $\mathcal{D}'(\Omega)$.

One example distribution that was used for defining the source terms for the EEG forward problem and that will be used further in different discretization schemes of it is the *delta distribution*:

Definition 1.4 (Dirac delta distribution)**.** *For a point $y \in \mathbb{R}^d$, the functional evaluating a test function, i.e.,*

$$\delta_y : \mathcal{D}(\Omega) \to \mathbb{R}; \xi \mapsto \xi(y)$$

is called Dirac delta distribution.

Note that the delta distribution is indeed a distribution, which can be seen directly by setting $N = 0$ and $C = 1$ in Definition 1.3. In addition to the delta distribution, each function $f \in L^2(\Omega)$ induces a distribution by using the functional $\xi \mapsto \langle f, \xi \rangle$. However, the converse is not true, as the delta distribution can not be represented by an L^2 function. For a distribution, we can define its derivative as

Definition 1.5 (Derivative of a distribution)**.** *Let $\Omega \subset \mathbb{R}^d$ be a domain. The distributional derivative of $u \in \mathcal{D}'(\Omega)$ with respect to $\alpha \in \mathbb{N}^d$ is defined as*

$$(D^\alpha u)(\xi) := (-1)^{|\alpha|_1} u(D^\alpha \xi),$$

for all $\xi \in \mathcal{D}(\Omega)$.

The derivative of a distribution is again a distribution and a distribution has derivatives of any order (Friedlander and Joshi, 1998, 2.1). This property can be directly applied to the source term $\nabla \cdot \boldsymbol{J}^p$ of the EEG forward problem.

Lemma 1.1. *For a dipole position $x_{\mathrm{dp}} \in \Omega$ and a dipole moment $\boldsymbol{M} \in \mathbb{R}^d$, the source term $f := \nabla \cdot \boldsymbol{J}^p = \nabla \cdot (\boldsymbol{M} \delta_{x_{\mathrm{dp}}})$ is a distribution, i.e., $f \in \mathcal{D}'(\Omega)$.*

Proof. The linearity follows immediately from the definition of the distributional derivative. Let $\xi \in C^\infty(\Omega)$. Using the triangle inequality we find

$$|f(\xi)| = |\nabla \cdot (\boldsymbol{M}\xi(x_{\mathrm{dp}}))| \leq \sum_{i=0}^{d-1} |M_i \partial_{x_i} \xi(x_{\mathrm{dp}})| \leq C \sum_{i=0}^{d-1} \|\partial_{x_i} \xi\|_\infty, \tag{1.8}$$

with $C := \sup_{i=0}^{d-1} |M_i|$. $\qquad \square$

When defining discrete approximations of the dipolar source term in a distributional form, we will make use of the *support* of a distribution.

Definition 1.6 (Support of a distribution (Friedlander and Joshi, 1998, Definition 1.4.1)). *Let* $\Omega \subset \mathbb{R}^d$ *be a domain and let* $u \in \mathcal{D}'(\Omega)$. *The support of* u, *written as* $\mathrm{supp}(u)$ *is defined as the complement of the set*

$$\left\{ x \in \mathbb{R}^d : u = 0 \text{ on a neighborhood of } x \right\}. \tag{1.9}$$

We will mainly need the support of a set of monopoles and the mathematical point dipole. A set of monopoles is defined by the distribution $f = \sum_i q_i \delta_{x_i}$, with monopoles located at $x_i \in \mathbb{R}^d$ with strength $q_i \in \mathbb{R}$. For this distribution, it holds that $f = 0$ on $\mathbb{R}^d \setminus \bigcup_i \{x_i\}$ and thus $\mathrm{supp}(f) = \bigcup_i \{x_i\}$. In a similar manner, the support of a dipolar source term given by the distribution $g = \nabla \cdot (M \delta_{x_{\mathrm{dp}}})$ is given by $\mathrm{supp}(g) = \{x_{\mathrm{dp}}\}$. A set of functions that will be the basis of the weak formulation of Poisson's equation, is the set of L^2 functions whose distributional derivatives are again L^2 functions:

Definition 1.7 (Sobolev space). *For* $\Omega \subset \mathbb{R}^d$ *and* $k \in \mathbb{N}$, *the Sobolev space is defined as*

$$H^k(\Omega) := \left\{ u \in L^2(\Omega) : D^\alpha u \in L^2(\Omega), |\alpha|_1 \leq k \right\}. \tag{1.10}$$

If the distributional derivative of a function is square-integrable, it will also be called the function's *weak derivative*. If a function is differentiable in a classical sense, then its weak derivative exists and both derivatives coincide. Based on the scalar product

$$\langle u, v \rangle_k := \sum_{|\alpha|_1 \leq k} \langle D^\alpha u, D^\alpha v \rangle_{L^2(\Omega)}$$

and its associated norm $\| \cdot \|_k$, H^k forms a Hilbert space. When dealing with the pure Neumann problem of Poisson's equation, the solution is only determined up to a constant. In order to select a fixed solution, we will restrict the Sobolev space $H^k(\Omega)$ to the space of functions with zero mean:

Definition 1.8 (Sobolev space with zero mean). *For* $\Omega \subset \mathbb{R}^d$ *and* $k \in \mathbb{N}$, *the Sobolev space with zero mean is defined as*

$$H^k_*(\Omega) := \left\{ u \in H^k(\Omega) : \int_\Omega u \, \mathrm{d}x = 0 \right\}. \tag{1.11}$$

Starting from the strong formulation of Poisson's equation, formally multiplying it with a test function v, integrating and applying integration by parts yields its weak formulation:

Definition 1.9 (Weak formulation). *The weak formulation of Poisson's equation is defined as: find* $u \in V := H^1(\Omega)$ *such that*

$$\langle \sigma \nabla u, \nabla v \rangle_{L^2(\Omega)} = \langle f, v \rangle_{L^2(\Omega)}$$

for all test functions $v \in V$.

Note that this definition assumes $f \in L^2(\Omega)$, which is not the case for the mathematical point dipole. The basis for the theoretical treatment of the weak formulation is given by the Lax-Milgram theorem, which can be used to show existence and uniqueness of solutions of the weak formulation.

Theorem 1.1 (Lax-Milgram Theorem (Brenner and Scott, 2007, Theorem (2.7.7))). *Given a Hilbert space $(V, \langle \cdot, \cdot \rangle)$, a continuous, coercive bilinear form $a(\cdot, \cdot)$ and a continuous linear functional $f \in V'$, there exists a unique $u \in V$ such that*

$$a(u, v) = f(v) \quad \forall v \in V$$

Proof. (Brenner and Scott, 2007, Theorem (2.7.7)) □

In (Wolters et al., 2007a) it is shown, that the bilinear form a of the weak formulation in Definition 1.9 is continuous and coercive and thus fulfills the prerequisites of Theorem 1.1. Under the assumption that there is a representation f of the right-hand side for the EEG forward problem such that $f \in V'$, Theorem 1.1 gives the main result for existence and uniqueness.

A Conforming Finite Element Method   Based on the mathematical foundation presented above, we introduce a discretization method to numerically solve the EEG forward problem: the conforming finite element method with Lagrangian elements.

There are several alternative approaches to solve the EEG forward problem, such as the boundary element method (Acar and Makeig, 2010; Gramfort et al., 2011; Mosher et al., 1999; Stenroos and Sarvas, 2012). The different domains are represented by different surfaces and Poisson's equation is transformed into an integral form. Introducing a finite dimensional function space on the surfaces, the resulting integral form can be solved numerically. A different class of methods takes the volume of the domain into account. Examples are the finite difference method (Montes-Restrepo et al., 2014; Vatta et al., 2009; Wendel et al., 2008) or the finite volume method (Cook and Koles, 2006).

For the description of the finite element method, we mainly follow (Braess, 2007) and will focus on the description of two and three spatial dimensions. The main idea of the finite element method is to use the weak formulation and replace the infinite dimensional space V with a finite dimension space V_h. It has been applied extensively for the EEG forward problem, e.g., see (Gençer and Acar, 2004; Lew et al., 2009; Medani et al., 2015; Pursiainen et al., 2011; Schimpf et al., 2002; Weinstein et al., 2000). The classical Lagrangian finite element method uses a conforming approach to construct the finite dimensional subspace, i.e., $V_h \subset V$. Instead of searching for a solution $u \in V$, we search for a solution $u_h \in V_h$ and the weak formulation then reads

$$a(u_h, v_h) = f(v_h), \quad \text{for all } v_h \in V_h, \tag{1.12}$$

with $a(u_h, v_h) = \int_\Omega \langle \sigma \nabla u_h, \nabla v_h \rangle \, \mathrm{d}x$ and a source term f which is to be defined below. Here $h \in \mathbb{R}$ denotes a discretization parameter which describes a convergence process to the original problem for $h \to 0$. We introduce a basis of the discrete function space V_h: $\varphi_0, \ldots, \varphi_{N-1}$, with $N = \dim(V_h)$. For the function u_h we introduce the form

$$u_h(x) = \sum_{i=0}^{N-1} z_i \varphi_i(x),$$

with the coefficients $z_i \in \mathbb{R}$. Then (1.12) is equivalent to

$$\sum_{i=0}^{N-1} z_i a(\varphi_i, \varphi_j) = f(\varphi_j) \quad \text{for } j = 0, \dots, N-1,$$

or in matrix form: Find $z \in \mathbb{R}^N$ such that

$$Az = b,$$

with $A_{ij} = a(\varphi_i, \varphi_j)$ and $b_i = f(\varphi_i)$. It can be shown that if the bilinear form a is coercive, the matrix A is positive definite and thus the linear system has a unique solution.

Lemma 1.2 (Céa's lemma (Brenner and Scott, 2007, Theorem 2.8.1)). *Given a Hilbert space $(V, \langle \cdot, \cdot \rangle)$, a continuous, coercive bilinear form $a(\cdot, \cdot)$, a continuous linear functional $f \in V'$ and $u \in V$ solving the weak formulation. For the solution $u_h \in V_h$ of the finite element variational problem we have*

$$\|u - u_h\|_V \leq \frac{C}{\alpha} \min_{v \in V_h} \|u - v\|_V$$

where C is the continuity constant and α is the coercivity constant of $a(\cdot, \cdot)$ on V.

According to Lemma 1.2, the accuracy of the finite element solution strongly depends on how the discrete function space is chosen to approximate the solution u. The basis of constructing this discrete function space is a partition of the computational domain Ω.

Definition 1.10 (Tessellation). *A tessellation of a domain Ω is a set $\mathcal{T}_h(\Omega) = \{E_0, \dots, E_{m-1}\}$ of open convex polytopes $E_i \subset \Omega$ such that*

$$\bigcup_{i=0}^{m-1} \overline{E}_i = \overline{\Omega},$$
$$E_i \cap E_j = \varnothing, \quad i \neq j.$$

A tessellation is called admissible, if the following conditions are met:

1. *if $\overline{E}_i \cap \overline{E}_j$ consists of exactly one point, this point is a common vertex of E_i and E_j.*

2. *if $\overline{E}_i \cap \overline{E}_j$ consists of more then one point for $i \neq j$, then $\overline{E}_i \cap \overline{E}_j$ is a common edge or, in three dimensions, a common face of E_i and E_j.*

A family of tessellations $\{\mathcal{T}_h\}$ is called shape-regular, if there is a $\kappa > 0$ such that every T in $\mathcal{T}_h$ contains a circle of radius ρ_T with

$$\rho_T \geq h_T/\kappa,$$

where h_T denotes the diameter of T. A family of tessellations is called uniform, if every T in $\mathcal{T}_h$ contains a circle of radius ρ_T with

$$\rho_T \geq h/\kappa,$$

with $h := \max_{T \in \mathcal{T}_h} h_T$.

A property of admissible tessellations is that they do not contain hanging nodes. In this thesis we will mainly focus on admissible tessellations and give a comment when a method is also applicable for non-admissible tessellations. When investigating convergence behavior in subsequent sections, we will use shape-regular tetrahedral tessellations and uniform hexahedral tessellations. On such tessellations, we define the finite-element space V_h^k:

Definition 1.11 (Finite element space). *The space V_h^k is defined as the space of continuous, piecewise polynomial functions, i.e.,*

$$V_h^k := \left\{ v_h \in C^0(\Omega) : v_h|_E \in P^k(E) \ \forall E \in \mathcal{T}_h(\Omega) \right\}$$

where $P^k(E)$ denotes a space of polynomials of degree $k \in \mathbb{N}$ on an element E.

In (Braess, 2007, Theorem 5.2) it is shown that this function space is a conforming space, i.e., $V_h^k \subset H^1(\Omega)$. We will usually employ first order polynomials, i.e., linear polynomials on tetrahedrons and multi-linear polynomials on hexahedrons. The basis functions φ_i for this piecewise linear function space are chosen as the *Lagrangian* basis functions

Definition 1.12 (Lagrangian basis functions). *Let $x_0, \ldots, x_{N-1} \in \mathbb{R}^d$ denote the vertices of a tessellation $\mathcal{T}_h$. The basis consisting of the linear functions $\varphi_i, i = 0, \ldots, N-1$ which fulfill the property*

$$\varphi_i(x_j) = \begin{cases} 1 & , i = j \\ 0 & , i \neq j \end{cases}$$

is called Lagrangian basis.

Due to their shape, the Lagrangian basis functions are also called *hat functions*.

Direct source models   The handling of the source-term for the EEG forward problem can be categorized into two main categories of direct and indirect source models. While the direct approaches perform a direct discretization of the dipolar source term, an indirect approach modifies the weak formulation.

The direct source models presented in the literature are the partial integration approach, the St. Venant source model and the Whitney approach. The partial integration approach resolves the distributional derivative of the mathematical point dipole onto the test function. As functions in L^2 are not uniquely defined on a set of zero measure, such as the set $\{x_{\mathrm{dp}}\}$, this source model is only applicable in the discrete case, when using a piecewise polynomial test function. We will use the implicit assumption that the dipole is not located exactly on the boundary of an element. If so, we will shift it by $\varepsilon \ll h$ into the volume of an element.

Definition 1.13 (Partial integration source model). *For a dipole at $x_{\mathrm{dp}} \in \mathbb{R}^d$ with moment $\boldsymbol{M} \in \mathbb{R}^d$ and a test function $v_h \in V_h$, the partial integration source model is defined as*

$$\langle f, v_h \rangle := \begin{cases} -\left\langle \boldsymbol{M}, \nabla v_h(x_{\mathrm{dp}}) \right\rangle, & x_{\mathrm{dp}} \in \mathrm{supp}(v_h) \\ 0, & else \end{cases} . \tag{1.13}$$

When using piecewise linear test functions, the partial integration approach is independent of the local position within an element, due to the piecewise constant gradient in (1.13). For piecewise multi-linear test functions, this is not the case.

Another direct source model is the St. Venant approach (Medani et al., 2015; Vorwerk, 2016; Wolters et al., 2007b). In its classical formulation, it replaces the mathematical point dipole, containing the derivative of the delta distribution, by a set of monopoles, which are weighted such that certain properties of the original source term are maintained. This approach is described in detail in Section 2.1.

A different discretization scheme is performed by the Whitney source model (Bauer et al., 2015; Pursiainen et al., 2011, 2016). Instead of discretizing the complete dipolar source term, the primary current J^p is discretized in a vector-valued function space which consists of functions with square-integrable divergence. Depending on the source-space, the Whitney approach shows high accuracies comparable to the Venant approach.

A Continuous Subtraction Approach   In the following, we present an indirect source model for discretizing the singular right-hand side of the EEG forward problem. As mentioned above, the dipole source term is a distribution that can not be represented as an element of the $L^2(\Omega)$ space. Through this lack of regularity, the common framework of finite element methods is not directly applicable. In (Wolters et al., 2007a), the theory of the *subtraction* approach for resolving the singularity has been presented, with an idea going back to (Bertrand et al., 1991). Furthermore, in (Drechsler et al., 2009), an extension of the approach, namely the *full subtraction* approach has been described, which we will recall in the following section. The main assumption behind this approach states, that we find an area around the dipole location, where the conductivity has a constant value $\sigma^\infty \in \mathbb{R}^{d \times d}$. If this is the case, then we can split the potential and the conductivity tensor into two parts, a singularity contribution and a correction part:

$$u = \tilde{u} + u^\infty \tag{1.14}$$

$$\sigma = \tilde{\sigma} + \sigma^\infty. \tag{1.15}$$

Here $u^\infty : \mathbb{R}^d \to \mathbb{R}$ solves the Poisson's equation in an unbounded domain with constant conductivity $\sigma^\infty \in \mathbb{R}^{d \times d}$, i.e.,

$$\nabla \cdot \sigma^\infty \nabla u^\infty = \nabla \cdot J^p \quad \text{in } \mathbb{R}^d. \tag{1.16}$$

This assumption is fulfilled, if the dipole has a certain distance from the next conductivity jump. As presented in (Hämäläinen et al., 1993) dipoles are located in the center of the gray matter compartment, which has an approximate width of 2 mm to 6 mm (Li et al., 2014). Thus, the assumption can be considered reasonable in a realistic scenario. The singularity potential u^∞ can be analytically computed and is given as

$$u^\infty(x) = \frac{1}{4\pi \sqrt{|\sigma^\infty|}} \frac{\left\langle M, (\sigma^\infty)^{-1}(x - x_{\mathrm{dp}}) \right\rangle}{\left\langle (\sigma^\infty)^{-1}(x - x_{\mathrm{dp}}), x - x_{\mathrm{dp}} \right\rangle^{\frac{3}{2}}}, \tag{1.17}$$

where $|\sigma^\infty| \in \mathbb{R}$ denotes the determinant of σ^∞ and x_{dp}, $\boldsymbol{M} \in \mathbb{R}^d$ denote the dipole position and the dipole moment respectively. Note that u^∞ has a singularity at the dipole position. In the following derivation we will need the gradient of u^∞, which can be formulated analytically as

$$
\nabla u^\infty(x) = \frac{1}{4\pi\sqrt{|\sigma^\infty|}} \frac{(\sigma^\infty)^{-1}\boldsymbol{M}}{\left\langle (\sigma^\infty)^{-1}(x-x_{\mathrm{dp}}), x-x_{\mathrm{dp}} \right\rangle^{\frac{3}{2}}}
$$
$$
- \frac{1}{4\pi\sqrt{|\sigma^\infty|}} \frac{3\left\langle \boldsymbol{M}, (\sigma^\infty)^{-1}(x-x_{\mathrm{dp}}) \right\rangle (\sigma^\infty)^{-1}(x-x_{\mathrm{dp}})}{\left\langle (\sigma^\infty)^{-1}(x-x_{\mathrm{dp}}), x-x_{\mathrm{dp}} \right\rangle^{\frac{5}{2}}}. \tag{1.18}
$$

If we can compute the correction potential $\tilde{u} \in H_*^1(\Omega)$, the full potential u can be obtained via (1.14) (cf. Definition 1.8 for the definition of $H_*^1(\Omega)$). Inserting (1.14) into the Poisson's equation and considering (1.15) gives the strong formulation of the subtraction approach:

$$
\nabla \cdot \sigma \nabla \tilde{u} = -\nabla \cdot \tilde{\sigma} \nabla u^\infty \quad \text{in } \Omega \tag{1.19}
$$
$$
\langle \sigma \nabla \tilde{u}, \boldsymbol{n} \rangle = -\langle \sigma \nabla u^\infty, \boldsymbol{n} \rangle \quad \text{on } \partial\Omega. \tag{1.20}
$$

Note that by this approach, the singularity has been effectively eliminated as $\sigma \equiv \sigma^\infty$ in an area around the dipole location and thus $\tilde{\sigma} \equiv 0$ in the same area. Even though u^∞ still has a singularity at the dipole location, $\tilde{\sigma}$ is constantly zero in this area. An advantageous property of the subtraction approach compared to the direct approaches can be seen in the accurate representation of the source term in the vicinity of the dipole position.

In order to derive a weak formulation for the subtraction approach, we multiply (1.19) with a test function $v \in H^1(\Omega)$, applying integration by parts while considering the inhomogeneous Neumann boundary condition in (1.20). The weak formulation of the subtraction approach then reads: Find $\tilde{u} \in H_*^1(\Omega)$ such that

$$
a(\tilde{u}, v) = l(v) \quad \text{for all } v \in H^1(\Omega)
$$

holds, with

$$
a(\tilde{u}, v) := \int_\Omega \langle \sigma \nabla \tilde{u}, \nabla v \rangle \, \mathrm{d}x
$$
$$
l(v) := \int_\Omega \langle \tilde{\sigma} \nabla u^\infty, \nabla v \rangle \, \mathrm{d}x - \int_{\partial\Omega} \langle \sigma^\infty \nabla u^\infty, \boldsymbol{n} \rangle \, \mathrm{d}s \,.
$$

In (Wolters et al., 2007a), the mathematical theory of the subtraction approach along with proofs for existence and uniqueness as well as error-estimates have been presented. The main theoretical result is the existence and uniqueness, which uses the Lax-Milgram theorem 1.1.

Theorem 1.2 (Existence and uniqueness (Wolters et al., 2007a, Theorem 3.7)). *Let $\Omega \subset \mathbb{R}^d$ be compact with a piecewise smooth boundary. Then the variational problem: Find $\tilde{u} \in H_*^1(\Omega)$ such that*

$$
a(\tilde{u}, v) = l(v) \quad \forall v \in H^1(\Omega) \tag{1.21}
$$

has a unique solution $\tilde{u} \in H_*^1(\Omega)$.

Proof. (Wolters et al., 2007a, Theorem 3.7) □

For the weak formulation of the subtraction approach, we can introduce a continuous finite element formulation in the same way as introduced in (1.12). Especially the bilinear form a is unchanged compared to the non-subtraction approach. For a one-layer model with homogeneous conductivities, (Wolters et al., 2007a) derived error estimates for the finite element solution of the correction potential. The first one gives an estimate of the error in the H^1 norm.

Theorem 1.3 (Quantitative error estimate for one-layer model (Wolters et al., 2007a, Theorem 3.8))**.**

$$\|\tilde{u} - \tilde{u}_h\|_1 \leq C_1 h \|\tilde{u}\|_2 \tag{1.22}$$

Proof. (Wolters et al., 2007a, Theorem 3.8) □

The second estimate considers the error in the L^2 norm.

Lemma 1.3 (Aubin-Nitsche (Wolters et al., 2007a, Lemma 3.9))**.**

$$\|\tilde{u} - \tilde{u}_h\|_0 \leq C_1 h^2 \|\tilde{u}\|_2 \tag{1.23}$$

Proof. (Wolters et al., 2007a, Lemma 3.9) □

Note that this error estimate only considers the error in the correction potential $\tilde{u}_h$ and not the full potential.

Transfer matrix approach Usually, the solution of the EEG forward problem u is used in an inverse procedure to find the electrical activity underlying data measured at electrodes on the head surface. Within these inverse procedures, the EEG forward problem has to be solved for many different source locations. These electrode evaluations can be represented as point evaluations or by considering the electrode impedances and their areas in the complete electrode model (Pursiainen et al., 2018, 2012). Let $N_e \in \mathbb{N}$ denote the number of electrodes. The evaluation for both of these approaches can be represented as the application of a linear operator $R \in \mathbb{R}^{N_e \times N}$:

$$U = Ru$$

where $U \in \mathbb{R}^{N_e}$ denotes the resulting discrete values. In the following, we will only consider the point electrode model for electrodes located at $p_0, \ldots, p_{N_e-1} \in \mathbb{R}^d$. The entries $r_{k,i}$ of the linear restriction operator are given as $r_{k,i} = \varphi_i(p_0) - \varphi_i(p_k)$, where φ_i denotes the i-th basis function of the finite element space. As the solution of the EEG forward problem is only determined up to a constant, the first electrode is chosen as a reference electrode and set to zero. Usually, the number of source locations N_s, for which the EEG forward problem has to be solved, strongly exceeds the number of electrodes, i.e., $N_s \gg N_e$. Standard electrode montages consist of up to a few hundred electrodes, e.g., the common 10-10 system contains 74 electrodes (Oostenveld and Praamstra, 2001), while the number of sources within a discrete source space might contain more than 100 000 sources (cf. Section 3.1) and the full solution of the EEG forward problem is computationally highly

expensive. An approach to circumvent this high computational cost can be found in the transfer matrix approach (De Munck et al., 2012; Gençer and Acar, 2004; Weinstein et al., 2000; Wolters et al., 2004), which is closely related to the adjoint approach (Vallaghé et al., 2008). Replacing the solution u by $A^{-1}b$ we get $U = RA^{-1}b = Tb$ with the transfer matrix $T = RA^{-1} \in \mathbb{R}^{N_e \times N}$, where n denotes the dimension of the finite element space. This transfer matrix T can be computed by solving $AT^t = R^t$, considering the symmetry of the stiffness matrix A. The solution can be performed for each column of T^t and R^t separately. Once the transfer matrix has been computed, the potential differences at the electrode positions can be computed by assembling the right-hand side vector and performing a matrix vector multiplication. Thus, in order to compute a full lead field matrix, the linear system has to be solved only N_e times. This approach can be used for almost any kind of discretization of the EEG forward problem, including the approaches presented in the subsequent chapters.

1.3 A Discontinuous Galerkin Finite Element Method

Compared to the continuous finite element methods described in Section 1.2, discontinuous Galerkin methods do not enforce a global continuity of the potential. In (Arnold et al., 2002), a unified definition and a common analysis of various discontinuous Galerkin methods has been presented. Of special interest are the results of (Engwer et al., 2017), where a discontinuous Galerkin method of the Subtraction approach for the EEG forward problem has been derived. In the following, we will briefly introduce the general formulation of the symmetric, weighted interior penalty discontinuous Galerkin method. Its description mainly follows (Arnold et al., 2002) but also takes ideas and notations from (Di Pietro and Ern, 2011) and (Engwer et al., 2017) into account.

Similar to the previous section, $\Omega \subset \mathbb{R}^d$ denotes a domain and $\mathcal{T}_h(\Omega)$ denotes a geometry conforming tessellation of Ω with an element diameter of $h \in \mathbb{R}$. The discrete space representing test and ansatz functions is given as the space of piecewise polynomial functions.

Definition 1.14 (Broken polynomial space)**.** *The broken polynomial space of degree $k \in \mathbb{N}$ is defined as*

$$V_h^k := \left\{ u \in L^2(\Omega) : u|_E \in P^k(E), E \in \mathcal{T}_h(\Omega) \right\}$$

for a space P^k of local polynomials of degree $k \in \mathbb{N}$.

Note that these functions are not assumed to be continuous across element boundaries. The polynomial space that is used depends on the shape of the elements of the tessellation. For tetrahedrons, we will use the space spanned by the basis functions

$$\mathbb{P}_k(E) = \left\{ x^\alpha : \alpha \in \mathbb{N}^d \wedge |\alpha|_1 \le k \right\},$$

using the multi-index notation $x^\alpha = \prod_i x_i^{\alpha_i}$ (cf. Definition 1.2). For hexahedrons we will use the space spanned by

$$\mathbb{Q}_k(E) = \left\{ x^\alpha : \alpha \in \mathbb{N}^d \wedge |\alpha|_\infty \le k \right\}.$$

In the following we will mainly use a first order space, i.e., $k = 1$ and will omit k if no ambiguities

arise. The set of intersections between two elements and between an element and the domain boundary is called the *skeleton* of the tessellation.

Definition 1.15 (Skeleton)**.** *The internal skeleton of a tessellation $\mathcal{T}_h(\Omega)$ is defined as*

$$\Gamma_h^{\text{int}} := \{\underbrace{\partial E_e \cap \partial E_f}_{=:\gamma_{ef}} : E_e, E_f \in \mathcal{T}_h(\Omega), E_e \neq E_f, |\gamma_{ef}| > 0\}$$

and the skeleton of a triangulation is defined as

$$\Gamma_h := \Gamma_h^{\text{int}} \cup \{\underbrace{\partial E_e \cap \partial \Omega}_{=:\gamma_e} : E_e \in \mathcal{T}_h(\Omega), |\gamma_e| > 0\}.$$

On the skeleton, the functions of the broken polynomial space are not uniquely defined but can be assigned two values, one from either side of the intersections. In the following descriptions, we will make use of an operator which expresses the difference between the values of both sides, i.e., the *jump* of the function on an interface.

Definition 1.16 (Jump)**.** *The jump of a scalar function u or a vector-valued function $\boldsymbol{v}$ on an edge γ_{ef} between two elements $E_e, E_f \in \mathcal{T}_h(\Omega)$ is defined as*

$$[\![u]\!] := u|_{E_e}\boldsymbol{n}_e + u|_{E_f}\boldsymbol{n}_f$$
$$[\![\boldsymbol{v}]\!] := \langle \boldsymbol{v}|_{E_e}, \boldsymbol{n}_e \rangle + \langle \boldsymbol{v}|_{E_f}, \boldsymbol{n}_f \rangle$$

where $\boldsymbol{n}_e, \boldsymbol{n}_f \in \mathbb{R}^d$ denote the unit outer normals on E_e and E_f, respectively.

Note that the jump of a scalar function is a vector and the jump of a vector-valued function is a scalar. Another operator on the skeleton that will be used in the definition of the discontinuous Galerkin method is the *weighted average* operator (Di Pietro and Ern, 2011).

Definition 1.17 (Weighted average)**.** *The weighted average of a (scalar or vector-valued) function u on an edge γ_{ef} between two elements $E_e, E_f \in \mathcal{T}_h(\Omega)$ is defined as*

$$\{u\} := \omega_e u|_{E_e} + \omega_f u|_{E_f}$$

with two weights $\omega_e, \omega_f \in \mathbb{R}$ with $\omega_e + \omega_f = 1$. If not stated differently, these weights will be defined as

$$\omega_e = \frac{\delta_f}{\delta_e + \delta_f} \qquad \omega_f = \frac{\delta_e}{\delta_e + \delta_f}$$
$$\delta_e = \boldsymbol{n}_e^t \sigma \boldsymbol{n}_e \qquad \delta_f = \boldsymbol{n}_f^t \sigma \boldsymbol{n}_f$$

where $\boldsymbol{n}_e, \boldsymbol{n}_f \in \mathbb{R}^d$ denote the unit outer normals on E_e and E_f, respectively and $\sigma : \Omega \to \mathbb{R}^{d \times d}$ denotes a symmetric, positive definite conductivity tensor. The skew-weighted average is denoted by

$$\{u\}^* := \omega_f u|_{E_e} + \omega_e u|_{E_f}.$$

A direct computation using the definitions of the jump and average shows the following *multiplicative property* which will be used in the subsequent sections.

Lemma 1.4. *For $u, v \in L^2(\Omega)$ and an edge $\gamma_{ef} \in \Gamma_h^{\text{int}}$ the following multiplicative property holds:*

$$[\![uv]\!] = [\![u]\!]\, \{v\}^* + \{u\}\, [\![v]\!]\,.$$

Proof. In the following, we use the notation $u_e := u|_{E_e}$.

$$
\begin{aligned}
[\![uv]\!] &= u_e v_e \boldsymbol{n}_e + u_f v_f \boldsymbol{n}_f \\
&= \underbrace{(\omega_e + \omega_f)}_{=1} u_e v_e \boldsymbol{n}_e + \underbrace{(\omega_e + \omega_f)}_{=1} u_f v_f \boldsymbol{n}_f + \omega_e u_e v_f \underbrace{(\boldsymbol{n}_e + \boldsymbol{n}_f)}_{=0} + \omega_f u_f v_e \underbrace{(\boldsymbol{n}_e + \boldsymbol{n}_f)}_{=0} \\
&= (u_e \boldsymbol{n}_e + u_f \boldsymbol{n}_f)(\omega_f v_e + \omega_e v_f) + (\omega_e u_e + \omega_f u_f)(v_e \boldsymbol{n}_e + v_f \boldsymbol{n}_f) \\
&= [\![u]\!]\, \{v\}^* + \{u\}\, [\![v]\!]
\end{aligned}
$$

$\square$

Using the definitions of the jump and weighted average terms, we can define the general symmetric weighted interior penalty discontinuous Galerkin method

Definition 1.18 (SWIPG)**.** *The symmetric weighted interior penalty discontinuous Galerkin method (SWIPG) is defined as: Find $u_h \in V_h$ such that*

$$a(u_h, v_h) + J(u_h, v_h) = l(v_h)$$

for all $v_h \in V_h$, where

$$a(u_h, v_h) = \int_\Omega \langle \sigma \nabla u_h, \nabla v_h \rangle \, \mathrm{d}x - \int_{\Gamma_h^{\text{int}}} \langle \{\sigma \nabla u_h\}, [\![v_h]\!] \rangle + \langle \{\sigma \nabla v_h\}, [\![u_h]\!] \rangle \, \mathrm{d}s$$

$$J(u_h, v_h) = \eta \int_{\Gamma_h^{\text{int}}} \frac{\hat{\sigma}_\gamma}{\hat{h}_\gamma} \langle [\![u_h]\!], [\![v_h]\!] \rangle \, \mathrm{d}s\,.$$

The term $l(v_h)$ describes a general source term and will be defined in subsequent sections. The weighting parameter $\hat{\sigma}_\gamma$ on an intersection γ between elements e and f is defined as the harmonic average of the projected conductivity tensors (cf. Definition 1.17)

$$\hat{\sigma}_\gamma = \frac{2\delta_e \delta_f}{\delta_e + \delta_f}$$

The local mesh-size parameter $\hat{h}_\gamma$ is chosen following (Georgoulis et al., 2007) as

$$\hat{h}_\gamma = \frac{\min(\text{meas}_d(E_e), \text{meas}_d(E_f))}{\text{meas}_{d-1}(\gamma)}$$

where meas_d and meas_{d-1} denote the d-dimensional volume measure and $d-1$-dimensional surface measure respectively.

The term J forms a penalty term that penalizes jumps in the potential on the internal skeleton and is used to obtain coercivity of the combined bilinear form using the penalty parameter $\eta \in \mathbb{R}$. The construction of the source term l in Definition 1.18 will be the subject of the following

sections. In (Di Pietro and Ern, 2011) theoretical properties of the SWIPG scheme with piecewise constant conductivity tensors are investigated. It is assumed that the exact solution follows a certain regularity $u \in V_*$ for $V_* := H^2$. Note that, in general, the solution of the EEG forward problem with the singular right-hand side does not fulfill this regularity assumption.

Lemma 1.5 (Consistency (Di Pietro and Ern, 2011, Lemma 4.49)). *Assume $u \in V_*$. Then, for all $v_h \in V_h$*

$$a(u, v_h) + J(u, v_h) = l(v_h)$$

Lemma 1.6 (Discrete Coercivity (Di Pietro and Ern, 2011, Lemma 4.51)). *Let η_0 and $\| \cdot \|_{swipg}$ be defined as in (Di Pietro and Ern, 2011, Eq. (4.69)). Then, for all $\eta > \eta_0$, the SWIPG bilinear form is coercive on V_h with respect to the $\| \cdot \|_{swipg}$-norm, i.e.,*

$$\forall v_h \in V_h, \quad a(v_h, v_h) + J(v_h, v_h) \geq C_\eta \|v_h\|_{swipg}^2$$

with a constant $C_\eta \in \mathbb{R}$.

Lemma 1.7 (Boundedness (Di Pietro and Ern, 2011, Lemma 4.52)). *Let V_{*h} and $\| \cdot \|_{swipg,*}$ be defined as in (Di Pietro and Ern, 2011). Then, there is a $C_{bnd} \in \mathbb{R}$, independent of h and σ, such that*

$$\forall (v, y_h) \in V_{*h} \times V_h, \quad a(v, y_h) + J(v, y_h) \leq C_{bnd} \|v\|_{swipg,*} \|y_h\|_{swipg}$$

Combining Lemmata 1.5, 1.6 and 1.7 provides existence and uniqueness of a solution for the SWIPG method, under the assumptions noted above.

A Discontinuous Subtraction Approach In (Engwer et al., 2017) a discontinuous Galerkin discretization of the subtraction approach (cf. Section 1.2) has been presented. Its main motivation stemmed from the observation of unphysical skull leakages in the continuous Galerkin discretization on hexahedral meshes (Sonntag et al., 2013). These leakages might occur if the resolution of the imaging data is very poor or if the skull compartment is very thin. This might be especially relevant in infant studies (Roche-Labarbe et al., 2008) or for temporal bone areas, where the skull thickness is 2 mm or even less (Kwon et al., 2006). In such cases, an element of the CSF compartment might be connected to an element of the skin compartment via a single node. Due to the nature of the Lagrange finite element method, a basis function at such a node provides a direct shortcut for the current between the CSF and the skin compartment. The resulting observations are unphysical hotspots in the current strength. In (Dannhauer et al., 2011) it was shown, that an appropriate modeling of the skull is especially important for an accurate EEG forward solution and thus errors in the skull compartment can severely impact the accuracy of the method.

One general property of Poisson's equation, which forms the basis and motivation of the discontinuous Galerkin approach in (Engwer et al., 2017), is the conservation of charge.

$$\int_{\partial K} \langle \sigma \nabla u, \boldsymbol{n} \rangle \, \mathrm{d}s = \int_K f_y \, \mathrm{d}x$$

for an arbitrary control volume $K \subset \Omega$ and $f_y := \nabla \cdot J^p$. Introducing the splitting of the potential

$u = \tilde{u} + u^{\infty}$ into the singularity potential u^{∞} and the correction potential $\tilde{u}$ and the corresponding splitting of the conductivity tensor $\sigma = \tilde{\sigma} + \sigma^{\infty}$, we obtain a conservation property for the subtraction approach

$$\int_{\partial K} \langle \sigma \nabla \tilde{u}, \boldsymbol{n} \rangle \, \mathrm{d}s = - \int_{K} \nabla \cdot \tilde{\sigma} \nabla u^{\infty} \, \mathrm{d}x \,.$$

We note that for an arbitrary control volume, the continuous Galerkin finite element method does not fulfill this conservation property, as the constant function on the control volume is not an element of the test function space. In (Engwer et al., 2017), a derivation of the SWIPG method for the subtraction approach is presented, which results in the discrete weak formulation: Find $\tilde{u}_h \in V_h$ such that

$$a(\tilde{u}_h, v_h) + J(\tilde{u}_h, v_h) = l(v_h) \quad \forall v_h \in V_h$$

with a and J as defined in the general SWIPG scheme in Definition 1.18 and the source term

$$l(v_h) = - \int_{\Omega} \langle \tilde{\sigma} \nabla u^{\infty}, \nabla v_h \rangle \, \mathrm{d}x + \int_{\Gamma_h^{\mathrm{int}}} \langle \{\tilde{\sigma} \nabla u^{\infty}\}, [\![v_h]\!] \rangle \, \mathrm{d}s - \int_{\partial \Omega} \langle \sigma^{\infty} \nabla u^{\infty}, \boldsymbol{n} \rangle \, v_h \, \mathrm{d}s \,.$$

For this SWIPG scheme, a corresponding discrete conservation property can be formulated as

$$\int_{\partial K} \{\sigma \nabla \tilde{u}_h\} - \eta \frac{\hat{\sigma}_{\gamma}}{\hat{h}_{\gamma}} [\![\tilde{u}_h]\!] \, ds = \int_{K} -\nabla \cdot \tilde{\sigma} \nabla u^{\infty} \, ds$$

which converges to the conservation property for the exact solution for $h \to 0$.

In (Engwer et al., 2017), numerical studies were performed to investigate convergence properties and to compare the discontinuous Subtraction approach with the continuous counterpart, both in a four-layer sphere model as well as in a realistic six-compartment head model. In the sphere studies, both methods showed similar results, while the DG method outperformed the CG method for lower mesh resolutions and for spheres with thinner skull compartments.

1.4 A Mixed Finite Element Method

In (Vorwerk et al., 2017) a mixed finite element method (MixedFEM) for solving the EEG forward problem has been presented. Instead of discretizing the scalar second order Poisson's equation, a system of first order equations is derived and subsequently discretized. The resulting method is, similarly to the DG-FEM approach, able to preserve the current on the discrete level.

The basis of the mixed approach is the reformulation of Poisson's equation as: Find $(\boldsymbol{j}, u)$ such that

$$\boldsymbol{j} + \sigma \nabla u = \boldsymbol{J}^p$$
$$\nabla \cdot \boldsymbol{j} = 0 \quad \text{in } \Omega,$$
$$\langle \boldsymbol{j}, \boldsymbol{n} \rangle = 0 \quad \text{on } \partial \Omega.$$

In order to derive a weak formulation for this system, we introduce the space of vector-valued L^2

functions with a square-integrable divergence:

$$H(\text{div}; \Omega) = \left\{ \boldsymbol{q} \in L^2(\Omega)^3 : \nabla \cdot \boldsymbol{q} \in L^2(\Omega) \right\}.$$

Together with a norm taking the divergence into account, $H(\text{div}; \Omega)$ forms a Hilbert space. The homogeneous Neumann boundary condition is embedded into the function space by setting:

$$H_0(\text{div}; \Omega) = \left\{ \boldsymbol{q} \in H(\text{div}; \Omega) : \langle \boldsymbol{q}, \boldsymbol{n} \rangle = 0 \text{ on } \partial\Omega \right\}.$$

The weak formulation of the MixedFEM approach then reads: Find $(u, \boldsymbol{j}) \in L^2(\Omega) \times H_0(\text{div}; \Omega)$, such that

$$a(\boldsymbol{j}, \boldsymbol{q}) + b(\boldsymbol{q}, u) = l(\boldsymbol{q}) \quad \text{for all } \boldsymbol{q} \in H_0(\text{div}; \Omega),$$
$$b(\boldsymbol{j}, v) = 0 \qquad \text{for all } v \in L^2(\Omega),$$

with

$$a(\boldsymbol{p}, \boldsymbol{q}) = \left\langle \sigma^{-1}\boldsymbol{p}, \boldsymbol{q} \right\rangle_{L^2(\Omega)^3}$$
$$b(\boldsymbol{p}, v) = \left\langle \nabla \cdot \boldsymbol{p}, v \right\rangle_{L^2(\Omega)}$$
$$l(\boldsymbol{q}) = \left\langle \sigma^{-1}\boldsymbol{J}^p, \boldsymbol{q} \right\rangle_{L^2(\Omega)^3}.$$

In (Vorwerk et al., 2017), conditions are presented for the existence and uniqueness of a solution for this weak formulation. Furthermore, discrete spaces for representing the vector-valued flux and the scalar potential are introduced. Using these spaces, two different representations of the dipolar source terms are introduced: a direct application of the delta distribution to the flux, and a projection of the source term into the potential space. The resulting discretized linear system has a saddle-point structure, and specifically tailored linear solvers have to be employed for its efficient solution.

Both sphere-model studies as well as simulations using a realistically shaped head model are performed in (Vorwerk et al., 2017). The MixedFEM approach was compared to the conforming Lagragian finite element method (CG-FEM) and the discontinuous Galerkin method (DG-FEM). So far, only evaluations in structured hexahedral meshes, but no evaluations in geometry-adapted hexahedral meshes or in tetrahedral meshes have been performed. However for the hexahedral models, MixedFEM showed comparable accuracies to CG-FEM in standard high resolution scenarios but outperformed CG-FEM in scenarios containing thin structures, where it showed an accuracy similar to DG-FEM.

1.5 Conclusion

In this chapter, we presented the established background and theory of finite element methods for solving the EEG forward problem. We introduced the physiological origin of the signals measured by EEG and recalled the derivation of Poisson's equation. Following the introduction of the weak formulation, we presented the classical conforming finite element method using Lagragian elements.

We described the discretization of the dipolar source term using direct source models such as the partial integration approach, the approach of St. Venant or the Whitney approach and using the indirect subtraction approach. Besides the classical conforming finite element method, we recalled the recent developments for a discontinuous Galerkin approach and a mixed finite element method.

Even though the methods presented in this chapter are well established, there are still some open questions. A common problem among finite element methods for the EEG forward problem is the handling of the singular source term provided by the mathematical point dipole. A popular choice is the approach following the principle of St. Venant which has been briefly mentioned above. It replaces the singular point dipole by a set of point monopoles which are still singular. Instead of using the monopolar sources, a conforming approach could be considered, which approximates the dipolar source term within the discrete function space. An open question is the relation of the Venant approach to the partial integration source model. For the discontinuous Galerkin method, the Venant approach has not yet been introduced and evaluated. A main disadvantage of the Subtraction approach compared to the direct models is its high computational cost due to the increased support of the right-hand side. This could be remedied by restricting the support of the introduced singularity potential to a small patch around the source location. These modifications to the Venant and subtraction source models will be addressed in Chapter 2. The approaches introduced in this chapter have in common that they require a tessellation that is adapted to the model domain. The construction of a highly accurate tessellation is not straightforward and might even involve manual interaction. Instead, discretization approaches which consider the model geometry without the need for tailored tessellation could be evaluated. Such approaches will be introduced and evaluated in Chapter 3.

Source Models for Modern Finite Element Methods

The conforming finite element method using Lagrangian elements is the predominant method when considering finite element methods for solving the EEG forward problem. For this approach, various discretizations of singularity provided by the dipolar source term have been presented. Among these source models the *Venant approach*, following the principle of St. Venant, is widely used in practice, due to its accuracy and comparatively low computational costs. In Section 2.1, we will address open questions regarding the Venant approach. We will show its connection to the partial integration source model and demonstrate the effect of including mixed higher order moments in its interpolation scheme. Instead of replacing the dipolar source term by a set of monopolar sources, we show the possibility of using a conforming source representation.

Recently, a non-conforming finite element method has been presented: the discontinuous Galerkin method. In this method, the discrete functions are coupled weakly on element boundaries, instead of using globally continuous ansatz functions. So far, only the partial integration and the subtraction approach have been described for this method. We will introduce the Venant approach in this discontinuous setting in Section 2.2.

While the subtraction approach shows a high accuracy and a mathematical theory is available for this approach, its main downside is its high computational cost, which makes it unfeasible in practice for many applications. In Section 2.3 we will present a modification of the subtraction approach which reduces this cost by decreasing the size of the support of the source discretization.

2.1 Source Models Following the Principle of St. Venant

The idea of the Venant approach for discretizing the dipolar source term of the EEG forward problem follows the principle of St. Venant. It replaces the source given by the mathematical point dipole by an equivalent source distribution which maintains certain properties of the original source. In the description and definition of the Venant approach, we will provide a generalization of the ideas given e.g., in (Vorwerk, 2016; Wolters et al., 2007b).

In (Vorwerk, 2016), $N \in \mathbb{N}$ monopoles are placed on mesh vertices $x_0, \dots, x_{N-1} \in \mathbb{R}^d$ close to the source location $x_{\mathrm{dp}} \in \mathbb{R}^d$. By scaling the monopoles with the strengths $q_0, \dots, q_{N-1} \in \mathbb{R}$, the discrete source distribution is given as $\rho := \sum_{i=0}^{N-1} q_i \delta_{x_i}$ where δ_{x_i} denotes the delta distribution at x_i. We will call this source distribution the *monopolar Venant approach*. The goal is to find a set of monopole strength, such that for $l \in \{0, \dots, N_m - 1\}, N_m \in \mathbb{N}$, the centered moments, defined as

$$S_l(f) := \int_\Omega (x - x_{\mathrm{dp}})^l f(x)\, dx, \tag{2.1}$$

are maintained. Inserting the discrete source distribution ρ into (2.1) and resolving the delta distribution results in

$$S_l(\rho) = \sum_{i=0}^{N-1} q_i S_l(\delta_{x_i}) = \sum_{i=0}^{N-1} q_i (x_i - x_{\mathrm{dp}})^l.$$

For the dipolar source term $\nabla \cdot \boldsymbol{J}^p = \nabla \cdot \boldsymbol{M} \delta_{x_{\mathrm{dp}}}$, where $\boldsymbol{M} \in \mathbb{R}^d$ denotes the dipole moment, we obtain

$$S_l(\nabla \cdot \boldsymbol{J}^p) = \begin{cases} -M, & l = 1 \\ 0, & \text{else} \end{cases}.$$

The monopole strengths are computed such that

$$\sum_{i=0} q_i S_l(\delta_{x_i}) = S_l(\nabla \cdot \boldsymbol{J}^p),$$

for all $l \in \{0, \dots, N_m - 1\}$.

In the following, we will generalize this monopolar Venant approach, such that it is applicable for different discretization schemes, as well as for different representations of the discrete source term. Our goal is to approximate the dipolar source term by a more simple, but equivalent source distribution. The equivalence of two source distributions will be measured by a linear operator $T : \mathcal{D}'(\Omega) \to \mathbb{R}^n, n \in \mathbb{N}$. We will call two distributions $f, g \in \mathcal{D}'(\Omega)$ equivalent with respect to the operator T, written as $f \cong_T g$, if the values of T are equal, i.e.,

$$f \cong_T g \quad \Leftrightarrow \quad T(f) = T(g). \tag{2.2}$$

Note that $\cong_T$ does indeed define an equivalence relation on $\mathcal{D}'(\Omega)$. The problem of finding an equivalent source distribution for the dipolar source term can be seen as a classical inverse problem: given measured observations $y := T(\nabla \cdot \boldsymbol{J}^p) \in \mathbb{R}^n$ of the dipolar source term $\nabla \cdot \boldsymbol{J}^p$, find $g \in G \subset \mathcal{D}'(\Omega)$ such that $T(g) = y$. Here, G denotes a discrete subspace of $\mathcal{D}'(\Omega)$ which forms the basis of a Venant approach and will be described further below. Once such an approximation is found, the right-hand side of the partial differential equation is given by $g(\varphi_i)$ for every test function φ_i. As the inverse problem usually admits to multiple solutions, we will formulate the problem in a variational

setting using Tikhonov regularization:

$$g = \arg\min_{\tilde{g} \in G} J(\tilde{g}), \quad J(\tilde{g}) := \frac{1}{2}\|T(\tilde{g}) - y\|_2^2 + \lambda\|L(\tilde{g})\|_2^2, \tag{2.3}$$

with a regularization parameter $\lambda \in \mathbb{R}^{\geq 0}$ and an operator $L : \mathcal{D}'(\Omega) \to \mathbb{R}^n$ which can be used to incorporate a-priori-knowledge of the desired source distribution. If we search for the equivalent source distribution in the finite dimensional space G, which is spanned by the basis $\xi_0, \dots \xi_{m-1} \in \mathcal{D}'(\Omega)$, $m \in \mathbb{N}$, the solution of (2.3) can be found by solving the linear system

$$(A^t A + \lambda B^t B)q = A^t y, \tag{2.4}$$

with $A = (T_i(\xi_j))_{i,j}$ and $B = (L_i(\xi_j))_{i,j}$, where T_i and L_i denote the i-th component of T and L respectively.

The monopolar Venant approach introduced above can be formulated within this general framework. The subspace G used to represent the approximated source term is chosen as the span of a set of monopolar sources. The monopoles are located at $x_0, \dots, x_{N-1} \in \mathbb{R}^d$ and lead to the basis functions $\xi_j = \delta_{x_j}$, where δ_x denotes the delta distribution at x. The linear operator $T : \mathcal{D}'(\Omega) \to \mathbb{R}^n$ that measures the equivalence is chosen as the one computing the centered moments around the source location x_{dp}. For $i \in \{0, \dots, n-1\}$ it is defined as

$$\begin{aligned} T_i(u) &:= u(t_i), \\ t_i(x) &:= \left(\frac{x - x_{\text{dp}}}{C}\right)^{\alpha_i}, \end{aligned} \tag{2.5}$$

for a set of multi-indices $\alpha_0, \dots, \alpha_{n-1} \in \mathbb{N}^d$, where $C \in \mathbb{R}$ denotes a scaling factor which is used to improve the conditioning of the linear system (2.4). In the description of the monopolar Venant approach that was presented above, the multi-indices where chosen as the zero vector and the vectors consisting of a single non-zero entry $l \in \mathbb{N}$ with $l < N_m$. In the following, we will also allow moments with mixed multi-indices, i.e., multi-indices with more than one non-zero entry. As the monopolar Venant approach has been developed with CG-FEM and first order ansatz functions in mind, it seems natural to choose a set of mesh vertices for the monopole locations. Following (Wolters et al., 2007b), for a dipole position x_{dp}, the closest mesh vertex is identified and monopoles are placed on all mesh vertices sharing an element with the closest vertex. As a weighting matrix B, which is the discretization of the a-priori operator L, the diagonal matrix consisting of entries

$$\left\|\frac{x_i - x_{\text{dp}}}{C}\right\|^s,$$

with $s \in \{0, 1\}$ is used. Setting $s = 0$ penalizes the overall strengths of the monopoles, independent on their location, while setting $s = 1$ leads to stronger monopoles closer to the source location. Note that it is also possible to choose different sets of vertices and thus increasing or decreasing the dimension of the discrete source space. As it turns out, choosing a small set of vertices consisting only of the vertices of the element containing the dipole, will lead to the same right-hand side as the partial integration approach (see below for a general statement).

While the choice of mesh vertices is beneficial for this specific finite element space, it is not directly

a) vertex monopoles   **b)** element monopoles   **c)** conforming
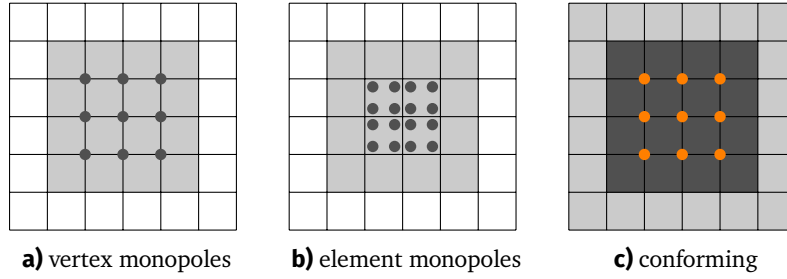
Figure 2.1: dark gray shows the monopoles or the support of the source approximation, light gray shows the domain of functions with non-zero right-hand side, orange shows the degrees of freedom in a CG discretization.source closest to the central vertex.

applicable to a DG-FEM space, as functions within the DG-FEM space can be discontinuous at the vertex locations. A strategy in this case can be found in choosing monopoles in the interior of the mesh elements. In order to simplify the choice of the internal positions, we use the points of a Gaussian quadrature rule on each element of a set of elements around the source location (Quarteroni et al., 2010).

The monopolar Venant is a simplification of the dipolar source term and offers a direct way to enrich the discrete source space compared to the partial integration approach but it is still a distribution that is not an element of $L^2(\Omega)$. However, the general definition of the Venant approach can also be used with a discrete source term in $L^2(\Omega)$. In the following, we will describe a conforming discretization that is a member of the finite element space. This approach will be called the *conforming Venant approach*. The basis functions of the source space are chosen as a set of basis functions $\varphi_j \in V_h$ of the finite element space. The equivalence, given by the linear operator T is again measured by the centered moments, however this time, we use the L^2 scalar product:

$$
\begin{aligned}
T_i(u) &:= \int_\Omega u(x) t_i(x)\, \mathrm{d}x\,, \\
t_i(x) &:= \left(\frac{x - x_{\mathrm{dp}}}{C} \right)^{\alpha_i}.
\end{aligned}
\tag{2.6}
$$

This approach can be directly applied to both CG-FEM and DG-FEM. Similar to the monopolar approach, we use the diagonal matrix consisting of the entries

$$
\int_\Omega \varphi_j(x) \left\| \frac{x - x_{\mathrm{dp}}}{C} \right\|^s \mathrm{d}x\,,
$$

with $s \in 0, 1$ as the discrete a-priori operator L. A visualization of the degrees of freedom and support of the different source models can be seen in Figure 2.1. Additionally, Figure 2.2 shows a visualization of the different source terms for a one-dimensional CG-FEM discretization.

In order to visualize the differences between the different source models, we use an L^2 projection to project the source terms into the ansatz space V_h. Given a right-hand side vector $g \in \mathbb{R}^N$, we are looking for a source term $f \in V_h$ which results in the same right-hand side when tested with a test function $\varphi_i \in V_h$, i.e.,

$$
\langle f, \varphi_i \rangle_{L^2} = g_i \quad \forall i, 0 \leq i < N.
\tag{2.7}
$$

As f is a member of the ansatz space, we have a discrete representation $f(x) = \sum_{j=0}^{N-1} f_j \varphi_j(x)$ for

a) vertex monopoles   **b)** element monopoles   **c)** conforming
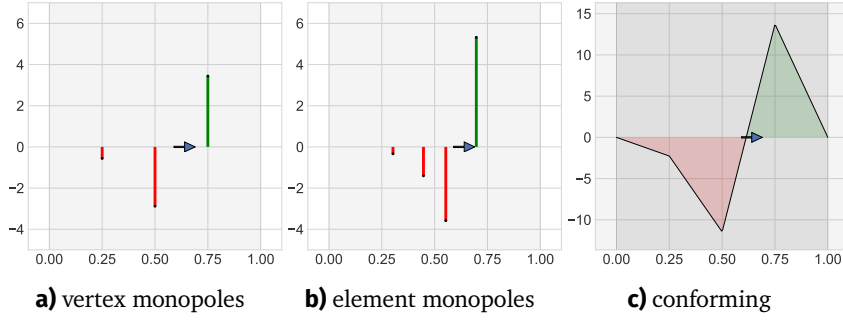
Figure 2.2: Source models of the different Venant approaches in 1d. Positive values are colored in green, negative values are colored in red. A Light gray background highlights the elements with a non-zero right hand side, a dark gray background highlights the support of the source distribution. The dipole is located at 0.59.

coefficients $f_j \in \mathbb{R}$ for $0 \leq j < N$. Inserting this representation into (2.7) gives

$$\sum_{j=0}^{N-1} f_j \left\langle \varphi_j, \varphi_i \right\rangle_{L^2} = g_i \quad \forall i, 0 \leq i < N \tag{2.8}$$

$$\Leftrightarrow Mf = g, \quad M = \left(\left\langle \varphi_i, \varphi_j \right\rangle \right)_{0 \leq i,j < N}, \tag{2.9}$$

with the mass matrix $M \in \mathbb{R}^{N \times N}$. Solving (2.9) will result in a source term $f \in V_h$ that produces the right-hand side g when tested with the basis functions of V_h. Note that (2.9) is uniquely solvable, as $\varphi_i, 0 \leq i < N$ is a basis for V_h.

We create a two dimensional four layer sphere model and put two dipoles into the inner most compartment. The first dipole is located such that the supports of all source models do not touch a compartment boundary. The second dipole is located within an element touching the first conductivity jump. The resulting projected source models can be seen in Figure 2.3. We first observe, that the projections of the monopolar approaches are very similar and mainly differ in magnitude. Although they have a local support, the projection into the ansatz space produces oscillations that have a bigger extent. In comparison, the conforming Venant approach retains its local support, as the discrete source model is already an element of the ansatz space and does not change when applying the projection.

In certain situations, the use of centered moments leads to a discretization that is identical to the partial integration approach (see 1.2). To proof this, we need the following theorem:

Theorem 2.1 (Taylor's formula (Forster, 2008, Chapter 7, Theorem 2)). *Let $E \subset \mathbb{R}^d$ be an open domain, $x,y \in E$ such that $x + t(y - x) \in E$ for all $0 \leq t \leq 1$. Further let $f : E \to \mathbb{R}$ denote a $(k + 1)$-times continuously differentiable function. Then there exists $\theta \in [0, 1]$ such that*

$$f(y) = \sum_{|\alpha| \leq k} \frac{D^\alpha f(x)}{\alpha!} (y - x)^\alpha + \sum_{|\alpha| = k+1} \frac{D^\alpha f\left(x + \theta(y - x)\right)}{\alpha!} (y - x)^\alpha \tag{2.10}$$

Proof. (Forster, 2008, Chapter 7, Theorem 2) □

A polynomial φ of degree $k \in \mathbb{N}$ fulfills the prerequisites of Theorem 2.1, as it is infinitely often

a) mesh   **b)** vertex monopoles   **c)** element monopoles   **d)** conforming
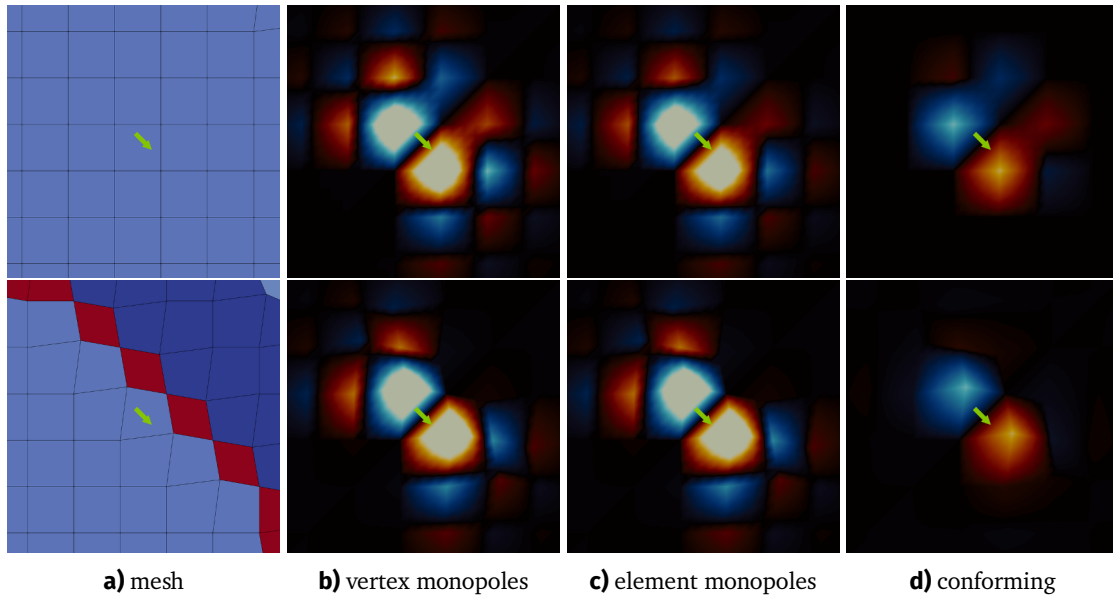
Figure 2.3: Visualization of the different Venant approaches. The two rows show two different source locations. The first column shows the hexahedral mesh. The elements are colored according to their conductivity value. The remaining columns show the different Venant approaches. Depicted is the L^2-projection of the source model into the ansatz space.

differentiable. However, the remainder of (2.10) is zero, as the derivative $D^\alpha \varphi$ is zero for $|\alpha| > k$. Thus, for such a polynomial it holds that

$$\varphi(y) = \sum_{|\alpha| \leq k} \frac{D^\alpha \varphi(x)}{\alpha!} (y - x)^\alpha. \tag{2.11}$$

Note that this also holds for $y \in \overline{E}$.

Corollar 2.1. *Let $E \subset \mathbb{R}^d$ be a convex domain, $x_{\mathrm{dp}} \in E, M \in \mathbb{R}^d$ and $\varphi : E \to \mathbb{R}$ a polynomial of degree $k \in \mathbb{N}$. Let f denote a source distribution fulfilling the Venant equivalence (2.2) for the centered moments up to $|\alpha| \leq k$ with $\mathrm{supp}(f) \subset \overline{E}$. Then it holds that*

$$f(\varphi) = -\left\langle M, \nabla \varphi(x_{\mathrm{dp}}) \right\rangle. \tag{2.12}$$

Proof. Given $x, x_{\mathrm{dp}} \in E$ then $x_{\mathrm{dp}} + t(x - x_{\mathrm{dp}}) \in E$ for all $t \in [0, 1]$ as E is assumed to be convex. Using (2.11) on φ gives

$$f(\varphi) = \sum_{|\alpha| \leq k} \frac{D^\alpha \varphi(x_{\mathrm{dp}})}{\alpha!} f\left((\cdot - x_{\mathrm{dp}})^\alpha \right) \tag{2.13}$$

As f is assumed to fulfill (2.2) with the centered moments, it holds that

$$f\left((\cdot - x_{\mathrm{dp}})^\alpha \right) = \begin{cases} -M_i, & |\alpha|_1 = 1, \alpha_i = 1 \\ 0, & \text{else} \end{cases}.$$

Inserting this property into (2.13) results in

$$f(\varphi) = -\left\langle \boldsymbol{M}, \nabla\varphi(x_{\mathrm{dp}}) \right\rangle.$$

□

For the definition of the support of a distribution see 1.6. Note that the Venant equivalence is only needed up to exponents $|\alpha| \leq k$, as the higher order derivatives of the polynomial vanish. Note additionally, that the right-hand side of (2.12) is the right-hand side of the partial integration approach. Especially the restriction on the support of the source distribution supp(f) $\subset \overline{E}$ makes Corollar 2.1 not applicable to an arbitrary Venant approach. However, if the support of the approximate source distribution is contained in the element which also contains the dipole and if the source distribution fulfills the Venant equivalence with respect to the centered moments, the resulting right-hand side is identical to the one given by the partial integration approach. This also means that in such a situation, increasing the number of degrees of freedom for representing the discrete source term above what is necessary to find a distribution that fulfills (2.2) does not lead to a different right-hand side with an increased accuracy. If the support of the discrete source distributions spans multiple elements the test functions are not polynomials on the support and Taylor's formula is not applicable.

2.1.1 Validation Studies

In this section we will validate the Venant approaches presented above and investigate different properties of the source models when solving the EEG forward problem in a four-layer sphere model.

Using Higher Order Mixed moments   In the monopolar Venant approach as reported in the literature (Vorwerk, 2011), only the diagonal moments, i.e., moments whose corresponding multi-index has only exactly one non-zero entry, are considered. When employing higher order moments, one can also include mixed moments, e.g., non-diagonal entries. The partial integration approach, seen as a special case of the Venant approach, uses these mixed moments in its natural formulation. We use a 1 mm hexahedral mesh as shown in Table A.2. The nodes of the mesh are shifted towards neighboring minority compartments following the geometry-adaption approach presented in (Wolters et al., 2007b). We use a shifting parameter of 0.3. We employ a four-layer sphere model which is described in Table A.1 and use the sources shown in Table A.3. Monopolar sources are placed on the corners of all elements which contain the mesh node that is closest to the source position. If an element is not part of the brain compartment, it is omitted from this patch. We include moments of orders 0,1 and 2 and use a reference length $C = 20$ mm. As a relaxation factor we set $\lambda = 10^{-6}$ and use the exponent $s = 1$ for the weighting matrix. If not stated differently, we will use these parameters in every subsequent study which uses the Venant approach. The results of the numerical solution at the electrodes are compared to the quasi-analytical solution (De Munck and Peters, 1993). We use two measures to quantify the difference between two solutions: the

relative difference measure (RDM)

$$RDM(u_{\mathrm{num}}, u_{\mathrm{ana}}) := 50 \left\| \frac{u_{\mathrm{num}}}{\|u_{\mathrm{num}}\|_2} - \frac{u_{\mathrm{ana}}}{\|u_{\mathrm{ana}}\|_2} \right\|_2 \% \tag{2.14}$$

and the *magnitude error* (MAG)

$$MAG(u_{\mathrm{num}}, u_{\mathrm{ana}}) := 100 \left(\frac{\|u_{\mathrm{num}}\|_2}{\|u_{\mathrm{ana}}\|_2} - 1 \right) \% \tag{2.15}$$

where $u_{\mathrm{num}}, u_{\mathrm{ana}} \in \mathbb{R}^{N_e}$ denote the potential values of the numerical and analytical solution evaluated at the electrodes and referenced to a zero average, respectively. The RDM can be interpreted as a measure of the error with respect to the topology. It is bound from below by 0 % and from above by 100 %, with an optimal value of 0 %. As the name suggests, the magnitude error measures the relative difference in the magnitude between the numerical and analytical solution. A positive MAG error indicates an overestimation of the magnitude by the numerical solution, while a negative values indicates an underestimation. It is bounded from below by –100 % and not bounded from above, with an optimal value of 0 %. Figure 2.4 shows the RDM and MAG measures of the monopolar Venant approach including and not including the mixed moments on a 1 mm geometry-adapted hexahedral mesh. For the inner sources, i.e., sources which do not lie in an element touching the first conductivity jump, we observe a general decrease of the inter-quartile ranges and the total ranges for the RDM of the mixed moments approach compared to the approach not using the mixed moments for both, radial and tangential source orientations. The MAG error is less affected and shows no significant difference for the inner sources. For more eccentric sources, the difference between both approaches is less clear. Figure 2.5 shows the effect of using mixed moments for the RDM and MAG errors on a tetrahedral sphere model. We create the sphere model using a constrained Delaunay-triangulation with a volume constraint (Si, 2015), resulting in a tetrahedral mesh with 274 401 nodes and 1 551 508 elements. In general, the trend of the error measures behaves similarly compared to the hexahedral model, but more pronounced. Overall, we observe a significant decrease of the RDM error for radial and tangential sources. For the highest eccentricities, the approach without mixed moments shows strong outliers with an increased RDM and MAG error. These outliers are not observed when including mixed moments. For both orientations, the total range of the MAG error is reduced, while tangential sources also show a reduced inter-quartile range.

In order to investigate the effect of mixed moments with respect to an inverse solution, we consider the process of a single dipole fitting method (Hämäläinen et al., 1993). The dipole fitting method moves a dipole through the computational domain while minimizing a goal function. As the solution of the forward problem depends non-linearly on the dipole position, the moving dipole fit performs a non-linear optimization scheme. We simulate a target potential by computing a forward solution u_{ana} using the quasi-analytical formula of (De Munck and Peters, 1993). We place two different target sources at an eccentricity of 0.8 with unit strength and radial and tangential orientations respectively. Let $L_x \in \mathbb{R}^{N_e \times d}$ denote the leadfield at a position $x \in \mathbb{R}^d$, i.e., the columns of L_x contain the forward solutions for the Cartesian directions evaluated at the electrodes. We define the residual norm as

$$r_x : \mathbb{R}^d \to \mathbb{R}; y \mapsto \|L_x y - u_{\mathrm{ana}}\|_2.$$

a) radial source orientations

b) tangential source orientations

Figure 2.4: Errors of a CG discretization with the monopolar Venant approach including and not including the mixed moments on a 1 mm hexahedral mesh. On the left side, the RDM error and on the right side, the MAG error is shown. The dots indicate sources not fully contained in the brain compartment. Sources with an eccentricity lower than the vertical yellow line are guaranteed to be within an element not touching the first conductivity jump. At eccentricities between the vertical yellow and red lines, sources might be within an element touching the first conductivity jump but are still guaranteed to be within the brain compartment. A bold eccentricity label indicates a significant difference (t-Test, $p < 0.01$) between the two boxplots.

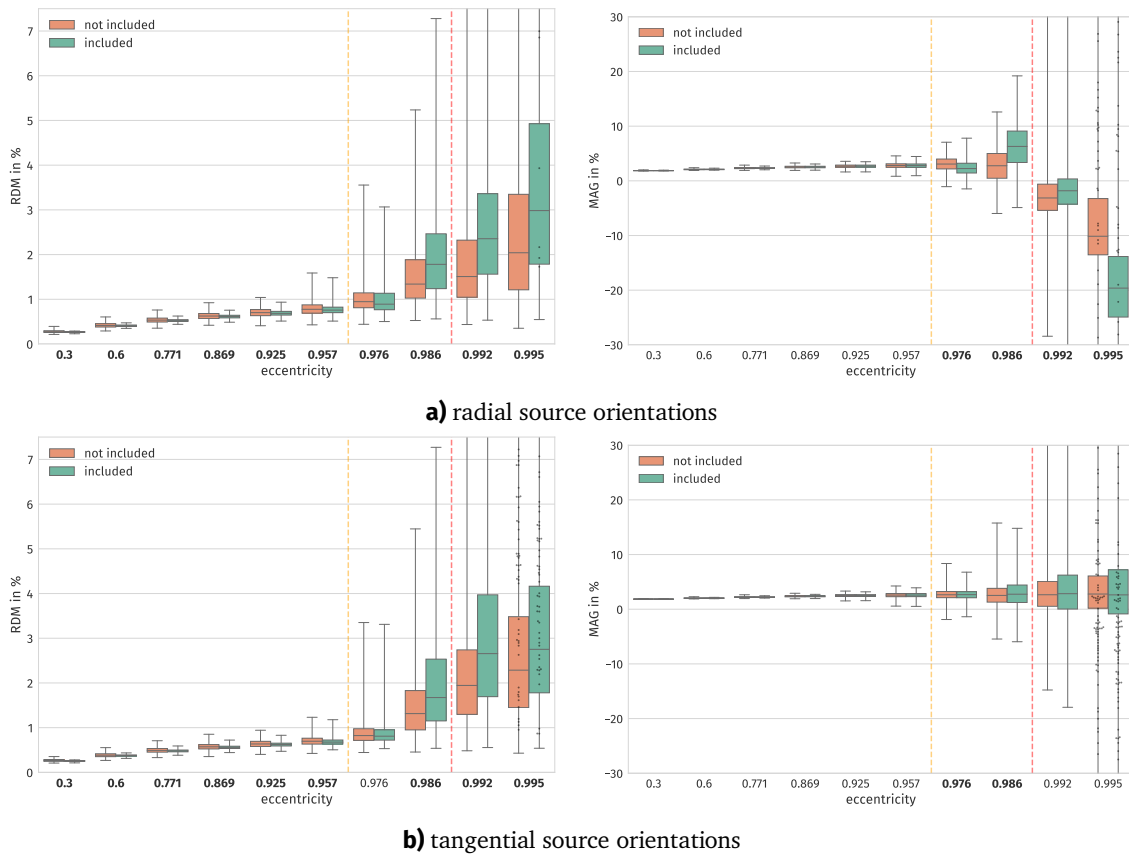**a)** radial source orientations

b) tangential source orientations

Figure 2.5: Errors of a CG discretization with the monopolar Venant approach including and not including the mixed moments on a tetrahedral mesh. On the left side, the RDM error and on the right side, the MAG error is shown. A bold eccentricity label indicates a significant difference (t-Test, $p < 0.01$) between the two boxplots.

a) radial target orientations   **b)** tangential target orientations

Figure 2.6: Goal function for a dipole fitting approach using monopolar Venant approaches including (green) and not including (orange) mixed moments on a 1 mm hexahedral mesh. The left column contains results for a radial target, the right column for a tangential target. Each column contains an overview plot of the goal function (top), a zoomed-in plot of the goal function (middle) and a plot of the difference between two neighboring values of the zoomed-in data (bottom). The dashed vertical line shows the location of the target source. The shaded area in the top plot indicates the zoomed-in area of the two lower plots.

The goal function of the dipole fitting approach is given as

$$gf : \mathbb{R}^d \to \mathbb{R}; x \mapsto r_x(\arg\min_y(r_x(y))),$$

i.e., the residual norm of the optimal source orientation at the given location. On a diagonal line from the center of the sphere to the first conductivity jump which passes the source location, we distribute test dipoles with a spacing of 0.1 mm, resulting in 780 dipole locations. For each of these source positions, we compute the goal function of the dipole fitting method using the different forward modeling approaches. Note that for a given position, the optimal strength and orientation can be computed using least squares. In order to investigate the smoothness of the goal function curve, we compute the difference between the goal function values of two neighboring dipole positions. Figure 2.6 shows the goal function of a dipole fit including and not including mixed moments on a 1 mm geometry-adapted hexahedral mesh. We observe a convex shape of the goal function plots for both approaches and both target source orientations. The minimum of the goal functions, i.e., the zero-crossing of the difference plots, lies below the target position at the eccentricity of 0.8. The goal function of the source model without mixed moments shows kinks, which correspond to the locations where the closest mesh vertex of the source changes. These kinks can be seen as spikes in the corresponding difference plots. The monopolar Venant approach including the mixed moments does not show these kinks in the vicinity of the target and provides an overall smoother goal function. Figure 2.7 shows the goal function of a dipole fit including and not including mixed moments on the tetrahedral mesh. The minimum of the goal function is closer to 0.8 than for the hexahedral approaches. The approach without mixed moments shows a stronger dependency on the local mesh

a) radial target orientations   **b)** tangential target orientations
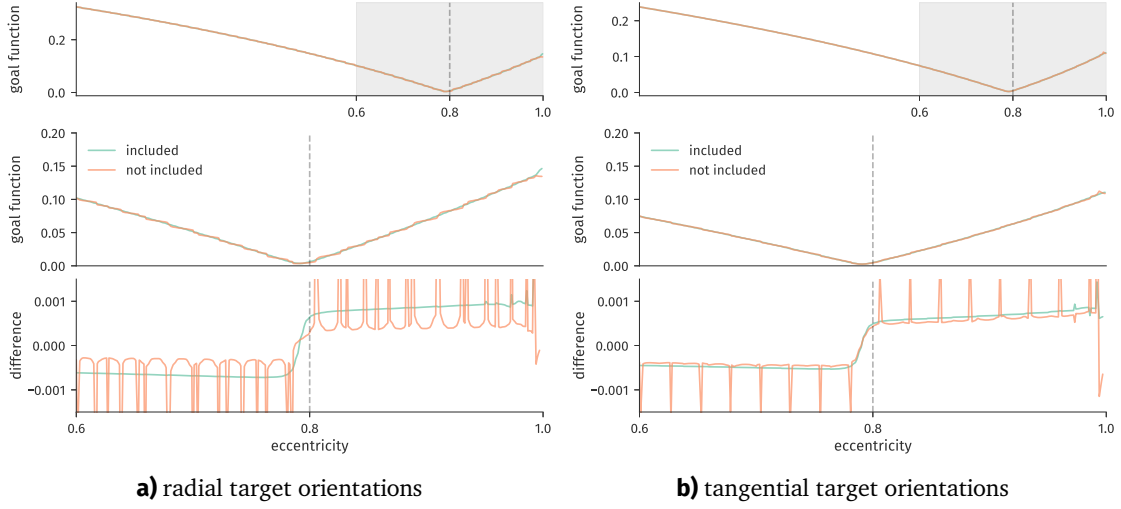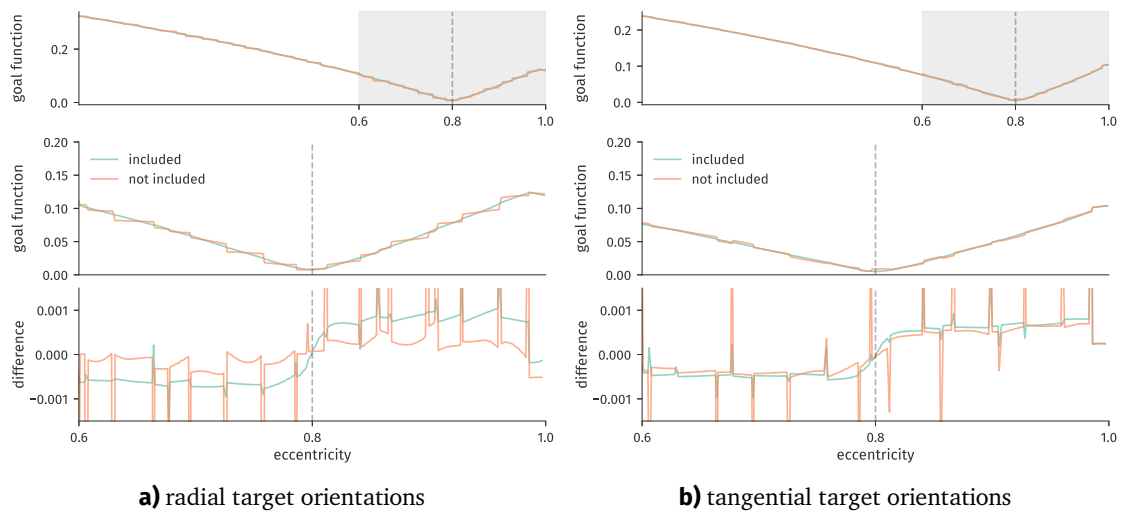
Figure 2.7: Goal function for a dipole fitting approach using monopolar Venant approaches including (green) and not including (orange) mixed moments on a tetrahedral mesh. The left column contains results for a radial target, the right column for a tangential target. Each column contains an overview plot of the goal function (top), a zoomed-in plot of the goal function (middle) and a plot of the difference between two neighboring values of the zoomed-in data (bottom). The dashed vertical line shows the location of the target source. The shaded area in the top plot indicates the zoomed-in area of the two lower plots.

structure and the goal function contains many jumps and plateaus. In some cases, especially for the tangential target orientation, local minima can be found. The approach including the mixed moments still includes some of the jumps at element boundaries, but is overall smoother. A clear zero-crossing of the difference plot at approximately 0.8 can be observed for both orientations.

To conclude, we can see slight increases in accuracy with respect to RDM and MAG when including the mixed moments for interior sources. These increases are more pronounced for tangential orientations and when using tetrahedral meshes. When performing a dipole fit, the mixed moments lead to an overall smoother goal function curve. For a moving dipole fit, the goal function is used within a non-linear optimization procedure, which might fail for non-smooth or non-convex goal functions. Computationally, including mixed moments leads to a slight increase in the time consumption for solving the local system as its size depends on the number of moments. For up to second order moments in 3D, the total number of moments increases from 7 to 10. In the practical applications considered in this thesis, this increase is irrelevant. However, if computation time is the main concern, e.g., in real-time applications, one would rather use the partial integration approach. In the following studies, we will always include the mixed moments.

Monopolar or Conforming Source Representation   In this study, we evaluate the difference between the non-conforming source representation using monopoles and the conforming representation as an element of the ansatz space. Based on the results of the previous study, both approaches include the mixed higher order moments. The remaining parameters of the Venant approach are chosen as described above, and are identical for both approaches. Figure 2.8 shows the RDM and MAG error for the conforming and monopolar Venant approach on a 1 mm geometry-adapted hex-

a) radial source orientations

b) tangential source orientations
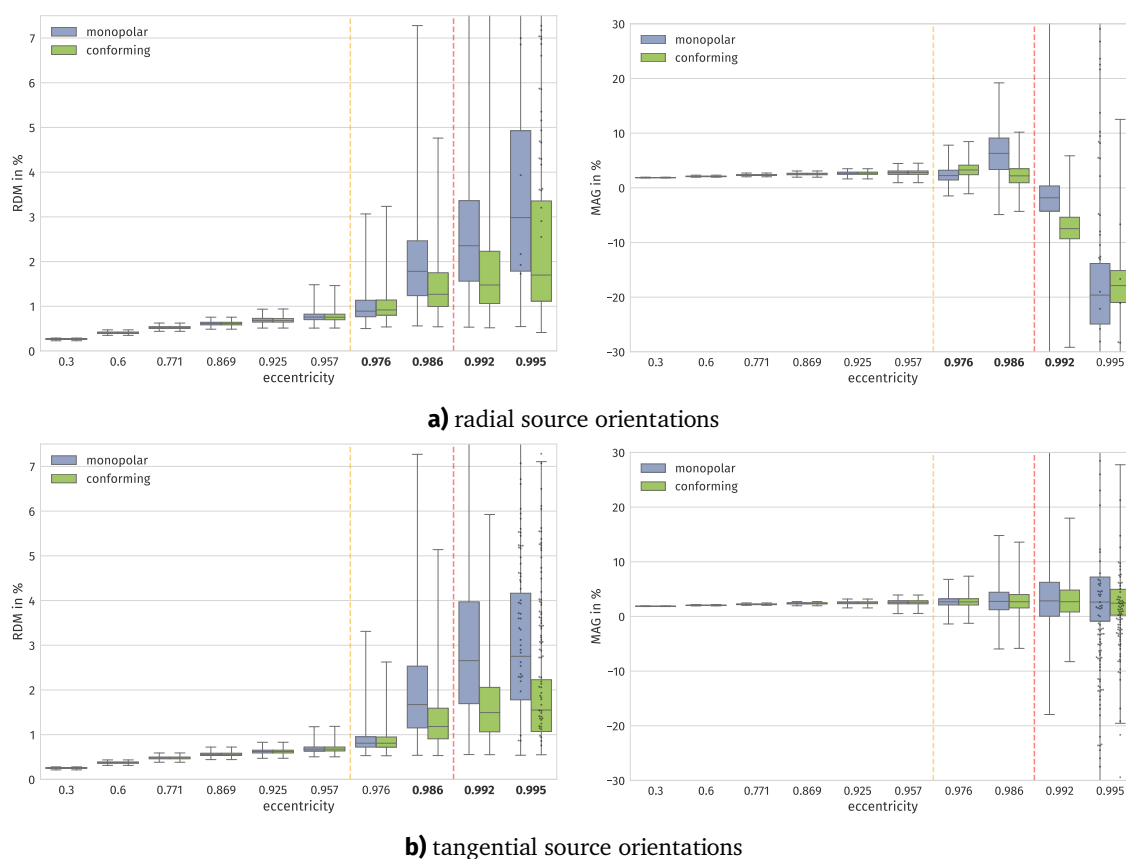
Figure 2.8: Errors of a CG discretization with the monopolar Venant approach and the conforming Venant approach on a 1 mm hexahedral mesh. On the left side, the RDM error and on the right side, the MAG error is shown. The dots indicate sources not fully contained in the brain compartment. Sources with an eccentricity lower than the vertical yellow line are guaranteed to be within an element not touching the first conductivity jump. At eccentricities between the vertical yellow and red lines, sources might be within an element touching the first conductivity jump but are still guaranteed to be within the brain compartment. A bold eccentricity label indicates a significant difference (t-Test, $p < 0.01$) between the two boxplots.

a) radial source orientations

b) tangential source orientations
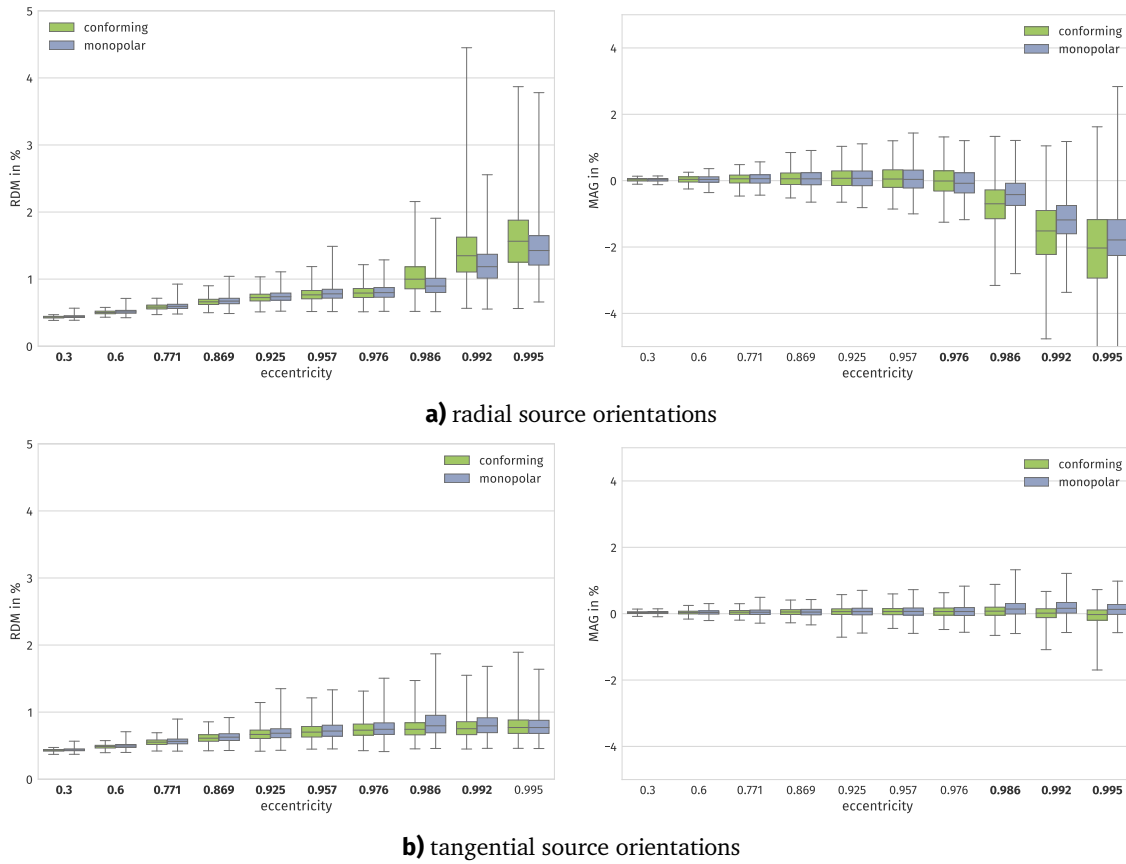
Figure 2.9: Errors of a CG discretization with the monopolar Venant approach and the conforming Venant approach on a tetrahedral mesh. On the left side, the RDM error and on the right side, the MAG error is shown. The dots indicate sources not fully contained in the brain compartment. Sources with an eccentricity lower than the vertical yellow line are guaranteed to be within an element not touching the first conductivity jump. At eccentricities between the vertical yellow and red lines, sources might be within an element touching the first conductivity jump but are still guaranteed to be within the brain compartment. A bold eccentricity label indicates a significant difference (t-Test, $p < 0.01$) between the two boxplots.

ahedral mesh. For interior sources, i.e., sources that do not lie within an element touching the first conductivity jump, we do not observe any significant or visually discernible difference between the two approaches, neither for the RDM nor for the MAG error. For higher eccentricities, the conforming approach shows lower RDM errors, while the effect on the MAG error is not as clear. Figure 2.9 shows the RDM and MAG error for the conforming and monopolar Venant approach on a tetrahedral mesh. The tetrahedral mesh is the same as in the previous study. The conforming approach shows slightly lower RDM errors for interior sources. For tangential orientations, the RDM error is also reduced for more eccentric sources, while for radial sources, the RDM error is slightly higher. With respect to the MAG error, there is no clear trend between both approaches and orientations.

To conclude, we do not see a strong difference with respect to numerical accuracy when comparing the conforming and the monopolar Venant approach. This effect might be due to the piecewise linear ansatz functions that are commonly used when solving the EEG forward problem and might

be more pronounced when employing higher-order polynomials. Note that the assembly of the local system is computationally more expensive when using the conforming approach, as we need to integrate over the element volumes instead of only evaluating the basis functions at the monopole locations. Additionally, the resulting right-hand side contains more entries due to the additional coupling introduced by the ramping-down at the boundary layer of the patch. However, in the practical computations in this study, the absolute time increase was not significant and we used the conforming approach in subsequent studies.

2.2 The St. Venant Source Model for Discontinuous Galerkin

So far, two different source models have been described in the literature for discontinuous Galerkin discretizations of the EEG forward problem (Engwer et al., 2017; Vorwerk, 2016): the partial integration and the subtraction approach. The results obtained by these two approaches replicate findings for conforming approaches, where the subtraction approach shows a higher accuracy but it is computationally more expensive than the partial integration approach. For the conforming finite element method, a popular source model is the monopolar Venant approach, see e.g., (Medani et al., 2015; Vorwerk, 2016), where monopoles are placed on the vertices of the mesh and their strengths are computed such that they form an equivalent source term when seen from a distance (cf. Section 2.1).

In the following, we will use the Venant approach in a discontinuous Galerkin setting. The monopoles within the classical formulation are modeled as singular Dirac distributions. While this approach fits to the setting of conforming Lagrange finite elements where discrete functions are defined by their nodal values, it is not directly applicable to a discontinuous Galerkin discretization. As described in Section 1.3, the test and ansatz functions are not strongly coupled between elements and thus they might be discontinuous on element boundaries which include the nodes of the mesh. The point-evaluation of these functions on element boundaries is thus not well defined and the delta source terms cannot be placed on the mesh nodes. One straightforward extension of the Venant approach with node monopoles has been presented in Section 2.1. Instead of placing monopoles on the mesh nodes, where the discrete functions are not uniquely defined, we place monopoles in the interior of the elements. In this domain, the discrete functions are polynomials and thus have a unique value and the delta distribution is applicable and well defined. We will call this approach the *monopolar Venant approach* for a discontinuous Galerkin discretization. A different concept for the Venant approach that has been described in Section 2.1 is the *conforming Venant approach*. Instead of replacing the singularity of the dipolar source term by a set of singularities given by monopolar sources, we replace the term in a conforming way using a piecewise polynomial function of the discrete ansatz space. The same approach can be directly used for a discontinuous Galerkin method. In addition to the discontinuities on the patch boundary, the interpolated source term might also be discontinuous on the internal skeleton of the mesh in the interior of the patch. All parameters that were described in Section 2.1 and used in the validation studies remain valid and are used in the same way for the discontinuous case. As the time consumption of a source model is strongly dependent on the number of degrees of freedom it considers, an idea might be to reduce the size of the local patch where the Venant approach is employed to a single element. However, the theoretical considerations in Section 2.1 show that this would result in a source model

producing the same right-hand side as the partial integration approach. It would thus not increase the accuracy compared to the partial integration approach.

Validation: Partial Integration, Venant for DG   We evaluate the Venant approaches for a discontinuous Galerkin discretization in a four-layer sphere scenario. As a comparison, we use the partial integration approach, which can be applied directly in a discontinuous setting (Vorwerk, 2016). In this case, the support of the source model is completely contained within a single element and the right-hand side has only as many entries as the number of basis functions for the local polynomial space. For the Venant approaches, we use a monopolar Venant approach and the conforming Venant approach. For the monopolar Venant approach, we create monopoles within the dipole element and all elements sharing a mesh vertex with the dipole element. Elements which are not part of the gray matter compartment are omitted, similar to the modified Venant approach described in (Medani et al., 2015). On each element, we place 8 monopoles at the positions of the Gauss-Legendre quadrature points (Quarteroni et al., 2010). For the conforming Venant approach, we use the same elements as for the monopolar approach. As we use the linear ansatz functions to represent the source term, the number of degrees of freedom used for the interpolation is the same for both approaches. For the regularization and for the solution of the local system we use the same parameters as described above for the conforming finite element method. Based on the investigation in Section 2.1, both Venant approaches include the mixed higher-order moments. We use the sphere radii and conductivity values shown in Table A.1, the 1 mm geometry-adapted hexahedral mesh shown in Table A.2 and the source positions shown in Table A.3. For each source position and radial and tangential orientation, we compute the RDM and MAG errors with respect to the quasi-analytical solution (cf. Eq. (2.14), (2.15)). The results of this comparison can be seen in Figure 2.10. Similar to previous results, we observe an increasing RDM error with increasing source eccentricity. The RDM error for both Venant approaches is almost identical, while the partial integration approach yields slightly higher errors. This holds true for both, radial and tangential source orientations. Results in (Li et al., 2014) indicate that, depending on the location, the cortex has a thickness of 2 mm to 6 mm. The generators underlying the electrical activity measured by EEG are located in the center of gray matter. From the range of eccentricities chosen here, we will provide a detailed description of the eccentricity of 0.986 which corresponds to a distance of approximately 1.1 mm from the first conductivity jump. At the eccentricity of 0.986, the median of the RDM for radial source orientations is 1.6 % for the partial integration approach, 1.2 % for the monopolar Venant approach and 1.2 % for the conforming Venant approach. The maximal RDM error at this eccentricity is 6.6 %, 4.5 % and 4.8 % for the different source models, respectively. For tangential source orientations, the median is 1.3 % for the partial integration approach, 1.0 % for the monopolar Venant approach and 1.0 % for the conforming Venant approach. The respective maximal RDM errors are 9.0 %, 5.0 % and 5.1 %. With respect to the MAG error, we observe an increase in total range and inter-quartile range for the partial integration approach as compared to the Venant approaches. The latter again provide similar errors, both for radial and tangential sources. We observe a shift in the positive direction of the MAG error over all eccentricities and for both orientations. At the eccentricity of 0.986, the total range of the MAG error for radial orientations is 23.4 % for the partial integration approach, 15.4 % for the monopolar Venant approach and 15.3 % for the conforming Venant approach. The inter-quartile range at this eccentricity is 5.3 %,

a) radial source orientations

b) tangential source orientations
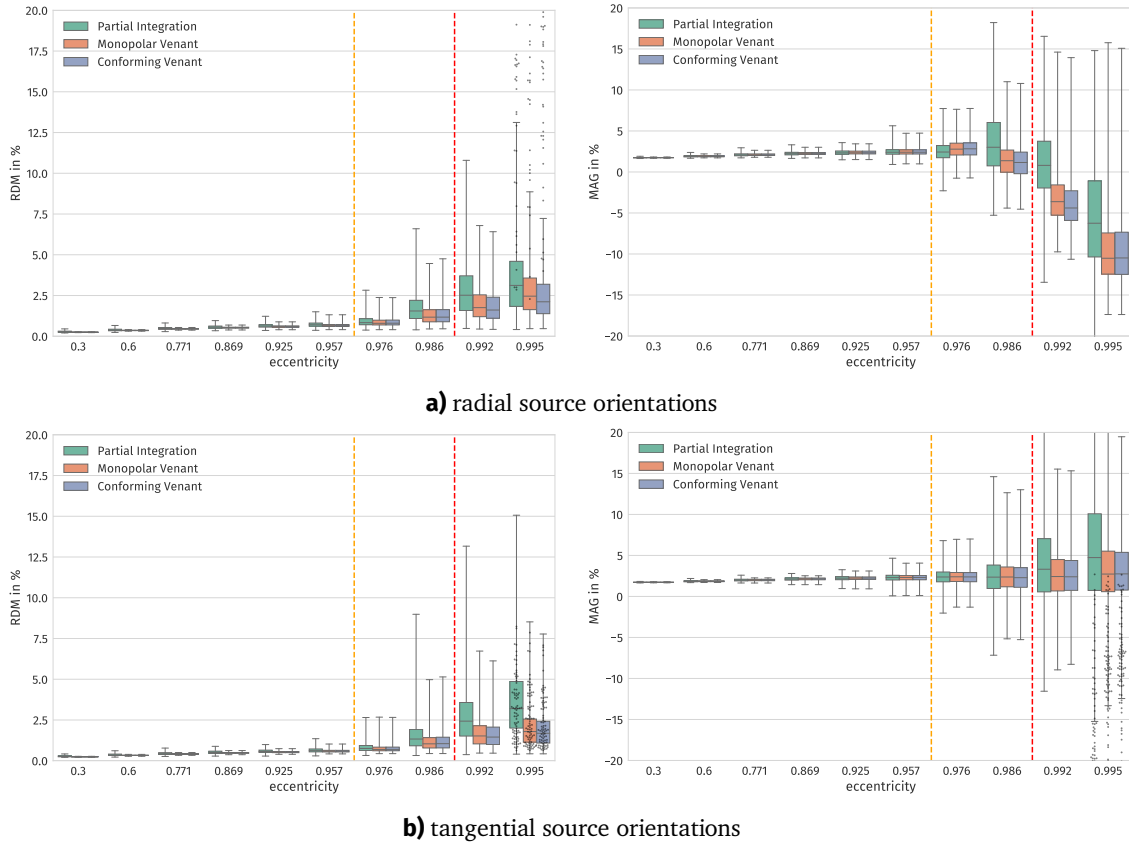
Figure 2.10: Comparison of the partial integration and the Venant approaches for a DG discretization on a 1 mm geometry-adapted hexahedral mesh. On the left side, the RDM error and on the right side, the MAG error is shown (both in %). The dots indicate sources not fully contained in the brain compartment. Sources with an eccentricity lower than the vertical yellow line are guaranteed to be within an element not touching the first conductivity jump. At eccentricities between the vertical yellow and red lines, sources might be within an element touching the first conductivity jump but are still guaranteed to be within the brain compartment.

2.7 % and 2.6 % for the different source models, respectively. For tangential source orientations, the total range if 21.8 % for the partial integration approach, 17.8 % for the monopolar Venant approach and 18.3 % for the conforming Venant approach. The respective inter-quartile ranges are 2.9 %, 2.4 % and 2.4 %.

The results for these direct approaches reproduce the results reported in the literature as well as in the previous section for the continuous Galerkin method. In Vorwerk (2016), the partial integration approach was found to provide increased error rates when compared to the monopolar Venant approach for a continuous Galerkin approach. In Section 2.1, the monopolar and conforming Venant approaches were compared in a continuous Galerkin finite element methods. Similar to the results here, both showed comparable error measures, for both RDM and MAG errors as well as for both source orientations. To conclude, when using the Venant approach in a discontinuous Galerkin discretization scheme, using a conforming representation within the ansatz space gives the same accuracy than using the non-conforming monopolar approach and we can thus avoid using the singular delta distribution. In addition, the accuracy of the partial integration approach can be increased by using the Venant approach in a discontinuous Galerkin setting.

2.3 A Localization of the Subtraction Source Model

When using the transfer matrix approach, the time it takes to solve the EEG forward problem for a single dipole can be split into two parts: the time for assembling the right-hand side vector and the time for performing the matrix vector multiplication. When employing sparse vector types, the run time of both parts is directly proportional to the number of non-zero entries in the right-hand side. It is thus desirable to reduce the support of the source term to decrease the computation time. Considering the subtraction approach introduced in Section 1.3, we can observe a densely populated right-hand side, as the singularity potential u^∞ has a support covering the whole domain Ω. In addition, performing the assembly of the source term necessitates the integration over the whole computational domain. Comparing this to the sparse structure of the direct approaches such as the partial integration approach presented in Section 1.2 or the Venant approach in Section 2.2, we can observe a dramatic increase in computation time for the subtraction approach. As the support of the right-hand side of the subtraction approach is directly coupled to the support of the singularity potential, the idea of this section is to reduce this support by restricting the singularity potential to a subset $\Omega^\infty \subset \Omega$ which is significantly smaller than Ω. A schematic representation on Ω (in a multi-layer sphere model) and Ω^∞ is shown in Figure 2.11.

We will call this splitting approach the *localized subtraction* source model. In the following derivation, we will mainly follow (Engwer et al., 2017), where the full discontinuous Galerkin formulation of the subtraction approach has been derived. We recall (see equation (1.14)) that the subtraction approach is introduced by providing a splitting of the potential

$$u_h = \tilde{u}_h + u^\infty,$$

where u^∞ is the solution of

$$-\nabla \cdot \sigma^\infty \nabla u^\infty = \nabla \cdot \boldsymbol{J}^p \quad \text{in } \mathbb{R}^d, \tag{2.16}$$
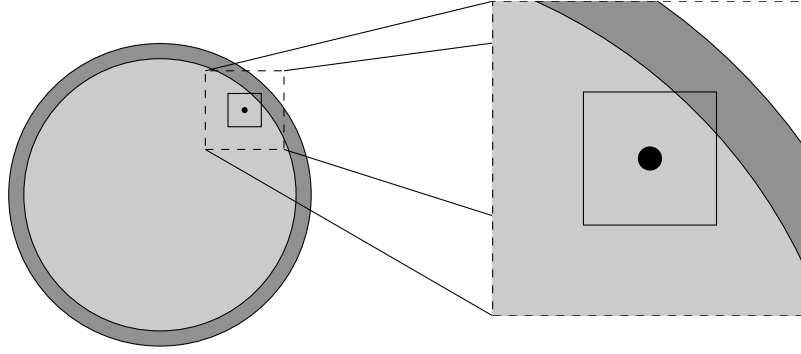
Figure 2.11: Schematic representation of the domain Ω and the patch Ω^∞ centered in the source location (black dot). The different gray tones indicate different tissue compartments.

a) u^∞ **b)** $u^\infty \chi_{\Omega^\infty}$
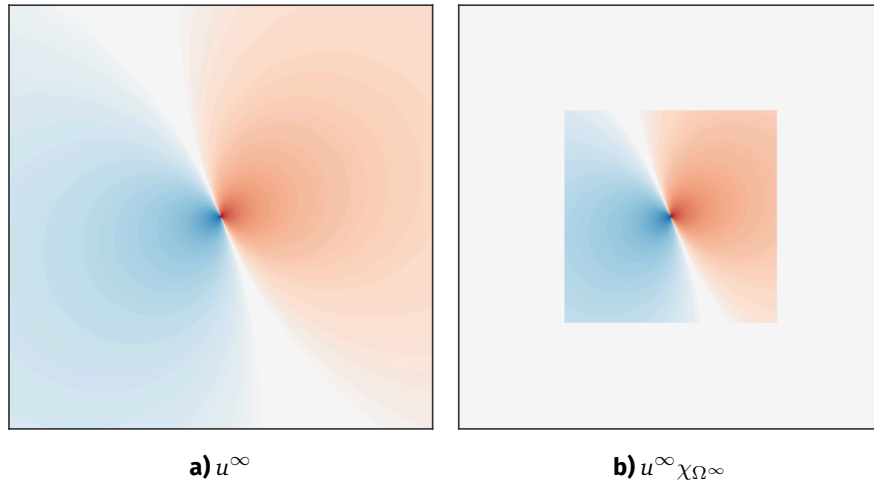
Figure 2.12: Singularity potential u^∞ and its restriction to a patch on a two dimension domain. A blue color indicates negative values and a red color indicates positive values. The colormap is scaled logarithmically towards zero.

which can be computed analytically. In this splitting, the singularity potential is considered in the whole domain Ω. The main idea of the localization and the main difference to the full subtraction approach is to consider u^∞ only on a volumetric patch $\Omega^\infty \subset \Omega$ around the source location. The splitting of the potential for this localization approach can be given as

$$u = \tilde{u} + \chi_{\Omega^\infty} u^\infty, \tag{2.17}$$

where χ_{Ω^∞} denotes the indicator function of the domain Ω^∞. For the coupling on the boundary of the patch, we require that

$$[\![\sigma \nabla u]\!] = 0, \quad \text{on } \partial\Omega^\infty, \tag{2.18}$$

with the jump $[\![\cdot]\!]$ as defined in Definition 1.16. This coupling condition means that the flux is continuous across the boundary of the patch. Figure 2.12 visualizes both u^∞ and $\chi_{\Omega^\infty} u^\infty$ for a dipolar source in a two dimensional setting. We observe that the magnitude of u^∞ in Figure

2.12 falls off quickly away from the source position and similarly the magnitude of the gradient becomes smaller. This observation leads to the assumption that cutting off u^∞ outside of Ω^∞ does not lead to a large decrease in accuracy and it can be recovered by the correction potential. Since the restricted singularity potential $\chi_{\Omega^\infty} u^\infty$ has a jump on $\partial \Omega^\infty$, it is not weakly differentiable and thus not a member of $H^1(\Omega)$. As we require the full potential to be continuous on the boundary, the correction potential will contain a jump in the opposite direction and will thus also not be a member of $H^1(\Omega)$.

In (Engwer et al., 2017) a conservation property for the correction potential has been derived and can be formulated as

$$\int_{\partial K} \langle \sigma \nabla \tilde{u}, \boldsymbol{n} \rangle \, \mathrm{d}s = \int_K -\nabla \cdot (\tilde{\sigma} \nabla u^\infty) \, \mathrm{d}x \,, \tag{2.19}$$

for an arbitrary control volume $K \subset \Omega$. Here, $\boldsymbol{n}$ denotes the unit outer normal in K. In following surface integrals $\boldsymbol{n}$ denotes the normal with respect to the integration domain. We start the derivation of an equivalent property for the localized subtraction from the general conservation of charge, which reads

$$\int_{\partial K} \langle \sigma \nabla u, \boldsymbol{n} \rangle \, \mathrm{d}s = \int_K f dx, \tag{2.20}$$

with $f = \nabla \cdot \boldsymbol{J}^p$. We define $\tilde{\Omega} := \Omega \setminus \overline{\Omega}^\infty$ and transform the left-hand side by adding 0 using (2.18) as

$$\begin{aligned}
&\int_{\partial K} \langle \sigma \nabla u, \boldsymbol{n} \rangle \, \mathrm{d}s \\
&= \int_{\partial K} \langle \sigma \nabla u, \boldsymbol{n} \rangle \, \mathrm{d}s + \int_{(\partial \Omega^\infty) \cap K} [\![\sigma \nabla u]\!] \, \mathrm{d}s \\
&= \int_{\partial K} \langle \sigma \nabla u, \boldsymbol{n} \rangle \, \mathrm{d}s - \int_{(\partial \Omega^\infty) \cap K} \langle \sigma \nabla u, \boldsymbol{n}^\infty \rangle \, \mathrm{d}s + \int_{(\partial \Omega^\infty) \cap K} \langle \sigma \nabla u, \boldsymbol{n}^\infty \rangle \, \mathrm{d}s \\
&= \int_{\partial(K \setminus \Omega^\infty)} \langle \sigma \nabla u |_{\tilde{\Omega}}, \boldsymbol{n} \rangle \, \mathrm{d}s + \int_{\partial(K \cap \Omega^\infty)} \langle \sigma \nabla u |_{\Omega^\infty}, \boldsymbol{n} \rangle \, \mathrm{d}s \,,
\end{aligned}$$

where $\boldsymbol{n}^\infty$ denotes the unit outer normal on $\partial \Omega^\infty$. For the first term, i.e., the integral of the flux over the boundary of the part of the control volume outside of Ω^∞, we derive

$$\int_{\partial(K \setminus \Omega^\infty)} \langle \sigma \nabla u |_{\tilde{\Omega}}, \boldsymbol{n} \rangle \, \mathrm{d}s = \int_{\partial(K \setminus \Omega^\infty)} \langle \sigma \nabla \tilde{u} |_{\tilde{\Omega}}, \boldsymbol{n} \rangle \, \mathrm{d}s \,,$$

as the singularity potential is restricted to Ω^∞. By inserting the splitting of the potential into the second term, i.e., the integral over the boundary of the part of the control volume within Ω^∞, we get

$$\begin{aligned}
&\int_{\partial(K \cap \Omega^\infty)} \langle \sigma \nabla u |_{\Omega^\infty}, \boldsymbol{n} \rangle \, \mathrm{d}s \\
&= \int_{\partial(K \cap \Omega^\infty)} \langle \sigma \nabla \tilde{u} |_{\Omega^\infty}, \boldsymbol{n} \rangle \, \mathrm{d}s + \int_{\partial(K \cap \Omega^\infty)} \langle \tilde{\sigma} \nabla u^\infty, \boldsymbol{n} \rangle \, \mathrm{d}s + \int_{\partial(K \cap \Omega^\infty)} \langle \sigma^\infty \nabla u^\infty, \boldsymbol{n} \rangle \, \mathrm{d}s \,.
\end{aligned}$$

Inserting both transformed terms into (2.20), the last term of the previous equation cancels out

with the source term on the right-hand side of (2.20) as u^∞ is the solution of (2.16) and we get

$$\int_{\partial(K\backslash\Omega^\infty)} \langle\sigma\nabla\tilde{u}|_{\tilde{\Omega}}, \boldsymbol{n}\rangle \, \mathrm{d}s + \int_{\partial(K\cap\Omega^\infty)} \langle\sigma\nabla\tilde{u}|_{\Omega^\infty}, \boldsymbol{n}\rangle \, \mathrm{d}s = -\int_{\partial(K\cap\Omega^\infty)} \langle\tilde{\sigma}\nabla u^\infty, \boldsymbol{n}\rangle \, \mathrm{d}s \, .$$

Applying Gauss' theorem to the right-hand side and extracting the boundary of Ω^∞, we arrive at

$$\int_{\partial K} \langle\sigma\nabla\tilde{u}, \boldsymbol{n}\rangle \, \mathrm{d}s + \int_{(\partial\Omega^\infty)\cap K} [\![\sigma\nabla\tilde{u}]\!] \, \mathrm{d}s = \int_K -\chi_{\Omega^\infty}\nabla\cdot\tilde{\sigma}\nabla u^\infty \, \mathrm{d}x \, . \tag{2.21}$$

Comparing 2.21 to 2.19, the source term on the right-hand side is only non-zero on the patch Ω^∞. In addition, another flux occurs on the boundary of the patch due to the cut-off of the singularity potential. Since we require continuity of the flux on the patch boundary, i.e., $[\![\sigma\nabla u]\!] = 0$ on $\partial\Omega^\infty$ (cf. (2.18)) this flux can also be expressed as $-\langle\sigma\nabla u^\infty, \boldsymbol{n}^\infty\rangle$. Equation 2.21 can be seen as a conservation property for the localized subtraction approach with a source term on the patch and an additional flux on its boundary both due to the singularity potential.

As mentioned above, due to the cutoff of the singularity potential at the boundary of Ω^∞, the correction potential will have a jump and will not be an element of $H^1(\Omega)$, but only of $L^2(\Omega)$. Thus the conforming finite element method with piecewise linear ansatz functions is not directly applicable as such jumps cannot be resolved. However, it directly fits into the framework of the discontinuous Galerkin methods which are able to represent such discontinuous solutions (cf. Section 1.3). In the following derivation, we assume that we have the tessellations $\mathcal{T}_h(\Omega^\infty)$ and $\mathcal{T}_h(\tilde{\Omega})$ of Ω^∞ and $\tilde{\Omega} = \Omega\backslash\overline{\Omega}^\infty$ respectively, that together form a conforming tessellation of Ω. In practice, we extract the elements of the singularity patch from a tessellation of the domain.

To start the derivation of the localized subtraction approach, we multiply Poisson's equation with a test function and integrate over an element $K \in \mathcal{T}_h(\Omega^\infty)$.

$$-\int_K (\nabla\cdot\sigma\nabla u_h)v_h \, \mathrm{d}x = \int_K (\nabla\cdot\boldsymbol{J}^p)v_h \, \mathrm{d}x \, .$$

Using the splitting of the potential for the localized subtraction approach (2.17) and the splitting of the conductivity tensor $\sigma = \tilde{\sigma} + \sigma^\infty$, the left-hand side can be transformed to

$$-\int_K (\nabla\cdot\sigma\nabla\tilde{u}_h)v_h + (\nabla\cdot\tilde{\sigma}\nabla u^\infty)v_h + (\nabla\cdot\sigma^\infty\nabla u^\infty)v_h \, \mathrm{d}x \, .$$

As u^∞ is the solution of (2.16), the last term cancels out with the source term on the right-hand side resulting in

$$-\int_K (\nabla\cdot\sigma\nabla\tilde{u}_h)v_h \, \mathrm{d}x = \int_K (\nabla\cdot\tilde{\sigma}\nabla u^\infty)v_h \, \mathrm{d}x \, .$$

Applying integration by parts to both sides gives

$$\int_K \langle\sigma\nabla\tilde{u}_h, \nabla v_h\rangle \, \mathrm{d}x - \int_{\partial K} v_h \langle\sigma\nabla\tilde{u}_h|_{\Omega^\infty}, \boldsymbol{n}\rangle \, \mathrm{d}s$$
$$= -\int_K \langle\tilde{\sigma}\nabla u^\infty, \nabla v_h\rangle \, \mathrm{d}x + \int_{\partial K} v_h \langle\tilde{\sigma}\nabla u^\infty, \boldsymbol{n}\rangle \, \mathrm{d}s \, .$$

We sum over all elements $K \in \mathcal{T}_h(\Omega^\infty)$ of the triangulation of the patch and get

$$
\int_{\Omega^\infty} \langle \sigma \nabla \tilde{u}_h, \nabla v_h \rangle \, \mathrm{d}x - \int_{\Gamma^\infty} [\![v_h \sigma \nabla \tilde{u}_h]\!] \, \mathrm{d}s - \int_{\partial\Omega^\infty} v_h |_{\Omega^\infty} \langle \sigma \nabla \tilde{u}_h |_{\Omega^\infty}, \boldsymbol{n}^\infty \rangle \, \mathrm{d}s
$$
$$
= - \int_{\Omega^\infty} \langle \tilde{\sigma} \nabla u^\infty, \nabla v_h \rangle \, \mathrm{d}x + \int_{\Gamma^\infty} [\![v_h \tilde{\sigma} \nabla u^\infty]\!] \, \mathrm{d}s + \int_{\partial\Omega^\infty} v_h |_{\Omega^\infty} \langle \tilde{\sigma} \nabla u^\infty, \boldsymbol{n}^\infty \rangle \, \mathrm{d}s \, ,
$$

where $\boldsymbol{n}^\infty$ again denotes the unit outer normal on $\partial\Omega^\infty$ and Γ^∞ denotes the internal skeleton of the patch. Using the multiplicative property of the jump (cf. Lemma 1.4), the left-hand side of the above equation can be transformed to

$$
\int_{\Omega^\infty} \langle \sigma \nabla \tilde{u}_h, \nabla v_h \rangle \, \mathrm{d}x - \int_{\Gamma^\infty} \underbrace{[\![\sigma \nabla \tilde{u}_h]\!] \{ v_h \}^*}_{\dagger^1} + \langle \{ \sigma \nabla \tilde{u}_h \}, [\![v_h]\!] \rangle \, \mathrm{d}s - \int_{\partial\Omega^\infty} v_h |_{\Omega^\infty} \langle \sigma \nabla \tilde{u}_h |_{\Omega^\infty}, \boldsymbol{n}^\infty \rangle \, \mathrm{d}s \, ,
$$

and similarly, the right-hand side transforms to:

$$
- \int_{\Omega^\infty} \langle \tilde{\sigma} \nabla u^\infty, \nabla v_h \rangle \, \mathrm{d}x + \int_{\Gamma^\infty} \underbrace{[\![\tilde{\sigma} \nabla u^\infty]\!] \{ v_h \}^*}_{\dagger^2} + \langle \{ \tilde{\sigma} \nabla u^\infty \}, [\![v_h]\!] \rangle \, \mathrm{d}s + \int_{\partial\Omega^\infty} v_h |_{\Omega^\infty} \langle \tilde{\sigma} \nabla u^\infty, \boldsymbol{n}^\infty \rangle \, \mathrm{d}s \, .
$$

The terms $\dagger^1$ and $\dagger^2$ cancel each other out as $[\![\sigma \nabla \tilde{u}_h + \tilde{\sigma} \nabla u^\infty]\!] = 0$ holds (cf. (Engwer et al., 2017, Lemma 2.2)) and, combining the left-hand side and the right-hand side, we arrive at

$$
\int_{\Omega^\infty} \langle \sigma \nabla \tilde{u}_h, \nabla v_h \rangle \, \mathrm{d}x - \int_{\Gamma^\infty} \langle \{ \sigma \nabla \tilde{u}_h \}, [\![v_h]\!] \rangle \, \mathrm{d}s - \int_{\partial\Omega^\infty} v_h |_{\Omega^\infty} \langle \sigma \nabla \tilde{u}_h |_{\Omega^\infty}, \boldsymbol{n}^\infty \rangle \, \mathrm{d}s
$$
$$
= - \int_{\Omega^\infty} \langle \tilde{\sigma} \nabla u^\infty, \nabla v_h \rangle \, \mathrm{d}x + \int_{\Gamma^\infty} \langle \{ \tilde{\sigma} \nabla u^\infty \}, [\![v_h]\!] \rangle \, \mathrm{d}s + \int_{\partial\Omega^\infty} v_h |_{\Omega^\infty} \langle \tilde{\sigma} \nabla u^\infty, \boldsymbol{n}^\infty \rangle \, \mathrm{d}s \, .
$$

$$(2.22)$$

Next, we consider an element of the triangulation of the domain outside of the patch. For a $K \in \mathcal{T}_h(\tilde{\Omega})$ we have $u_h \equiv \tilde{u}_h$ and

$$
- \int_K (\nabla \cdot \sigma \nabla \tilde{u}_h) v_h \, \mathrm{d}x = 0
$$
$$
\Leftrightarrow \int_K \langle \sigma \nabla \tilde{u}_h, \nabla v_h \rangle \, \mathrm{d}x - \int_{\partial K} v_h |_{\tilde{\Omega}} \langle \sigma \nabla \tilde{u}_h |_{\tilde{\Omega}}, \boldsymbol{n} \rangle \, \mathrm{d}s = 0 \, .
$$

We again sum over all $K \in \mathcal{T}_h(\tilde{\Omega})$ and consider the homogeneous Neumann boundary condition at the outer surface of the domain Ω:

$$
\int_{\tilde{\Omega}} \langle \sigma \nabla \tilde{u}_h, \nabla v_h \rangle \, \mathrm{d}x - \int_{\Gamma \setminus (\Gamma^\infty \cup \partial\Omega^\infty)} [\![v_h \sigma \nabla \tilde{u}_h]\!] \, \mathrm{d}s + \int_{\partial\Omega^\infty} v_h |_{\tilde{\Omega}} \langle \sigma \nabla \tilde{u}_h |_{\tilde{\Omega}}, \boldsymbol{n}^\infty \rangle \, \mathrm{d}s = 0 \, .
$$

Using the multiplicative property of the jump (cf. Lemma 1.4), this transforms to

$$
\int_{\tilde{\Omega}} \langle \sigma \nabla \tilde{u}_h, \nabla v_h \rangle \, \mathrm{d}x - \int_{\Gamma \setminus (\Gamma^\infty \cup \partial\Omega^\infty)} [\![\sigma \nabla \tilde{u}_h]\!] \{ v_h \}^* + \langle \{ \sigma \nabla \tilde{u}_h \}, [\![v_h]\!] \rangle \, \mathrm{d}s
$$
$$
+ \int_{\partial\Omega^\infty} v_h |_{\tilde{\Omega}} \langle \sigma \nabla \tilde{u}_h |_{\tilde{\Omega}}, \boldsymbol{n}^\infty \rangle \, \mathrm{d}s = 0 \, .
$$

$$(2.23)$$

Summing the contributions from the patch in (2.22) and the remaining domain in (2.23) while

considering the interface condition $[\![\sigma\nabla\tilde{u}_h]\!] = 0$ on all internal edges in $\Gamma \setminus (\Gamma^\infty \cup \partial\Omega^\infty)$ gives:

$$\int_\Omega \langle \sigma\nabla\tilde{u}_h, \nabla v_h \rangle \, \mathrm{d}x - \int_{\Gamma\setminus\partial\Omega^\infty} \langle \{\sigma\nabla\tilde{u}_h\}, [\![v_h]\!] \rangle \, \mathrm{d}s - \int_{\partial\Omega^\infty} \underbrace{[\![v_h \sigma\nabla\tilde{u}_h]\!]}_{\ddagger} \, \mathrm{d}s$$

$$= - \int_{\Omega^\infty} \langle \tilde{\sigma}\nabla u^\infty, \nabla v_h \rangle \, \mathrm{d}x + \int_{\Gamma^\infty} \langle \{\tilde{\sigma}\nabla u^\infty\}, [\![v_h]\!] \rangle \, \mathrm{d}s + \int_{\partial\Omega^\infty} v_h|_{\Omega^\infty} \langle \tilde{\sigma}\nabla u^\infty, \boldsymbol{n}^\infty \rangle \, \mathrm{d}s \, .$$

Splitting the term $\ddagger$ on the boundary of the patch using the multiplicative property transforms the left-hand side to

$$\int_\Omega \langle \sigma\nabla\tilde{u}_h, \nabla v_h \rangle \, \mathrm{d}x - \int_\Gamma \langle \{\sigma\nabla\tilde{u}_h\}, [\![v_h]\!] \rangle \, \mathrm{d}s - \int_{\partial\Omega^\infty} [\![\sigma\nabla\tilde{u}_h]\!] \{v_h\}^* \, \mathrm{d}s \, . \tag{2.24}$$

On a face on the patch boundary between two elements $e \in \mathcal{T}_h(\Omega^\infty)$ and $f \in \mathcal{T}_h(\tilde{\Omega})$ we can use the continuity condition for the full flux $\sigma\nabla u$ and derive

$$0 = [\![\sigma\nabla u]\!] = \langle \sigma\nabla\tilde{u}_h|_e, \boldsymbol{n}_e \rangle + \langle \sigma\nabla u^\infty, \boldsymbol{n}_e \rangle + \langle \sigma\nabla\tilde{u}_h|_f, \boldsymbol{n}_f \rangle = [\![\sigma\nabla\tilde{u}_h]\!] + \langle \sigma\nabla u^\infty, \boldsymbol{n}_e \rangle \, ,$$

which gives $[\![\sigma\nabla\tilde{u}_h]\!] = -\langle \sigma\nabla u^\infty, \boldsymbol{n}_e \rangle$, where $\boldsymbol{n}_e$ and $\boldsymbol{n}_f$ denote the unit outer normals on e and f, respectively. Inserting this equation into the left-hand side (2.24) results in

$$\int_\Omega \langle \sigma\nabla\tilde{u}_h, \nabla v_h \rangle \, \mathrm{d}x - \int_\Gamma \langle \{\sigma\nabla\tilde{u}_h\}, [\![v_h]\!] \rangle \, \mathrm{d}s + \int_{\partial\Omega^\infty} \{v_h\}^* \langle \sigma\nabla u^\infty, \boldsymbol{n}^\infty \rangle \, \mathrm{d}s \, .$$

As the last term does not depend on $\tilde{u}_h$ anymore, we transfer it to the right-hand side and arrive at

$$\int_\Omega \langle \sigma\nabla\tilde{u}_h, \nabla v_h \rangle \, \mathrm{d}x - \int_\Gamma \langle \{\sigma\nabla\tilde{u}_h\}, [\![v_h]\!] \rangle \, \mathrm{d}s$$

$$= - \int_{\Omega^\infty} \langle \tilde{\sigma}\nabla u^\infty, \nabla v_h \rangle \, \mathrm{d}x + \int_{\Gamma^\infty} \langle \{\tilde{\sigma}\nabla u^\infty\}, [\![v_h]\!] \rangle \, \mathrm{d}s$$

$$+ \int_{\partial\Omega^\infty} v_h|_{\Omega^\infty} \langle \tilde{\sigma}\nabla u^\infty, \boldsymbol{n}^\infty \rangle \, \mathrm{d}s - \int_{\partial\Omega^\infty} \{v_h\}^* \langle \sigma\nabla u^\infty, \boldsymbol{n}^\infty \rangle \, \mathrm{d}s \, .$$

Note that all terms on the right-hand side do not depend on the correction potential $\tilde{u}_h$. To gain consistency, we subtract the symmetry term for the full potential $\int_\Gamma \langle \{\sigma\nabla v_h\}, [\![u_h]\!] \rangle \, ds$ from the left-hand side. On an intersection within Ω^∞ or within $\tilde{\Omega}$ it holds that $[\![u_h]\!] = [\![\tilde{u}_h]\!]$ as the singularity potential is continuous. On a face on the boundary of the patch between two elements $e \in \mathcal{T}_h(\Omega^\infty)$ and $f \in \mathcal{T}_h(\tilde{\Omega})$ it holds that

$$[\![u_h]\!] = u_h|_e \boldsymbol{n}_e + u_h|_f \boldsymbol{n}_f = \tilde{u}_h|_e \boldsymbol{n}_e + u^\infty \boldsymbol{n}_e + \tilde{u}_h|_f \boldsymbol{n}_f = [\![\tilde{u}_h]\!] + u^\infty \boldsymbol{n}_e. \tag{2.25}$$

The symmetry term thus transforms to the symmetry term for the correction potential with an additional term on the patch boundary

$$\int_\Gamma \langle \{\sigma\nabla v_h\}, [\![u_h]\!] \rangle \, \mathrm{d}s = \int_\Gamma \langle \{\sigma\nabla v_h\}, [\![\tilde{u}_h]\!] \rangle \, \mathrm{d}s + \int_{\partial\Omega^\infty} u^\infty \langle \{\sigma\nabla v_h|_{\Omega^\infty}\}, \boldsymbol{n}^\infty \rangle \, \mathrm{d}s$$

Within the jump term $J(u_h, v_h) = \eta \int_\Gamma \frac{\hat{\sigma}}{h} \langle [\![u_h]\!], [\![v_h]\!] \rangle \, \mathrm{d}s$ of the discontinuous Galerkin method, the modified singularity potential has to be considered as well: Using the same transformation (2.25)

of the jump on $\partial\Omega^\infty$ we get

$$J(u_h, v_h) = \eta \int_\Gamma \frac{\hat{\sigma}}{h} \langle [\![u_h]\!], [\![v_h]\!] \rangle \, \mathrm{d}s$$

$$= J(\tilde{u}_h, v_h) + \eta \int_{\partial\Omega^\infty} \frac{\hat{\sigma}}{h} u^\infty \langle [\![v_h]\!], \boldsymbol{n}^\infty \rangle \, \mathrm{d}s$$

We bring all terms that do not depend on $\tilde{u}_h$ over to the right-hand side and arrive at

$$a(\tilde{u}_h, v_h) + J(\tilde{u}_h, v_h) =$$
$$- \int_{\Omega^\infty} \langle \tilde{\sigma}\nabla u^\infty, \nabla v_h \rangle \, \mathrm{d}x + \int_{\Gamma^\infty} \langle \{\tilde{\sigma}\nabla u^\infty\}, [\![v_h]\!] \rangle \, \mathrm{d}s + \int_{\partial\Omega^\infty} v_h|_{\Omega^\infty} \langle \tilde{\sigma}\nabla u^\infty, \boldsymbol{n}^\infty \rangle \, \mathrm{d}s$$
$$- \int_{\partial\Omega^\infty} \{v_h\}^* \langle \sigma\nabla u^\infty, \boldsymbol{n}^\infty \rangle \, \mathrm{d}s + \int_{\partial\Omega^\infty} u^\infty \langle \{\sigma\nabla v_h\}, \boldsymbol{n}^\infty \rangle \, \mathrm{d}s - \eta \int_{\partial\Omega^\infty} \frac{\hat{\sigma}}{h} u^\infty \langle [\![v_h]\!], \boldsymbol{n}^\infty \rangle \, \mathrm{d}s \, .$$

We use $\tilde{\sigma} = \sigma - \sigma^\infty$ to split the third term of the right-hand side and consider $(v_h|_{\Omega^\infty} - \{v_h\}^*)\boldsymbol{n}^\infty = \omega^\infty [\![v_h]\!]$, where ω^∞ denotes the average weight on the side of Ω^∞. Finally, we get the *localized subtraction* approach:

Definition 2.1 (Localized Subtraction). *The localized Subtraction approach for a discontinuous Galerkin discretization on a patch Ω^∞ is given as: Find $\tilde{u}_h \in V_h$ such that*

$$a(\tilde{u}_h, v_h) + J(\tilde{u}_h, v_h) = \tag{2.26}$$

$$- \int_{\Omega^\infty} \langle \tilde{\sigma}\nabla u^\infty, \nabla v_h \rangle \, \mathrm{d}x + \int_{\Gamma^\infty} \langle \{\tilde{\sigma}\nabla u^\infty\}, [\![v_h]\!] \rangle \, \mathrm{d}s - \int_{\partial\Omega^\infty} v_h|_{\Omega^\infty} \langle \sigma^\infty\nabla u^\infty, \boldsymbol{n}^\infty \rangle \, \mathrm{d}s \tag{2.27}$$

$$+ \int_{\partial\Omega^\infty} \omega^\infty \langle \sigma\nabla u^\infty, [\![v_h]\!] \rangle \, \mathrm{d}s + \int_{\partial\Omega^\infty} u^\infty \left\langle \{\sigma\nabla v_h\} - \eta\frac{\hat{\sigma}}{h} [\![v_h]\!], \boldsymbol{n}^\infty \right\rangle \, \mathrm{d}s \tag{2.28}$$

holds, for all $v_h \in V_h$.

First, we want to remark, that the bilinear form in (2.26) for the localized subtraction approach is the same as for the other DG approaches. This means, in particular, that transfer matrices can be directly reused with the new right-hand side. Another observation can be made about the first three right-hand side terms (2.27). They are identical to the right-hand side of the standard subtraction approach, if one replaces Ω^∞ by Ω, Γ^∞ by Γ and $\boldsymbol{n}^\infty$ by $\boldsymbol{n}$. With regard to a software implementation of this localized source model, the last point is especially advantageous, as one can reuse the implementation of the standard subtraction approach. The main difference of the localization as compared to the non-localized subtraction is the addition of the last two terms in (2.28). A short reformulation of the last two terms shows

$$\int_{\partial\Omega^\infty} \omega^\infty \langle \sigma\nabla u^\infty, [\![v_h]\!] \rangle \, \mathrm{d}s + \int_{\partial\Omega^\infty} u^\infty \left\langle \{\sigma\nabla v_h\} - \eta\frac{\hat{\sigma}}{h} [\![v_h]\!], \boldsymbol{n}^\infty \right\rangle \, \mathrm{d}s$$
$$= \int_{\partial\Omega^\infty} \langle \{\sigma\nabla(\chi_{\Omega^\infty}u^\infty)\}, [\![v_h]\!] \rangle + \langle \{\sigma\nabla v_h\}, [\![\chi_{\Omega^\infty}u^\infty]\!] \rangle \, \mathrm{d}s - \eta\frac{\hat{\sigma}}{h} \int_{\partial\Omega^\infty} \langle [\![v_h]\!], [\![\chi_{\Omega^\infty}u^\infty]\!] \rangle \, \mathrm{d}s$$

which directly gives insight into their origin, as these integrals can be seen to stem from a Nitsche-type weak enforcement of continuity of $\tilde{u}_h + \chi_{\Omega^\infty}u^\infty$ on $\partial\Omega^\infty$ (Nitsche, 1971).
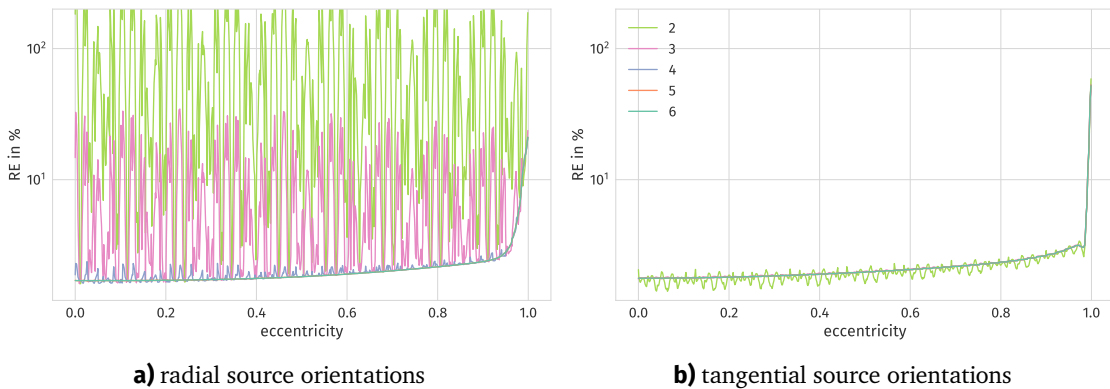
a) radial source orientations   **b)** tangential source orientations

Figure 2.13: Relative error in percent for radial and tangential dipoles along a diagonal line within a 1 mm geometry-adapted hexahedral four-layer sphere model, using the localized subtraction approach with different integration orders. Each plot corresponds to a different integration order. The ordinate is depicted on a logarithmic scale.

2.3.1 Validation Studies

In this section we will validate the localized subtraction source model for solving the EEG forward problem in a four-layer sphere model. We investigate the numerical integration and the size of the patch Ω^∞. Subsequently, we compare the localized subtraction approach to the full subtraction approach with respect to the accuracy as well as the time consumption.

Choosing the Integration Order   In a first study, we investigate the effect of the numerical integration for the integrals of the localized subtraction approach. The quadrature rule used for the integration is based on Gaussian quadrature using Legendre points (Quarteroni et al., 2010). For hexahedral models, we use two and three dimensional tensor-product quadrature rules. We will denote a tensor-product quadrature rule by its number of one-dimensional quadrature points $n \in \mathbb{N}$ which we will call its order. The number of points for a rule of order n is n^3 for three spatial dimensions and n^2 for two dimensions. A quadrature rule of order n is able to exactly integrate polynomials of degree $2n-1$ and less. Note that this order does not correspond to the quadrature rule order of the Dune toolbox, where the order is the maximal degree of the polynomial functions for which the rule is exact. We distribute dipoles along a line from the center of the sphere to the first conductivity jump, spaced regularly at 0.1 mm intervals, resulting in 780 positions. Starting from the integration order of 2 for both surface and volume integrals, which was proposed by (Drechsler et al., 2009) for tetrahedral models, we increase the order by 1 up to an order of 6. For each point and each integration order, we compute the relative error for radial and tangential source orientations. The investigation is performed in a geometry-adapted hexahedral four-layer sphere model with a 1 mm resolution. Details of the spheres are found in Table A.1 and details of the discretization are found in table A.2. For Ω^∞, we use a patch that consists of the dipole element and all elements that share a mesh vertex with the dipole element. Figure 2.13 shows the relative error in percent for radial and tangential sources for the different integration orders. We observe a stronger effect of the integration order for radial orientations compared to tangential orientations. For radial orientations, the relative error decreases with increasing integration order. Especially orders 2 and
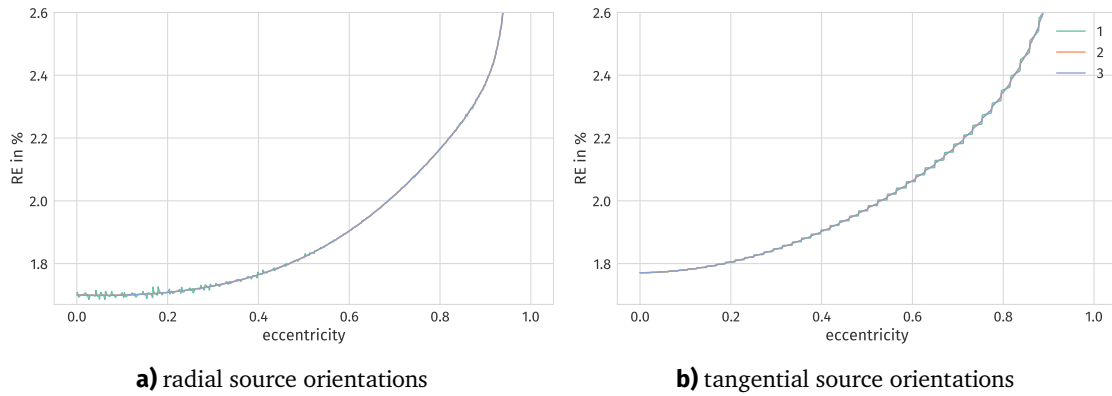
a) radial source orientations

b) tangential source orientations

Figure 2.14: Relative error in percent for radial and tangential dipoles along a diagonal line within a 1 mm geometry-adapted hexahedral four-layer sphere model, using the localized subtraction approach with patch sizes. Each plot corresponds to a different patch size.

3 show a high error which is varying strongly with the eccentricity. The results for order 5 and 6 are visually not distinguishable. The relative error for tangential sources is not as strongly affected by the integration order and results for order 4 and higher are not distinguishable.

The different integrands within the localized subtraction approach consist of products of the test function v_h, or its gradient, and the singularity potential and its gradient as well as the Jacobian determinant of the transformation from global to local coordinates. The test function and the Jacobian determinant both are first order polynomials and their product is a polynomial of second order. Note that Jacobian determinant is first order since we use a geometry-adapted mesh and the element transformation is a multi-linear function. We thus need at least a quadrature rule of order 2 in order to perform an accurate integration. Additionally, we need to integrate the singularity potential and its gradient which are both not polynomial functions. In (Drechsler et al., 2009), a second order quadrature rule was sufficient for accurate integration in the full subtraction approach on tetrahedral meshes. We did not investigate the effect of the patch size on the quadrature rule. A larger patch might reduce the necessary quadrature rule order as the boundary of the patch is further away from the singularity and thus the restricted singularity potential is smoother. As a conclusion, we will use a quadrature rule of order 5 in the following sections, based on the results of this study.

Effect of the Patch Size   Similar to the previous study of the quadrature rule order, we investigate the size of the patch for the localized subtraction approach. Starting from the single dipole element, we extent the patch by including elements which share a vertex with an element that is already part of the patch. This extension approach is applied recursively 1, 2 and 3 times. Note that in contrast to the Venant approach, elements are added to the patch independently of their conductivity value. We again use the geometry-adapted hexahedral four-layer sphere model with a resolution of 1 mm. The patch with 1, 2 and 3 extensions thus consists of $3^3 = 27$, $5^3 = 125$ and $7^3 = 343$ elements and thus has a diameter of 3 mm, 5 mm and 7 mm, respectively. Note that the number of elements within the patch does not depend on the mesh resolution. Figure 2.14 shows the relative error in percent for radial and tangential sources for the various patch sizes. For radial source orientations, we observe slight jumps in the relative error for the smaller patch size. For tangential sources and

the smallest patch size, the relative error shows a dependency on the position of the source in the element and we observe jumps corresponding to the crossing of element boundaries. The plots for the two and three times extended patches are visually not distinguishable both for radial and tangential sources.

We note that different patch sizes have no strong effect on the overall relative error and the localized subtraction approach performs similarly for all sizes. The main difference between the patches lies in the smoothness of the relative error curve. If smoothness is not the main concern, a smaller patch size and thus a computationally cheaper source model can be considered sufficient. Due to the results of this investigation, we will use the two times extended patch, consisting of 125 elements, for the remainder of this section. We did not investigate different shapes or different extension strategies of the local patch. It might be beneficial to create a patch that is more spherical or that is adapted to the singularity potential or to the source orientation.

Convergence of the Localized Subtraction Approach   In this study, we will investigate the convergence behavior of the localized subtraction approach. We employ geometry-adapted hexahedral meshes of a four-layer sphere scenario with increasing resolutions (see Table A.1 for the sphere radii and conductivity values). The number of elements as well as the number of degrees of freedom of the model can be found in Table A.2. The patch Ω^∞ is chosen as the two-times extended patch around the dipole element (see the results of the previous study). For hexahedral meshes, this patch consists of $5^3 = 125$ elements and thus $125 \cdot 8 = 1000$ degrees of freedom, independently of the mesh resolution. Note that when refining the mesh, the diameter of the mesh elements gets smaller and the boundary of the patch approaches the singularity and thus the jump of singularity potential at the boundary of the patch increases. We generate a total number of $29\,884$ source locations in the innermost compartment of the sphere model, distributed over 10 eccentricities. The number of sources on each eccentricity are scaled with the surface area of the corresponding sphere and the eccentricities are scaled logarithmically towards the first conductivity jump. Each position is generated randomly within its assigned eccentricity, and the number of positions within each eccentricity are shown in Table A.3. Note that depending on the mesh resolution, certain source positions at higher eccentricities might lie in a different compartment than the brain compartment. The number of sources for which this is the case are indicated in Table A.3 as well. In the following boxplots, sources which do not lie in a brain element are displayed separately as small dots. For each source position, we compute the unique radial orientation as well as a random tangential orientation. Figure 2.15 shows the convergence behavior of the RDM and MAG measures when increasing the mesh resolution. In general, we observe an increase of the RDM error with increasing eccentricity for both radial and tangential source orientations. The same behavior can be seen for the total range and the inter-quartile range of the MAG error. For all eccentricities, we see a clear convergence behavior for both measures when increasing the mesh resolution. At the eccentricity of 0.925, which corresponds to a distance of approximately 5.9 mm from the conductivity jump, all source positions lie in the gray matter compartment for resolutions of 4 mm and higher. At this eccentricity, the maximal RDM error for radial source orientations decrease from 9.6 % over 5.8 % to 0.9 % for the resolutions of 4 mm, 2 mm and 1 mm respectively. For tangential orientations, a decrease from 7.6 % over 4.0 % to 0.7 % can be observed. The total range of the MAG error decreases at the same eccentricity from 48.7 % over 20.6 % to 3.4 % for radial orientations and from

a) radial source orientations

b) tangential source orientations
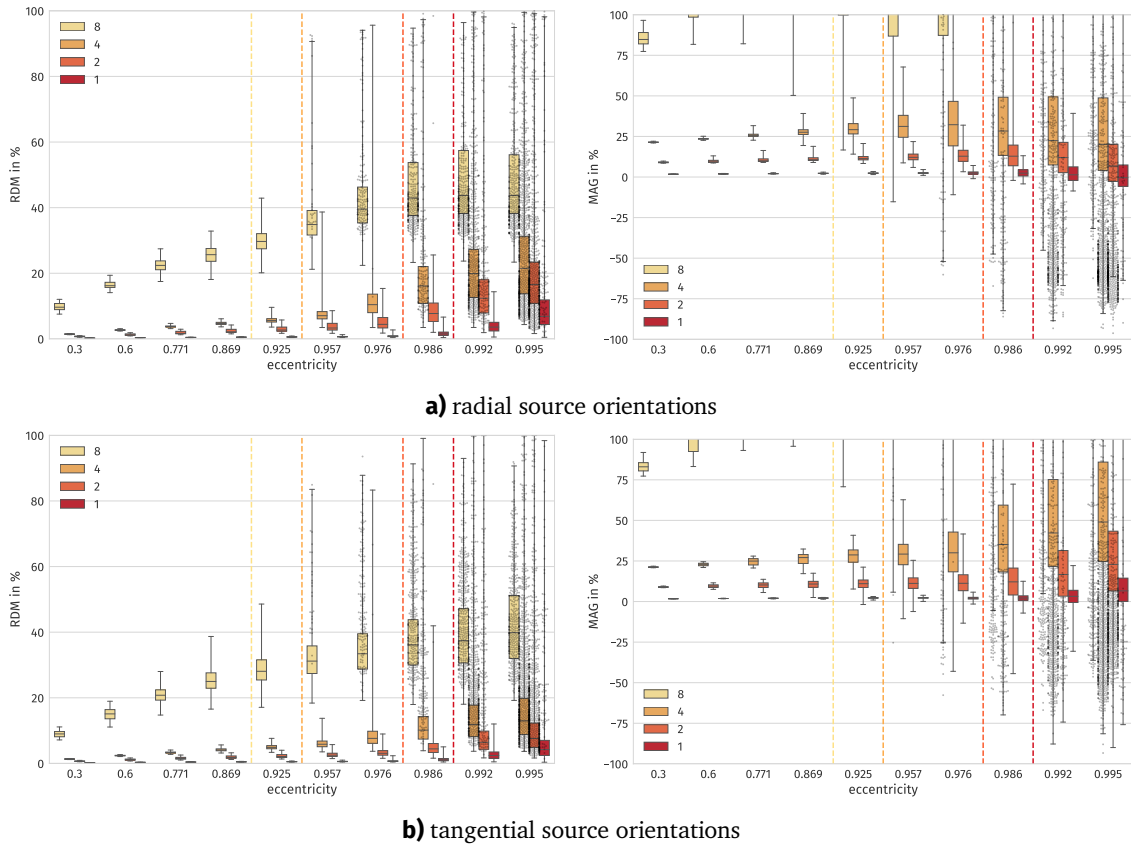
Figure 2.15: Convergence of the errors of a DG discretization with the localized subtraction approach on hexahedral meshes with increasing resolution. On the left side, the RDM error and on the right side, the MAG error is shown (both in %). The dots indicate sources that do not lie within the brain compartment. Sources with an eccentricity lower than the vertical dashed lines are guaranteed to be in the brain compartment, for the resolution with the same color as the line.

a) radial source orientations   **b)** tangential source orientations
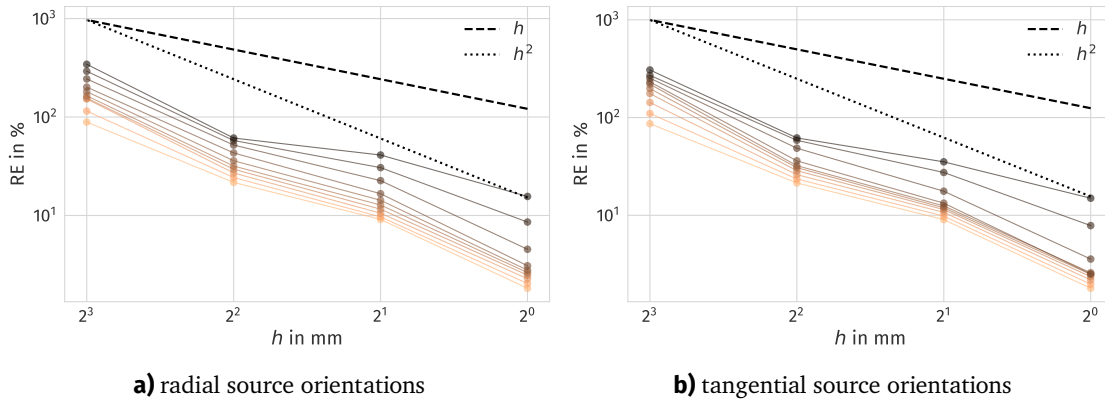
Figure 2.16: Convergence order of the localized subtraction approach. Each brown line represents the convergence of the median relative error in percent of a single eccentricity, where a darker color represents a higher eccentricity. The black dashed line shows a linear convergence while the dotted line shows a quadratic convergence.

40.8 % over 21.2 % to 3.1 % for tangential orientations. Results in Li et al. (2014) indicate that the cortex has a thickness of approximately 2 mm to 6 mm, depending on the exact location. As the generators of the measured activity lie in the center of the gray matter, we can assume a distance of 1 mm to 3 mm. Among the 10 chosen eccentricity values, the eccentricities of 0.986 and 0.976, corresponding to a distance of approximately 1.1 mm and 1.9 mm to the first conductivity jump, are within this range and we focus a detailed description of the results on the eccentricity of 0.986. Only the highest resolution of 1 mm guarantees that sources at the eccentricity of 0.986 are within an element of the brain compartment. We do not investigate the effect on the error measures when moving the dipole to a different location or interpolating the leadfield from nearby valid sources. The total range of the RDM error at this eccentricity for radial source orientations is 6.2 %, the inter-quartile range is 0.04 % with the median being at 1.5 % and the maximum at 6.6 %. For tangential source orientations, the total range of the RDM error is 4.6 %, the inter-quartile range is 0.03 % with the median being at 1.1 % and the maximum at 5.0 %. The total range of the MAG error for radial source orientations is 17.3 %, the inter-quartile range is 0.9 % with the median being at 2.4 % and the maximal absolute value lies at 13.1 %. For tangential source orientations, The total range of the MAG error is 19.6 %, the inter-quartile range is 0.7 % with the median being at 2.2 % and the maximal absolute value lies at 12.5 %. Figure 2.16 shows a visualization of the order of convergences of the median relative error for each eccentricity when increasing the mesh resolution. Each plot corresponds to the median values of a single eccentricity, where a darker color represents a higher eccentricity. We observe a clear convergence behavior of the median relative error for all eccentricities and source orientations. For higher eccentricities, the slope of the convergence plot is less steep than for the lower eccentricities. With each mesh resolution, we see again the increase of the error for increasing eccentricities.

  Comparing the results of the error measures between radial and tangential measures, we see a reduced RDM error for tangential orientations while there is no clear trend for the MAG error. The convergence behavior does not differ significantly between the two different orientations. The exact convergence order is not clearly observable, but we can see a trend towards second order for lower eccentricities and towards first order convergence for higher eccentricities. This is in line with the

theoretical findings of (Wolters et al., 2007a) for the full subtraction approach. Note however that the results are not directly comparable, as the relative error evaluated here only considers point evaluations on the model surface for the full potential, while the results in (Wolters et al., 2007a) are given for the L^2 and H^1 norm errors of the correction potential. Results not shown here indicate that the accuracies and the general convergence behavior remains valid also for a lower patch size of the dipole element and a single layer of neighboring elements, while the patch consisting of only the dipole element did not show stable results.

Comparison to the Full Subtraction Approach   In this study, we compare the results of the localized subtraction approach to the results of the full subtraction approach. The main assumption behind restricting the singularity potential was its lower contribution in the splitting at a distance to the singularity. Note that in contrast to the other results presented in this section, this statistical comparison uses a 2 mm mesh resolution, due to the high time consumption of the full subtraction approach (see below). Figure 2.17 shows the direct comparison between the full and the localized subtraction on a 2 mm hexahedral mesh. Aside from one eccentricity (0.995) for the RDM of tangential sources, there is no significant difference between the boxplots of the two approaches. The RDM increases with increasing eccentricity for both source orientations and we observe a steeper ascend for the highest eccentricities. Due to the small difference between the two approaches, we will report the results for the localized subtraction approach. For internal sources (sources that do not lie within an element on the compartment boundary, delimited by the yellow line) the maximal RDM error of the localized subtraction is 5.8 % for radial sources and 4.0 % for tangential sources and occurs at an eccentricity of 0.925 for both cases. For boundary sources (sources which might lie in an element at the compartment boundary, but not in an element within the CSF, between yellow and red line), the maximal RDM error is 15.4 % for radial sources and 9.0 % for tangential sources and occurs at an eccentricity of 0.976 for both orientations. Corresponding to the increase in the RDM, the inter-quartile range (IQR) and total range (TR) of the MAG increases with increasing source eccentricity and the increase becomes more pronounced for the highest eccentricities. For internal sources (see above), the maximal IQR of the MAG is 2.1 % for radial sources and 4.7 % for tangential sources. The maximal TR for these sources is 12.3 % for radial orientations and 23.0 % for tangential orientations. These maxima for the MAG are observed at the eccentricity of 0.925. For boundary sources, the maximal IQR of the MAG for radial sources is 6.8 % and for tangential sources it is 9.9 %. The maximal TR is 28.7 % for radial orientations and 54.9 % for tangential orientations. Figure 2.18 shows the relative difference between the leadfields of the full subtraction L_{full} and the localized subtraction approach L_{local}, i.e.

$$\frac{\|L_{\text{local}} - L_{\text{full}}\|_F}{\|L_{\text{full}}\|_F}, \tag{2.29}$$

where $\| \cdot \|_F$ denotes the Frobenius norm and L denotes the respective leadfield matrix consisting of the potential at the electrodes for all source positions and the three Cartesian directions. Note that only sources which lie within an element of the brain compartment are considered in this comparison. Based on the mesh resolution, the sources are split into three categories: *internal*, *boundary* and *possibly external* sources. Internal sources are located within a mesh element that is not touching the conductivity jump. Boundary sources might be located within an element touching

a) radial source orientations

b) tangential source orientations
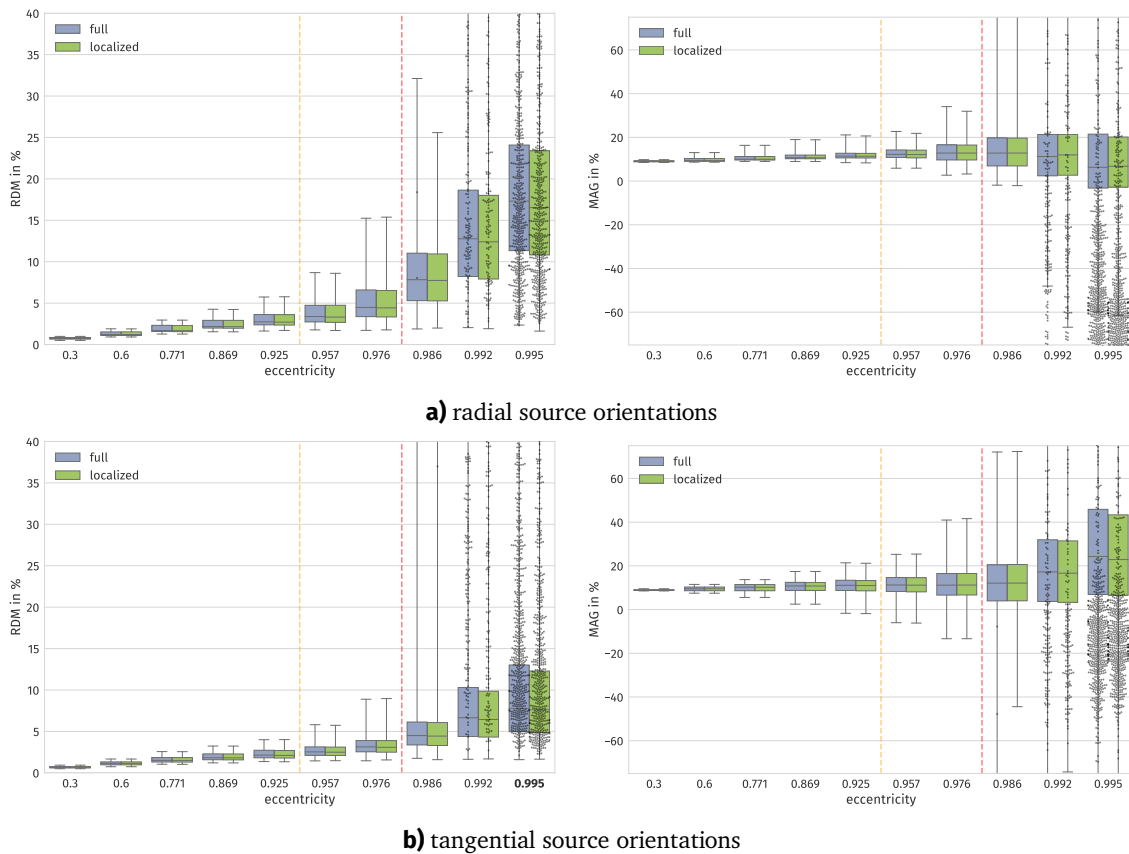
Figure 2.17: Errors of a DG discretization with the full and localized subtraction approach on a 2 mm hexahedral mesh. On the left side, the RDM error and on the right side, the MAG error is shown (both in percent) for both radial and tangential sources. The dots indicate sources not fully contained in the brain compartment. Sources with an eccentricity lower than the vertical yellow line are guaranteed to be within an element not touching the first conductivity jump. At eccentricities between the vertical yellow and red lines, sources might be within an element touching the first conductivity jump but are still guaranteed to be within the brain compartment. A bold eccentricity label indicates a significant difference (t-Test, $p < 0.01$) between the two boxplots.
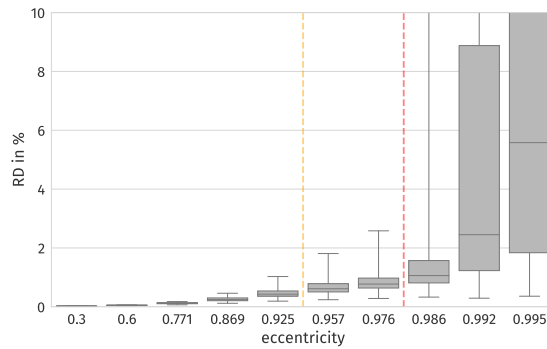
Figure 2.18: Relative difference between the leadfields of the full and the localized subtraction approach on a 2 mm hexahedral mesh using (2.29). Sources with an eccentricity lower than the vertical yellow line are guaranteed to be within an element not touching the first conductivity jump. At eccentricities between the vertical yellow and red lines, sources might be within an element touching the first conductivity jump but are still guaranteed to be within the brain compartment.

the first conductivity jump, but are still within the gray matter compartment. Possibly external sources might be within an element of a different compartment. In Figure 2.18, these categories are separated by vertical lines. We observe an increasing difference between the two approaches with increasing eccentricity. The maximal relative difference for internal sources of 1.0 % occurs at the eccentricity of 0.925. At the lowest eccentricity of 0.3, the maximal relative difference is 0.03 %. For boundary sources, the maximal relative difference is 2.6 % occurring at the eccentricity of 0.976. The difference between both approaches increases strongly for possibly external sources.

Figure 2.19 shows the goal function of a dipole fitting approach for the full and the localized subtraction approach in a 1 mm model for a target source at an eccentricity of 0.8 with a radial and a tangential orientation. The reference solution of the target source was created using the quasi-analytical solution of the forward problem. The plots of the goal functions overlap and are, on this scale, visually not distinguishable from each other. For both radial and tangential orientations, we see a convex shape of the goal function plots with a minimum slightly below the eccentricity of 0.8. When computing the difference between two neighboring source locations, the localized subtraction approach shows small jumps for a tangential target source. These jumps in the difference mean that the goal function plot contains small kinks at the corresponding locations. These kinks are regularly spaced and correspond approximately to the diagonal diameter of the mesh elements. The magnitude of these jumps is larger for tangential orientations, but the direction of the jump, i.e., the sign of the difference, points towards the minimum of the goal function. Results not shown here indicate that the magnitude of these jumps is reduced when increasing the patch size and slightly increased when reducing the patch size to a single extension.

To evaluate the time consumption of the different approaches, we measure the time for applying the transfer matrix to a single dipole. The time consumption is averaged over 1000 runs on a single core of a conventional laptop (Intel i7 6700HQ, 2.6 GHz). The results are shown in Figure 2.20. We observe an increase of the time consumption for the full subtraction approach with decreasing h in the order of h^{-3}. The mean time at the resolution of $h = 2$ mm is $10\,008$ ms ≈ 10 s. The time consumption for the localized subtraction approach stays approximately constant, and is 88 ms $\approx$

a) radial target   **b)** tangential target
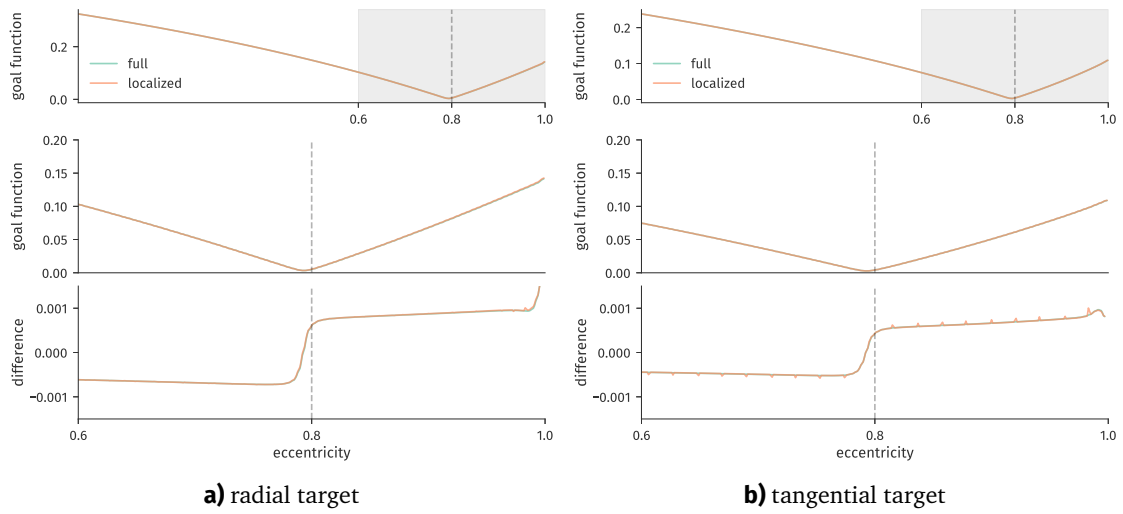
Figure 2.19: Goal function for a dipole fitting approach using the full (green) and the localized (orange) subtraction approach on a 1 mm geometry-adapted hexahedral mesh. The left column contains results for a radial target, the right column for a tangential target. Each column contains an overview plot of the goal function (top), a zoomed-in plot of the goal function (middle) and a plot of the difference between two neighboring values of the zoomed-in data (bottom). The dashed vertical line shows the location of the target source. The shaded area in the top plot indicates the zoomed-in area of the two lower plots.
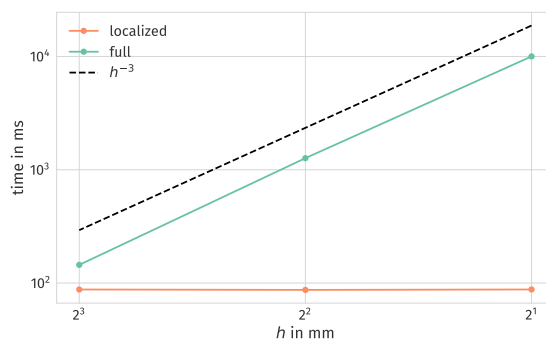
Figure 2.20: Time consumption for applying the transfer matrix for the full subtraction approach and the localized subtraction approach on a series of hexahedral meshes. The y-axis shows the time consumption in milliseconds for a single dipole averaged over 1000 runs and the x-axis shows the mesh resolution. Both axes are scaled logarithmically.

0.09 s at the resolution of $h = 2$ mm. The time for locating the element containing the dipole is 0.017 ms, 0.021 ms and 0.037 ms for resolutions of 8 mm, 4 mm and 2 mm, respectively.

In the following, we discuss the results of the comparison between the full subtraction approach and the localized subtraction approach. First we note that the measures for the RDM and MAG are in line with the values reported in (Engwer et al., 2017) (after applying the necessary transformations due to the usage of rdm and lnmag instead of RDM and MAG in percent that were used here). For internal and boundary sources, the only observable difference between the full and the localized subtraction approach can be seen in the slight kinks of the goal function and in highly eccentric sources. With respect to the RDM and MAG measures, both approaches can be used interchangeably.

The largest difference between the two approaches can be seen with respect to the computational load. The main difference shown in Figure 2.20 is the linear increase with increasing number of elements for the full subtraction approach, while the time consumption of the localized approach stays approximately constant. The time consumption for both approaches can be split into three parts: the time for localization of the dipole element, the time for the assembly of the right-hand side and the time for the multiplication with the transfer matrix. The duration of the first step is identical for both approaches. It depends on h but it is significantly smaller than the total time taken for both the full and the localized subtraction approach. The second step, i.e., the assembly of the right-hand side, shows a different time consumption for the two approaches. For the full subtraction approach, integrals have to be evaluated over the volume of all elements, over the internal skeleton and over the external domain boundary. For the localized subtraction approach, these integrals are only evaluated on a patch around the source location which contains a constant number of hexahedrons, that is independent of h. A similar difference can be found for the time consumption of the third step, the multiplication of the assembled right-hand side with the transfer matrix. The right-hand side of the full subtraction approach is densely populated, leading to a multiplication that depends of the number of mesh elements. The right-hand side of the localized approach is sparse, as it consists only of those entries whose degrees of freedom are associated with the patch, leading to a multiplication independent of the number of mesh elements (excluding the increased size of the transfer matrix itself). Thus the time consumption of the full subtraction approach strongly depends on the number of mesh elements. The only part of the time consumption for the localized approach that depends on the number of elements is the localization of the dipole element, which takes significantly less time than the remaining assembly. Note that this might change for higher resolutions of the mesh. However, using an efficient nearest neighbor search, the time consumption for locating the dipole element scales with $\log(N)$, where N denotes the number of mesh elements.

We can conclude, that this high time consumption of the full subtraction approach makes it currently unfeasible for computations with many sources on 1 mm hexahedral meshes. The localized subtraction approach however is an attractive alternative to the full subtraction approach. It maintains the high accuracy of the full subtraction approach, while strongly reducing the time consumption.

2.4 Conclusion

In this chapter, we presented extensions to two discrete source models for modern finite element approaches. In Section 2.1 we recalled the existing monopolar Venant approach and showed its con-

nection to the partial integration approach. We introduced a conforming Venant approach, which uses a conforming source representation instead of non-conforming monopoles. By using mixed higher-order moments, the smoothness of the goal function could be increased. We presented the first application of a Venant approach for a discontinuous Galerkin discretization in Section 2.2. In Section 2.3 we introduced a localized subtraction approach which reduced the high computational load while maintaining the general behavior and accuracy. This localization makes the subtraction approach feasible for practical applications even in high-resolution head models.

There are still some open questions regarding the extensions presented in this chapter. As the source term of the Venant approach is now representable in a conforming way, it could be possible to represent the interpolation process as a classical regularization approach and replacing the singular source term by a regularized dipolar source term. In addition, it should be possible to derive convergence properties of the conforming Venant approach, by estimating the norm of the resulting source term, which should depend on the mesh size h. For the localized subtraction approach, an investigation on the effect to the magnetoencephalography forward problem should be considered, as the classical full subtraction approach outperformed the partial integration and the Venant approaches for this application. With regard to the construction of the local patch, different strategies can be considered and investigated, such as constructing a spherical shaped patch or adapting to the form of the singularity potential or the orientation of the dipolar source. Furthermore, the idea of the localization can be transferred to the conforming finite element method. Instead of cutting off the singularity potential on the patch boundary, one can consider a splitting of the form

$$u_h = \tilde{u}_h + k^\infty u^\infty$$

where $k^\infty \in H^1(\Omega)$ is a regularization of the indicator function. This regularization could for example be built as an interpolation of the indicator function into the conforming finite element space.

Unfitted Finite Element Methods
for Solving the EEG Forward Problem

In Chapter 1, two different finite element methods for solving the EEG forward problem have been presented, namely the continuous and discontinuous Galerkin methods. Both methods have in common that they use a tetrahedral or hexahedral mesh that is adapted to conform to the model geometry. Using a geometry conforming tetrahedral mesh provides a highly accurate representation of the smooth head surface and the surfaces of the different tissue compartments. This accuracy comes at the cost of a more involved modeling pipeline. In order to create the tetrahedral mesh from a segmented MRI image, triangular surfaces separating the different tissue compartments have to be created from which a volume tetrahedralization can be derived. Most algorithms for creating a tetrahedralization impose restrictions onto the regularity of the surfaces, such as not intersecting and not touching each other. In contrast to the tetrahedral approach, the creation of a hexahedral mesh is straightforward. The nodes and mesh elements can be derived directly from a voxel segmentation. While this approach provides a very simple simulation pipeline, it imposes a larger geometry error, as the adaption to the model geometry is limited. In order to provide a reasonable approximation of the geometry, a higher mesh resolution has to be used, leading to an increase in computation time.

In this chapter, we present two methods based on a different approach to incorporate the model geometry. Instead of creating a mesh that conforms to the model geometry, we use a structured hexahedral mesh and incorporate the geometry weakly into the discretized mathematical model. The different surfaces are represented by level-set functions (Osher and Sethian, 1988).

For the EEG forward problem, a similar approach has been presented and evaluated in (Vallaghé and Papadopoulo, 2010). Based on the level-set representation of the different surfaces, the local basis functions of a hexahedral approach are modified to conform to the different tissue compartments. This modification is restricted to the case of a single interface per mesh element or two interfaces that do not intersect each other. Furthermore, it is tailored to multi-linear test and ansatz

functions. It was shown that the accuracy of a geometry-conforming tetrahedral approach could be met, while offering a simpler simulation pipeline.

In Section 3.1, we first describe and evaluate the CutFEM approach in a multi-domain setting. It uses a standard, conforming Lagrangian finite element space without modification within each subdomain, but introduces a weak coupling between the different tissue compartments. Section 3.2 presents the unfitted discontinuous Galerkin method, which additionally allows for discontinuities between mesh elements and allows for using higher-order ansatz functions, similar to the discontinuous Galerkin method presented in Section 1.3. Both methods share the discretizations of the dipolar source term, which will be presented in Section 3.3. In Section 3.4, several validation studies are performed to evaluate the performance of the presented methods, compared to each other and in comparison to the existing finite element methods. Finally, a summary and conclusion will be given in Section 3.5.

3.1 A Cut Finite Element Method

For the description of the CutFEM method, we mainly follow (Burman and Hansbo, 2012) and (Burman et al., 2015) but take ideas and notations from (Engwer, 2009) into account. The origin of the CutFEM method goes back to the unfitted finite element method (Barrett and Elliott, 1987; Hansbo and Hansbo, 2002). Instead of incorporating the different tissues only into the conductivity tensor, we split the domain into different subdomains, based on a level-set representation of the different tissue compartments, allowing for a sub-voxel resolution of the domain boundaries. On each subdomain, we employ a conforming Lagrange finite element method and couple the subdomains weakly on their boundaries. An additional penalty term in the boundary zone of each subdomain ensures the stability and robustness of the resulting discretization method independent on the interface positions.

First of all we require that the domain Ω is embedded in an auxiliary domain $\hat{\Omega} \subset \mathbb{R}^d$, i.e., $\Omega \subset \hat{\Omega}$. This auxiliary domain will also be called the *background domain*. Usually, this background domain is given as a box, i.e., a d-dimension Cartesian product of intervals. We now assume that the domain Ω can be split into non-overlapping subdomains, i.e., that there are $\Omega_0, \ldots, \Omega_{m-1} \subset \mathbb{R}^d$ such that

$$\overline{\Omega} = \bigcup_{i=0}^{m-1} \overline{\Omega}_i$$
$$\Omega_i \cap \Omega_j = \varnothing, \text{ for } i \neq j$$

hold. In our case, these subdomains describe the different tissue compartments, e.g., the skull or the white matter compartment. The tissue compartments usually differ between each other by the values of a symmetric and positive definite conductivity tensor $\sigma : \Omega \to \mathbb{R}^{d \times d}$. By $\mathcal{G} \subset \mathbb{R}^d$, we denote the internal skeleton between the different subdomains, i.e., the intersections of their closures:

$$\mathcal{G} := \bigcup_{\substack{0 \leq i,j < m \\ i \neq j}} \left(\overline{\Omega}_i \cap \overline{\Omega}_j \right).$$

a) fundamental mesh $\mathcal{T}_{\hat{h}}(\hat{\Omega})$ **b)** submesh $\mathcal{T}_{\hat{h}}^0(\hat{\Omega})$ **c)** submesh $\mathcal{T}_{\hat{h}}^1(\hat{\Omega})$
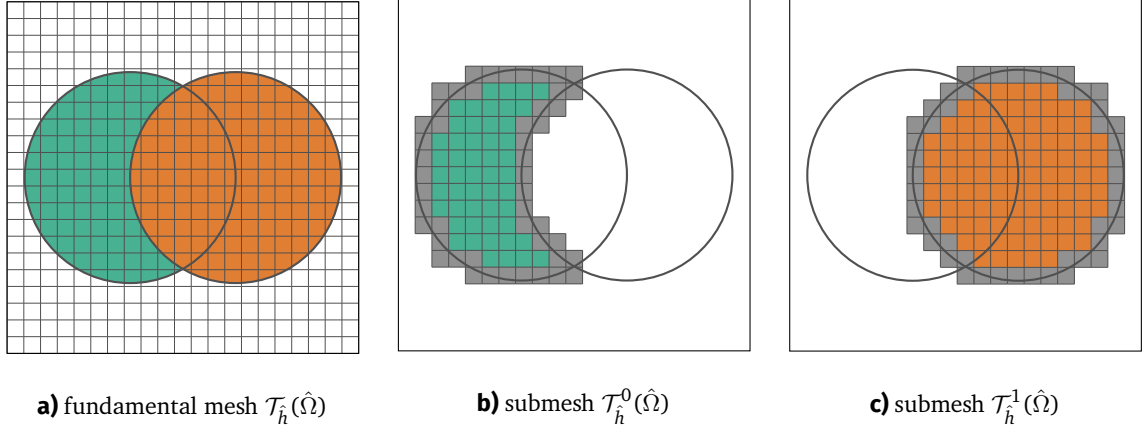
Figure 3.1: Fundamental mesh of a CutFEM discretization with two subdomains Ω_0 (green) and Ω_1 (red) delimited by two intersecting spheres. The elements colored in gray indicate elements cut by an interface.

In this multi-domain setting, we can formulate the strong Poisson's equation for the potential u as:

$$\nabla \cdot \sigma \nabla u = f \quad \text{in } \bigcup_{i=0}^{m-1} \Omega_i,$$

$$\langle \sigma \nabla u, \boldsymbol{n} \rangle = 0 \quad \text{on } \partial\Omega,$$

$$[\![u]\!] = 0 \quad \text{on } \mathcal{G},$$

$$[\![\sigma \nabla u]\!] = 0 \quad \text{on } \mathcal{G},$$

where f denotes the dipolar source term and $[\![\cdot]\!]$ denotes the jump of a quantity on an interface (cf. Definition 1.16). Similar to the previous chapters, the potential is only determined up to a constant due to the pure Neumann boundary condition on $\partial\Omega$. To determine a unique solution, we fix the value of the integral of u by requiring $\int_{\Omega} u \, dx = 0$. To discretize the multi-domain Poisson's equation, we introduce a tessellation $\mathcal{T}_{\hat{h}}(\hat{\Omega})$ of the background domain $\hat{\Omega}$, called the *fundamental mesh* or the *background mesh*. In contrast to the methods presented in the previous chapters, the mesh does not conform to the domain Ω or the different tissue compartments, i.e., the element boundaries are not fitted to $\partial\Omega$ nor to $\mathcal{G}$. Usually, the fundamental mesh will be a structured hexahedral mesh with elements of a fixed diameter $\hat{h} \in \mathbb{R}$. When intersecting each subdomain with the fundamental mesh, the resulting submesh is defined as

$$\mathcal{T}_{\hat{h}}^i(\hat{\Omega}) := \left\{ E \in \mathcal{T}_{\hat{h}}(\hat{\Omega}) : E \cap \Omega_i \neq \varnothing \right\} \subset \mathcal{T}_{\hat{h}}(\hat{\Omega}).$$

The submeshes are formed of those elements of the fundamental mesh, that contain parts of the corresponding subdomain. Figure 3.1 shows a visualization of a two domain scenario along with the fundamental mesh and two submeshes. We see that the submeshes overlap on each element that contains an interface between two subdomains. On each of these submeshes $\mathcal{T}^i$, we define a finite element space $V_{\hat{h}}^i$, which we will choose as the space of continuous, piecewise linear functions. Each space is spanned by a set of global basis functions: $V_{\hat{h}}^i = \text{span}\left\{ \varphi_0^i, \ldots, \varphi_{N_i-1}^i \right\}$. Combining

the local finite element spaces, we define the global finite element space as

$$V_{\hat{h}} := \prod_{i=0}^{m-1} V_{\hat{h}}^i.$$

Note that the discrete functions within this global space have multiple values on elements that are cut by an interface between subdomains. As the functions are continuous on each subdomain, they are strongly coupled within the different tissue compartments. On this finite element space, we define the bilinear form of the weak formulation of Poisson's equation as

$$\tilde{a}(u_h, v_h) := \sum_{i=0}^{m-1} \int_{\Omega_i} \left\langle \sigma \nabla u_h^i, \nabla v_h^i \right\rangle \mathrm{d}x\,, \tag{3.1}$$

where u_h^i and v_h^i denote the restriction of u_h and v_h to the local space on Ω_i, respectively. In the following, we will omit the index of the domain if no ambiguities arise and will write $\int_\Omega \langle \sigma \nabla u_h, \nabla v_h \rangle \, \mathrm{d}x$ instead. Note that the functions within each discrete subspace are only integrated over the parts of the domain that lie within the associated subdomain, even though their support extends over the subdomain boundary. The numerical integration over domains that are defined implicitly via level-set functions is described in detail in Section 4.1.

The coupling between the different subdomains is performed weakly using Nitsche's method (Nitsche, 1971). This coupling is employed on the discrete subdomain skeleton, defined as

$$\Gamma := \left\{ E \cap \left(\overline{\Omega}_i \cap \overline{\Omega}_j \right) : E \in \mathcal{T}(\hat{\Omega}), 0 \le i, j < m, i \ne j, \mathrm{meas}_{d-1}(E \cap (\overline{\Omega}_i \cap \overline{\Omega}_j)) > 0 \right\}$$

where meas_{d-1} denotes the $d-1$-dimensional measure in d-dimensional space. Thus, for each intersection $\gamma \in \Gamma$, there is an element E of the fundamental mesh and two subdomains Ω_i and Ω_j such that γ forms the interface between these two subdomains in the element E. Note that, since the model problem considered here is Poisson's equation with a homogeneous Neumann boundary condition, this discrete skeleton only contains intersections between two subdomains and no intersection on the domain boundary. The weak coupling between the subdomains provided by Nitsche's method is defined as:

$$\bar{a}(u_h, v_h) := -\int_\Gamma \langle \llbracket u_h \rrbracket, \{\sigma \nabla v_h\} \rangle + \langle \{\sigma \nabla u_h\}, \llbracket v_h \rrbracket \rangle \, \mathrm{d}s + \eta \nu_k \int_\Gamma \frac{\hat{\sigma}}{\hat{h}} \langle \llbracket u_h \rrbracket, \llbracket v_h \rrbracket \rangle \, \mathrm{d}s\,, \tag{3.2}$$

with the jump operator $\llbracket \cdot \rrbracket$ and average operator $\{\cdot\}$ as in Definitions 1.16 and 1.17, respectively, adapted to the formulation of two subdomains instead of two elements on the two sides of an interface. Here $\hat{h}$, denotes the diameter of the element of the fundamental mesh and $\eta \in \mathbb{R}$ is a scalar penalty constant. The last term in (3.2) describes a penalty which penalizes jumps on the boundary between the subdomains. Following (Di Pietro and Ern, 2011) (cf. Section 1.3), it is scaled by the harmonic average $\hat{\sigma}$ of the conductivity tensors: on an intersection $\gamma \in \Gamma$ between subdomains Ω_i and Ω_j, $\hat{\sigma}$ is defined as

$$\hat{\sigma}_\gamma := \frac{2\delta_i \delta_j}{\delta_i + \delta_j},$$

with $\delta_k := \boldsymbol{n}^t \sigma_k \boldsymbol{n}$, $k = i, j$, where $\boldsymbol{n}$ denotes a unit normal vector on γ and σ_k denotes the conductivity tensor on the respective side of the interface. To accommodate for different polynomial degrees, the penalty term is additionally scaled by $\nu_k = k(k + d - 1) \in \mathbb{R}$ following (Epshteyn and Rivière, 2007). As we mainly use linear polynomials in three spatial dimensions, we obtain $\nu_1 = 3$. Summing the two bilinear forms $\tilde{a}$ from (3.1) and $\overline{a}$ from (3.2), we obtain the bilinear form of the coupled multi-domain equation:

$$a(u_h, v_h) := \tilde{a}(u_h, v_h) + \overline{a}(u_h, v_h) \tag{3.3}$$

Using this bilinear form, we can state a discrete analogue to the weak formulation of the multi-domain Poisson's equation. However, theoretical considerations of (Burman and Hansbo, 2012) show that the resulting discretization is not stable with respect to how the interfaces cut the fundamental mesh elements. As no restrictions on the occurring level-set functions have been made, the cut of the interface with the elements of the fundamental mesh can become arbitrarily small, which deteriorates the robustness of the method. One approach to circumvent this problem is called *cell-merging* or *cell-aggregation* (Badia et al., 2017). Cut-cells of small size are identified and their contribution is attributed to a neighboring cell of larger size. However in practice, especially in a multi-domain setting, the identification of the neighboring cell is an involved process and might fail if the neighboring cell is also of smaller size. (Burman and Hansbo, 2012) propose an approach which is called *edge penalization* or *ghost penalty* to remedy this problem. This penalty term is defined on the skeleton of the fundamental mesh and ensures a weak coupling between neighboring cut cells independent of the actual size of the cut cells. By $\hat{\Gamma}$, we denote the skeleton of the fundamental mesh, i.e., we define

$$\hat{\Gamma} := \left\{ \overline{E}_i \cap \overline{E}_j : E_i, E_j \in \mathcal{T}_{\hat{h}}(\hat{\Omega}), i \neq j, \text{meas}_{d-1}(\overline{E}_i \cap \overline{E}_j) > 0 \right\},$$

which consists of the intersections of the closures of two fundamental mesh elements. On this skeleton, the ghost penalty is defined as

$$b(u_h, v_h) := \tilde{\eta} \int_{\hat{\Gamma}} \hat{h} \left[\!\left[\sigma \nabla u_h \right]\!\right] \left[\!\left[\nabla v_h \right]\!\right] \, \mathrm{d}s \,, \tag{3.4}$$

where $\tilde{\eta} \in \mathbb{R}$ is a penalty constant independent of $\hat{h}$ and of how the interface cuts the mesh, but not independent of η. Note that this ghost penalty term is only appropriate for piecewise linear ansatz functions considered here and has to be modified if higher polynomial degrees should be considered (Burman, 2010). The integral of the ghost penalty is to be understood to affect only the interface zone of each subdomain and σ is thus well-defined on $\hat{\Gamma}$. Figure 3.2 shows a visualization of the different penalties for a two-dimensional example. Summing the bilinear form (3.3) and the ghost penalty (3.4) gives the CutFEM method.

Definition 3.1 (CutFEM). *The CutFEM approach for solving the EEG forward problem is defined as: Find $u_h \in V_{\hat{h}}$ such that*

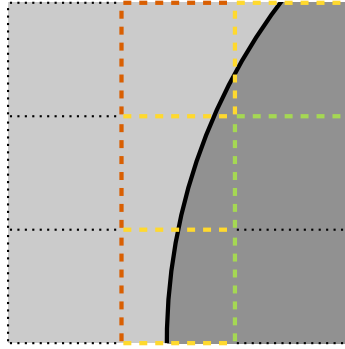$$a(u_h, v_h) + b(u_h, v_h) = l(v_h)$$

Figure 3.2: Visualization of the different penalty terms in the CutFEM discretization between two subdomains, light gray and dark gray. The dashed lines indicate faces on which a ghost penalty is added. The red lines indicate a ghost penalty affecting the light gray domain, the green lines affecting the dark gray domain and the yellow lines affecting both domains. On the solid black line, the penalty of Nitsche's method is added. No penalty is considered on the dotted lines.

for all $v_h \in V_{\hat{h}}$, with a and b defined in (3.3) *and* (3.4)*, respectively.*

In (Burman and Hansbo, 2012), coercivity and continuity of the bilinear form $a + b$ as well as optimal convergence is shown for the single compartment model with a regular source term.

3.2 An Unfitted Discontinuous Galerkin Method

The unfitted discontinuous Galerkin (UDG) method extends concepts of the CutFEM approach (cf. Section 3.1) to the whole domain. The general approach can be seen similar to the step from the fitted continuous Galerkin finite element method presented in Section 1.2 to the discontinuous Galerkin finite element method in Section 1.3. In addition to the weak coupling between different subdomains and on the domain boundary that was introduced by Nitsche's method, also the coupling between different cut-cells within the same subdomain is performed weakly. This approach leads to a discretization scheme that provides local conservation of charge within each set of cut-cells. The description of the UDG method and parts of the validation results that will be presented in Section 3.4 have been published in (Nüßing et al., 2016).

The unfitted discontinuous Galerkin method was first presented in (Bastian and Engwer, 2009; Engwer, 2009) and applied in the context of micro-scale simulations in porous media. Its main advantage was seen in the direct usability of surfaces obtained from a level-set segmentation of imaging data, and the straightforward use of higher order polynomial functions. Since then, it has found different applications (Burman et al., 2017; Engwer and Westerheide, 2014; Gürkan and Massing, 2018; Heimann et al., 2013). In general, a discrete weak formulation for this unfitted discontinuous Galerkin method can be defined similarly to the fitted discontinuous Galerkin method (DG) from Section 1.3, while redefining the computational domain.

The description follows closely the definition of the CutFEM method and we refer to Section 3.1 for the definition of most concepts. We start with a domain $\Omega \subset \mathbb{R}^d$ which is embedded within an auxiliary domain $\hat{\Omega}$. By $\Omega_0, \ldots, \Omega_{m-1}$ we denote a partition of Ω into non-overlapping subdomains. Let $\mathcal{T}_{\hat{h}}(\hat{\Omega}) = \{E_0, \ldots, E_{n-1}\}$ denote the fundamental mesh, i.e., a tessellation of $\hat{\Omega}$. By intersecting

the elements of the fundamental mesh with the different subdomains, we obtain the cut-cell mesh

$$\overline{\mathcal{T}}_{\hat{h}} = \bigcup_{i=0}^{n-1} \underbrace{\{E_i \cap \Omega_j : E_i \cap \Omega_j \neq \varnothing\}}_{=:E_i^j}.$$

The elements E_i^j of this mesh are called *cut-cells*. In order to couple the cut-cells within and between the different domains, we define the inter-domain skeleton

$$\overline{\Gamma}_{\hat{h}}^d := \left\{ \gamma_i^{j,k} := \overline{E}_i^j \cap \overline{E}_i^k : E_i^j, E_i^k \in \overline{\mathcal{T}}_{\hat{h}}, k \neq j, \mathrm{meas}_{d-1}(\gamma_i^{j,k}) > 0 \right\}$$

and the inter-element skeleton as

$$\overline{\Gamma}_{\hat{h}}^e := \left\{ \gamma_{i,j}^k := \overline{E}_i^k \cap \overline{E}_j^k : E_i^k, E_j^k \in \overline{\mathcal{T}}_{\hat{h}}, i \neq j, \mathrm{meas}_{d-1}(\gamma_{i,j}^k) > 0 \right\}.$$

The inter-domain skeleton contains the intersection of cut-cells of different domains on the same fundamental mesh element, while the inter-element skeleton contains intersections between cut-cells of the same domain but on different fundamental mesh elements. The union of the two skeleton parts is defined as $\overline{\Gamma}_{\hat{h}} := \overline{\Gamma}_{\hat{h}}^e \cup \overline{\Gamma}_{\hat{h}}^d$. We introduce the space of piecewise polynomial functions $V_h^k := \{v_h \in L^2(\Omega) : v_h|_E \in \mathcal{P}^k(E) \forall E \in \overline{\mathcal{T}}_{\hat{h}}\}$. $\mathcal{P}^k(E)$ denotes a space of polynomials on E of degree $k \in \mathbb{N}$. On the cut-cell mesh and its skeleton, we define the UDG discretization as: Find $u_h \in V_h^k$ such that for all test functions $v_h \in V_h^k$

$$a(u_h, v_h) + J(u_h, v_h) = l(v_h) \tag{3.5}$$

holds. The bilinear forms a and J are given as

$$a(u_h, v_h) = \int_\Omega \langle \sigma \nabla u_h, \nabla v_h \rangle \, \mathrm{d}x - \int_{\overline{\Gamma}_{\hat{h}}} \langle [\![u_h]\!], \{\sigma \nabla v_h\} \rangle \, \mathrm{d}s - \int_{\overline{\Gamma}_{\hat{h}}} \langle [\![v_h]\!], \{\sigma \nabla u_h\} \rangle \, \mathrm{d}s, \tag{3.6}$$

$$J(u_h, v_h) = \eta \nu_k \int_{\overline{\Gamma}_{\hat{h}}} \frac{\hat{\sigma}_\gamma}{h_\gamma} \langle [\![u_h]\!], [\![v_h]\!] \rangle \, \mathrm{d}s, \tag{3.7}$$

$$l(v_h) = \int_\Omega f v_h \, \mathrm{d}x. \tag{3.8}$$

Following (Georgoulis et al., 2007) and similar to the discontinuous Galerkin method introduced in Section 1.3, the penalty term is scaled with the local cut-cell size h_γ, which is defined as

$$h_\gamma := \frac{\min(\mathrm{meas}_d(E_i), \mathrm{meas}_d(E_j))}{\mathrm{meas}_{d-1}(\gamma)},$$

where $\gamma \in \overline{\Gamma}_{\hat{h}}$ denotes the interface between two cut-cells E_i and E_j. To accommodate for different polynomial degrees, the penalty term is additionally scaled by $\nu_k = k(k + d - 1) \in \mathbb{R}$ following (Epshteyn and Rivière, 2007). On each cut-cell, we introduce a local basis of the polynomial space and assemble the system matrix. The right-hand side is discretized following methods similar to those presented for the geometry-conforming approaches. Differences to those approaches with respect to the source model are shown in Section 3.3. Compared to the CutFEM approach presented

in Section 3.1, the UDG method offers additionally local conservation of charge within each subdomain. It can be shown that the condition number of the linear system depends on the cut-cell size. In (Engwer, 2009), the local basis functions on each cut-cell are scaled with respect to the respective bounding box, which resulted in a reduction of the condition number. To additionally reduce the computational load, small cut-cells were merged with larger neighboring cells in (Heimann et al., 2013). A different approach, following the principles presented for the CutFEM approach, has been presented in (Gürkan and Massing, 2018). A ghost-penalty term, that is independent of the cut-cell size, is added on faces of the fundamental mesh.

3.3 Source Models for Cut-Cell Methods

The source models presented in Chapter 1.2 for the standard Lagrange finite element method can also be applied in a CutFEM discretization, but they have to be modified to fit the unfitted framework. The partial integration approach can be applied with almost no modifications using the basis functions defined on the background mesh. For the UDG method, we have to take the scaling of the basis functions to the bounding box of the cut-cell into account, which results in an additional scaling of the gradient in the partial integration approach. Note that, even if a source lies slightly outside of the discrete representation of the gray matter compartment, we can still evaluate the gradient as long as the dipole position lies within an element containing a cut-cell of the gray matter compartment. The monopolar Venant approach can be transferred to the unfitted case by placing the monopoles with respect to the fundamental mesh. However, distributing the monopoles on the nodes of the background mesh might be a poor choice, as the nodes are independent of the interface and might thus also lie at a distance from the interface or geometrically in the next compartment. Instead, we place the monopoles in the volume of the elements of the fundamental mesh. Their local positions are chosen based on a Gauss-Legendre quadrature rule of a certain order. For the placement of the monopoles, we only consider elements that contain cut-cells of the gray-matter compartment. When using local positions with respect to the fundamental mesh elements, some monopoles might geometrically lie in a different compartment, even though they contribute only to the basis functions belonging to the dipole compartment. Instead of distributing the positions in the element, it might thus be beneficial to consider the local positions obtained from the quadrature rule with respect to the bounding box of intersection of the element and the domain. A further extension might be to find a better distribution of the monopoles by taking the local interface into account. The formulation of the subtraction approach can be given in a similar way as for the DG method by taking the weak coupling of Nitsche's method on the domain boundaries into account. However, the high computational load that was observed for the geometry-conforming approaches will be even more pronounced in the Unfitted case, as the integration over the implicitly defined domain is computationally more expensive than the direct integration of the elements of a tessellation. The restriction of the support of the singularity potential that was presented in Section 2.3, which strongly reduces the support of the source-term, can be adapted for the UDG approach in a straightforward way, but has not been implemented so far.

3.4 Validation Studies

In this section we present validation studies for the CutFEM method presented in Section 3.1 and the UDG method presented in Section 3.2. In Section 3.4.1, we study the CutFEM discretization in four-layer sphere models. We evaluate different source models, study the convergence behavior and compare the method to the conforming finite element method on tetrahedral and hexahedral meshes. The UDG method is evaluated in four-layer sphere models in Section 3.4.2. We present the convergence behavior, compare the UDG method to the CutFEM method and investigate the use of higher order polynomials within the UDG discretization. In Section 3.4.3, we evaluate the CutFEM method in a scenario using a realistically shaped head model.

3.4.1 CutFEM Sphere Model Studies

In this section we evaluate the CutFEM method in four-layer sphere models.

Source Models   As a first study, we investigate different source models for the CutFEM approach in an isotropic four-layer sphere model. The radii and conductivity values can be found in Table A.1. We distribute dipolar sources of different orientations in the innermost compartment of the multi-layer sphere model. In previous studies it was observed that the accuracy of a numerical solution of the EEG forward problem in a multi-layer sphere model differs between radial and tangential dipoles and the errors increase the closer a source is to the first conductivity jump. A theoretical reasoning for the latter has also been given in (Wolters et al., 2007a). On each of 10 different eccentricities we generate a number of random source positions and for each position we compute the radially outwards pointing and a random tangential source orientation. An eccentricity of 0 corresponds to the center of the sphere, while an eccentricity of 1 corresponds to the first conductivity jump, e.g., the innermost sphere. The number of sources at a given eccentricity is scaled proportional to the surface area of a sphere with a radius corresponding to that eccentricity in order to get a uniform sampling of the source space over all eccentricities. Table A.3 shows the number of source positions that are generated for each eccentricity. Results in (Li et al., 2014) indicate that, depending on the location, the cortex has a thickness of 2 mm to 6 mm. The generators underlying the electrical activity measured by EEG are located in the center of the gray matter. From the range of eccentricities chosen here, we will focus a detailed description on the eccentricity of 0.986 that corresponds to a distance of approximately 1.1 mm from the first conductivity jump. The numerical solutions at the electrode positions are compared to the quasi-analytical solution (De Munck and Peters, 1993) using the RDM and MAG measures (cf. (2.14) and (2.15)). We compare the partial integration source model with two variants of the monopolar Venant approach using a fundamental mesh with a resolution of 1 mm. Both Venant approaches use a patch consisting of those elements of the fundamental mesh that share a vertex with the element containing the dipole. For the first version we scale the monopoles with respect to the local coordinates of the fundamental mesh element. For the second version we consider the local coordinates with respect to the bounding boxes of the cut-cells. The remaining parameters of the Venant approaches are chosen in the same way as presented in Section 2.1. Figure 3.3 shows the RDM and MAG errors for the different source models. Up to the eccentricity of 0.976, both Venant approaches are identical regarding the RDM

a) radial source orientations

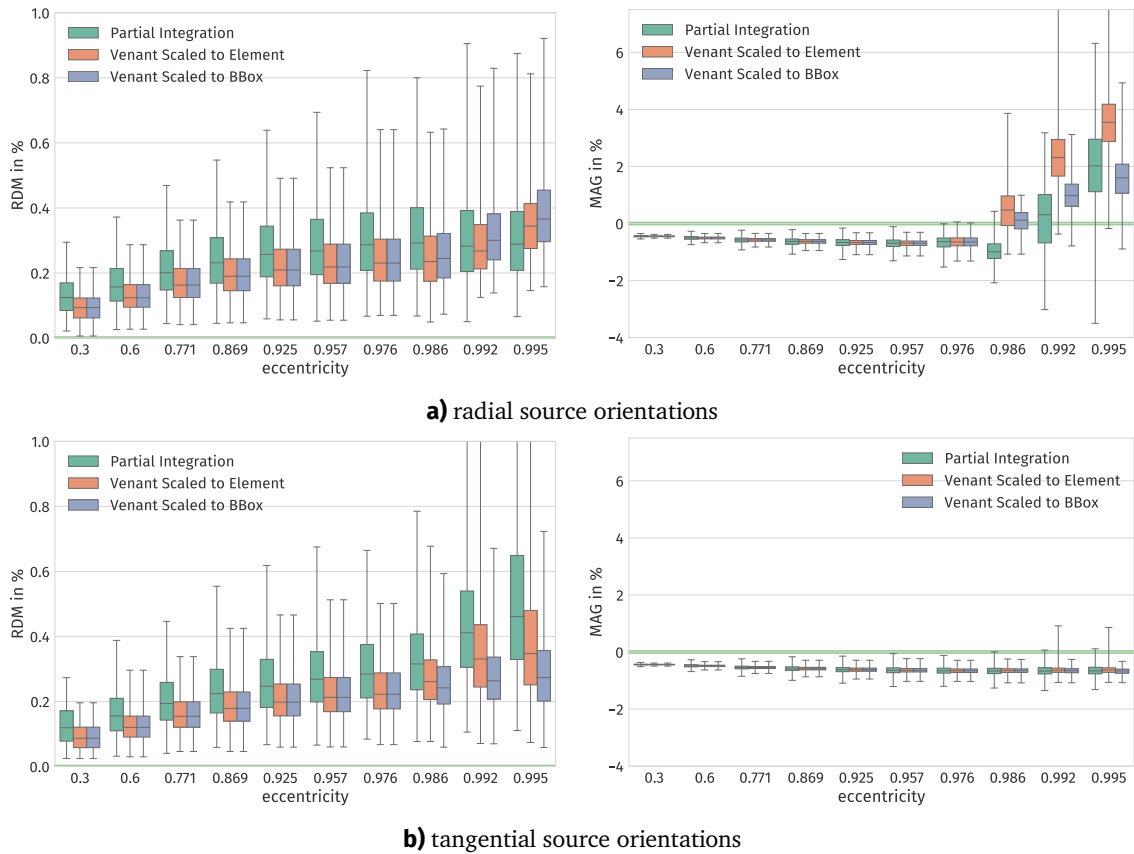**b)** tangential source orientations

Figure 3.3: Comparison of different source models for a 1 mm CutFEM discretization. Left: relative difference measure in percent. Right: magnitude error in percent. Top: radial source orientations. Bottom: tangential source orientations. Each boxplot contains the respective measure of a set of sources. The horizontal green lines show the optimal values at 0 %.

and MAG errors, as no element in the respective patches is cut by the interface and the bounding boxes coincide with the fundamental mesh elements. For the RDM error we see an overall increase of the error with increasing source eccentricity. For radial sources at the eccentricity of 0.986 the median RDM error for the partial integration approach is 0.29 %, for the element Venant approach it is 0.24 % and for the bounding box Venant approach it is 0.24 %. The respective maximal values are 0.80 %, 0.63 % and 0.64 %. For tangential orientations the median RDM error for the partial integration approach is 0.32 %, for the element Venant approach it is 0.26 % and for the bounding box Venant approach it is 0.24 %, while the corresponding maximal errors are 0.78 %, 0.68 % and 0.59 % respectively. For the highest eccentricities of 0.992 and higher, only the Venant approach scaled to the bounding box yields an RDM error lower than 1 % for both source orientations. With respect to the MAG error we observe an increase in the total and inter-quartile range for both source orientations and all source models. For radial sources, we see a strong increase in the MAG error for eccentricities of 0.986 and higher. At the eccentricity of 0.986, the total range of the MAG error for the partial integration approach is 2.51 %, for the element Venant approach it is 4.94 % and for the bounding box Venant approach is is 2.07 %. The respective maximal absolute values are 2.08 %, 3.86 % and 1.07 %. For tangential orientations the MAG error does not show the strong increase that occurred for radial sources. The total range of the MAG error at the eccentricity of 0.986 is 1.27 % for the partial integration approach, 0.84 % for the element Venant approach and 0.82 % for the bounding box Venant approach, while the corresponding maximal absolute values are 1.26 %, 1.08 % and 1.08 % respectively.

Overall, we observe a clear increase in accuracy when using the Venant approach compared to the partial integration approach with respect to both error measures, as well as both source orientations. The scaling of the local positions of the monopoles only becomes relevant in areas that are cut by an interface. Especially for the tangential sources with the highest eccentricity the scaling has a positive effect on the stability and on the magnitude of the RDM error. Based on these results we will use the monopolar Venant approach with local positions scaled to the bounding boxes for the subsequent CutFEM studies.

Convergence   In this study, we evaluate the convergence behavior of the CutFEM discretization in a four-layer sphere model. We create fundamental meshes of different resolutions and employ the CutFEM discretization. The level-set function Φ for a sphere centered at $c \in \mathbb{R}^d$ with a radius of $r \in \mathbb{R}$ is defined as

$$\Phi : \hat{\Omega} \to \mathbb{R}; x \mapsto \|x - c\|_2 - r$$

The radii and conductivity values of the different tissue compartments can be seen in Table A.1. Figure 3.4 shows the discrete reconstructions of the unfitted meshes obtained by the marching cubes method for mesh resolutions from 8 mm to 1 mm. As described in Section 4.1, these reconstructions are used for performing the integrations in the discrete forms, but do not influence the representation of the discrete functions. We can observe the structured hexahedral background mesh along with its nodes. The discrete representation of the geometry is created on the fundamental mesh without any subrefinement. Through the increased resolution we observe a better approximation of the smooth surfaces of the spheres. The number of degrees of freedom for the different mesh res-
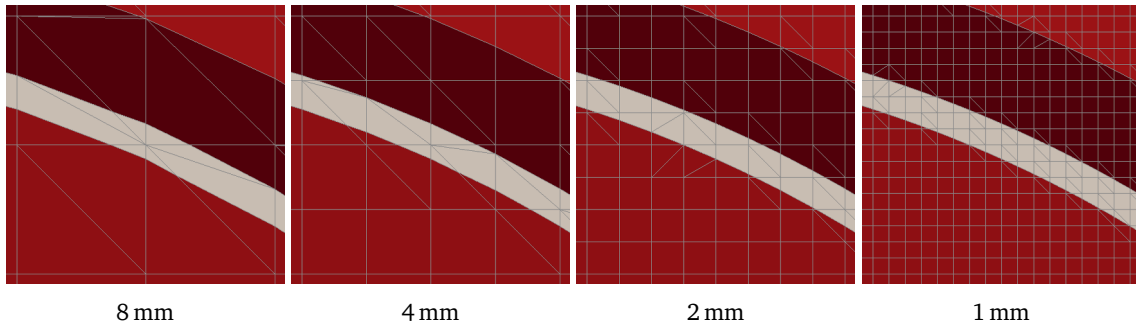
<div align="center">
8 mm   4 mm   2 mm   1 mm
</div>

Figure 3.4: Discrete unfitted meshes of the four-layer sphere model obtained with the marching cubes method. From left to right, the resolution increases. A brighter color indicates a higher conductivity and a darker color indicates a lower conductivity.

Table 3.1: Number of degrees of freedom for the different CutFEM discretizations of the four-layer sphere model.

resolution	16 mm	8 mm	4 mm	2 mm	1 mm
#DOFs	4731	21 825	108 352	635 581	4 173 085

olutions are presented in Table 3.1. We use the same sources as described in the previous study (cf. Table A.3). The results of the numerical computations are compared to a quasi-analytical solution using the RDM and MAG errors (cf. (2.14), (2.15)). The results for the convergence evaluation are shown in Figure 3.5. For the RDM error we observe an overall increase of the error with increasing source eccentricity, both for radial and tangential orientations. Considering radial sources at the eccentricity of 0.986, the median RDM errors for resolutions 16 mm, 8 mm, 4 mm, 2 mm and 1 mm decrease as 6.0 %, 3.0 %, 1.5 %, 0.6 % and 0.2 % respectively. The maximal RDM errors have the values of 11.8 %, 6.6 %, 3.4 %, 1.6 % and 0.6 %. For tangential source orientation, the median RDM errors reduce from 4.3 %, 2.1 %, 1.0 % and 0.5 % down to 0.2 % while the reduction of the maximal RDM errors is 7.9 %, 5.0 %, 2.4 %, 1.1 % down to 0.6 %. Note that over all eccentricities (i.e., including the highest eccentricity of 0.995 that corresponds to a distance of 0.4 mm from the conductivity jump) and both orientations, the maximal RDM errors for the different mesh resolutions are 12.8 %, 7.5 %, 4.0 %, 2.1 % and 0.9 %. For the MAG error we observe an overall increase of the TR and the IQR with increasing eccentricity. For radial sources at the eccentricity of 0.986 the TR of the MAG error from coarse to fine resolutions are 21.1 %, 13.0 %, 7.8 %, 4.2 % and 2.1 %. For the same sources, the maximal absolute values of the MAG error are 17.9 %, 10.1 %, 4.9 %, 2.2 % and 1.1 %. Considering tangential source orientations, the total range reduces from 16.4 %, 5.3 %, 3.0 %, 1.5 % to 0.8 % while the maximal absolute values are 11.7 %, 7.0 %, 3.9 %, 2.1 % and 1.1 %.

Figure 3.6 shows a visualization of the order of convergences of the relative error when increasing the mesh resolution. As the error depends on the eccentricity, we evaluate the convergence behavior for each eccentricity separately. Each plot corresponds to the median values of a single eccentricity, where a darker color represents a higher eccentricity. We observe a clear convergence behavior of the median relative error for all eccentricities and source orientations. Especially for tangential sources, the convergence curves are smooth over all eccentricities, while the convergence curves for higher eccentricities of radial orientations are flatter. Note that the convergence order deviates from
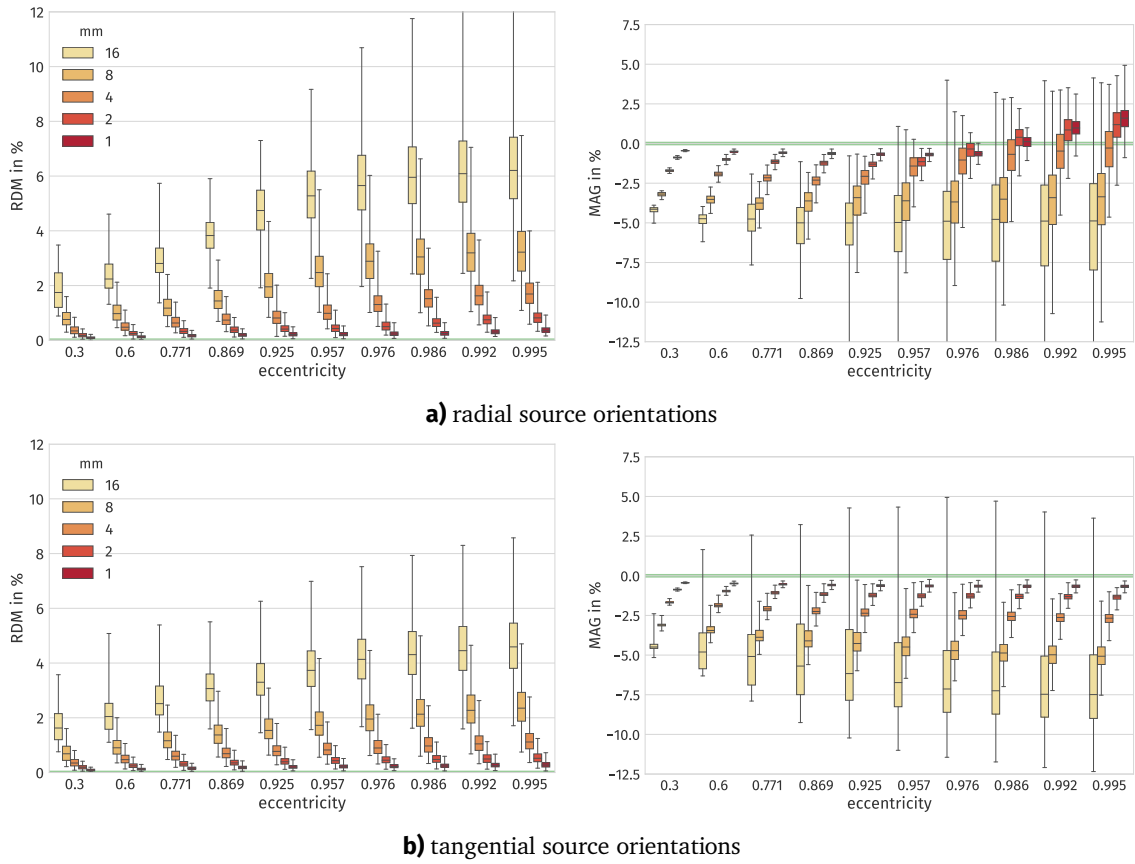
Figure 3.5: Convergence study of the CutFEM discretization. Left: relative difference measure in percent, Right: magnitude error in percent. Top: radial source orientations, Bottom: tangential source orientations. Each boxplot contains the respective measure of a set of sources. The horizontal green lines show the optimal values at 0 %.
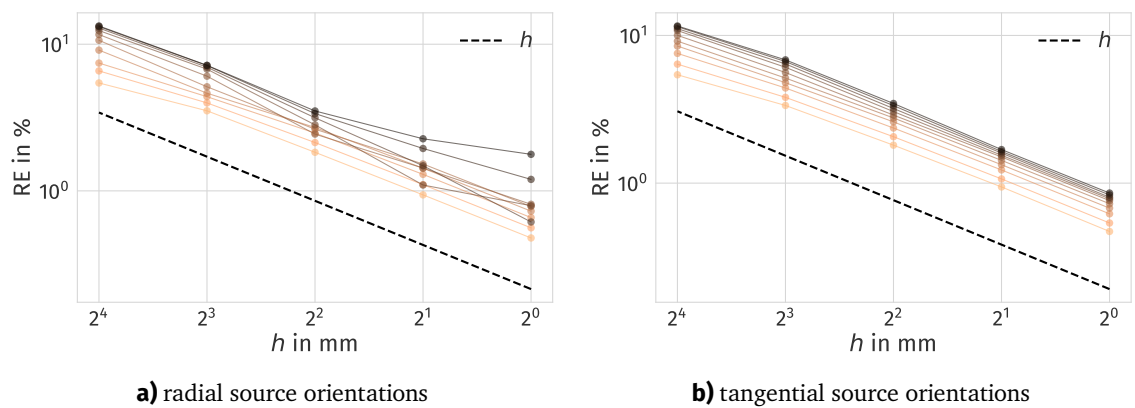
Figure 3.6: Convergence order of the CutFEM discretization. Each brown line represents the convergence of the median relative error in percent of a single eccentricity, where a darker color represents a higher eccentricity. The black dashed line shows a linear convergence.

a) radial source orientations

b) tangential source orientations

Figure 3.7: Comparison between a 2 mm CutFEM discretization (green) and a 1 mm hexahedral CG discretization (red). Left: relative difference measure in percent. Right: magnitude error in percent. Top: radial source orientations. Bottom: tangential source orientations. Each boxplot contains the respective measure of a set of sources. The horizontal green lines show the optimal values at 0 %.
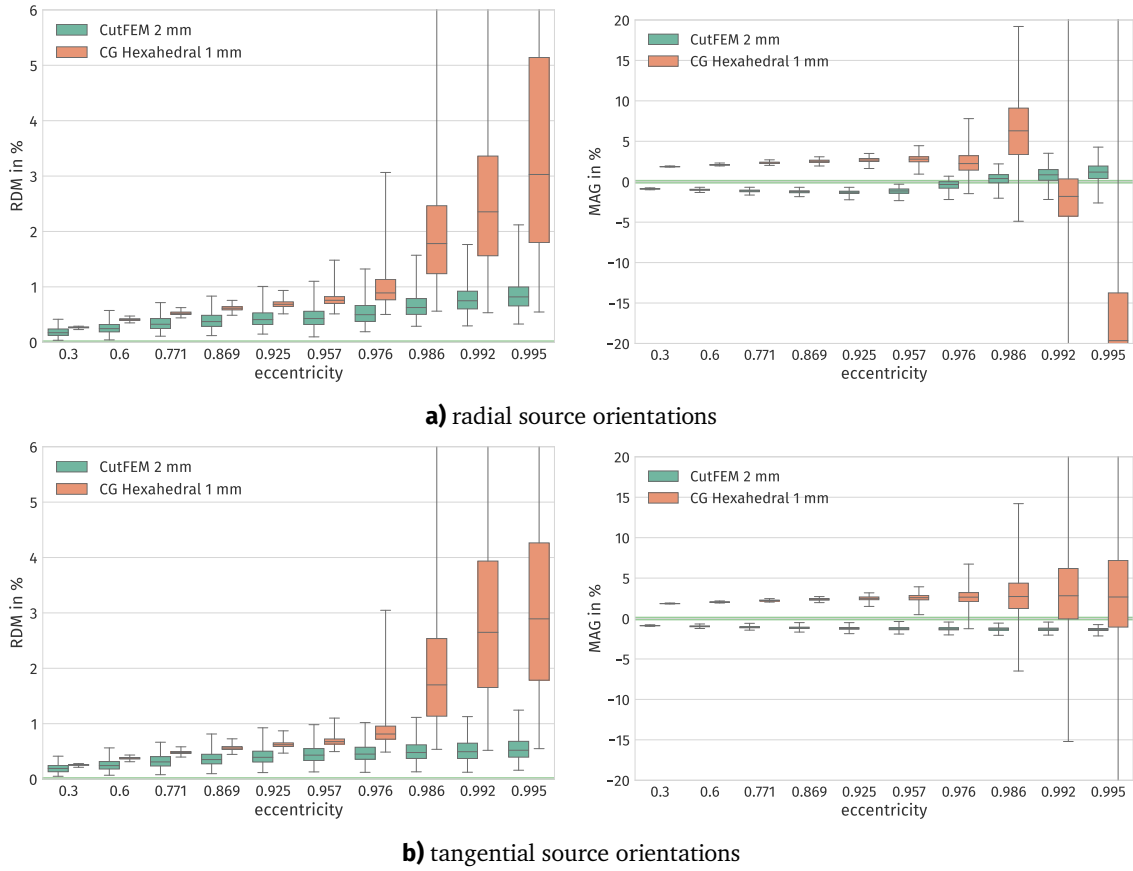
the theoretical order derived in (Burman and Hansbo, 2012) for the single compartment model. In general, the relative errors obtained from the point evaluations are not directly comparable to the volumetric L^2 and H^1 norms. In addition, we employ a multi-domain model and a right-hand side that depends on the mesh-size $\hat{h}$. We might obtain an improved convergence behavior when using the subtraction approach for the CutFEM method.

Comparison to fitted methods   In this study, we compare the CutFEM discretization with the conforming finite element method (CG) on hexahedral and tetrahedral meshes. We use a 1 mm geometry-adapted mesh with a shifting parameter of 0.3 following (Wolters et al., 2007b). We compare the hexahedral model with the CutFEM discretization on a fundamental mesh with a 2 mm resolution. The hexahedral model makes use of 3 263 152 DOFs while the CutFEM discretization uses 635 581 DOFs which corresponds to a factor of approximately 5.1 more DOFs for the hexahedral model. For both approaches we employ a monopolar Venant source model with monopoles distributed within the volume of the elements around the dipole element. Both, CutFEM and CG use the same parameters (cf. Section 2.1) for the monopolar Venant approach. Figure 3.7 shows

the RDM and MAG error for the two methods with respect to the quasi-analytical solution. As the general behavior of the RDM and MAG errors has been described in the previous section, we now focus mainly on describing the differences between the two approaches. With respect to the RDM error and lower eccentricities both approaches show similar error values for both orientations. The total ranges and the inter-quartile ranges of the hexahedral approach are lower, but the CutFEM approach shows lower median values. Closer to the conductivity jump starting from the eccentricities of 0.925 and 0.975, the RDM error of the hexahedral approach strongly increases compared to the CutFEM approach. Regarding the MAG error at inner eccentricities, the total ranges and the inter-quartile ranges of both approaches are similar. The hexahedral approach is in general shifted towards positive values, i.e., an overestimation of the magnitude, while the CutFEM approach tends towards negative values, corresponding to an underestimation of the magnitude. The absolute values of the MAG error of the CutFEM approach are closer to the optimal value of 0 %. Similar to the behavior of the RDM error the total ranges and inter-quartile ranges of the MAG error for the hexahedral approach increases for more eccentric source positions while the CutFEM approach is comparatively less affected by the source eccentricity.

For the comparison with a tetrahedral model we use the same sphere model that was used in Section 2.1 and we again use a conforming finite element method. Similar to the comparison of the hexahedral model we compare the tetrahedral approach to the 2 mm CutFEM model. The tetrahedral model uses 274 401 DOFs which is a factor of 2.3 less than the 635 581 DOFs of the CutFEM model. As in the previous study, we use the monopolar Venant approach for the tetrahedral model as well. The resulting RDM and MAG errors with respect to the quasi-analytical solution are shown in Figure 3.8. With respect to the RDM measure the CutFEM approach shows an increased accuracy over all eccentricities. However, the inter-quartile ranges of the tetrahedral model are smaller. Considering the MAG error both approaches show similar total and inter-quartile ranges, but the median values of the CutFEM approach are shifted away from 0 % by approximately –1 %. This behavior of the CutFEM approach was also observed in the convergence study and is also present when considering the discontinuous Galerkin method on a geometry conforming mesh. This shift is reduced with increasing mesh resolution.

With respect to the time consumption of the two fitted approaches and the CutFEM approach we measure the time used for computing the results presented in this section, which consists of computing the transfer matrix and solving the forward problem for all 29 884 source locations and the three Cartesian source orientations for each location. All measurements were performed sequentially on a single core of a conventional laptop (Intel i7 6700, 2.6 GHz). As the different forward approaches behave differently with respect to the construction of the forward model and contain a different number of DOFs, we split the time measurements into five different steps. The initial setup phase constructs the volume conductor model. For the conforming approaches this step consists of reading and constructing the geometry conforming mesh, while the CutFEM model performs some initial computations, such as determining the bounding boxes of the different cut-cells. The assembly step consists of the computation of the sparsity pattern of the system matrix and the numerical integration of the bilinear form. After the system matrix has been setup, the solver is constructed, which includes the construction of the algebraic multigrid preconditioner and its matrix hierarchy (cf. Section 4.2). In the solution phase, the transfer matrix system is solved for all electrodes sequentially. The last step consists of assembling the right-hand side vectors for

a) radial source orientations

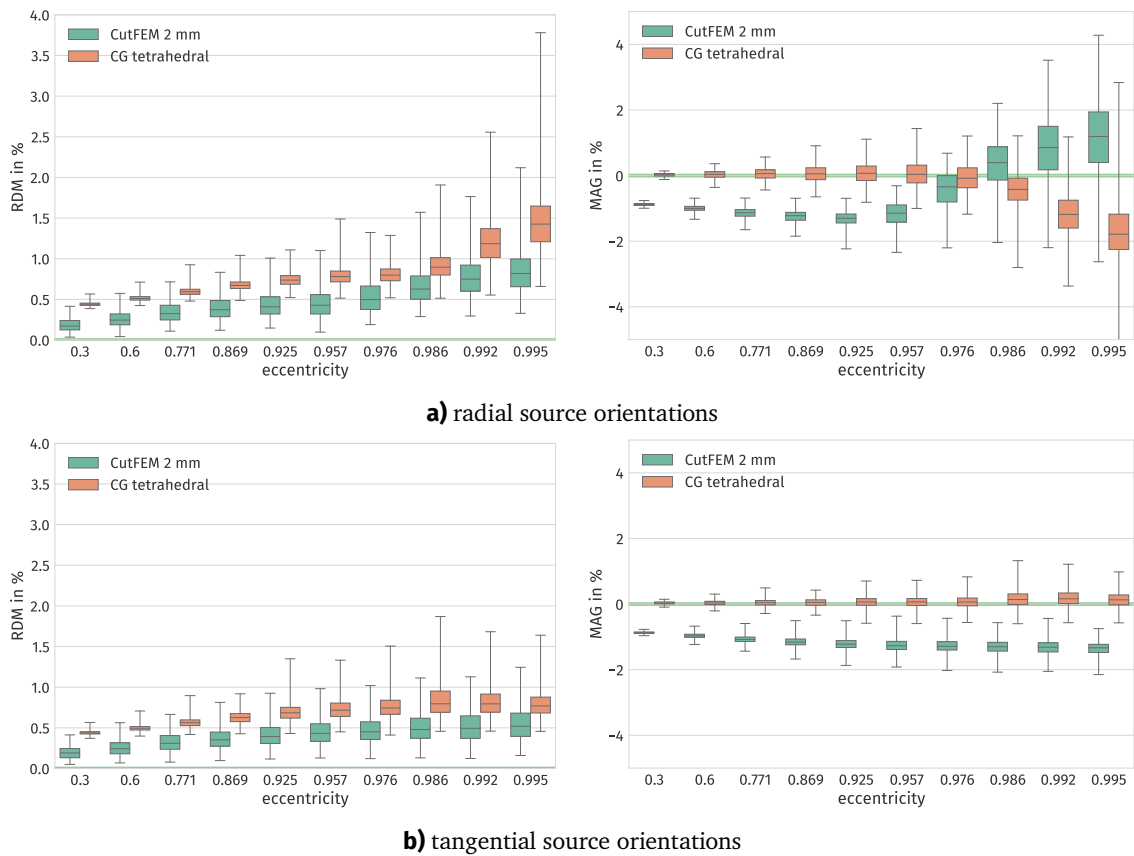**b)** tangential source orientations

Figure 3.8: Comparison between 2 mm CutFEM discretization and tetrahedral CG. Left: relative difference measure in percent, Right: magnitude error in percent. Top: radial source orientations, Bottom: tangential source orientations. Each boxplot contains the respective measure of a set of sources. The horizontal green lines show the optimal values at 0 %.

Table 3.2: Time consumption for computing the transfer matrix and solving the EEG forward problem with the 2 mm CutFEM approach compared to the 1 mm geometry-adapted hexahedral conforming CG and tetrahedral conforming CG. The different steps are: the time for initial setup (initial), assembly of the linear system (assembly), setup of the solver (setup), solution for all electrodes (solution), application of the transfer matrix to all dipoles (forward) and the accumulated total time (total).

model	initial	assembly	setup	solution	forward	total
CutFEM	32.69 s	514.60 s	50.19 s	9837.26 s	459.70 s	10 894.44 s
hexahedral	95.33 s	58.61 s	39.34 s	11 675.76 s	27.19 s	11 896.23 s
tetrahedral	60.14 s	11.24 s	2.53 s	1323.96 s	18.74 s	1416.61 s

all dipole positions and orientations and the sparse matrix-vector multiplication. The results of the time measurements are presented in Table 3.2. Overall, we observe a reduced time consumption of approximately 25 min for the tetrahedral approach, while the CutFEM method and the hexahedral approach both take a similar amount of time of approximately 3 h. For all approaches, most of the time is spent in the solution phase. Relative to the total time the solution phases consume 90.3 %, 98.2 % and 93.5 % for the CutFEM, hexahedral and tetrahedral method respectively. Since the integration over the model domain is more involved for the CutFEM approach compared to the conforming approaches, the former uses more time for assembling the system matrix than the latter approaches. In a similar manner the time consumption for the application of the transfer matrix is increased for the CutFEM method. Note that the solution phase consists of the solution of a linear system for multiple right-hand sides, which is easily parallelizable via multi-threading or vectorization. Similarly, the dipoles within the forward phase can be splitted and handled in parallel. By this parallelization, even the transfer matrix for the 1 mm CutFEM approach can be computed in an overnight computation with a subsequent application of the transfer matrix that is mainly independent of the mesh-size.

Summarizing the results of the comparison to the fitted method we can conclude that the 2 mm CutFEM approach outperforms the 1 mm geometry conforming hexahedral approach while maintaining the high accuracy of the tetrahedral models. However, it does so without the need for constructing triangular surfaces and a volume tetrahedralization. Its time consumption is comparable to the one of a hexahedral approach.

3.4.2 UDG Sphere Model Studies

In this section, we evaluate the UDG method in four-layer sphere models.

Convergence   First we study the convergence behavior for a four-layer sphere model using the UDG method with increasing mesh resolution, similar to the convergence study for the CutFEM approach. For this study we create UDG meshes of 16 mm, 8 mm, 4 mm and 2 mm fundamental mesh resolution. Table 3.3 shows the number of fundamental mesh elements, the number of cut-cells and the number of degrees of freedom for the different UDG discretizations. For the lowest mesh resolution of 16 mm the number of cut-cells is larger than the number of elements, indicating

Table 3.3: Number of fundamental mesh elements, cut-cells and number of degrees of freedom for the different UDG discretizations of the four-layer sphere model.

resolution	16 mm	8 mm	4 mm	2 mm
#elements	1728	13 824	110 592	884 736
#cut-cells	2576	13 544	79 480	521 304
#DOFs	20 608	108 352	635 840	4 170 432

that a high percentage of fundamental mesh elements are cut by the interfaces. On each of 10 different eccentricities we generate a number of random source positions and for each position, we compute the radially outwards pointing and a random tangential source orientation. Table A.3 shows the number of source positions that were generated for each eccentricity. As a source model we employ the monopolar Venant approach with monopoles distributed in the dipole element and all elements sharing a vertex with the dipole element. An element is excluded from this patch if it contains no cut-cell of the gray matter compartment. On each element the local coordinates of the monopoles are scaled with respect to the bounding box of the cut-cell. The positions are chosen based on the Gauss-Legendre quadrature of second order resulting in 8 monopoles per element. We use mixed moments up to second order, a relaxation factor of 10^{-6} and a reference scaling of 20 mm. The penalty parameter of the UDG method is set to $\eta = 4$. When computing the transfer matrix, the iteration of the linear solver is stopped at relative reduction of the l_2-norm of the residuum of 10^{-12}. Figure 3.9 shows RDM and MAG errors for the radial and tangential orientations. With respect to the RDM error we see a clear convergence behavior for both orientations over all eccentricities. In line with previous results we observe an increasing error with increasing source eccentricities. Considering radial orientations at the eccentricity of 0.986, the median RDM error decreases from 8.3 %, 2.9 %, 1.4 % down to 0.6 % for the resolutions of 16 mm, 8 mm, 4 mm and 2 mm respectively. For tangential orientations at the same eccentricity the error reduces as 5.2 %, 2.0 %, 0.9 % down to 0.5 %. For the finest resolution of 2 mm the largest RDM error over all source positions for radial orientations occurring at the eccentricity of 0.995 is 2.0 %. The largest error for tangential orientations is 2.0 %, also occurring at the eccentricity of 0.995. For the MAG error we observe a convergence behavior of the median and total ranges, excluding the coarsest resolution of 16 mm. In general, we see a shift of the median values towards negative MAG error, i.e., an underestimation of the magnitude. At the eccentricity of 0.986 for radial orientations the median MAG error from coarse to fine resolutions is 2.6 %, –2.5 %, –0.1 % and 0.9 % while the total range is 33.7 %, 13.9 %, 8.7 % and 6.2 %. For tangential orientations the median takes the values of 0.1 %, –3.9 %, –2.3 % and –1.2 % with a total range of 22.3 %, 6.4 %, 2.9 % and 1.6 %. For the mesh resolution of 2 mm the largest absolute value of the MAG error over all eccentricities for radial orientations is 5.9 % and occurs at the eccentricity of 0.995, while the largest absolute value for tangential orientations is 2.1 % occurring at the eccentricity of 0.995.

Figure 3.10 shows a visualization of the order of convergence of the relative error when increasing the mesh resolution. As the error depends on the eccentricity, we evaluate the convergence behavior for each eccentricity separately. Each plot corresponds to the median values of a single eccentricity, where a darker color represents a higher eccentricity. Over all eccentricities we again observe the

a) radial source orientations

b) tangential source orientations
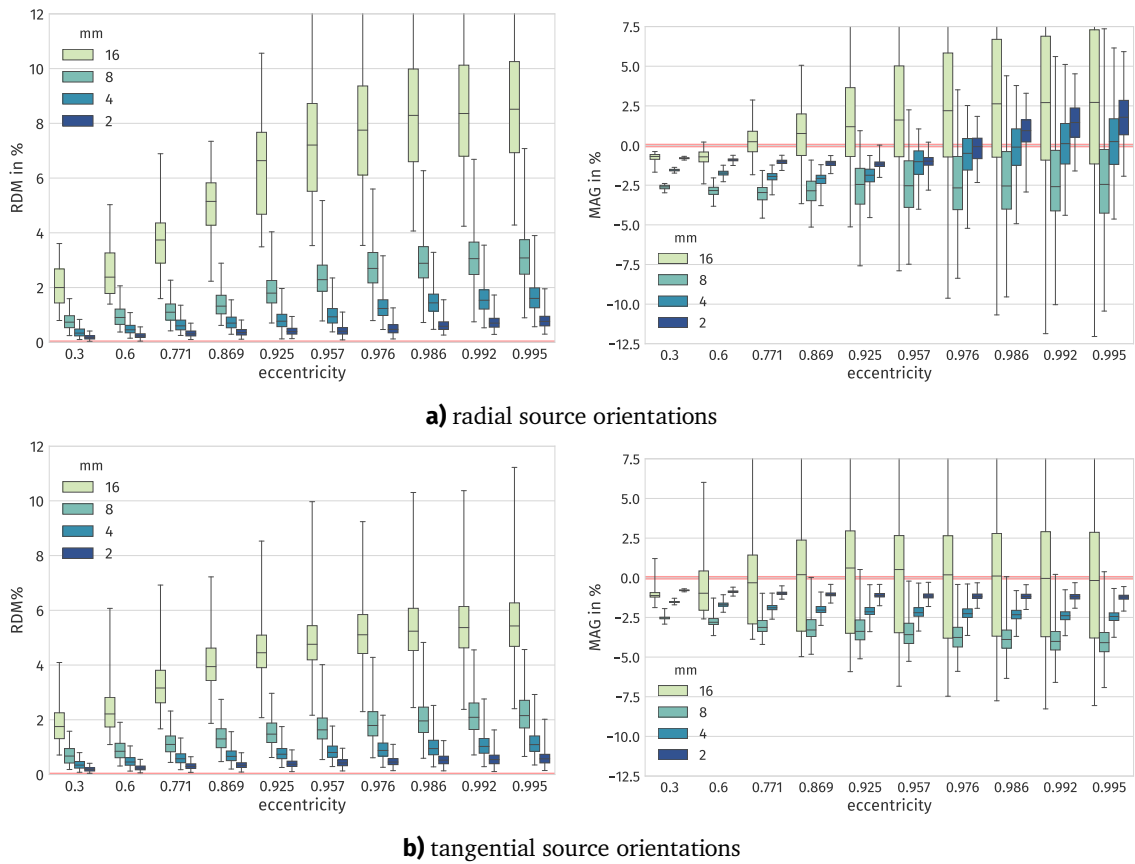
Figure 3.9: Convergence study of the UDG discretization. Left: relative difference measure in percent, Right: magnitude error in percent. Top: radial source orientations, Bottom: tangential source orientations. Each boxplot contains the respective measure of a set of sources. The horizontal red lines show the optimal values at 0 %.

a) radial source orientations

b) tangential source orientations
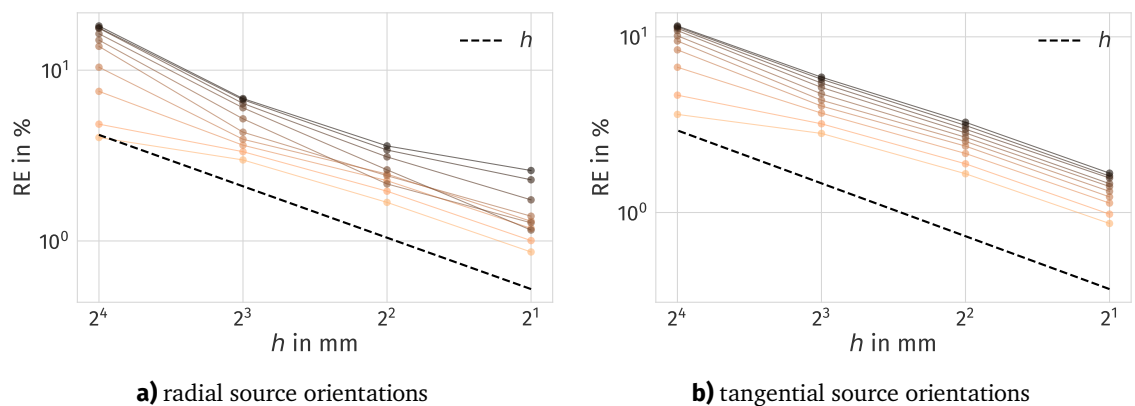
Figure 3.10: Convergence order of the UDG discretization. Each brown line represents the convergence of the median relative error in percent of a single eccentricity, where a darker color represents a higher eccentricity. The black dashed line shows a linear convergence.

convergence behavior with a general linear order. For the step from 16 mm to 8 mm the order is slightly lower for internal sources of both orientations. For radial sources we observe a slightly lower reduction at the step from 4 mm to 2 mm for the highest eccentricities. Comparing the convergence results to the results of the convergence study of the CutFEM method, we can see strong similarities between the two approaches, both with respect to the convergence of the boxplots as well as the convergence of the median relative error plots.

Comparison with CutFEM   In this study we directly compare the UDG method with the CutFEM method on a fundamental mesh of 2 mm resolution. Both methods use the same fundamental mesh resolution and the same level-set functions without any additional refinement. The UDG method uses 4 170 432 DOFs, while the CutFEM method employs only 635 581 DOFs which corresponds to a factor of approximately 6.6. The DOFs of the UDG method are associated with the elements of the fundamental mesh, while the DOFs of the CutFEM method are associated with the fundamental mesh nodes. For both methods we use the monopolar Venant approach with the local monopole positions scaled to the respective bounding boxes and the source model parameters as reported above. The UDG method uses a global penalty parameter of $\eta = 4$, while the CutFEM method uses a penalty parameter of $\eta = 16$ and a ghost-penalty parameter of $\tilde{\eta} = 0.005$. The different scaling of the penalty parameter for both approaches is assumed to be mainly due to the different scaling of the parameter with respect to the local mesh size. Figure 3.11 shows the RDM and MAG errors for the UDG approach and the CutFEM approach. The individual results are already described in the previous study for the UDG method and in Section 3.1 for the CutFEM method. With respect to the RDM error both methods perform very similarly for both source orientations. The CutFEM method produces slightly lower RDM errors for tangential source orientations and higher eccentricities but the overall trend is mainly identical. Note that with a different choice of the respective penalty parameter an even closer result might be obtained. In general, these results show that the UDG and CutFEM approach can be used interchangeably for this scenario. As the CutFEM method uses less DOFs, the resulting linear system is smaller and thus the time needed for the construction of the transfer matrix is reduced. In the subsequent realistic head model studies we thus choose the CutFEM approach over the UDG method.

Second order study   An advantage of the UDG method that is reported in the literature, e.g., (Engwer, 2009), is the direct use of higher-order ansatz functions in the discretization. In previous studies second-order ansatz functions have been investigated for the conforming finite element method on geometry conforming tetrahedral meshes (Grüne, 2014; Van Uitert et al., 2001; Zhang et al., 2004). While these studies could find an effect on the approximation quality of the use of higher order polynomials, it was concluded that this effect might be more pronounced with a better geometric approximation of the different tissue compartments. Instead of using second order polynomials, it was proposed to increase the mesh resolution and use linear ansatz functions on the finer mesh. For the UDG method the geometric representation and the discrete function space are treated separately. This especially means that a more accurate geometric representation of the model domain can be used without increasing the resolution of the Ansatz space. We note that polynomials of higher degrees can also be used for the CutFEM approach. In this case a different ghost-penalty has to be applied as presented in Burman and Hansbo (2012).

a) radial source orientations

b) tangential source orientations

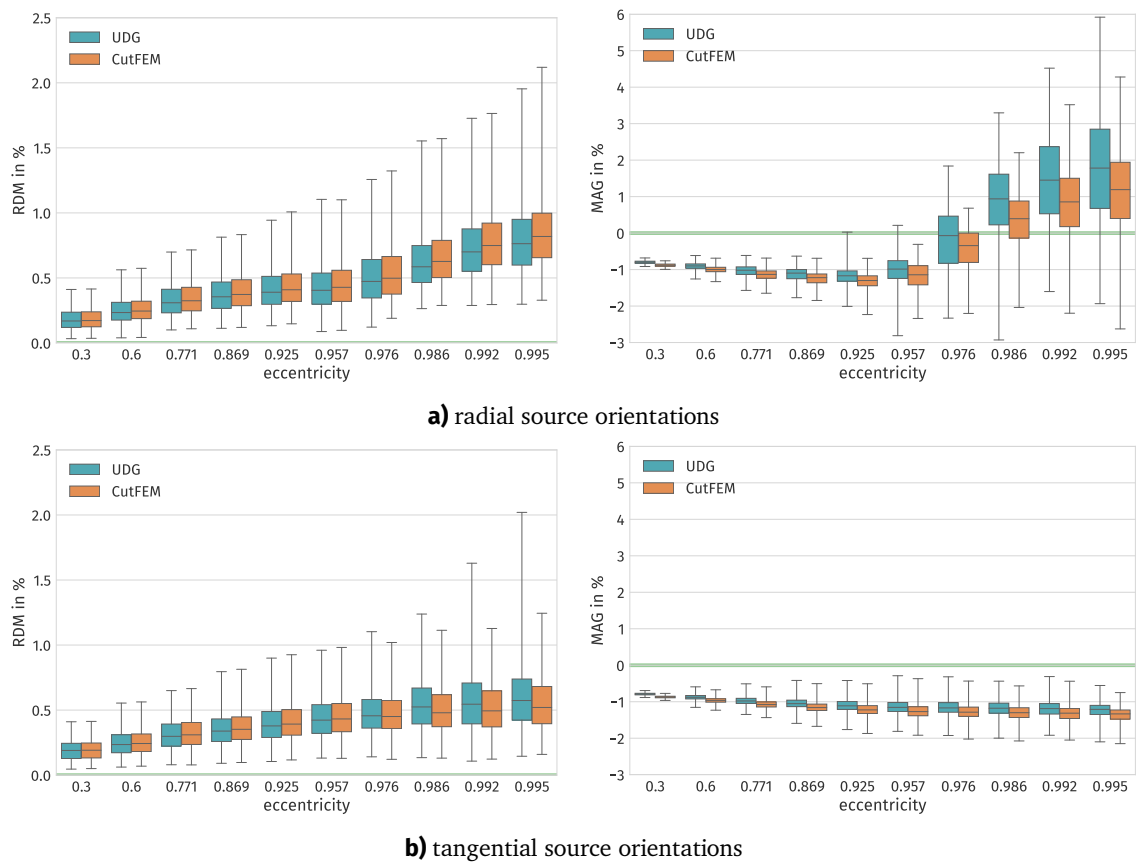**Figure 3.11:** Comparison study between a UDG discretization (blue) and a CutFEM discretization (red) on a 2 mm fundamental mesh. Left: relative difference measure in percent, Right: magnitude error in percent. Top: radial source orientations, Bottom: tangential source orientations. Each boxplot contains the respective measure of a set of sources.

a) radial source orientations

b) tangential source orientations

Figure 3.12: Comparison study of the UDG discretization using linear and quadratic polynomials. Left: relative difference measure in percent, Right: magnitude error in percent. Top: radial source orientations, Bottom: tangential source orientations. Each boxplot contains the respective measure of a set of sources. The horizontal green lines show the optimal values at 0 %.
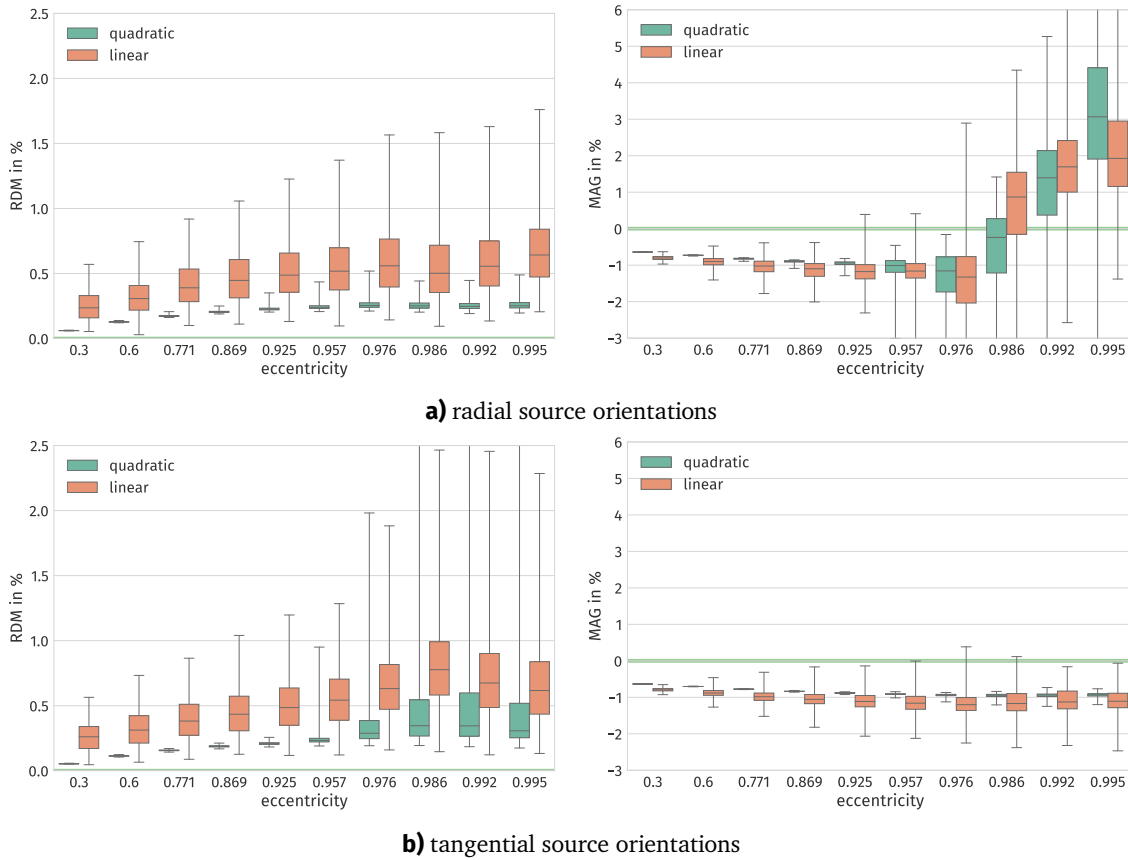
We compare the UDG method with piecewise linear ansatz functions on a 2 mm fundamental mesh with the UDG method with quadratic ansatz functions on a 4 mm mesh. For both methods we use the same geometric information from a level-set function on a 1 mm mesh. The linear UDG method uses 4 170 432 DOFs while the UDG method with quadratic polynomials uses 2 145 960 DOFs which corresponds to a factor of approximately 1.9. Note however that the second order method uses more DOFs per element (27 instead of 8) and thus has an increased coupling stencil when compared to the first order method. As a source model, we employ the partial integration approach. Figure 3.12 shows the RDM and MAG errors of the comparison. For all eccentricities of the radial orientation and for the lower eccentricities of the tangential orientation we see a strong reduction of the RDM error. For tangential source orientations and higher eccentricities the RDM error of the approach using the quadratic polynomials increases and shows a wider spread of the total range. With respect to the MAG error the behavior regarding the source orientation is swapped. For all eccentricities of the tangential orientation and for the lower eccentricities of the radial orientation we see a strong decrease of the total and inter-quartile range. For the higher eccentricities and radial orientations both approaches with linear and quadratic polynomials perform similarly

and show an increase in the total and inter-quartile range as well as a shifting median value.

To conclude, we see a strong increase in accuracy for the lower eccentricities. For the highest eccentricities this increase is less pronounced or the results are on a similar level. Note that we employed the partial integration source model in this study. The results, especially close to the conductivity jump, might be different, when using a different source model. An investigation of the Venant approach with respect to higher-order moments or a varying number of monopoles within each element might be worthwhile. Additionally, the localized subtraction approach presented in Section 2.3 might improve the results close to the conductivity jump.

3.4.3 CutFEM Realistic Head Model Study

In this study, we evaluate the effect of the CutFEM discretization on a realistically shaped head model. We create four head models, each consisting of six compartments, that are used in the evaluation: a geometry conforming tetrahedral model, a geometry-adapted hexahedral model, a CutFEM model using level-sets derived from the tetrahedral surfaces and a CutFEM model using level-sets derived from the hexahedral mesh. Throughout this section, the CutFEM model obtained from the tetrahedral surfaces is used as a reference model.

Surfaces The surfaces used as initial data for creating the tetrahedral model as well as the CutFEM model were created in (Vorwerk et al., 2014) and used for a single solution of the EEG forward problem with an unfitted finite element method in (Nüßing et al., 2016). In the following, we will describe the main process of creating these surfaces. T1-weighted (T1w-) and T2-weighted (T2w-) MRI scans of a healthy 25-year-old male subject were acquired in a 3 T MR scanner (MagnetomTrio, Siemens, Munich, Germany) with a 32-channel head coil. For the T1w-MRI, an MP-RAGE pulse sequence (TR/TE/TI/FA = 2300 ms/3.03 ms/1100 ms/8°, FOV = $256 \times 256 \times 192$ mm, voxel size = $1 \times 1 \times 1$ mm) with fat suppression and GRAPPA parallel imaging (acceleration factor = 2) was used. For the T2w image, an SPC pulse sequence (TR/TE = 2000 ms/307 ms, FOV = $255 \times 255 \times 176$ mm, voxel size = $0.99 \times 1.0 \times 1.0$ mm interpolated to $0.498 \times 0.498 \times 1.00$ mm) was used. MR images were resampled to 1 mm isotropic resolution. The T2w-MRI was registered onto the T1w-MRI using a rigid registration approach and mutual information as a cost-function as implemented in the FSL-toolbox[1]. The skin and skull compartments were segmented by applying a gray-value based active contour approach (Vese and Chan, 2002). Subsequently, the segmentation was manually corrected and, because of the importance of modeling skull holes for source analysis (Oostenveld and Oostendorp, 2002; Roche-Labarbe et al., 2008), the foramen magnum and the two optic canals were correctly modeled as skull openings. The model was not cut off directly below the skull but realistically extended at the neck. CURRY7[2] was used to extract high-resolution surfaces of skin and skull compartments. A Taubin smoothing was applied to remove staircase-like effects (Taubin, 1995). Cortex segmentation and surface reconstruction were performed using the FreeSurfer-toolbox[3]. In order to construct a tetrahedral mesh using a constrained Delaunay tetrahedralization, the extracted surfaces where manually corrected to ensure that the surfaces are not intersecting and have a minimal distance from each other. Note however that this manual correction step is in general

---

[1]http://fsl.fmrib.ox.ac.uk/fsl/fslwiki/FSL
[2]http://www.neuroscan.com
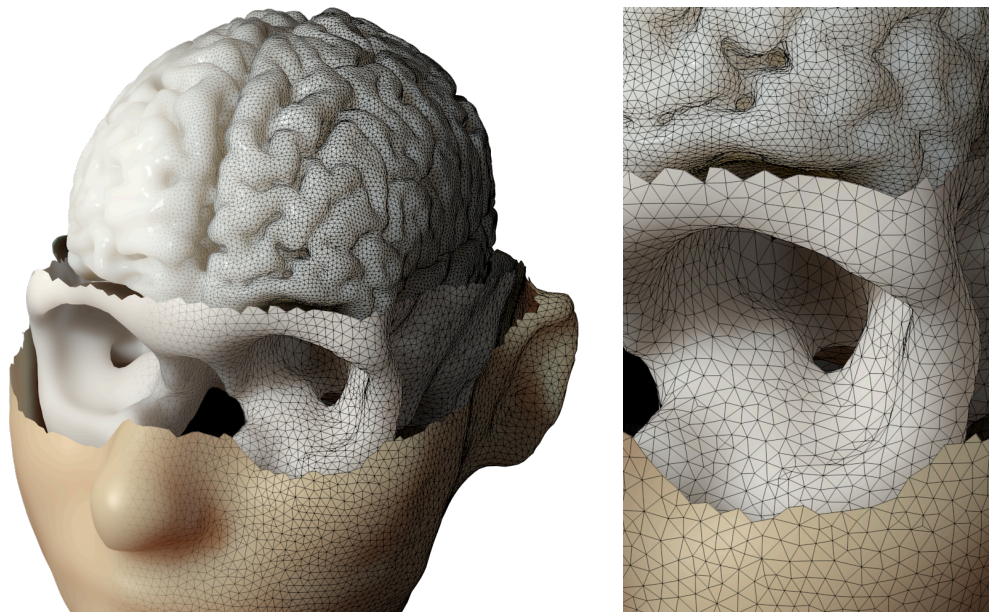[3]https://surfer.nmr.mgh.harvard.edu

Figure 3.13: Visualization of the triangular surfaces used for the realistic head model study. Depicted are the skin, skull and gray matter surface.

not necessary for an unfitted approach, which can also deal with touching or intersecting surfaces. A visualization of the surfaces used for creating the head models is shown in Figure 3.13.

For the sensors, we used a realistic 10-10 electrode montage consisting of 74 electrode positions. In (Vorwerk et al., 2014), the positions were digitized using a Polhemus FASTTRAK device[4] and projected onto the skin surface. For the tetrahedral and hexahedral model, each electrode position was moved to the closest vertex of the mesh. The solutions obtained by the unfitted methods were directly evaluated at the position of the electrodes, which were all located in an element of the fundamental mesh containing a cut-cell of the skin compartment.

Discretization schemes   The construction of the tetrahedral model is described in (Vorwerk et al., 2014), where a constrained Delaunay tetrahedralization has been applied to the triangulation surfaces (Si, 2015). For the smooth CutFEM model, we created signed distance functions on an auxiliary domain with a resolution of 1 mm for each triangular surface that was used for the construction of the tetrahedral model. These signed distance functions were subsequently used as level-set functions for the description of the CutFEM domain. We employed a CutFEM discretization on a 1 mm background mesh with penalty parameter $\eta = 16$ and ghost penalty $\tilde{\eta} = 0.005$. This CutFEM is used as a reference model in the following investigations. From the smooth CutFEM model we derived a hexahedral mesh by assigning to each voxel of the fundamental mesh that conductivity value with the highest volume within that voxel. We use the geometry-adaption approach described in (Wolters et al., 2007b) with a shifting parameter of 0.3. In order to simulate a CutFEM approach in a situation where no smooth surfaces are available, we extract surfaces from the hexahedral mesh constructed in the previous step. For these surfaces, we follow the processing pipeline that was used for creating the smooth surfaces for the tetrahedral model, without applying any manual correc-

---

[4]https://polhemus.com

tions to the surfaces. In order to create a reference for the quantitative effects of the aforementioned models, we create a four-compartment CutFEM model, which does not distinguish between gray and white matter and which does not contain a skull spongiosa compartment. This model is created by excluding the level-set functions for white matter and skull spongiosa and assigning the conductivity values for gray matter and skull compacta in the whole respective compartment. The remaining surfaces are identical to the full six-compartment model. The CutFEM model consists of 5 825 336 DOFs, the tetrahedral model of 984 569 DOFs, the geometry-adapted model of 4 193 359 DOFs and the CutFEM model constructed from the hexahedralized surfaces consists of 5 966 398 DOFs. The four-compartment CutFEM model consists of 5 065 074 DOFs. Among all models, the tetrahedral model has the lowest number of degrees of freedom by a factor of approximately 4. The highest number of DOFs is used by the hexahedralized CutFEM method which uses only slightly more DOFs than the original CutFEM mesh.

Source space   We created a source space based on the level-set functions used in the CutFEM approach. As mentioned in the previous chapters, the generators of the electric activity are located in the gray matter compartment with orientation normal to the cortical surface. First, we created a level-set function representing the source space by interpolating between the gray and white matter surfaces:

$$\Phi s := \alpha \Phi_{\mathrm{wm}} + (1 - \alpha)\Phi_{gm}$$

with a parameter $\alpha \in [0, 1]$. As the used gray and white matter surfaces were nested, $\Phi_{\mathrm{wm}} < \Phi_{\mathrm{gm}}$ and the resulting source space lies in between both surfaces. If α is closer to 1, the resulting source space will be closer to the white matter surface, the closer it is to 0, the closer it will be to the gray matter surface. For the following investigations, we fixed $\alpha = .8$ and thus created a surface that is closer to the white matter compartment, which is similar to the source space construction in (Vorwerk, 2016). In order to create approximately evenly spaced sources, we discretized the level-set using the marching cubes algorithm (cf. Section 4.1). To create a more uniform distribution of the nodes, we used the tool MeshLab[5] to clean the surfaces and applied a Taubin smoothing (50 iterations, parameters -0.25 and 0.25). In this process, the unit surface normal vectors at the vertices were computed and fixed as the dipole moments. The resulting source space consists of 271 864 dipoles. For a clearer visualization, we created an inflated version of the source space by applying a Laplacian smoothing. Note however, that all computations were performed using the original source space. The source space and the inflation are shown in Figure 3.14. The mean curvature of the surface is colored in gray, where a dark gray color corresponds to a negative mean curvature, while a light gray color corresponds to a positive mean curvature. In general, areas with a positive mean curvature are located on the crowns of the gyri, while a negative curvature occurs within the sulci. At the transition from the light to the dark gray areas, the curvature is close to zero, corresponding mainly to the walls of the cortical folding. Figure 3.15 shows the distance to the skull compacta compartment and the local thickness of the gray matter compartment. The distance to the compacta compartment is measured by evaluating the signed distance function used for generating the CutFEM model. It ranges from approximately 2 mm to 54 mm and is in general

---

[5]http://www.meshlab.net

a) original   **b)** inflation

Figure 3.14: Visualization of the source space used for the realistic head model study. Left the original source space, right its inflation. The dark gray areas have a negative mean curvature in the original model, while the light gray areas have a positive mean curvature.

a) distance to compacta   **b)** gray matter thickness
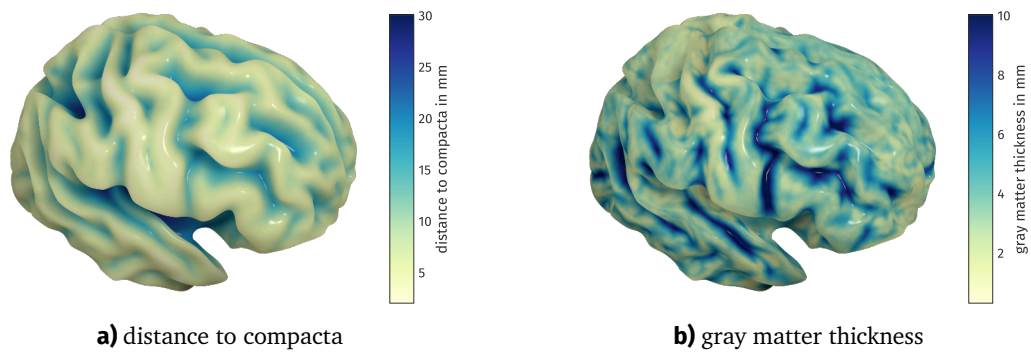
Figure 3.15: Left: Distance of the source space to the skull compacta compartment. A darker color corresponds to a higher distance. Right: Local thickness of the gray matter compartment. A darker color corresponds to a thicker compartment.

lower for superficial areas such as the gyral crowns. In order to better visualize the distance differences for the visible superficial areas, the color map was cut off at a distance of 30 mm. The local gray matter thickness at a position is defined as the sum of the distance to the white matter surface and the distance to the gray matter surface. It is computed using the signed distance function for the white matter and gray matter compartments as: $\Phi_{wm} - \Phi_{gm}$. Due to the location of the source space, it is proportional to the distance of the source to the gray matter surface and it ranges from approximately 0.3 mm to 15.3 mm. Again, in favor of a clearer visualization, the color map was cut at a thickness of 10 mm. The highest distances are located in deep sulcal areas that are not resolved by the gray matter surface. The thickness is lower in gyral areas while being smallest on the central gyri and in frontal areas.

For the fitted methods, especially when using the hexahedral mesh, and for the CutFEM method using the hexahedralized level-set functions, certain source positions do not lie in an element of the gray matter compartment, but might lie within a CSF element or an element of the white matter, due to inaccuracies on representing the compartment boundaries. In order to avoid errors due to the use of the different tissue compartment and thus the different conductivity value, we move sources which do not lie within a gray matter element to the closest center of a gray matter element. For the hexahedral model, 4577 out of the 271 864 sources were moved to a different location with a maximal distance of 1.55 mm and a median distance (among the moved dipoles) of 0.68 mm. Note that the maximal distance is below the diagonal of a 1 mm cube and thus no source position was shifted more than a single voxel. For the tetrahedral model, 4955 sources were moved with a maximal distance of 1.0 mm and a median distance, again among the moved dipoles, of 0.51 mm. For the CutFEM model using the level-set functions obtained from the hexahedral mesh, 158 sources of the original source space were located in a fundamental element with no cut-cells of the gray matter compartment. Similarly to the previous process, these sources were moved to the next closest center of a cut-cell with gray matter contributions. The maximal distance between a moved source and its original location is 0.96 mm with a median distance (among the moved dipoles) of 0.72 mm.

Source models   For the CutFEM models, we use the monopolar Venant approach as a source model. We create monopoles in the dipole element and all elements which share a vertex with the dipole element. We exclude elements which do not contain cut-cells of the gray matter compartment. On each fundamental element, the monopoles are scaled to the bounding boxes of the respective cut-cell. We additionally use the partial integration approach on the smooth CutFEM model in order to compare the results obtained from the different models and surface representations with the effect of choosing a different source model. Based on the results of Sections 2.1 and 2.2 we use the conforming spatial Venant approach for the fitted methods, on a patch consisting of the dipole element and all elements sharing a vertex with the dipole element. The remaining parameters of the Venant approaches, such as the relaxation factor or the number of moments are chosen as described in Section 2.1 and are identical for all models.

Measures and Visualizations   In order to compare the different approaches, we use the RDM and MAG measures introduced in the previous sections (cf. (2.14) and (2.15)) to compare the forward solutions of a model with the results of the smooth CutFEM approach, which is used as a reference model. These measures are visualized directly on the source space. Note that in contrast to the
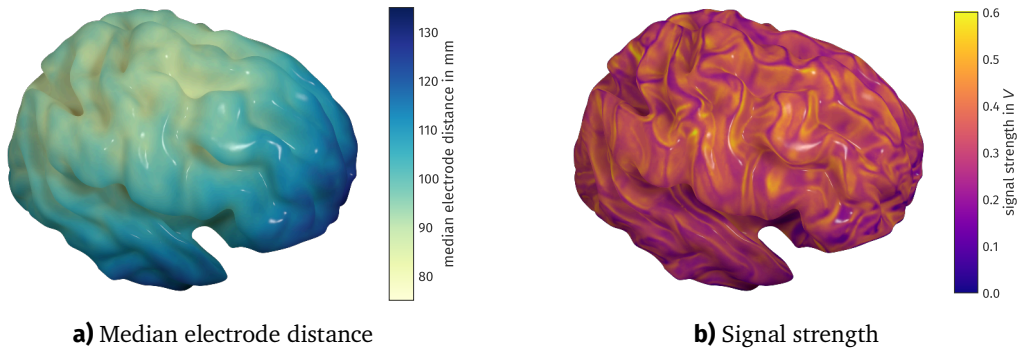
a) Median electrode distance   **b)** Signal strength

Figure 3.16: Left: median distance to the electrodes. A lighter color indicates a smaller median distance to the electrodes. Right: Signal strength of the 1 mm CutFEM discretization with the monopolar Venant source model. A light color indicates a higher signal strength.

evaluations in the previous studies, these measures mainly show differences in topography and magnitude compared to the reference model, but not to a correct analytical solution. In order to obtain a general impression of the effect of the different models, we compute the cumulative relative frequencies (CRF) for the RDM and MAG errors. For a vector of observations $v \in \mathbb{R}^n$ they are defined as

$$\text{CRF} : \mathbb{R} \to [0, 1]; \; x \mapsto \frac{1}{n} \sum_{i=0}^{n-1} \chi_{(-\infty, x]}(v_i),$$

where $\chi_{(-\infty, x]}$ denotes the indicator function on the interval from $-\infty$ to x. The function $CRF(x)$ is monotone since it describes the percentage of sources which show an observation of x or lower. The support of the CRF curve is limited by the support of the respective measure, with an optimal curve showing a jump from 0 to 1 at $x = 0$ for both, RDM and MAG. For the RDM error, we indicate the critical value of 95 % of the sources, while for the MAG error, we show the critical values at 2.5 % and 97.5 %, which delimit the central 95 %. In addition to the visualization of the different error measures on the surface of the inflated source space, we show two-dimensional histograms to compare the dependency between two different measures. For each measure, we distribute the respective observation into uniformly distributed bins and visualize the number of entries in each bin. For each column, the number of entries in a bin are scaled with the maximal number within a bin of that column. Additionally, we show classical one dimensional histograms for each of the two measures.

Results   We first present general results of the signals of the smooth CutFEM model, which serves as the reference model. Figure 3.16 shows the median distance of each source position to the electrodes and the signal strength of the reference model using the Venant approach. We observe higher median electrode distances in the frontal lobe and in frontal areas of the temporal lobes. In general more medial areas have a lower median distance to the electrodes and positions on the gyral crowns show a larger median distance. The signal strength is measured as the $l2$-norm of the mean referenced lead field at each location. Overall, we observe a smooth distribution of the norm over the cortex. We observe a higher signal strength for tangential sources close to the gyral
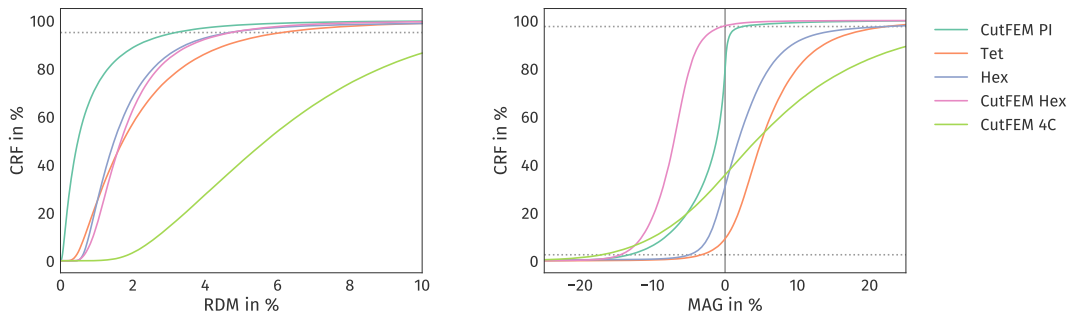
Figure 3.17: Cumulative relative frequencies of the RDM (left) and MAG (right) errors in percent. Each plot corresponds to a different model. For the RDM error, the dotted horizontal line indicates a frequency of 95 %. For the MAG error, the two dotted horizontal lines correspond to frequencies of 2.5 % and 95.7 % respectively.

crowns while we can see a decrease of the norm for the radial orientations on the gyral crowns. We can see a trend of reduced signal strength for source positions with a higher median distance to the electrodes.

In order to compare the general effect sizes of the RDM and MAG errors with respect to the reference model we compute the corresponding CRF values for the different models. We compare the tetrahedral and hexahedral approaches and the CutFEM approach using hexahedralized level-sets. All of these models use six-compartments. To obtain quantitative references for the CRF values of these approaches, we show the results of using a partial integration approach in the reference model and the results of using a four-compartment model with the CutFEM approach. The cumulative relative frequencies for the RDM and MAG error of the different models are shown in Figure 3.17. For the RDM error, the curve of the partial integration approach on the smooth CutFEM model shows the lowest values, with 95 % of the sources showing an RDM error of 3.2 % or lower. The hexahedral model and the CutFEM model with the hexahedralized surfaces show a similar behavior, the respective plots are closely correlated and the intersection with the 95 % mark occurs at approximately 4.7 % for both approaches. The plot for the tetrahedral model crosses the plots of the hexahedral approaches, i.e., it contains more sources with a lower RDM, but the bulk of the sources shows a higher measure. At a CRF of 95 %, the RDM error is 6.1 % The largest RDM errors can be observed for the four-compartment model, where 95 % of the sources show and RDM error of 12.8 % or lower. For the MAG error, the plot of the partial integration approach is closest to the optimal jump at 0 %. Additionally, 95 % of the sources have a MAG error between –13.2 % and 2.4 %. The tetrahedral and hexahedral MAG plots show a similar curve, where the majority of the sources show a positive MAG error. The bulk of the sources for the tetrahedral model shows a MAG error between –3.2 % and 22.3 % while for the hexahedral model, the boundaries are –4.7 % and 22.1 %. For the CutFEM approach with the hexahedralized surfaces, the overall trend of the MAG error is towards negative values, with a 95 % interval between –14.4 % and –0.4 %. The largest spread over all models can be observed for the four-compartment model. Here, the bulk of the sources shows a MAG error between –17.1 % and 43.2 %.

In the following, we show the distribution of the RDM and MAG errors visualized on the source space for the different models presented above. First, we present results for using the partial integration approach on the reference model. Figure 3.18 shows the results of the comparison between
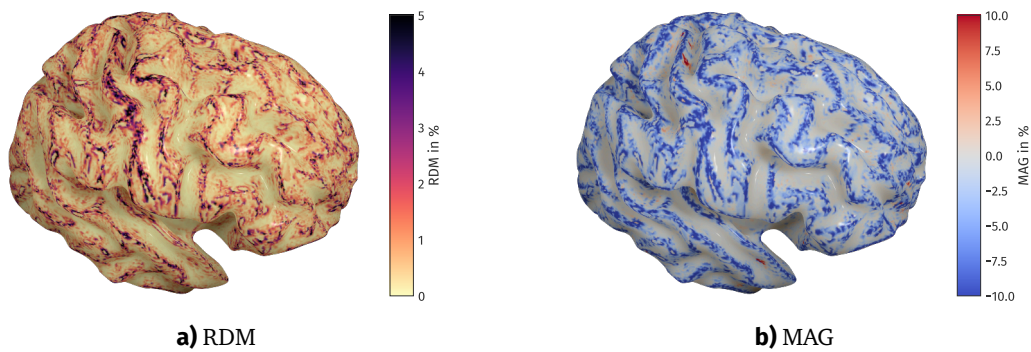
a) RDM   **b)** MAG

Figure 3.18: RDM and MAG errors on the inflated source space between the partial integration source model and the Venant source model source model on a 1 mm CutFEM discretization. For the RDM error, a darker color indicates a higher error. For the MAG error, a blue color corresponds to negative values, a red color corresponds to positive values.
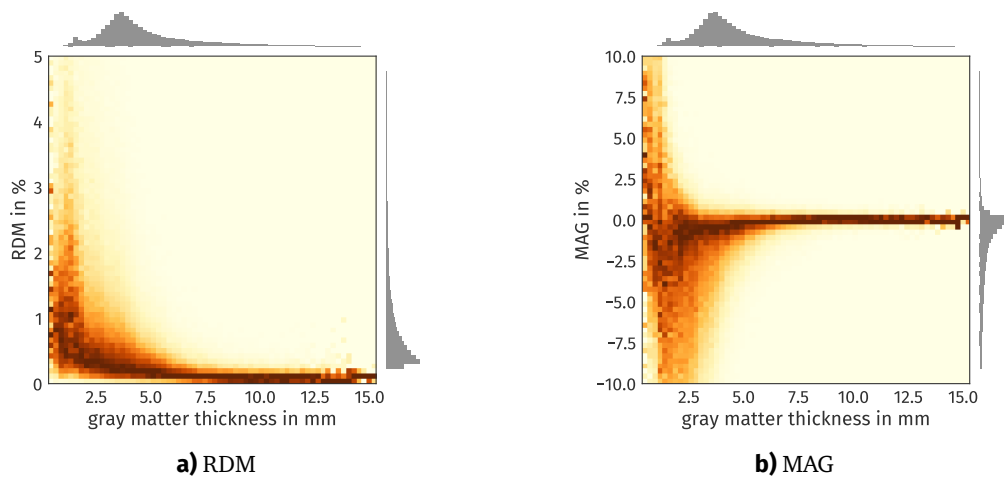

a) RDM   **b)** MAG

Figure 3.19: Dependency between RDM and MAG errors and gray matter thickness between the partial integration the Venant source model on the reference model. The color indicates the frequency of a box relative to the maximum frequency within each column. The gray barplots at the top and right side show the histograms within each dimension.

the partial integration and the Venant approach on the reference model. With respect to the RDM error we see the main errors located on the gyral crowns which are reduced closer to the sulci. The highest RDM errors can be observed in more lateral areas of the central gyri. With respect to the MAG error the main errors are again located on the gyral crowns, while areas in the sulci show a reduced MAG error. With a few exceptions the main trend of the MAG error is negative, i.e., the magnitude of the partial integration approach is lower than the magnitude of the Venant approach. Comparing the RDM and MAG error, we observe a strong correlation between the magnitude of the RDM error and the MAG error. In addition, considering the gray matter thickness in Figure 3.15, we see a positive correlation between increased error measures and a lower gray matter thickness. In order to further investigate this correlation, Figure 3.19 shows 2D histograms for the relationship between the two error measures and the thickness of the gray matter compartment. The range of both error measures is identical to the range of the color map in Figure 3.18. For the RDM we see

the aforementioned increase of the RDM with decreasing gray matter thickness. For sources with a thickness higher than approximately 7.5 mm the RDM stays below 0.5 % and increases for sources in thinner areas. Both observations transfer to the MAG error where the total range of the error increases with a thinner gray matter compartment.

Next, we perform the same investigation for the geometry-conforming tetrahedral mesh. In Figure 3.20 we present the results of the RDM and MAG errors compared to the reference model. With respect to the RDM error, we see an overall increase of the RDM error especially in superficial areas and a reduced error in the sulci. Similar to the previous results, the highest RDM values are located on the post-central gyrus. The MAG error shows an overall trend towards positive values, i.e., the magnitude of the CG approach is higher than the magnitude of the CutFEM approach. In some areas mainly located on the gyri, the MAG error becomes negative. The highest MAG errors are located in areas around the post-central gyrus as well as in frontal areas. We observe a correlation between the thickness of the gray matter and the RDM and MAG error and show the dependency in 2D boxplots in Figure 3.21. We see the effects described based on the visual inspection on the source space also in these histograms. The spread of the RDM error increases for thinner gray matter compartments and the MAG error is increased towards positive values. For source positions at locations thinner than 1 mm, we see a higher spread of the MAG error and also the aforementioned negative values.

a) RDM   **b)** MAG
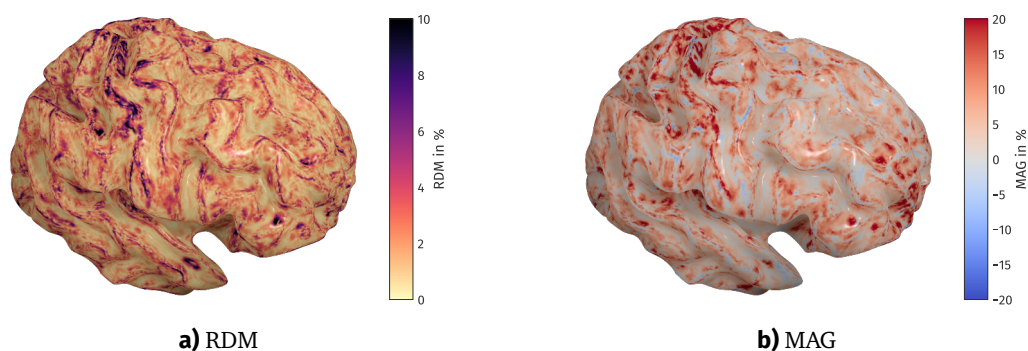
Figure 3.20: RDM and MAG errors on the inflated source space between the conforming finite element method with a tetrahedral mesh and the 1 mm CutFEM reference model. For the RDM error, a darker color indicates a higher error. For the MAG error, a blue color corresponds to negative values, a red color corresponds to positive values.

a) RDM   **b)** MAG

Figure 3.21: Dependency between RDM and MAG errors and gray matter thickness between the conforming Venant for a CG method with a tetrahedral mesh and the monopolar Venant on a 1 mm CutFEM discretization. The color indicates the frequency of a box relative to the maximum frequency within each column. The gray barplots at the top and right side show the histograms within each dimension.

The second fitted approach that is investigated in this section is the conforming finite element method using a 1 mm geometry-adapted hexahedral mesh. In Figure 3.22 we show the results of the comparison between the CG approach and the reference model. With respect to the RDM error the results are similar to the tetrahedral approach in their general distribution, while their absolute values are overall slightly reduced. The highest error values can be found on the gyral crowns, especially of the central gyri. The MAG error shows positive values on and close to the gyral crowns. Compared to the tetrahedral model, the MAG error in frontal areas is reduced. Again, in Figure 3.23 we show the dependency between the RDM and MAG errors and the gray matter thickness. The RDM error increases for thinner gray matter areas, with a strong increase of the error range for the thinnest locations. This effect is stronger when considering the MAG error, which is increasing with a thinner gray matter compartment and shows a similar spread for the thinnest locations. Compared

a) RDM   **b)** MAG

Figure 3.22: RDM and MAG errors on the inflated source space between the conforming finite element method on a 1 mm geometry-adapted hexahedral mesh and the reference model. For the RDM error, a darker color indicates a higher error. For the MAG error, a blue color corresponds to negative values, a red color corresponds to positive values.
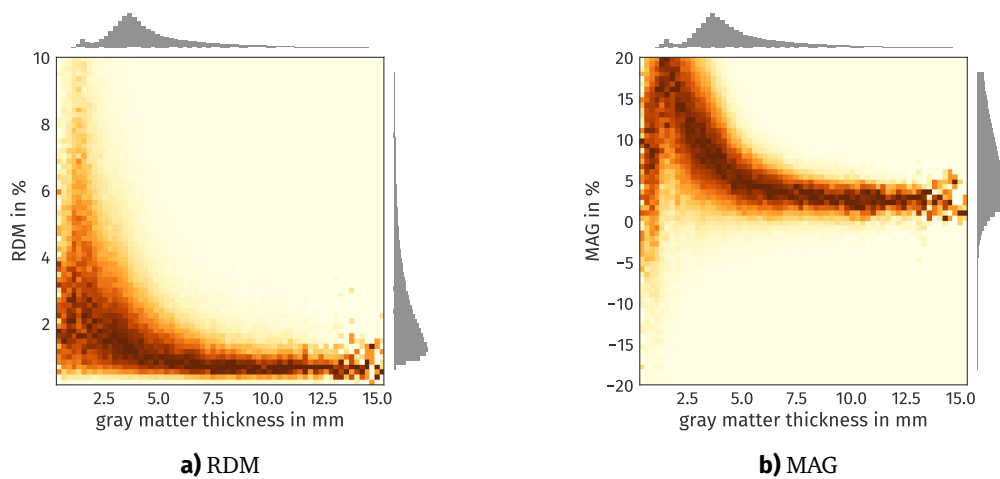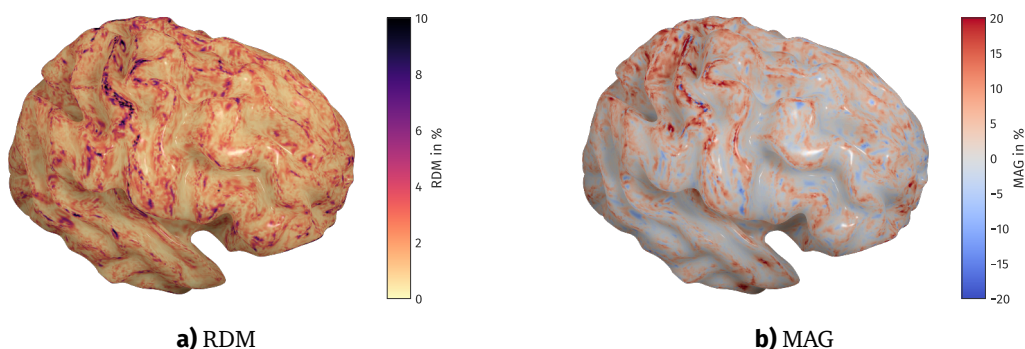
a) RDM

b) MAG

Figure 3.23: Dependency between RDM and MAG errors and gray matter thickness between the conforming finite element method on a 1 mm geometry-adapted hexahedral mesh and the reference model. The color indicates the frequency of a box relative to the maximum frequency within each column. The gray barplots at the top and right side show the histograms within each dimension.

to the tetrahedral case, the RDM error is slightly reduced and the MAG error shows a smaller total range and is closer to the zero line.

For the next model we extracted the surfaces of the hexahedral mesh and applied a smoothing procedure to construct level-set functions. Using these level-set functions, we created a CutFEM model and compare it to the reference model. Figure 3.24 shows the RDM and MAG errors of this comparison. The general distribution of the RDM error is comparable to the hexahedral and tetrahedral models. We can observe a smoother distribution of the RDM error and slightly higher values in frontal areas and large values around the post-central gyrus. The most notable feature of the MAG error is the shift towards negative values, that was already observed in the cumulative relative frequency plots above. This trend towards negative values can be observed over almost all source positions, with a reduction on small strips on the gyral crowns. It seems slightly stronger

a) RDM

b) MAG

Figure 3.24: RDM and MAG errors on the inflated source space between the 1 mm CutFEM discretization from hexahedralized level-set functions and the reference model. For the RDM error, a darker color indicates a higher error. For the MAG error, a blue color corresponds to negative values, a red color corresponds to positive values.
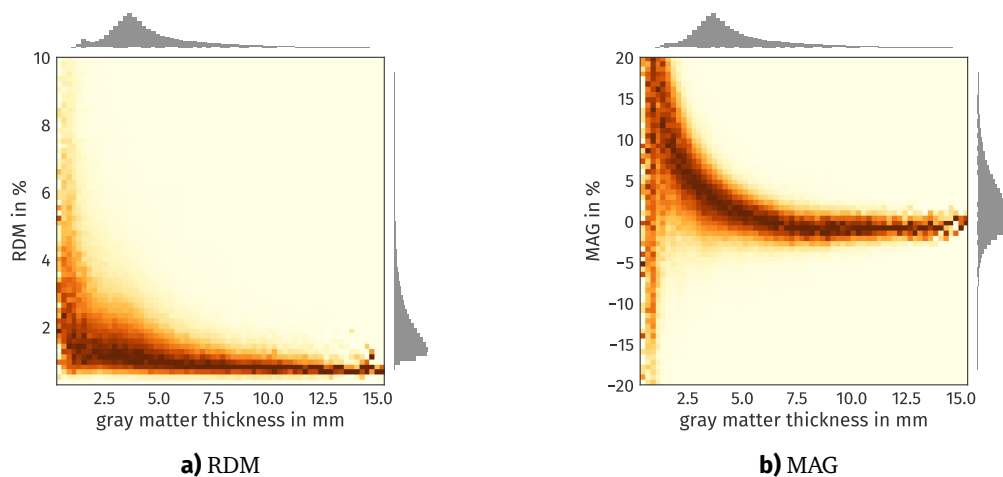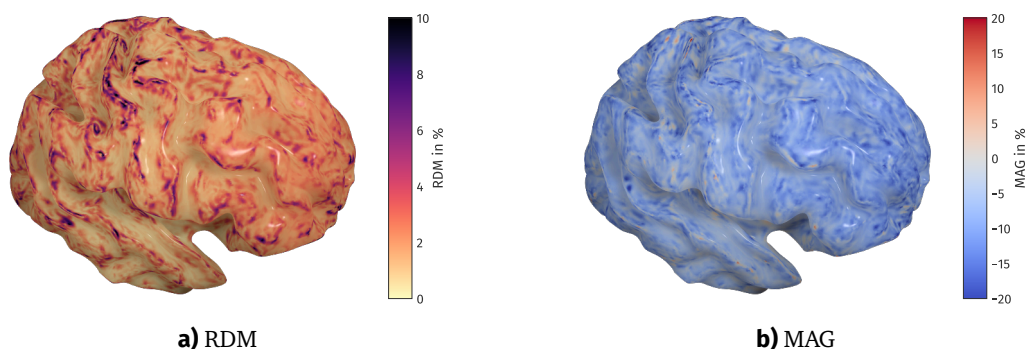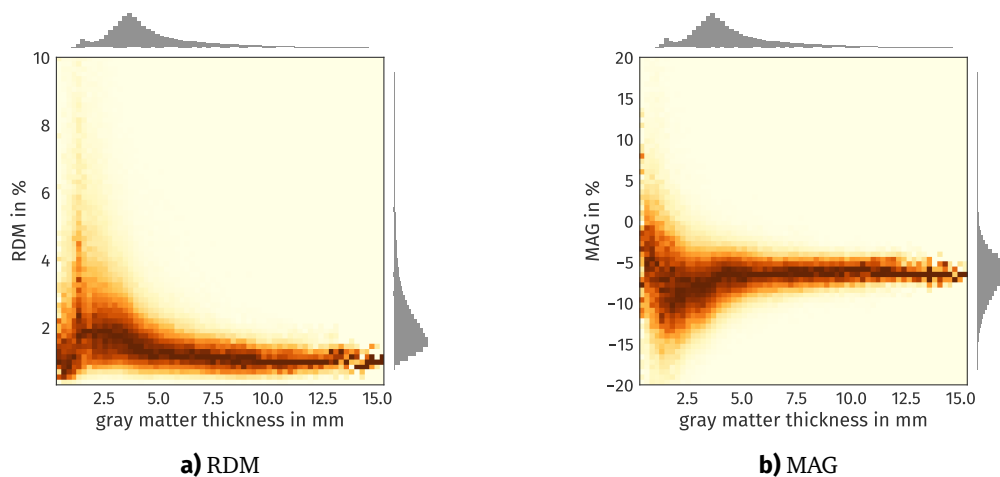
a) RDM   **b)** MAG

Figure 3.25: Dependency between RDM and MAG errors and gray matter thickness between the 1 mm CutFEM discretization from hexahedralized level-set functions and the reference model. The color indicates the frequency of a box relative to the maximum frequency within each column. The gray barplots at the top and right side show the histograms within each dimension.

close to the small strips on top of the gyri. Similar to the previous results, we observe a correlation between the gray matter thickness and the RDM and MAG errors, which is visualized using 2D boxplots in Figure 3.25. The general correlation between gray matter thickness and the RDM error is not as strong as for the conforming approaches when considering the thinnest gray matter areas. The histogram for the MAG error shows the shift of the error curve at approximately –6 %, which was already observed with regard to the CRF values. The absolute MAG error increases in areas thinner than 5 mm while the MAG error in the thinnest areas is also not as strong compared to the conforming methods.

In order to obtain a quantitative reference of the RDM and MAG errors in the different models described above, we compare a four-compartment CutFEM model with the six-compartment reference model. The four-compartment model does not distinguish between gray and white mater nor between skull compacta and skull spongiosa. Figure 3.26 shows the RDM and MAG error of this comparison. Note the different scaling of the color maps compared to the results of the six compartment models. The highest RDM errors are mainly located close to the gyral crowns, while small strips on the crests of the gyri show a lower RDM value. The general distribution with respect to the gray matter thickness that was observed in the six-compartment model is not present. The MAG error shows positive values on top of the gyri which are largest in temporal areas and on the temporal lobes. In the sulci the MAG error is mostly negative.

Discussion   In the previous paragraph we presented the results of the comparison between different realistically shaped head models and a CutFEM reference model.

The lowest RDM and MAG errors were observed for the partial integration approach on the reference model. As the approach used the same forward model the only difference to the reference is the discretization of the source term. In the results for the comparison of different source models for the CutFEM discretization of the four-layer sphere model, the main difference could be found
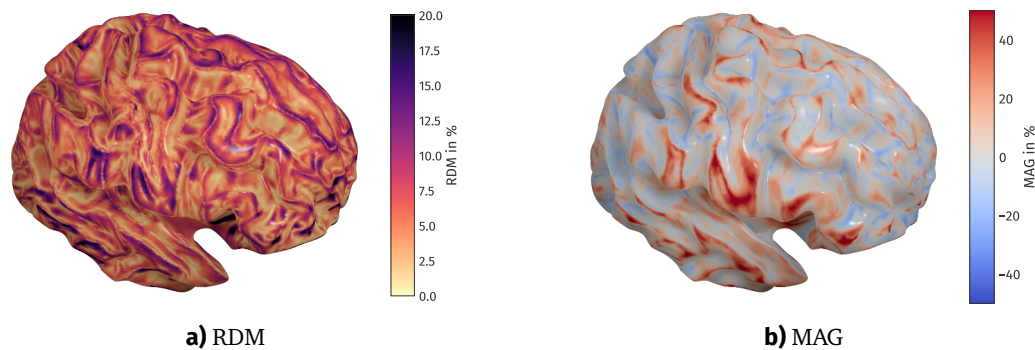
a) RDM   **b)** MAG

Figure 3.26: RDM and MAG errors on the inflated source space between the four-compartment 1 mm CutFEM discretization and the six-compartment reference model. The six-compartment model additionally includes the distinction between gray matter and white matter and between skull compacta and skull spongiosa. For the RDM error, a darker color indicates a higher error. For the MAG error, a blue color corresponds to negative values, a red color corresponds to positive values.

close to the conductivity jumps. For the realistically shaped head model the sources that are closest to the conductivity jumps are located on the gyral crowns and in areas with a thin gray matter compartment. For these sources we observe an increased RDM and MAG error for the partial integration approach. In addition, the distribution of the error is not smooth, which represents the stronger dependency of the partial integration approach to the local mesh structure.

The results for the two fitted approaches, the conforming finite element method with a geometry-conforming tetrahedral or hexahedral mesh, are very similar with respect to both error measures. The main differences to the reference model could be found in areas with a thin gray matter compartment. As already noted in the reasoning for the partial integration approach sources in these areas are closer to the conductivity jumps. The comparison between the fitted approaches and the CutFEM discretization in sphere model studies indicated a larger difference for higher eccentricities. In the sphere model studies the MAG error of the fitted approaches was overall more positive than the MAG error of the CutFEM approach. This is reflected in the results of the realistically shaped model where the MAG error tends towards positive values. The differences between the two fitted approaches could be seen in the different surface representations and in the different representations of the discrete functions. Compared to the partial integration approach on the reference model the RDM and MAG errors for the fitted approaches are approximately twice as large.

For the hexahedralized model the general distribution of the RDM and MAG errors are similar to the fitted approaches. We can see the effect of the smoothing of the different surfaces by an overall smoother distribution of the error measures. The shift of the MAG error towards negative values could be due to the construction of the surfaces and the additional smoothing procedure. This should be part of further investigations, and alternative smoothing approaches should be taken into account. In (Whitaker, 2000), an approach for anti-aliasing of binary voxel images has been presented, which uses a constrained smoothing based mean curvature of the surface (see also Section 5.4 for an application of this smoothing approach).

Summarizing the results of all six-compartment models we see that especially areas on the gyral crowns or close to them are sensitive to the different models with respect to topography changes

measured by the RDM. These are also the areas, closer to the electrodes and with a higher curvature of the surface and thus areas that show a stronger change in orientation for close source locations. The main effects for all different six-compartment models were found in areas with a thin gray matter compartment. Studies using the multi-layer sphere models showed an increasing error as well as a higher variance of the error when sources are located closer to a conductivity jump. As the source space is located in the gray matter compartment, the closest surfaces are the gray and white matter surface. These surfaces are closer to the source space, the thinner the gray matter compartment is. In addition, the representation of the different tissue surfaces can also be seen as a main difference between the discretization schemes. In the tetrahedral model, the surfaces are represented as triangular surfaces while in the hexahedral model they have a staircase-like structure. The hexahedralized CutFEM approach represents the surfaces via level-set functions that are obtained by smoothing the staircase-like representation of the hexahedral model. Due to these differences higher errors in areas with a thinner gray matter compartment can be expected.

However, all effects between the different discretization schemes are below the effect of excluding the gray/white-matter and compacta/spongiosa distinction which is approximately twice as big as the aforementioned effects. We note that the effect of the error measures for the four-compartment model reproduces similar findings in (Vorwerk, 2016). We observe the highest MAG values mainly in areas that are not covered by the skull spongiosa compartment and on gyral crowns. In these areas, the MAG error is positive, i.e., we see an overestimation of the magnitude compared to the six-compartment model.

We conclude that especially areas with thin structures are sensitive to modeling differences and special care should be taken when considering the forward modeling approach for such models.

3.5 Conclusion

In this chapter, we presented two cut-cell methods for solving the EEG forward problem. The main goal was to provide a more simple simulation pipeline without the need for creating a geometry-conforming tetrahedral mesh, while still allowing for an accurate representation of the different tissue compartments. The first approach was the CutFEM method which uses a conforming discretization within each tissue compartment and couples the different subdomains weakly. The second approach presented here was the UDG method, which employs the weak coupling also in between elements within each subdomain. These methods were evaluated in four-layer sphere models as well as in a study using a realistically shaped head model. The accuracy exceeded the accuracy of a staircase-like representation offered by a hexahedral approach, and the accuracy of the tetrahedral approach could be met while offering a more simple simulation pipeline. A potential benefit of the separation of the model geometry and the computational domain was found in the use of second order polynomials. In realistically shaped head models the effects that were observed in sphere model studies could be confirmed. Chapter 4 discusses some implementational aspects of cut-cell methods that were omitted from this chapter, such as the integration over the implicitly defined domains, or the efficient solution of resulting linear systems.

In future studies, it would be worthwhile to evaluate the cut-cell methods in realistic head model scenarios where a modeling with geometry-conforming approaches might be difficult, such as cases with a very thin bone structure. Directly connected to the EEG forward solution is the magnetoen-

cephalography, which considers the magnetic field outside of the head model. An investigation of the cut-cell methods for magnetoencephalography (MEG) might show an advantage of the geometry representation in the source area. In addition, a higher polynomial degree might be beneficial of the MEG forward solution. In further studies, the effect on other biomedical applications should be considered, for example the simulation of transcranial electric stimulation. Such applications perform a reciprocal approach by injecting current on the head surface to modulate electric activity in the head. Especially if an area below thin bone structures as in temporal regions should be stimulated, an accurate representation of the thin structures might be needed.

Implementational Aspects of Cut-Cell Methods

In this chapter, we will discuss two aspects of implementing cut-cell methods with a focus on solving the EEG forward problem. In Section 4.1 a method for integrating functions over implicitly defined domains and interfaces is introduced: a topology preserving marching cubes. It generates quadrature rules by discretizing the implicitly defined domain on each element of an auxiliary mesh. In Section 4.2 we present algebraic multigrid (AMG) techniques which can be used to numerically solve the linear system of a cut-cell discretization. We introduce multigrid methods for the CutFEM approach as well as for the UDG method. Finally, a short conclusion will be given in Section 4.3.

4.1 Geometric Integration Over Implicitly Defined Domains

Within the context of the cut-cell methods presented in Section 3.1 and Section 3.2, one subtask is the numerical evaluation of integrals over implicitly defined domains and surfaces. In the special case of the CutFEM method, these integrals are performed over the volume of domain as well as on interfaces between the different tissue compartments. The UDG method contains the same integrals as the CutFEM method, but additionally contains integrals over the intersections between two fundamental mesh elements. In the following, we will present a method to numerically evaluate such integrals. The main results have been published in (Engwer and Nüßing, 2017). The following description of the method only considers the case of a single interface. A description of the extension to multiple interfaces will be given further below.

Let $\hat{\Omega}, \Omega \subset \mathbb{R}^d$ be domains with $\Omega \subset \hat{\Omega}$. Ω describes the computational domain which lies within a auxiliary domain $\hat{\Omega}$. Instead of giving an explicit definition of Ω, it can also be defined as a level-set of a continuous function $\Phi : \hat{\Omega} \to \mathbb{R}$ by setting $\Omega := \{x \in \hat{\Omega} : \Phi(x) < 0\} = \{\Phi < 0\}$. The boundary of Ω is then given as $\partial\Omega = \{\Phi = 0\}$. Note that without loss of generality we restrict ourselves to the case of the zero level-set. A general level-set of $\alpha \in \mathbb{R}$ can be used by considering the zero level-set of the shifted function $\tilde{\Phi}(x) := \Phi(x) - \alpha$. As mentioned above we are interested in the evaluation

of integrals of certain integrable functions $f : \Omega \to \mathbb{R}, g : \partial\Omega \to \mathbb{R}$, i.e., integrals of the form

$$\int_{\hat{\Omega}\cap\{\Phi<0\}} f \, \mathrm{d}x \, , \quad \int_{\hat{\Omega}\cap\{\Phi>0\}} f \, \mathrm{d}x \, , \quad \int_{\hat{\Omega}\cap\{\Phi=0\}} g \, \mathrm{d}s \tag{4.1}$$

In the literature several methods to evaluate such integrals have been presented. One class of such methods involves generating quadrature rules based on a moment-fitting approach (Müller et al., 2013; Sudhakar and Wall, 2013). These methods have been shown to lead to an accurate approximation of the integrals which is especially useful for higher order methods. Another category of approaches uses a piecewise linear sub-triangulation of the computational domain Ω or of its boundary $\partial\Omega$. One such approach is presented in (Min and Gibou, 2007). Based on a partition of the auxiliary domain into cubes each cube is split into tetrahedrons using a Kuhn triangulation (Freudenthal, 1942). This splitting is performed independently of the level-set function. On each tetrahedron, a sub-triangulation is constructed based on a marching tetrahedron approach (Gueziec and Hummel, 1995).

In the following we will present a similar approach to the one mentioned above which is based on the marching cubes method (Chernyaev, 1995; Lewiner et al., 2003; Lorensen and Cline, 1987). We first introduce a tessellation $\mathcal{T}_h(\hat{\Omega})$ of the auxiliary domain $\hat{\Omega}$, i.e., a set $\mathcal{T}_h(\hat{\Omega}) := \{E_0, \ldots, E_{n-1} \subset \hat{\Omega}\}$ such that

$$E_i \cap E_j \neq \varnothing, \quad \text{for } i \neq j \tag{4.2}$$

$$\bigcup_{i=0}^{n-1} \overline{E_i} = \overline{\hat{\Omega}} \tag{4.3}$$

hold. On this tessellation, we approximate the level-set Φ by a piecewise multi-linear level-set Φ_h. The main idea of the algorithm is to approximate the domain Ω, its complement $\hat{\Omega} \setminus \Omega$ and its boundary $\partial\Omega$ by a set of simple polytopes on each element of this tessellation. The polytopes are generated such that common quadrature rules are available for them, e.g., they are given as simplices or cubes. Subsequently, the integration can be carried out on these more simple elements. Let $E_i \in \mathcal{T}_h(\hat{\Omega})$ be an element of the tessellation of the auxiliary domain. With $\mathcal{S}_{<0}(E_i) := \{E_i^0, \ldots, E_i^{m_i-1} : E_i^j \subset E_i, 0 \leq j < m_i\}$ we denote the set of polytopes for which

$$\bigcup_{j=0}^{m_i-1} E_i^j \approx E_i \cap \{\Phi_h < 0\} \tag{4.4}$$

should hold. Similarly, we define $\mathcal{S}_{>0}$ and $\mathcal{S}_{=0}$. The construction of the subtessellation is the main contribution of the proposed algorithm and will be described in the remainder of this section. Once
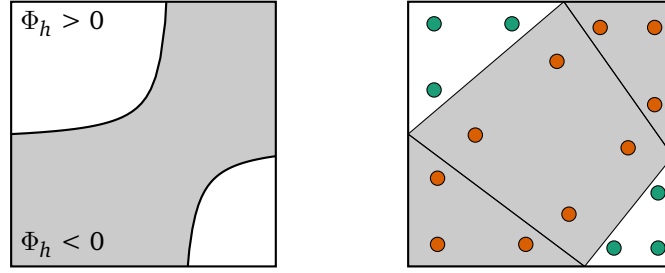
Figure 4.1: Discrete level-set function (left) and subtessellation (right) on a square. The gray area indicates the interior, the white area the exterior part of the domain. The circles indicate the generated quadrature points.

$\mathcal{S}(E_i)$ has been constructed for every $E_i \in \mathcal{T}_h(\hat{\Omega})$ the integration over Ω can be carried out as

$$\int_\Omega f \, dx = \int_{\hat{\Omega} \cap \{\Phi < 0\}} f \, dx \tag{4.5}$$

$$\approx \int_{\hat{\Omega} \cap \{\Phi_h < 0\}} f \, dx \tag{4.6}$$

$$= \sum_{i=0}^{n-1} \int_{E_i \cap \{\Phi_h < 0\}} f \, dx \tag{4.7}$$

$$\approx \sum_{i=0}^{n-1} \sum_{j=0}^{m_i-1} \int_{E_i^j} f \, dx \tag{4.8}$$

 An example of a multi-linear level-set along with the reconstruction and the resulting quadrature points can be seen in Figure 4.1. In the above equations, two approximations take place. The first one is the replacement of the analytical level-set function Φ with the multi-linear level-set function Φ_h in (4.6). The second approximation can be found in (4.8) where the domain delimited by the multi-linear level-set function on a single element of the tessellation $\mathcal{T}_h$ is replaced by the domain given by the elements of the subtessellation. The first approximation is a necessary prerequisite of the algorithm described below. Within the setting of solving forward problems in biomedical applications there is in fact no approximation taking place, as the analytical level-set function is usually already given as a multi-linear function obtained by a level-set segmentation of patient-specific imaging data. Note that in general this is not the case and should be taken into account when evaluating the method in an analytical setting such as the multi-layer sphere model used below. The second approximation is due to the core idea of the marching cubes algorithm. Due to the choice of simple polytopes, the boundary approximation will be piecewise linear. This might be of special interest in the setting of finite element methods, if higher order ansatz functions should be used. In this case, a higher resolution of the tessellation of the auxiliary domain than of the tessellation used for representing the basis functions might be needed in order to benefit from the increase in accuracy provided by the higher polynomial degree. Note that through an additional transformation of the background element, a higher order approximation of the boundary might be achieved, as for example described in (Lehrenfeld, 2016).

The remainder of this section will provide the description of the algorithm to produce the subtessellation of the implicit domains such as $E_i \cap \{\Phi_h < 0\}$. This process can be described solely within
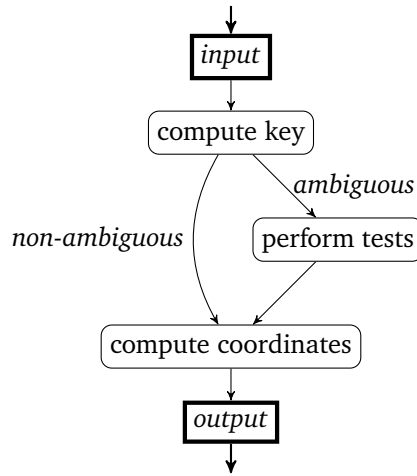
Figure 4.2: General algorithm to construct a subtessellation on the reference geometry (Engwer and Nüßing, 2017).

coordinates of the reference element $\hat{E}_i$ of E_i. The resulting subtessellation can then be transformed into global coordinates via the local-to-global mapping associated with E_i.

In the following we will describe an algorithm to construct a tessellation of a domain implicitly defined via a multi-linear level-set function. All descriptions will be given on the unit cube, serving as a reference element in a hexahedral mesh. Other reference geometries, such as simplices or prisms can be handled in the same way and will not be described here (see for example the comments in (Engwer and Nüßing, 2017)). The general structure of the algorithm to construct a subtessellation is depicted in Figure 4.2. Based on the corner values of the discrete level-set function we compute a key corresponding to the topology of the reconstruction. Depending on the corner values this key might already uniquely define the topology or additional tests have to be performed to obtain a unique reconstruction. Once these disambiguities have been resolved a generic reconstruction is retrieved from pre-computed look-up tables and the exact coordinates of the reconstruction are computed based on the corner values.

We will first describe the requirements that we pose on the discrete reconstructions. Foremost, we require that the subtessellations $\mathcal{S}_{<0}$ and $\mathcal{S}_{>0}$ of the interior and exterior, respectively, fulfill

$$E \cap F = \varnothing \quad \forall E, F \in \mathcal{S}_{<0} \cup \mathcal{S}_{>0} \text{ with } E \neq F$$

$$\left(\bigcup_{E \in \mathcal{S}_{<0}} \overline{E} \right) \cup \left(\bigcup_{F \in \mathcal{S}_{>0}} \overline{F} \right) = \overline{\hat{R}},$$

where $\hat{R}$ denotes the reference geometry. This means that the subtessellations of interior and exterior do not overlap and fill the complete reference element. For the interface $\mathcal{S}_{=0}$ we require that

$$\forall \gamma \in \mathcal{S}_{=0} \exists E \in \mathcal{S}_{<0}, F \in \mathcal{S}_{>0} : \gamma = \overline{E} \cap \overline{F} \tag{4.9}$$

holds, i.e., $\mathcal{S}_{=0}$ is the discrete interface between the two volume subtessellations. In order to obtain

a tessellation that is robust and applicable in various scenarios we require it to additionally fulfill the following topological guarantees:

preservation of connectivity pattern We require that the connectivity pattern of the cell vertices must be preserved within each subentity. This means that for every subentity (edge, face or volume) and every pair of cell vertices it holds that if and only if there is a path in this subentity from one vertex to the other that lies completely on the one side of the level-set, then there is also such a path in the discrete reconstruction.

preservation of connected components The number of path-connected components and their domain association is preserved by the discrete reconstruction, i.e., there is a bijective mapping between the different equivalence classes of the path-connected relation that maps only between classes of the same domain.

robustness of reconstructed vertices All vertices of the reconstruction that are not corners of the reference element should lie on the zero level-set of the discrete level-set function.

These guarantees should make sure that the reconstruction captures important structures from the discrete level-set representation.

In order to create a reconstruction that fulfills the aforementioned guarantees and that can be computed efficiently we note that a multi-linear level-set function on the reference cube is uniquely defined by its values at the corner of the reference geometry. Let $x_0, \ldots, x_{n-1} \in \mathbb{R}^d$ denote these corners and denote by $v_i := \Phi_h(x_i), i = 0, \ldots, n-1$ the value of the level-set function. Using these level-set values at the corners, we generate a key

$$\text{key}(v_0, \ldots, v_{n-1}) = \sum_{i=0}^{n-1} \chi_{\mathbb{R}_-}(v_i) 2^i, \tag{4.10}$$

where $\chi_{\mathbb{R}_-}$ denotes the indicator function of the negative half of the real axis, i.e.

$$\chi_{\mathbb{R}_-}(x) = \begin{cases} 1, & x < 0 \\ 0, & \text{else} \end{cases}. \tag{4.11}$$

Based on the key, we can categorize each set of corner values into one out of 2^n cases. For a hexahedral reference geometry we have $n = 8$ and thus 256 cases. We assume that for the unit cube the corners are ordered in a tensor-product fashion (analogue to the unit square in Figure 4.3). Figure 4.3 shows an exemplary key-computation on a square. The reference geometries considered here have certain symmetries that can be exploited, to reduce the number of cases to a set of base cases. For example, the reference hexahedron can be rotated symmetrically by 90 degrees along the three Cartesian axes as well as mirrored along the three Cartesian planes. Using these symmetric transformations, each set of corner values can be assigned a unique base case based only on the signs of the values. As the discrete level-set Φ_h is assumed to be multi-linear, some of these base cases, such as the one depicted in 4.3, already uniquely define the topology of the different domains on the reference element. The topology for other cases, such as the one depicted in Figure 4.4 cannot be uniquely determined based solely on the corner values. The two pairs of diagonally opposing vertices have the same signs but different signs than their horizontal and vertical neighbors. Based
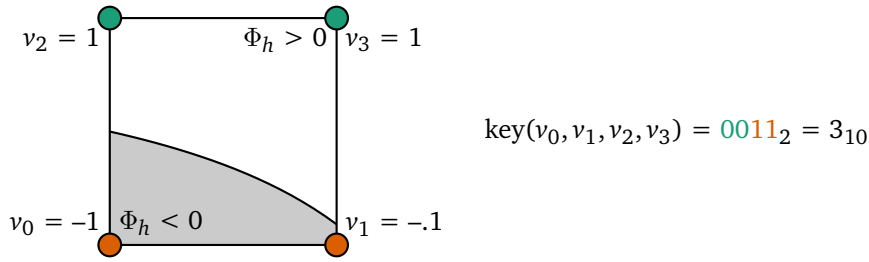
Figure 4.3: Exemplary key-computation on a unit-square. The gray area indicates the part of the square on the negative side of the level-set function. The circles indicate the sign of the corner values, where a red circle indicates a negative value and a green circle indicates a positive value. The subscript number indicates the base of the numbers representation.
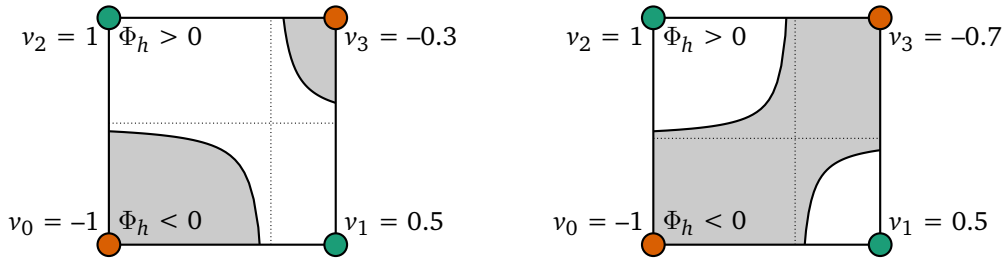

Figure 4.4: Two level-set functions on the unit-square showing the ambiguity in the key-computation based on the corner signs. The level-set functions differ in the corner value of v_3. Note the identical corner signs but the different topologies. The center of the hyperbola is located at the intersection of the dotted lines.

on the sign of the corner values alone, we can not determine whether two diagonally opposing vertices are connected through the square. As presented in (Chernyaev, 1995), this ambiguity can be resolved by evaluating the multi-linear level-set function at a specific point. We can observe, that the zero level-set function on a square forms a hyperbola for which we can compute the center.

$$(c_x, c_y) := \left(\frac{v_0 - v_2}{v_0 - v_1 - v_2 + v_3}, \frac{v_0 - v_1}{v_0 - v_1 - v_2 + v_3} \right). \tag{4.12}$$

A visualization of this center is also depicted in Figure 4.4. Depending on the sign of the level-set function at the center, the two different cases can be separated. For the sign, a closed formula consisting of the four corner values can be given.

$$\operatorname{sgn}(v_0) \operatorname{sgn}(v_0 v_3 - v_1 v_2) \tag{4.13}$$

Evaluating the sign in (4.13) resolves the ambiguity.

In three space dimensions, another type of ambiguity can occur in the unit cube. If there are two diagonally opposing vertices (e.g., v_0 and v_7), that are not connected via a path over faces of the cube, they can still be connected through the cubes volume. The connection can be formed by a tube-like structure which is illustrated further below in Figure 4.5. In order to test for this ambiguity, the level-set function can be evaluated in the center of the tube-like structure, as presented in (Chernyaev, 1995). Without loss of generality we assume that these two vertices are v_0 and v_7, i.e., we assume that their values have the same sign and the cannot be connected via a set of faces. If

and only if v_0 and v_7 are connected through the volume of the cube, there exists a plane parallel to a face of the cube, on which the projections of v_0 and v_7 are connected. Again, the existence of such a plane can be computed using the corner values. In order to simplify the notation, we will assume that the corner values of v_0 and v_7 are both positive. We will denote the corner values at the corners of the face containing v_0 by a_0, b_0, c_0 and d_0 while the corner values of the face containing v_7 will be denoted by a_1, b_1, c_1 and d_1. Along the edges that are perpendicular to the faces, the level-set function varies linearly and is given as $a : [0, 1] \to \mathbb{R}; t \mapsto a_0 + t(a_1 - a_0)$. The functions b, c and d for the remaining edges are defined accordingly. For each t, we compute the expression for evaluating the sign at the center of hyperbola (4.13), i.e.

$$p : [0, 1] \to \mathbb{R}; t \mapsto a(t)d(t) - b(t)c(t) = \alpha t^2 + \beta t + \gamma \tag{4.14}$$

with the coefficients $\alpha, \beta, \gamma \in \mathbb{R}$ defined as

$$\alpha = (a_1 - a_0)(d_1 - d_0) - (b_1 - b_0)(c_1 - c_0) \tag{4.15}$$

$$\beta = d_0(a_1 - a_0) + a_0(d_1 - d_0) - b_0(c_1 - c_0) - c_0(b_1 - b_0) \tag{4.16}$$

$$\gamma = a_0 d_0 - b_0 c_0 \tag{4.17}$$

The positive areas at v_0 and v_7 are connected, if p has a maximum $t_{\max} \in [0, 1]$ with $p(t_{\max}) > 0$ and the values $a(t_{\max}), b(t_{\max}), c(t_{\max})$ and $d(t_{\max})$ have the correct sign. Again, we refer to Chernyaev (1995) for more details.

Now that the topological case can be uniquely determined, we can use the marching cubes approach to use pre-generated look-up tables to obtain a reconstruction. These look-up tables contain the subtessellations of the interior, exterior and the interface. In (Lewiner et al., 2003), a complete list of reconstructions for the different base cases has been presented. However, these subtessellations do not fulfill the topological guarantees specified above. They include additional internal vertices that do not lie on the discrete interface or do not preserve the connectivity patterns. In the following we will describe an approach to construct reconstructions that fulfill the specified guarantees. First we will describe the different kinds of vertices used.

corner vertices These vertices are located at the corners of the reference element. In general, they do not lie on the zero level-set of the discrete level-set function and thus do not fulfill the third guarantee. In the reconstruction, they are used as helper vertices when employing *internal* vertices (see below).

edge vertices As the discrete level-set function is assumed to be multi-linear, each edge of the reference geometry can contain at most one intersection with the interface. The edge vertices describe these possible intersections and can be identified with the associated edge.

In order to construct subtessellations that satisfy the topological guarantees, we need to introduce additional vertices in the interior of the reference element in order to resolve certain base cases:

maximum vertices These vertices are defined using the quadratic function p that was used above to resolve the internal ambiguity in the volume. As noted above, the maximum of this function is located at the center of tube-like structures within the volume. In order to resolve these structures in the discrete reconstruction, the maximum vertices are located at the position
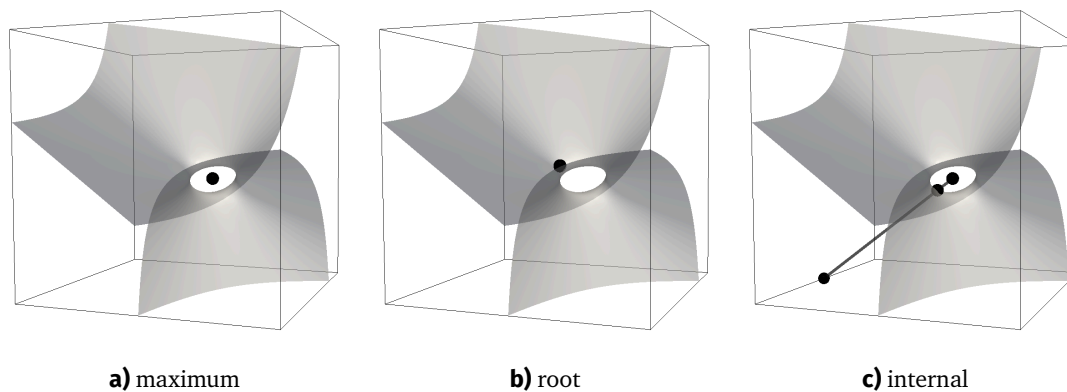
a) maximum   **b)** root   **c)** internal

Figure 4.5: Visualization of the different additional vertices in the discrete reconstruction of a level-set function (Engwer and Nüßing, 2017).

where p assumes its maximum. Similar to the corner vertices, these vertices do not lie on the discrete interface, but are used as helper vertices.

root vertices The root vertices are defined similarly to the maximum vertices above, as they use properties of the quadratic function p. As the name suggests, instead of using the maximum, they are located at the roots of p and thus lie on the discrete interface.

internal vertices Internal vertices are defined as intersections of arbitrary lines with the discrete interface. As the discrete level-set function is assumed to be multi-linear, its restriction to a line will be a polynomial. This intersection can be found using a root-finding algorithm for polynomials such as the Aberth-method (Aberth, 1973).

Figure 4.5 shows a visualization of the last three vertex types.

Using the presented vertices a generic subtriangulation for each specific base can be created manually and stored in a lookup table. After all ambiguities for a set of corner values have been resolved the generic subtriangulation can be retrieved from this table and the precise positions of the vertices described above can be calculated. For details on the software implementation and the usage of the look-up tables we refer to (Engwer and Nüßing, 2017).

Usage within a cut-cell method   The descriptions presented so far have been restricted to the case of a single subdomain. However, considering the case of EEG source analysis, the computational domain consists of different tissue compartments that are separated by more than a single interface. In order to include these different compartments in the construction of the quadrature rules we assume that they are described by a set of level-set functions $\Phi^0, \ldots, \Phi^{m-1}$. We extend the presented algorithm to multiple level-set functions by applying the reconstruction algorithm to functions recursively on the interior, exterior and interface reconstruction. The output of the reconstruction of the volume parts for the first level-set function is again a set of polytopes. On each of these polytopes we can approximate the second level-set function by a function that is multi-linear on this polytope. Applying the reconstruction algorithm again produce an approximate reconstruction for these two domains. A recursive application extends this idea to any number of level-set functions. We first note, that the resulting subtessellation depends on the ordering of the level-set functions.

Additionally, by applying the algorithm multiple times, we introduce an approximation as the original discrete level-set function is not necessarily multi-linear on an arbitrary set of polytopes. An approach to circumvent this problem would be to restrict the analytical level-set to a piecewise linear instead of a piecewise multi-linear discrete level-set function in the beginning, which would be linear on any subset of the original reference geometry. Note however that this would introduce a further approximation of the analytical level-set function. In order to construct quadrature rules on the interfaces in the multi-domain setting we follow again a recursive approach. After obtaining the reconstruction with respect to the first interface we obtain a set of surface elements. On these surface elements we can apply the reconstruction method using the second interface in a lower-dimensional setting. Additionally the interface parts that are obtained from a reconstruction with the second interface on the reference domain have to be included.

When computing the bilinear form of the cut-cell approaches three different types of integrals appear in the formulation. The first type consists of the volume integrals for the different domains and the second type consists of surface integrals on the discrete interfaces between different sub-domains. These integrals can be computed directly using the volume subtriangulation and the interface subtriangulation resulting from the marching cubes method. For the UDG method an additional third type of integrals has to be computed. This type consists of the surface integrals on the cut faces of the fundamental mesh between cut-cells which belong to the same domain but lie within different fundamental mesh elements. In order to generate quadrature rules for these intersections we apply a lower-dimensional marching cubes algorithm to the face of the fundamental mesh.

4.1.1 Validation Studies

Results   In the following we validate the proposed topology preserving marching cubes algorithm for the purposes of solving the EEG forward problem using cut-cell methods. We use a four-layer sphere model with the radii given in Table A.1. As a first validation we measure the volume and surface area of the different tissue compartments of the discrete reconstruction when increasing the mesh resolution. The analytical volume and surface areas of the different compartments can be subsequently used to compute the relative error of the results given by the discretization. We compare these results to the ones obtained by employing a geometry-adapted hexahedral mesh with the same resolution and a node-shift parameter of 0.3.

Figure 4.6 shows the relative error of the volumes of the different tissue compartments in the four-layer sphere model when increasing the mesh resolution. For the unfitted method, we observe an overall monotone decrease of the relative error for all tissue compartments with increasing mesh resolution. Starting from a resolution of 8 mm the relative error for all tissue compartments is below 1 %. At the highest resolution of 1 mm the relative error for all compartments is below 0.01 %. We can observe a second order convergence of the relative error for all tissue compartments over all mesh resolutions. For the hexahedral method, we can observe a monotone decrease of the relative error for all tissue compartments with increasing mesh resolution, with the exception of the skull compartment when increasing the resolution from 8 mm to 4 mm. The highest resolution of 1 mm is the first resolution where all compartments have an error below 1 %. At the coarsest resolution of 16 mm, no CSF compartment is present. Over all mesh resolution, the relative error in the volume
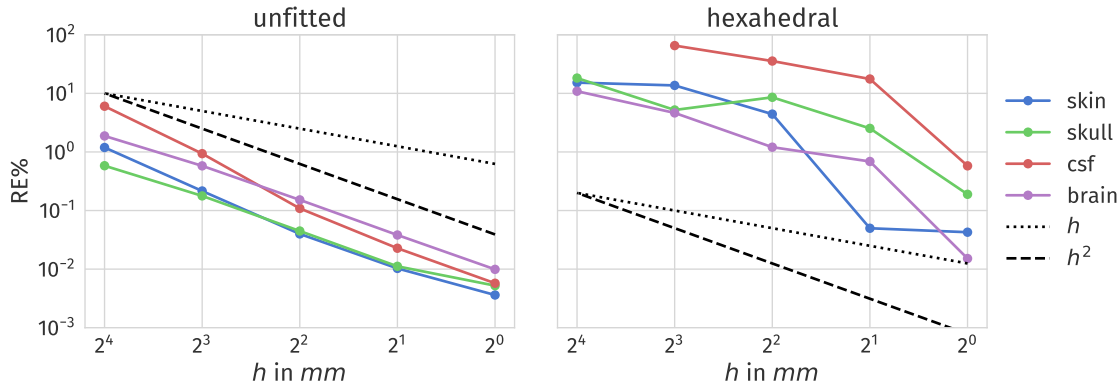
Figure 4.6: Relative error (in percent) of the volumes of the different tissue compartments in a multi-layer sphere model. Left using an unfitted mesh, right using a geometry-adapted hexahedral mesh. Each colored plot corresponds to a tissue compartment, the dotted and dashed black lines correspond to the linear and quadratic functions respectively.

Figure 4.7: Relative error (in percent) of the surfaces of the different tissue compartments in a multi-layer sphere model. Left using an unfitted mesh, right using a geometry-adapted hexahedral mesh. Each colored plot corresponds to a tissue compartment, the dotted and dashed black lines correspond to the linear and quadratic functions respectively.
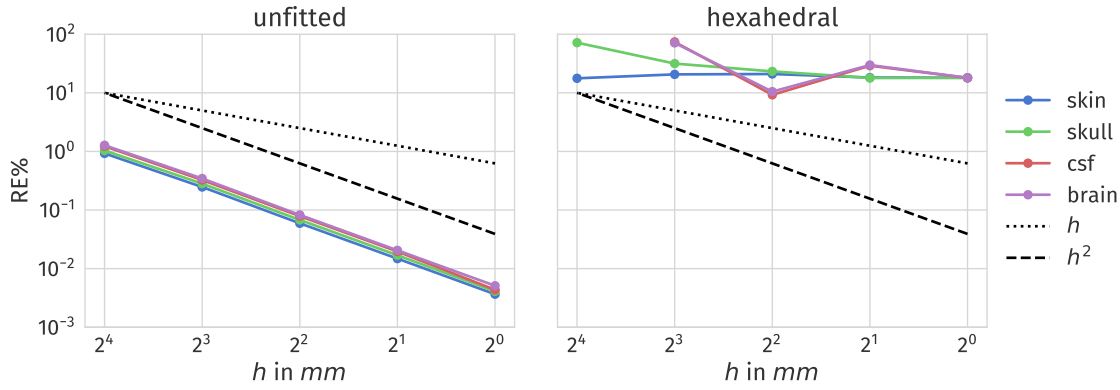
of the CSF compartment is the highest. The convergence order up to the highest eccentricity can be seen as second order, although it is reduced to first order up to a resolution of 2 mm and has an increased jump from 2 mm to 1 mm. For each mesh resolution and all tissue compartments the relative errors for the geometry-adapted hexahedral mesh are higher than the corresponding values for the unfitted mesh.

Figure 4.7 shows the relative error of the surfaces of the different tissue compartments in the four-layer sphere model when increasing the mesh resolution. We depict the interfaces between brain and CSF, CSF and skull, skull and skin as well as skin and air, denoted by the inner compartment. For the unfitted method, we observe an overall monotone decrease of the relative error for all tissue compartments with increasing mesh resolution. For mesh resolutions higher than 8 mm, the error is below 1 % and at the highest resolution of 1 mm it is below 0.01 %. We can observe a second order convergence of the relative error for all tissue compartments over all mesh resolutions. For the hexahedral mesh, the relative error of the surfaces stays approximately constant above a value
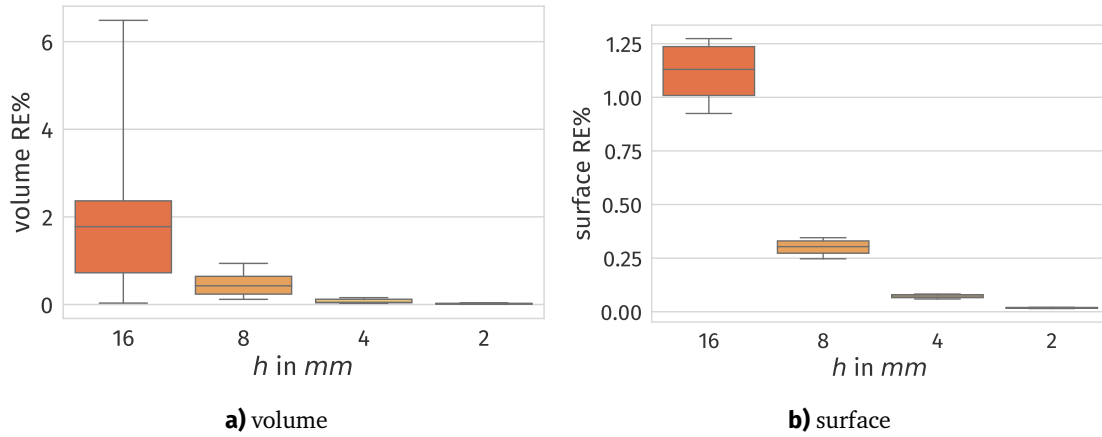
a) volume   **b)** surface

Figure 4.8: Boxplots showing the relative error (in percent) of the volumes (left) and surfaces (right) for different orderings of level-set functions. Each boxplots contains the results for all possible orderings and all compartments at that mesh resolution.

Table 4.1: Statistical properties of the boxplots presented in Figure 4.8. Each row corresponds to a background mesh resolution, the different columns show different statistical properties of the relative error of the volumes and surfaces.

	VOLUME			SURFACE		
h	IQR in %	TR in %	max in %	IQR in %	TR in %	max in %
16 mm	1.642	6.454	6.486	0.228	0.349	1.274
8 mm	0.406	0.821	0.938	0.057	0.098	0.345
4 mm	0.080	0.128	0.156	0.014	0.023	0.082
2 mm	0.016	0.034	0.039	0.003	0.006	0.021

of 10 %. We do not observe a reduction with increasing mesh resolution. For the coarsest resolution of 16 mm no CSF compartment and thus no interface between brain and CSF and between CSF and skull is present. Thus, for each mesh resolution and all tissue compartments the relative errors for the geometry-adapted hexahedral mesh are higher than the corresponding values for the unfitted mesh.

The approach for using the presented marching cubes method to generate quadrature rule in a multi-domain setting is to recursively apply the algorithm on the resulting subtessellations. One property of this approach is that the resulting quadrature rule depends on the order in which the level-set functions are cut. Cutting the first level-set function will produce a set of polytopes, which are used as an input for the cut with a second level-set function. This approach is in general not symmetric. In order to investigate the effect of this dependency on the ordering, we consider the four-layer sphere scenario and background meshes of different resolutions. For each possible ordering of the level-set functions we compute the relative error of the volumes of the different tissue compartments and the area of the different sphere surfaces. Figure 4.8 shows the relative error of the volumes and surfaces for the different orderings of the level-set functions. In addition, Table 4.1

shows statistical properties corresponding to the boxplots in Figure 4.8. We observe a decrease of all statistical measures, i.e., the IQR, the TR as well as the maximum for both volumes and surfaces of approximately second order. The highest measures are observed at the coarsest resolution of 16 mm. Starting from a resolution of 8 mm, the maximal relative error of both the volumes and the surfaces is below 1 %. Note that 1 mm results are omitted as no element is cut by more than one level-set function and thus the ordering in which the level-set functions are cut has no influence on the resulting error.

Discussion   We first note that the results presented here replicate the convergence results presented in (Engwer and Nüßing, 2017). In (Engwer and Nüßing, 2017) the convergence of the volume and surface errors for two entangled tori when increasing the mesh resolution has been investigated. For both, the volume and surface error a second order convergence has been reported as could be expected for a first order method. The results for the volume and surface errors in the four-layer sphere validation replicate this finding.

In this study it was observed that the surface error of the nested spheres was not reduced when using the hexahedral mesh. This is due to the constant area of the model surface under refinement of the mesh, which is due to the staircase-like representations of the surfaces. During refinement steps the overall surfaces representation is still staircase-like and not improved. When considering the level-set ordering, we can see a strong decrease of the effect of the ordering for increasing mesh resolutions. At the practically relevant resolution of 2 mm the total range of both volume and surface errors is below 0.04 %. In addition, the maximal volume and surface error does not exceed a value of 0.04 %. We conclude that the difference due to the level-set ordering is negligible for finer resolutions of the level-set mesh.

An additional validation which especially considers the robustness of the presented marching cubes method with respect to rotation of the model geometry and the preservation of the topological guarantees is presented in (Engwer and Nüßing, 2017). The validation compared the presented topology preserving marching cubes method with the original marching cubes method which selects an arbitrary reconstruction in an ambiguous case. It could be demonstrated that the new method is robust with respect to the rotation of the two tori and could achieve a subvoxel resolution of the correct topology.

4.2 Algebraic Multigrid Preconditioner for Cut-Cell Methods

In this section we present an evaluation of AMG techniques for solving linear systems arising from cut-cell discretizations of the EEG forward problem. We describe a general AMG method that is used for CutFEM discretization as well as modifications for a UDG method. The description is followed by a validation of the two approaches in a four-layer sphere model.

AMG for CutFEM   When using certain iterative procedures, such as the Gauss-Seidel method or the Jacobi-method, one can observe a smoothing effect of the error in each iteration. When separating the error into components of different spatial frequencies, components with a higher frequency are quickly reduced while the reduction of components with a lower frequency takes more iterations. This observation forms the basis of the geometric multigrid methods which employ a nested grid

```
void multigrid(l, ν₀, ν₁, γ) {
  if (l == 0) {
    xₗ ← Aₗ⁻¹bₗ // coarse solution
  } else {
    for (i=0; i<ν₀; ++i) { // pre smoothing
      xₗ ← xₗ + Sₗ(bₗ − Aₗxₗ)
    }
    bₗ₋₁ ← Rₗ(bₗ − Aₗxₗ)
    xₗ₋₁ ← 0
    for (i=0; i<γ; ++i) { // recursive call
      multigrid(l-1, ν₀, ν₁, γ)
    }
    xₗ ← xₗ + Pₗxₗ₋₁
    for (i=0; i<ν₁; ++i) { // post smoothing
      xₗ ← xₗ + Sₗ(bₗ − Aₗxₗ)
    }
  }
}
```

Listing 4.1: Pseudocode of general multigrid method on level l with ν_0 pre- and ν_1 post-smoothing steps, γ recursive calls and an exact solution on the coarsest level.

hierarchy with increasingly coarser resolutions. After performing a few iterations with a smoothing algorithm on the finest level the defect is transported to the next coarser level. Error components with a lower spatial frequency on the fine level show a higher frequency on the coarser level and can thus be efficiently reduced using a smoothing method. The transport to a coarser level is repeated recursively, until the coarsest level has been reached, where the remaining system is solved exactly. Additional smoothing steps are performed after updating the solution with the correction obtained by the recursive call. A pseudocode description of the general algorithm of a multigrid method is shown in Listing 4.1. A common property of multigrid techniques is the optimal convergence, which means that the convergence rate is independent on the sizes of the finest level. A challenge for the practical use of geometric multigrid methods is the construction of a grid hierarchy. Especially when starting with an unstructured mesh, the coarsening procedure is not straightforward. To circumvent this problem AMG has been introduced. Instead of constructing the coarser levels using the geometric information of the mesh, algebraic information of the linear system is taken into account, while the remaining general algorithm remains the same. The AMG has been shown to perform well as a preconditioner in a Krylow space solver, such as the conjugate gradient method.

In (Lew et al., 2009; Wolters et al., 2002) an AMG is presented and evaluated for solving the linear system obtained from a conforming finite element method for the EEG forward problem. The method is based on work of (Ruge and Stüben, 1987) and constructs coarser mesh levels by selecting certain subsets of the degrees of freedom to be transferred to the coarser level. A different approach of constructing the coarser levels is used by the AMG presented in (Blatt, 2010). Groups of degrees of freedom are aggregated to form the coarse degrees of freedom. A special algorithm is presented to construct the aggregates which is tailored to elliptic problems with highly discontinuous coefficients and allows for an aggressive coarsening strategy. The aggregates are built based on the connection strength between different degrees of freedom which is measured

by properties of the corresponding matrix entries. Given a scalar matrix $A = (a_{ij})_{i,j} \in \mathbb{R}^{n \times n}$, the weight $w_v(i)$ of a matrix entry $i \in \{0, \ldots, n-1\}$ and the weight $w_v(i,j)$ of a coupling between entries $i, j \in \{0, \ldots, n-1\}$ are defined as

$$w_v(i) = a_{ii}, \quad w_e(i,j) = \min(a_{ij}, 0).$$

Using these weights the strength of a connection between two matrix entries is measured as

$$s(i,j) = \frac{w_e(i,j)w_e(j,i)}{w_v(i)w_v(j)}.$$

A connection between two entries i and j is called strong if $s(i,j) > \alpha \min(\max_k(s(i,k)), \max_k(s(j,k)))$ holds. This definition of strong connections is used to construct the aggregates that define the coarsening between the different levels (see (Blatt, 2010) for a detailed description of the aggregation process). The resulting AMG method can be applied for symmetric and unsymmetric problems. For the model problem of a three-dimensional Poisson's equation an efficient multigrid scheme was observed with slightly suboptimal convergence rates that depended logarithmically on the number of degrees of freedom. According to (Burman et al., 2015) using the ghost penalty parameter within the CutFEM method enables the use of linear algebra techniques for the discrete linear system. Below, we will employ and evaluate the described aggregation-based AMG for a CutFEM discretization.

AMG for UDG   The idea of the AMG method using aggregation presented above has been applied to discontinuous Galerkin discretizations in (Bastian et al., 2012; Blatt, 2010). Its description follows the framework of subspace correction methods for a fine and a coarse space (Xu, 1992). The fine space is given as the space of piecewise linear, (possibly) discontinuous function $V_h^{\mathrm{DG}}(\Omega)$. The coarse space is defined as the space of piecewise linear, continuous functions and denoted by $V_h^{\mathrm{CG}}(\Omega)$. It holds that $V_h^{\mathrm{CG}}(\Omega) \subset V_h^{\mathrm{DG}}(\Omega)$ and thus an implicit discrete prolongation operator $P : V_h^{\mathrm{CG}} \to V_h^{\mathrm{DG}}$ can be defined. In order to obtain a symmetric method, the restriction operator is chosen as the transpose of the prolongation operator. It is assumed, that the error components introduced by the discontinuities have a high frequency and can be reduced efficiently using a smoother on the fine level. The remaining low frequency components and components of the continuous subspace can be treated by a transfer to the coarse space. On the coarse level the AMG method presented above is used as an inexact solver.

In the following we use a similar idea to create a multigrid perconditioner for a UDG discretization. Instead of restricting the defect to a piecewise linear, globally conforming space, we restrict the defect to the space of functions that are piecewise linear and continuous on each subdomain. Note that this space is a subspace of the function space used for the UDG discretization. In addition, this subspace is the same space as the one used for the CutFEM discretization. After transferring the defect to the coarse space, we again use the AMG method as an inexact solver. On the fine level we use a block symmetric successive overrelaxation (SSOR) method on the cut-cell blocks as a smoother.

Compared to the AMG for CutFEM no ghost penalty is applied to the coarse space, which might lead to suboptimal convergence properties for small cut-cells in the interface zone. To resolve
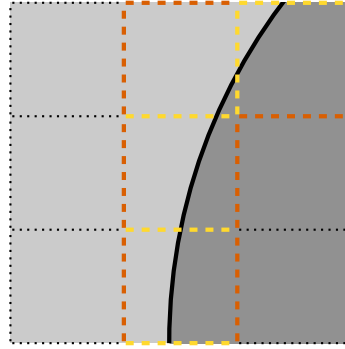
Figure 4.9: Visualization of the overlapping smoother for a UDG discretization with two domains, shaded in light gray and dark gray, separated by a single interface, depicted by the solid black line. The red lines delimit the area of the overlapping patches. Each yellow line marks a cut fundamental mesh intersection which forms an overlapping patch of all cut-cells of any domain belonging to the fundamental mesh elements touching the intersection.

this problem, we take ideas from (Engwer et al., 2016; Johannsen, 2006; Nüßing, 2013) into account where an overlapping Schwarz method was used as a smoother for a discontinuous Galerkin discretization. The overlapping subdomains were constructed around the vertices of a geometry-conforming mesh. Using this idea, we construct overlapping patches to smooth over contributions from small cut-cells. For each intersection of the fundamental mesh that is cut by an interface we create a subdomain consisting of all cut-cells belonging to either of both neighboring elements. Each remaining cut-cell, that does not touch an intersection of the fundamental mesh that is cut by an interface, forms its own subdomain. Figure 4.9 shows a visualization of the overlapping patches. The resulting set of subdomains forms the basis of an overlapping Schwarz method which we use in a multiplicative approach. In order to obtain a symmetric preconditioner each smoothing step consist of applying the overlapping smoother forward and backward.

Instead of choosing the CutFEM space as a coarse space we could also choose a cell-centered finite volume space. Results in (Blatt, 2010) show a good performance of the AMG method for such discretizations. The restriction operator R is defined by restricting a function to its mean over each cut-cell. For a function $u(x) = \sum_k u_k \varphi_k(x)$ this can be formulated as

$$U_i = \frac{1}{|E_i|} \int_{E_i} u(x)\, \mathrm{d}x = \sum_k u_k \underbrace{\frac{1}{|E_i|} \int_{E_i} \varphi_k(x)\, \mathrm{d}x}_{=:r_{i,k}},$$

where E_i denotes a cut-cell and $U_i \in \mathbb{R}$ denotes the new degree of freedom. However this restriction approach has not been investigated in detail so far.

4.2.1 Validation Studies

In this section we investigate the convergence behavior and the robustness with respect to the cut-cell size of the multigrid algorithms for a CutFEM discretization and a UDG discretization.
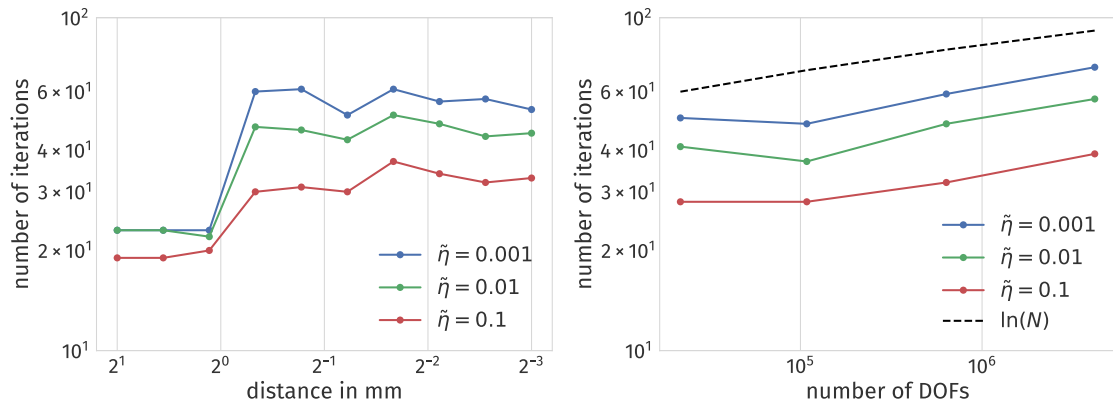
Figure 4.10: Convergence of the multigrid solver for CutFEM discretizations with a shifted innermost sphere. Left: fixed resolution of 2 mm and shifting innermost sphere center. The x-axis shows the minimal distance between the innermost sphere and the next sphere. The y-axis shows the number of iterations until a relative reduction of the residuum of 10^{-8}. Both axes are scaled logarithmically. Each plot corresponds to a different ghost penalty. Right: Varying resolution and fixed distance of 0.25 mm. The x-axis shows the number of degrees of freedom. The y-axis shows the number of iterations until the residuum has been reduced. Each plot corresponds to a different ghost penalty. Both axis are scaled logarithmically.

AMG for CutFEM   First we investigate the behavior of the AMG method for a CutFEM discretization for solving the EEG forward problem in a four-layer sphere model. We create level-set functions for four spheres with radii and conductivity values depicted in Table A.1. In order to investigate the effect of varying cut-cell sizes, we move the center of the innermost sphere in positive x-direction. This corresponds to the scenario where the gray matter compartment touches the inner skull boundary which occurs for example when creating MRI images in reclined positions (Rice et al., 2013). The discrete values of the minimal distances between the inner two spheres range from 2 mm (i.e., no shift) to approximately 0.125 mm. Even though the cut-cells delimited by the two inner spheres become smaller for lower distances also discretizations at larger distances can contain small cut-cells depending on how the inner sphere cuts the elements of the fundamental mesh. The multigrid method is used as a preconditioner in a conjugate gradient method (AMG-CG). The iteration of the linear solver is stopped at a relative reduction of the l_2 norm of the residuum of 10^{-8}. We fix a penalty parameter of $\eta = 16$ and evaluate two different scenarios for different ghost penalty values $\tilde{\eta} \in \{0.001, 0.01, 0.1\}$. For the first scenario we use a fixed resolution of 2 mm and evaluate the effect of the distance between the inner two spheres. For the second scenario we fix the distance between the two spheres at 0.25 mm and choose the fundamental mesh resolutions of 8 mm, 4 mm, 2 mm and 1 mm. The different CutFEM discretization consist of 21 825, 108 352, 635 581 and 4 173 085 degrees of freedom.

Figure 4.10 shows the number of iterations until convergence with respect to varying distance between the spheres and with respect to increasing fundamental mesh resolution. We see a decreasing number of iterations with increasing ghost penalty. The number of iterations for distances smaller than 1 mm is increased for all ghost penalty values. The strength of this increase is reduced for higher ghost penalties. With respect to the convergence plot, we observe an approximately loga-

rithmic dependency on the number of DOFs. Again we observe a reduced number of iterations with increasing ghost penalty.

The observed convergence order with respect to an increasing mesh resolution are in line with findings in (Blatt, 2010), where a suboptimal convergence rate for three-dimensional problems was observed. Even though the number of iterations increases, it only grows logarithmically and is still in a feasible range for all practical applications considered in this thesis. As presented in (Burman and Hansbo, 2012) the condition number of the linear system is reduced when increasing the ghost penalty. Since the convergence rate of the conjugate gradient method depends on the condition number of the preconditioned linear system, an increased ghost penalty leads to a lower number of iterations. For a higher ghost penalty value, the number of iterations is almost independent of the distance of the two innermost spheres. One might conclude to increase the ghost penalty value even further. However, results in (Burman and Hansbo, 2012) show an increase in the numerical error when choosing a ghost penalty value that is too large. For the validation studies in Section 3.4 we chose a value of $\tilde{\eta} = 0.005$, that led to a reasonable number of iterations while providing accurate error values. We did not investigate the effect of the smoother on the convergence properties. As the CutFEM discretization contains discontinuities on the interfaces between two subdomains, it might be beneficial to use an overlapping smoother in the interface zone on the finest level (cf. (Johannsen, 2006)). In addition, the coarsening strategy was not modified and the default values from (Blatt, 2010) where used. A tailored strategy which takes properties of the CutFEM discretization into account might be worthwhile.

AMG for UDG   For the validation of the AMG method of UDG, we use the same problem setup that was used in the previous validation study for the AMG for CutFEM. For the first study we move the center of the inntermost sphere in positive x-direction and for the second study, we increase the mesh resolution. The UDG discretizations consist of 20 608, 108 352, 635 840 and 4 170 432 DOFs for the mesh resolutions of 16 mm, 8 mm, 4 mm and 2 mm, respectively. Note that we do not use a ghost penalty within the UDG discretization. Instead, we evaluate the performance of two different smoothing methods on the UDG space, which forms the finest level of the multigrid method. The two smoothers are the block SSOR method and the symmetric multiplicative overlapping Schwarz method described above. Again, the multigrid method is used as a preconditioner in a conjugate gradient method and the iteration process is stopped at a relative reduction of the l_2-norm of the residuum of 10^{-8}.

Figure 4.11 shows the number of iterations until convergence with respect to varying distance between the spheres and with respect to increasing fundamental mesh resolution. For varying distance between the innermost sphere, we observe an increase of iterations for the SSOR smoother for distances lower than 1 mm. The number of iterations for the overlapping smoother is almost independent on the distance between the spheres. Considering the convergence with respect to h, the SSOR smoother does not lead to a stable convergence scheme. The number of iterations is strongly increased for the resolution of 8 mm. For the overlapping smoother, the number of iterations increases with increasing mesh resolution and we observe an approximately logarithmic dependency on the number of DOFs.

Comparing the results of the AMG for the UDG method to the results obtained for the CutFEM methods, we see a similar behavior with respect to the size of the cut-cells for the SSOR smoother
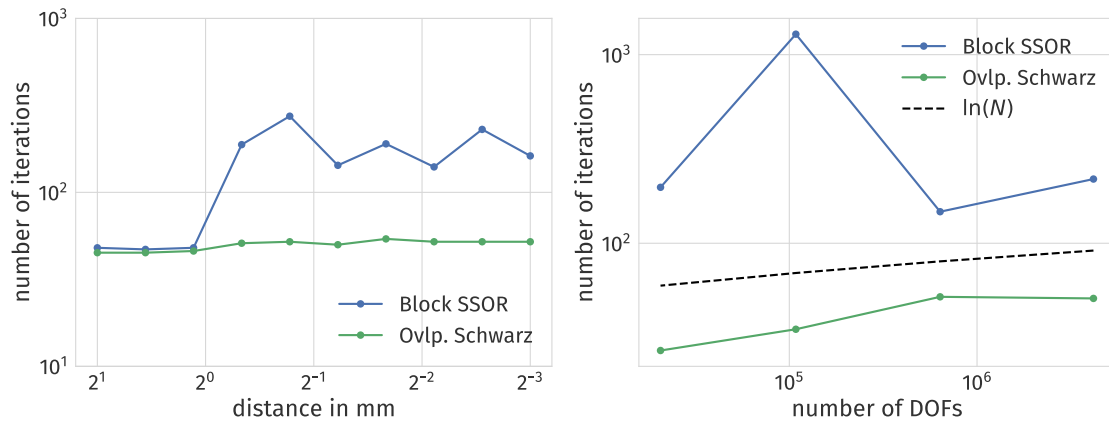
Figure 4.11: Convergence of the multigrid solver for UDG discretizations with a shifted innermost sphere. Left: fixed resolution of 2 mm and shifting innermost sphere center. The x-axis shows the minimal distance between the innermost sphere and the next sphere. The y-axis shows the number of iterations until a relative reduction of the residuum of 10^{-8}. Both axes are scaled logarithmically. Each plot corresponds to a different smoother method. Right: Varying resolution and fixed distance of 0.25 mm. The x-axis shows the number of degrees of freedom. The y-axis shows the number of iterations until the residuum has been reduced. Each plot corresponds to a different smoother method. Both axis are scaled logarithmically.

and the lower ghost penalty values. Both approaches show an increase of the number of iterations for distances smaller than 1 mm. The overlapping smoother strongly reduces this dependency on the size of the cut-cells. The suboptimal convergence rates for the overlapping smoother can be assumed to be due to the suboptimal rates of AMG method for CutFEM on the coarse level. It might be worthwile to investigate a combination of the overlapping smoother on the fine level and the use of a ghost penalty (cf. (Gürkan and Massing, 2018)). This might combine the robustness of the overlapping smoother with a reduction of the condition number of the linear system on the coarse space.

4.3 Conclusion

In this chapter we focused on two different implementational aspects of cut-cell methods.

In Section 4.1 we presented a topology preserving marching cubes method which can be used to generate quadrature rules for implicitly defined domains. We introduced the general method and performed an evaluation with respect to the multi-domain setting of solving the EEG forward problem. As the model geometry is approximated by a piecewise linear reconstruction, second order convergence of the volume and surface errors was observed. To apply the method in a multi-domain setting the algorithm was applied recursively on the various level-set functions. We showed that the ordering of the level-set functions has a negligible effect for higher mesh resolutions.

In Section 4.2 we introduced algebraic multigrid techniques for solving the linear system resulting from a cut-cell discretization of the EEG forward problem. For the CutFEM approach we investigated the use of a multigrid preconditioner based on an agglomeration strategy. It showed a slightly sub-optimal convergence which is in line with results from the literature for conforming discretizations.

The robustness with respect to the cut-cell sizes could be improved by increasing the value of the ghost penalty parameter. For the UDG method we used the algebraic multigrid method as a coarse grid solver for the subspace of piecewise linear functions that are continuous on each subdomain. We investigated the effect of the coarse grid smoother and observed an increasing robustness when using an overlapping smoothing approach.

duneuro – A Software Toolbox
for Forward Modeling in Neuroscience

In this chapter, we present *duneuro*, a software toolbox for forward modeling in neuroscience. Its main focus is to provide an extendible and easy-to-use framework for using various finite element methods for different neuroscientific applications, such as the EEG or MEG forward problem. We first give a general description of the toolbox and its use of existing frameworks for solving partial differential equations. In Section 5.1 we introduce the main concepts of different interfaces used within the library. Section 5.2 describes a method for localizing elements within a tessellation based on a global coordinate. The interaction of a user with duneuro is done through bindings with a scripting language, which will be presented in Section 5.3. In Section 5.4, we use the duneuro toolbox to perform source analysis on EEG data obtained from a somatosensory experiment. Finally, a short conclusion is given in Section 5.5.

The general view on a software toolbox can be split into two parts: the user perspective and the developer perspective. From the perspective of a user, the toolbox should be accessible and easy to use. Similar methods should work in a similar way though a common interface and it should be possible to quickly exchange the forward modeling approach. For example performing computations using the discontinuous Galerkin method should be as straightforward as using the conforming finite element method. The user should not be confronted with the high complexity of a C++ finite element code. Additionally, it should be possible to embed the forward approach into an already existing processing pipeline. From the point of view of a developer, who wants to implement different forward approaches or extend already existing approaches, further aspects are important. As the different finite element methods share several subcomponents, such as the representation of the computational domain or the solver of the linear system, the toolbox should bundle the different implementations and enable code reuse. The toolbox should be extendible, especially with respect to common variable components, such as the forward discretization scheme or the representation of the source model. In addition, as there are already several libraries offering codes for finite

element computations, it would be advantageous to make use of existing components and benefit from existing maintenance and testing infrastructure.

One such existing library is the *distributed and unified numerics environment (Dune)*[1], which is a general purpose open-source C++ library for solving partial differential equations using mesh-based methods. It is extendible by offering a modular structure and providing abstract interfaces and separation between data structures and algorithms. Due to the modular structure, a user of Dune only has to use those modules that are needed. At the core of the Dune library is an abstract definition of a grid interface (Bastian et al., 2008a,b). Using the abstract interface allows writing reusable code that is independent of the concrete implementation of the grid or the type of the grids elements. Then the identical code can be used in multiple spatial dimensions and for tetrahedral or hexahedral or other element types.

The duneuro library makes use of several existing Dune modules. For representing geometry-conforming tetrahedral and hexahedral meshes, we use the grid implementations provided by the dune-alugrid module (Alkämper et al., 2016) and the dune-uggrid module (Bastian et al., 1997). In order to reduce the memory consumption and to simplify the user-code when using a geometry-adapted hexahedral mesh, we use the dune-subgrid module to extract parts of a mesh that is given as a segmented voxel image (Gräser and Sander, 2009). The discretization of the partial differential equation makes use of the dune-pdelab module (Bastian et al., 2010). In dune-pdelab, many different discretization schemes along with appropriate finite elements are implemented allowing a rapid prototyping of new models. It offers abstractions for the concept of a function space on a grid or for the linear operator used in the discretization. The implementation of the unfitted discontinuous Galerkin method is provided in the dune-udg module (Engwer and Heimann, 2012). This module has been extended to support also the CutFEM method presented in Section 3.1. The topology preserving marching cubes method described in Section 4.1 is implemented in a C++ library tpmc[2]. Within the Dune context, the tpmc library is wrapped within its own Dune module. For the solution of the linear system, we make use of the *iterative solver template library (ISTL)* offered by the dune-istl module (Blatt and Bastian, 2006).

5.1 Library Interfaces

In this section we present in detail several subcomponents and interfaces of the duneuro toolbox and give information on the extendibility of each component. We describe the driver interface, the discretization of the forward model and the EEG source model and provide information about the MEG implementation.

The EEG-MEG Driver Interface   As seen in the chapters of this thesis, there are several different discretization schemes available for solving the EEG forward problem and each scheme provides different source models. The finite element methods presented here can be split into two different categories: the *fitted* and *unfitted* discretization methods. The fitted category refers to a discretization method that uses a grid whose geometry is fitted to the model geometry. The basis of this approach is a `VolumeConductor` class, that stores the grid along with the conductivity tensor of

---

[1]http://www.dune-project.org
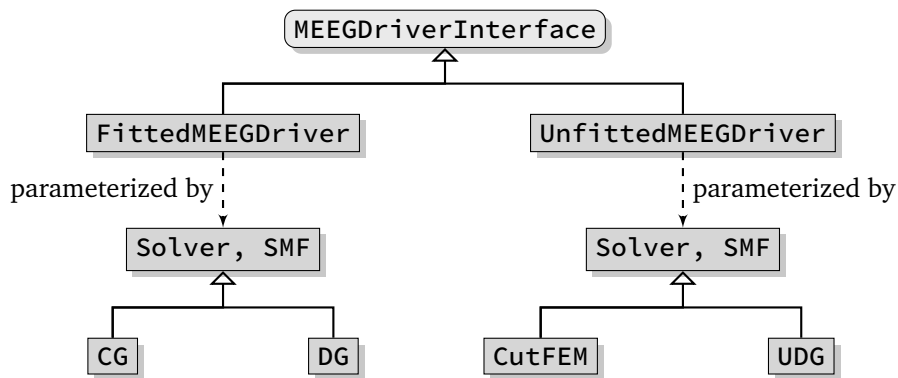[2]http://github.com/tpmc

Figure 5.1: Diagram showing the structure of the driver interface and its implementations.

each grid element. Currently, there are two different fitted discretization schemes implemented in duneuro: the conforming Galerkin (CG-FEM) and the discontinuous Galerkin (DG-FEM) finite element methods. Methods that fall into this category but are not yet available are mixed finite element methods (cf. Section 1.4) or finite volume schemes. The unfitted category refers to a discretization method that uses a grid which is independent of the model geometry and employs the model geometry weakly. The model geometry is provided implicitly via level-set functions and considered in the weak formulation. The currently implemented discretization schemes in the unfitted category are: the CutFEM method and the unfitted discontinuous Galerkin method (cf. Chapter 3). From the user perspective of a software framework, it should be simple and intuitive to change from a fitted to an unfitted discretization or between different discretization schemes within each category. For example switching from CG-FEM to DG-FEM should not require fundamental changes in the user code. A further consideration when designing the interface of the software is the way the user will interact with it. As described in more detail below, we want to provide bindings to languages a potential user is already familiar with, such as Python or Matlab (see Section 5.3). In order to simplify both, the overall user interface as well as the process of creating such bindings, we define a single coarse grained interface class to interact with the internal toolbox. This interface class is called the `MEEGDriverInterface`. It describes the general concepts of solving EEG and MEG forward problems. Each of the two discretization categories is implemented by its own driver class, the `FittedMEEGDriver` and the `UnfittedMEEGDriver` respectively. Figure 5.1 shows a general diagram of the `MEEGDriverInterface`. For each category, the implementation of the discretization scheme is provided via two template parameters: a `Solver` and a `SourceModelFactory`. The purpose of the solver class is to bundle the handling of the system matrix and the solution of the resulting linear system. The source model factory will construct source models whose purpose is the assembly of the right-hand side. Both, the solver and the source model factory, are further described below. The user of the toolbox will not directly interact with the implementation of the drivers, but only with the driver interface class.

The Solver and the Source-Model-Factory   The purpose of the solver class is the assembly of the system matrix and the solution of the linear system. It contains the discretization scheme as well as the necessary functionspaces for representing discrete functions. The main interface method is a `solve` method which, given a right-hand side vector, solves Poisson's equation and returns the

discrete solution. Several forward problems in bioelectromagnetism, e.g., the EEG forward problem, electric or magnetic stimulation or the computation of a transfer matrix, mainly differ with respect to the right-hand side of the linear system. The solver class can thus be reused for any such purpose. By using a single solver class, the system matrix has to be assembled only once and can be reused for further purposes. As the different discretization schemes differ in the way the matrix is stored, e.g., with respect to the blocking scheme of the matrix entries, this information is hidden from the interface. The purpose of the source model factory is to construct the different source models dynamically based on a configuration provided by the user. All source models provide a common interface which is described below.

We will illustrate the extendibility with respect to the discretization scheme using the example of a mixed finite element method (MixedFEM, cf. Section 1.4). MixedFEM is based on a first order representation of Poisson's equation and employs unknowns for both, the potential and the electric field. It derives a weak formulation and uses scalar and vector-valued finite elements on a geometry conforming grid as a discretization. It thus falls into the category of fitted discretization schemes. In order to use the described `FittedMEEGDriver`, one needs to provide two components: a `MixedFEMSolver` and a `MixedFEMSourceModelFactory`. The `MixedFEMSolver` contains the discretization of the Stiffness matrix as well as the definition to solve the resulting linear system. The implementation of such a solver class is heavily based on the `dune-pdelab` module, which contains for example the implementations of the local basis functions. The `MixedFEMSourceModelFactory` offers a method to create different source models for the MixedFEM approach, whose purpose is then to assemble the right-hand side vector for a given source position. In (Vorwerk et al., 2017), two different source models have been presented: a *direct approach* and a *projected approach*. Finally, one has to provide means to evaluate a discrete solution at electrode positions along with the resulting right-hand side of the transfer matrix approach. Once these components are implemented, the features of the driver, e.g., computing a transfer matrix or solving the EEG forward problem, are available.

Source Models   For each discretization method, there are several different source models that are used to discretize the mathematical point dipole. The common task of these source models can be stated as: given a dipole position and a dipole moment, assemble the right-hand side vector. This right-hand side vector will then be passed on to the respective solver class described above. As there is still research ongoing and new source models are being developed, it should be easy to provide an additional source model without having to modify the existing code. In addition, it should be possible to choose the source model at runtime, both for investigating the effects of different source models as well as ruling out the source model as a source of errors. Some source models, such as the subtraction approach or its localization, do not provide a right-hand side for the full potential, but need to apply an additional post-processing step to the resulting solution in order to obtain the full potential. For the subtraction approaches, this post-processing step consists of adding the singularity potential to the correction potential. As this post processing step depends on the type of the source model and the user should have the option to turn off the post-processing, it is provided as a method of the source model interface. Figure 5.2 shows a diagram of the general `SourceModelInterface` along with its implementations.

A main advantage of the direct source models such as the partial integration approach or the
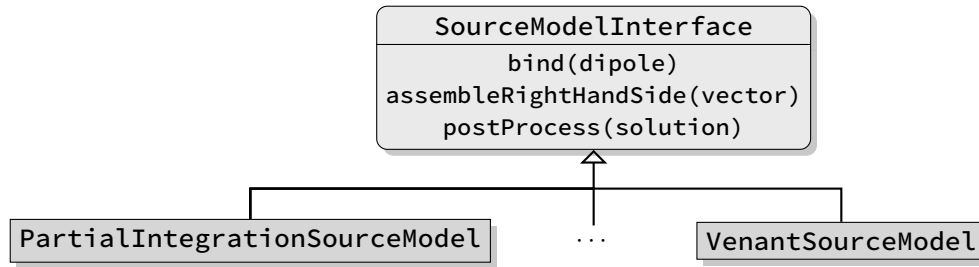
Figure 5.2: The structure of the source model interface and its implementations.

Venant approaches, is the sparsity of the right-hand side. When stored inside a sparse vector container, the time for applying the transfer matrix, i.e., multiplying the right-hand side with the transfer matrix, can be reduced. The complexity is $\mathcal{O}(N)$, where N denotes the number of mesh elements. The constant is proportional to the number of non-zero entries of the right-hand side. The latter is usually independent of the mesh resolution. For indirect source models such as the subtraction approach, using the same data type as for the sparse source models would introduce an additional overhead. Thus, in order to be able to handle dense and sparse vector types for the right-hand side, the vector type is provided as a template parameter of the source model interface.

We will illustrate the extendibility with respect to the source models on the example of a modified subtraction approach for CG-FEM. In Section 2.3 a modification of the subtraction approach has been presented: the *localized subtraction approach*. It restricts the contribution of the singularity part of the potential to a patch around the source location. As the functions within a DG-FEM discretization can be discontinuous, they can directly capture the jump occurring at the boundary of the patch. For a CG-FEM discretization, such jumps can not be directly resolved and thus the localization scheme has to be modified. Instead of using a restriction of the singularity contribution to patch, one can multiply the singularity contribution with a function that linearly interpolates within an interface zone of the patch between the singularity potential and zero. A source model implementing this localized subtraction approach would provide a class fulfilling the source model interface. Within the `bind` method, the local patch would be created and the linear interpolation in the interface zone could be constructed. The implementation of the `assembleRightHandSide` method contains the integration of the different model terms, resulting in the right-hand side. The `postProcess` method adds the singularity potential to the correction potential on the local patch.

MEG   In addition to the EEG forward problem that was described extensively throughout this thesis, the toolbox described in this chapter provides methods to solve the MEG forward problem (Piastra et al., 2018). Given the electric potential u, the secondary magnetic field B at a position $y \in \mathbb{R}^d$, resulting from the volume current $\sigma \nabla u$, can be expressed using the law of Biot-Savart (Hämäläinen et al., 1993):

$$B(y) = \frac{\mu_0}{4\pi} \int_\Omega \sigma \nabla u \times \frac{y-x}{\|y-x\|^3} \, \mathrm{d}x \, ,$$

where $\times$ denotes the three-dimensional cross product. For CG-FEM this integral can be directly evaluated using the discrete representation of the potential u_h (see ,e.g., (Vorwerk, 2016)). Results for the MEG approach for DG-FEM in (Piastra et al., 2018) indicate, that a direct usage of $\sigma \nabla u_h$

leads to suboptimal accuracies. Instead, the numerical flux of the discontinuous Galerkin method should be used, which is defined as

$$\{\sigma \nabla u_h\} - \frac{\eta}{h} [\![u_h]\!] \,.$$

In order to provide a single implementation for the integration using both flux representations, we split the MEG forward solution into two parts: the projection of the flux into a vector valued functionspace W_h and the evaluation of the integral functional for functions in W_h. In (Piastra et al., 2018), a lowest order Raviart-Thomas space was used for representing the continuous numerical flux, while a space representing gradients of piecewise multi-linear functions has been employed to represent the physical flux. The discrete potential u_h is given as

$$u_h(x) = \sum \alpha_i \phi_i(x)$$

and the discrete representation of the flux is given as

$$\sigma \nabla u_h(x) \approx \sum \beta_j \psi_j(x).$$

Using this discrete representation of the flux, the MEG integral for a fixed sensor position $y \in \mathbb{R}^d$ can be evaluated by computing

$$\text{MEG}(u) = \sum \beta_j \frac{\mu_0}{4\pi} \int_\Omega \psi_j \times \frac{y-x}{\|y-x\|^3} \, \mathrm{d}x =: \langle S(y), \beta \rangle \,.$$

The computation of the coefficients for the flux based on the coefficients of the discrete potential can be expressed as a linear operator

$$\beta = P\alpha$$

The exact definition of this linear operator depends on the interpolation scheme in the vector valued function space. Combining the projection and the integral evaluation, the MEG solution can be obtained from a discrete EEG solution by computing

$$\text{MEG}(u) = \langle P^t S(y), \alpha \rangle \,.$$

Using this representation, a transfer matrix approach for MEG can be defined following the description in Section 1.2, where $P^t S(y)$ takes the role of the restriction operator. The MEG forward solution is available for any source model. However, note that when using the subtraction approach or the localized subtraction approach, the resulting MEG solution does not include the contributions of the singularity potential.

5.2 Element Localization

A common subtask when assembling the right-hand side for a given dipole is the localization of the mesh element containing the dipole. For a sparse source model, this is especially relevant, as the

time of assembling the right-hand side is usually constant, once the dipole element has been found. The complexity of the right-hand side assembly thus strongly depends on the complexity of the method that is used for finding the dipole element. The most straight forward approach is given by a linear search among the mesh elements. Assuming an ordering of the mesh elements, we evaluate for each element of the mesh if it contains the dipole position. Once the result of the evaluation is positive, we return this element. This algorithm has an average and worst case complexity of $\mathcal{O}(N)$, where N denotes the number of mesh elements.

A first step to speed up the localization can be found by using geometric information when iterating the mesh elements instead of using a fixed ordering (Brown and Faigle, 1997). The method presented here is called *edge hopping*:

1. Start at given mesh element and iterate over all faces of the current element.

2. Compute the relative position of the dipole location and the hyperplane induced by the face center and its outer normal.

3. If the dipole lies in normal direction, continue the search at step 1 with the neighboring element if such an element exists.

4. If the face has no neighboring element, the dipole lies outside of the mesh or the mesh is not convex. Terminate the search.

5. If the dipole lies in the opposite direction, continue at step 2 with the evaluation of the next face.

6. If the dipole lies on the inside of all faces of the current element, the dipole element has been found.

A requirement of the edge-hopping method is the convexity of the mesh, that is usually only fulfilled by the multi-layer sphere models, and not by the realistically shaped head models. However, as the algorithm monotonously moves closer to the dipole element, we only need convexity of the mesh in a sphere around the dipole location and the starting point of the iteration. As the considered sources lie in the gray matter compartment, that is completely enclosed by the skin, we can easily find such a sphere around the source locations if the starting location is close to the source position. In order to find an element that is close to the source location, we insert the element centers into a *k-d Tree*, that is a datastructure to efficiently perform nearest neighbor searches (Bentley, 1975). It does so by recursively splitting the set of element centers along the Cartesian directions. Even though, the center of the element which is closest to the dipole location does not have to belong to the element containing the dipole, it can be assumed to be close to the desired element. It thus offers an efficient starting point for the edge-hopping algorithm.

5.3 Interface to Scripting Languages

In this section we describe the interaction of a user with the duneuro library. A common approach is to provide a compiled binary executable that the user is able to call directly. This executable would then load the data provided by the user from the hard disk, perform the desired computation and

```python
import duneuropy as dp
config = {
  'type' : 'fitted',
  'solver_type' : 'cg',
  'element_type' : 'tetrahedron',
  'volume_conductor : {
    'grid.filename' : 'path/to/grid.msh',
    'tensors.filename' : 'path/to/tensors.dat'
  }
}
driver = dp.MEEGDriver3d(config)
```

Listing 5.1: Example Python script for creating an `MEEGDriver`.

write the computed result back to the hard disk. As different users might want to perform different sets of computations, the computations to be performed can be configured by the user, either through command line parameters or through a configuration file. An advantage of this approach is its very simple and straight forward usage, similar to any other executable on the operating system. There is no need for additional packages or additional software and the executable can be used directly by the user. However, the computation of the solution to the forward problems is usually only a small part in a longer pipeline for source analysis. This pipeline usually consists of the data measurements and pre-processing steps and the forward solution is part of an inverse estimation process. When using the library directly in an executable, one has to provide methods for reading any input data as well as writing out the resulting output. Similarly, the configuration has to be transferred to the executable by the user.

A more convenient way to use the provided library can be found by offering bindings to a scripting language such as Matlab[3] or Python[4]. For both languages there are already existing software frameworks for processing EEG and MEG data (Gramfort et al., 2013; Oostenveld et al., 2011; Tadel et al., 2011). Thus by providing direct bindings one can include the forward modeling approach directly into an existing analysis pipeline. An example for such an integration is presented in (Vorwerk et al., 2018), where the authors introduce a pipeline for performing source analysis using the conforming finite element method together with the classical Venant source model. The forward models are implemented using the SimBio software[5] and integrated into the Matlab-based FieldTrip-toolbox[6]. The Python and Matlab bindings for the duneuro module are provided in separate Dune modules: *duneuro-py* and *duneuro-matlab*, respectively. The purpose of both modules is to translate the input data given as data structures in the respective programming language and translate them into the C++ counterparts. For some cases, this translation can be performed without copying any data, which is especially relevant for large matrices such as the transfer matrix. An example of the driver construction in a Python script is shown in Listing 5.1. The configuration of the discretization is provided as a python dictionary and the mesh is loaded from a file. Alternatively, the mesh can also be provided directly by specifying the vertices, elements, labels and conductivity tensors. Note that the discretization method, in this case `cg`, is provided as a parameter in the configuration. By

---

[3]`https://www.mathworks.com`
[4]`https://www.python.org`
[5]`https://www.mrt.uni-jena.de/simbio`
[6]`http://www.fieldtriptoolbox.org`

```
cfg = [];
cfg.type = 'fitted';
cfg.solver_type = 'cg';
cfg.element_type = 'tetrahedron';
cfg.volume_conductor.grid.filename = 'path/to/grid.msh';
cfg.volume_conductor.tensors.filename = 'path/to/tensors.dat';
driver = duneuro_meeg(cfg);
```

Listing 5.2: Example Matlab script for creating an `MEEGDriver`.

changing it to `dg` and adding the necessary additional parameters such as the penalty penalty η, one can directly use the discontinuous Galerkin method through the same interface. Thus, once a user is able to use the duneuro library for any discretization method, a switch to a different discretization method can be directly performed. Listing 5.2 shows the same construction of the driver object as in Listing 5.1 using the Matlab interface. The general structure of the Matlab script is similar to the Python script. The main differences are the use of Matlab syntax and the replacement of the Python dictionary by a Matlab struct array. Even though the wrapper code for creating the driver object is different, both scripting languages interface the C++ library and use the same codebase.

5.4   Example: Source Analysis of Somatosensory Evoked Potentials

As a practical example we use the duneuro toolbox to perform a dipole scan on somatosensory evoked potentials using the CutFEM method presented in Section 3.1. A right-handed, 49 years old, male subject participated in an electric stimulation experiment of the right median nerve with simultaneous EEG recordings. The EEG was measured using 74 electrodes, whose positions where digitized using a Polhemus FASTTRAK device[7]. The subject was stimulated in supine position in order to reduce modeling errors due to brain movement (Rice et al., 2013). In total, 1200 stimuli were applied, each with a duration of 200 ms. The inter-stimulus interval was randomized in the range of 350 ms to 450 ms. Using CURRY8[8], the EEG data was preprocessed using a band-pass filter from 20 Hz to 250 Hz and notch-filters at 50 Hz and harmonics to reduce power-line noise. After removing one bad channel the remaining trials where averaged to produce the evoked potential data. Figure 5.3 shows a butterfly plot of the resulting time series of the averaged potentials as well as a topography plot of the potential measured at the electrodes at the peak of the P20 component at the time point of 25.8 ms.

Using a 3 T MRI scanner (Siemens Medical Solutions, Erlangen, Germany), T1-weighted and T2-weighted MRI sequences were measured. Based on these MRI images, a six-compartment voxel segmentation has been constructed, distinguishing between skin, skull compacta, skull spongiosa, csf, gray matter and white matter using SPM12[9] via Fieldtrip[10], FSL[11] and internal Matlab rou-

---

[7]https://polhemus.com
[8]http://www.neuroscan.com
[9]http://www.fil.ion.ucl.ac.uk/spm/software/spm12
[10]http://fieldtriptoolbox.org
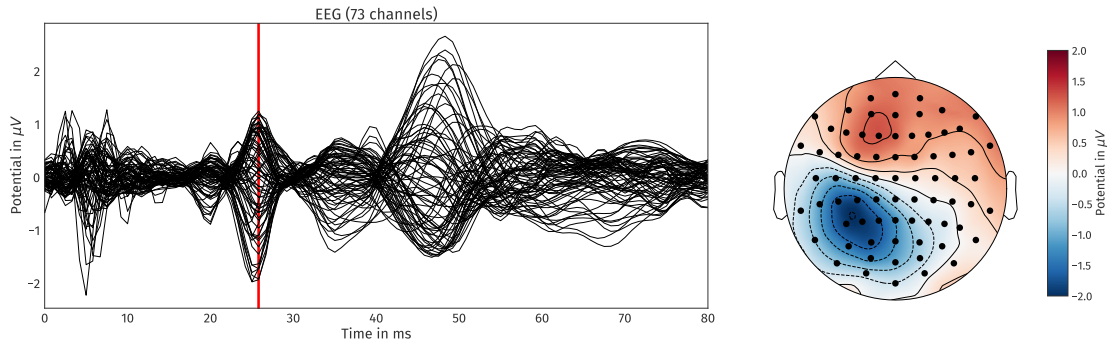[11]https://fsl.fmrib.ox.ac.uk/fsl

Figure 5.3: Left: Butterfly plot of the somatosensory evoked potentials. The vertical red line indicates the 25.8 ms time point. Right: topography plot of the averaged potential at the electrodes for $t = 25.8$ ms

tines. We extracted surfaces from this voxel segmentation to distinguish between the different tissue compartments. To smooth the surfaces while maintaining the available information from the voxel segmentation, we applied an anti aliasing algorithm created for binary voxel images presented in (Whitaker, 2000). The resulting smoothed surfaces are represented as level-set functions and the digitized electrodes were registered to the head surface. Especially in occipital and inferior regions, due to the lying position of the subject during MRI measurement, the gray matter compartment touches the inner skull surface. From Figure 5.3 we see a clear dipolar pattern in the topography plot. To estimate the location of the dipole, we performed a single dipole scan with fixed orientation and variable strength on a set of source locations within the gray matter compartment (Hämäläinen et al., 1993). The source space is created using a weighted sum of level-set functions for gray and white matter as $\alpha\Phi_{\text{wm}} + (1-\alpha)\Phi_{\text{gm}}$ with $\alpha = 0.8$. The resulting level-set function for the source space was discretized using the marching cubes algorithm presented in 4.1, which resulted in 269 417 source locations. For each location, we computed the dipole orientation normal to the surface of the source space. Note that there was no manual interaction or modification of the surfaces obtained by this process. Figure 5.4 shows the skin, skull and gray matter surfaces and the electrode positions as well as the source space that was used in the example computation.

Using the level-set functions, we constructed a CutFEM model and computed the EEG transfer matrix for all electrode positions. If the fundamental mesh element containing the electrode did not contain a cut-cell of the skin compartment, the electrode was shifted to the center of the next closest fundamental mesh element containing such a cut-cell. Using the transfer matrix, we computed the EEG forward solution for all dipole positions with the fixed orientation and unit strength using the monopolar Venant source model. The optimal strength s with respect to a given measurement m for a dipole with the leadfield l can be obtained by minimizing $\|ls - m\|_2$ over s. The resulting optimal strength for reproducing the measured data is given as

$$s = \max\left(\frac{\langle l, m\rangle_2}{\|l\|_2^2}, 0\right),$$

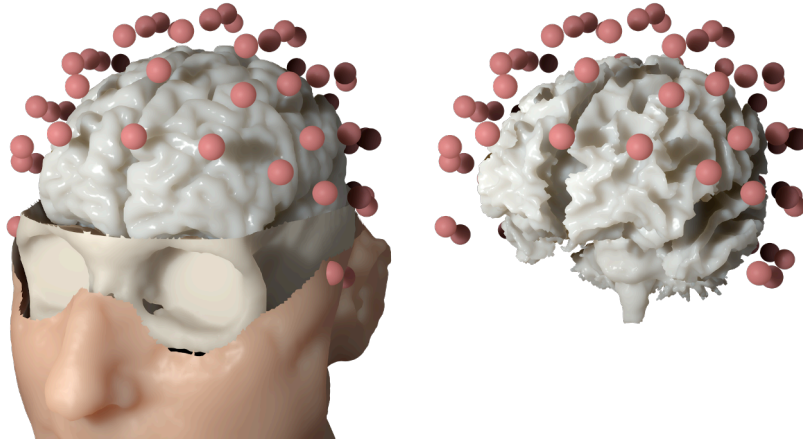The maximum with 0 is used in order to restrict the solution along the respective positive normal

Figure 5.4: Left: skin, skull and gray matter surfaces of the six-compartment isotropic head model along with the electrode montage used in the practical example. Right: source space relative to the electrode positions.
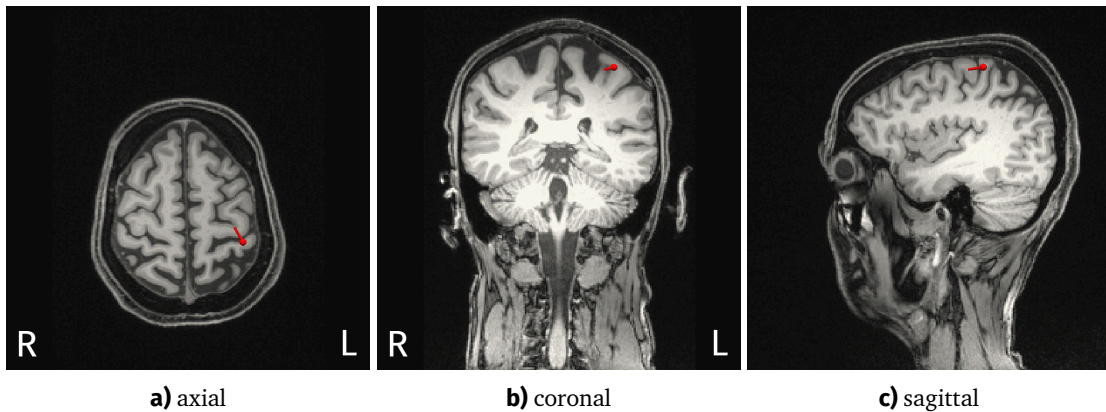

a) axial   **b)** coronal   **c)** sagittal

Figure 5.5: Reconstructed source (red) of the P20 component on a axial, coronal and sagittal slice of the MRI. Note the left-right orientation of the axial and coronal slices.

direction. This strength is embedded into the goodness of fit measure (GOF) that is defined as

$$\text{GOF} = 1 - \frac{\|ls - m\|_2^2}{\|m\|_2^2}$$

and measures the ability of the numerical solution to reproduce the measured data. In the case of a single dipole scan this includes how well the data can be represented as a single dipole. If the data can be exactly reproduced, the GOF has a value of 1. Figure 5.5 shows the source with the maximal GOF measure on three slices of the subjects MRI data. The GOF for this source is 0.974. The source is located in the primary somatosensory cortex in the wall of the post-central gyrus and has a mainly tangential orientation, which reproduces findings of (Buchner et al., 1994) and (Aydin, 2015). Figure 5.6 shows the source embedded in the source space along the distribution of the GOF measure. We see that the GOF measure is higher for source locations on the gyral walls with a tangentially oriented normal vector and that the higher values are located close to the central sulcus. Overall, the GOF measure shows a smooth distribution in these areas while being sensitive
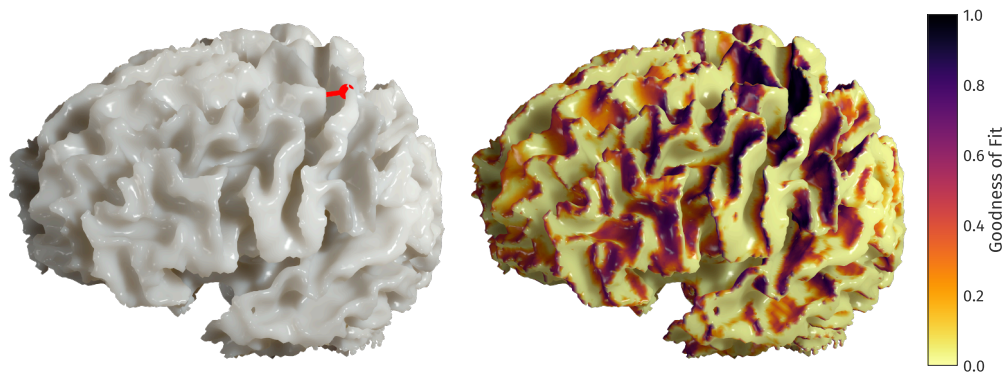
Figure 5.6: Left: Reconstructed source (red) of the P20 component and its location within the source space. Right: Distribution of the GOF measure on the source space. A darker color indicates a higher GOF.

to orientation changes.

5.5 Conclusion

In this chapter we presented the duneuro software, a toolbox for solving forward problems in neuroscience. We provided a general description of the toolbox as well as detailed information on the main concepts. Short examples showed the extendibility of the different subcomponents. We presented a method to efficiently localize positions within a given mesh and described bindings of the library for scripting languages. Finally the practical usability of the library was demonstrated by a source analysis of experimental data of a somatosensory stimulation. The duneuro toolbox offers a flexible and efficient way to perform the numerical computations throughout this thesis. However, there are several open goals regarding the software implementation. Foremost, a direct comparison with existing tools for computing forward solutions for EEG and MEG, such as the SimBio toolbox, should be performed. Similar to the latter toolbox, a closer integration into existing source analysis frameworks, such as FieldTrip, BrainStorm or mne-python should be considered. This integration would offer the use of duneuro for different inverse approaches. Several other forward problems, e.g., electric or magnetic brain stimulation, are only partially implemented and their support should be improved. Of special interest would then be a connection to optimization procedures for transcranial direct current stimulation. In order to improve the stability of the codebase and ensure the reliability of the results even under future modifications, a testing framework using continuous integration should be implemented.

Summary and Outlook

Summary   In this thesis, we presented fitted and unfitted finite element approaches for solving the EEG forward problem. After presenting the physiological background and the established mathematical theory of finite element methods for the EEG forward problem we addressed several open questions.

In Chapter 2 we showed extensions of two source models for modern finite element methods. One extension was presented in Section 2.1, where we introduced a conforming formulation of the Venant approach in a conforming finite element method. We showed the close connection of the Venant approach to the partial integration approach and evaluated various properties of the source model in four-layer sphere models. We provided a first application of the Venant approach for discontinuous Galerkin methods in Section 2.2 which also made use of the conforming formulation. In Section 2.3 we derived and analyzed the localized subtraction approach. It removed the main disadvantage of the full subtraction approach and made it practically feasible even in high resolution models. This could be achieved without a reduction of the accuracy of the subtraction approach.

In Chapter 3 we introduced two cut-cell methods for solving the EEG forward problem: the CutFEM approach and the UDG method. These methods were investigated extensively in multi-layer sphere studies as well as in realistically shaped head models. An accurate solution of the EEG forward problem was provided by these methods and a simpler modeling pipeline was offered.

Implementational aspects of cut-cell methods were presented in Chapter 4. A marching cubes methods for the numerical integration over implicitly defined domains was presented in 4.1. For efficiently solving the linear systems arising from cut-cell discretizations we introduced algebraic multigrid techniques for cut-cell methods in Section 4.2. Furthermore, we investigated the effect of the ghost penalty in a CutFEM discretization and the smoother for the UDG method.

In order to transfer the modern mathematical methods into application we presented the duneuro software toolbox in Chapter 5. Its practical use was illustrated by reconstructing the activity of a somatosensory experiment. Overall we were able to analyze and modify the forward modeling approach such that an accurate solution with a simpler simulation pipeline is practically feasible.

Outlook   Two main challenges for solving the EEG forward problem were addressed in this thesis: the discretization of the dipolar source term and the representation of the model geometry.

Not all of the subproblems regarding these challenges could be addressed in this thesis and some results gave rise to new questions for future research. The conforming formulation of the Venant source model offers a new way for the mathematical treatment of the discretization. This formulation can lead to more robust error estimates for the Venant approach which are not available so far. An additional idea is the reformulation of the interpolation process of the Venant approach using a mesh-dependent regularization of the delta distribution. A further investigation should be performed on the practical consequences of the smoothness properties that were observed when using higher-order mixed moments with respect to dipole fit source reconstructions. The localized subtraction approach offers an efficient way to use the subtraction approach even in highly resolved meshes. Up to now, it is only derived in the context of discontinuous Galerkin method. In principle, a similar approach can be derived for the conforming finite element method with Lagrangian elements. Instead of restricting the singularity potential to the patch it could be linearly interpolated towards zero in the boundary zone of the patch. Additionally, different strategies for constructing the local patch should be investigated. Both ideas can be transferred to the unfitted finite element methods.

With regard to the unfitted finite element methods, an evaluation in the context of an automated simulation pipeline for the construction of head models should be considered. Of special interest is the direct use of level-set segmentation data. In addition, some segmentation tools provide additional information such as tissue probability maps that could be used as additional information to distinguish different tissue compartments. For the algebraic multigrid techniques for cut-cell methods an investigation of the smoother on the fine level could be worthwhile. Especially an overlapping smoother for the CutFEM method and the effect of using a ghost-penalty for UDG should be considered. For the overlapping smoother different methods of constructing the local patch might lead to a better robustness with respect to the local cut-cell size. To improve the general convergence behavior one might evaluate different course level solvers.

In order to promote the presented methods in the field and to enable their use in various practical investigations, a close coupling of the duneuro toolbox to existing modeling pipelines should be implemented. Such a coupling would enable the neuroscience community to directly use the modern mathematical methods and to benefit from future developments through the extendibility of the presented framework.

A

Appendix

A.1 Parameters of Validation Studies

Table A.1: Radii and conductivity values of the different tissue compartments in a four-layer sphere model.

	skin	skull	CSF	brain
radius in mm	92	86	80	78
conductivity in S m^{-1}	0.43	0.01	1.79	0.33

Table A.2: Properties of the geometry-adapted hexahedral multi-layer sphere models. CG DOFs indicates the number of degrees of freedom of a conforming Lagrange finite lement method with piecewise multi-linear ansatz function. DG DOFs indicates the number of degrees of freedom of a discontinuous Galerkin discretization with piecewise multi-linear ansatz functions.

h	8 mm	4 mm	2 mm	1 mm
nodes	7304	55 984	428 185	3 343 541
elements	6031	50 883	407 904	3 263 152
CG DOFs	7304	55 984	428 185	3 343 541
DG DOFs	48 248	407 064	3 263 232	26 105 216

Table A.3: Sources used in the multi-layer sphere studies. For the hexahedral models of different resolutions, some source do not lie within a gray matter element, but in an element belonging to a different compartment. The respective number of sources an their corresponding compartment with respect to the mesh resolution are shown.

eccentricity		0.3	0.6	0.771	0.869	0.925	0.957	0.976	0.986	0.992	0.995
1 mm	brain	360	1439	2379	3022	3424	3665	3807	3889	3936	3884
	CSF	0	0	0	0	0	0	0	0	0	79
2 mm	brain	360	1439	2379	3022	3424	3665	3807	3887	3761	3362
	CSF	0	0	0	0	0	0	0	2	175	601
4 mm	brain	360	1439	2379	3022	3424	3665	3805	3713	3373	3069
	CSF	0	0	0	0	0	0	2	176	559	869
	skull	0	0	0	0	0	0	0	0	4	25
8 mm	brain	360	1439	2379	3022	3424	3638	3618	3468	3285	3161
	CSF	0	0	0	0	0	27	154	287	370	363
	skull	0	0	0	0	0	0	35	134	281	439

A.2 Software Tools

Several open-source tools were used to create the results and visualizations in this thesis (in alphabetic order):

Blender surface renderings in realistic head models

Dune implementation of the different finite element methods, using the modules: dune-common, dune-istl, dune-localfunctions, dune-geometry, dune-grid, dune-alugrid, dune-uggrid, dune-subgrid, dune-typetree, dune-pdelab, dune-functions, dune-udg, dune-tpmc, duneuro and duneuro-py

Gimp post-processing of visualizations

LaTeX type-setting this thesis

MeshLab processing of triangular surfaces

mne-python butterfly and topography plots for the SEP study

numpy performing numerical computations for the validation studies

pandas performing statistical evaluations for the validation studies

ParaView visualizing meshes and computational results

pybind11 providing the Python bindings for the duneuro module

seaborn plotting the results of the validation studies

SimpleITK extracting level-set information from binary images

Seg3D post-processing voxel segmentations

tikz creating schematic visualizations and graphs

Bibliography

Aberth, O. (1973). Iteration methods for finding all zeros of a polynomial simultaneously. *Mathematics of Computation*, 27(122):pp. 339–344.

Acar, Z. A. and Makeig, S. (2010). Neuroelectromagnetic forward head modeling toolbox. *Journal of neuroscience methods*, 190(2):258–270.

Alkämper, M., Dedner, A., Klöfkorn, R., and Nolte, M. (2016). The dune-alugrid module. *Archive of Numerical Software*, 4(1):1–28.

Arnold, D. N., Brezzi, F., Cockburn, B., and Marini, L. D. (2002). Unified analysis of discontinuous galerkin methods for elliptic problems. *SIAM journal on numerical analysis*, 39(5):1749–1779.

Aydin, Ü. (2015). *Combined EEG and MEG source analysis of epileptiform activity using calibrated realistic finite element head models*. PhD thesis.

Badia, S., Verdugo, F., and Martín, A. F. (2017). The aggregated unfitted finite element method for elliptic problems. *arXiv preprint arXiv:1709.09122*.

Barrett, J. W. and Elliott, C. M. (1987). Fitted and unfitted finite-element methods for elliptic equations with smooth interfaces. *IMA journal of numerical analysis*, 7(3):283–300.

Bastian, P., Birken, K., Johannsen, K., Lang, S., Neuß, N., Rentz-Reichert, H., and Wieners, C. (1997). Ug–a flexible software toolbox for solving partial differential equations. *Computing and Visualization in Science*, 1(1):27–40.

Bastian, P., Blatt, M., Dedner, A., Engwer, C., Klöfkorn, R., Kornhuber, R., Ohlberger, M., and Sander, O. (2008a). A generic grid interface for parallel and adaptive scientific computing. part ii: implementation and tests in dune. *Computing*, 82(2-3):121–138.

Bastian, P., Blatt, M., Dedner, A., Engwer, C., Klöfkorn, R., Ohlberger, M., and Sander, O. (2008b). A generic grid interface for parallel and adaptive scientific computing. part i: abstract framework. *Computing*, 82(2-3):103–119.

Bastian, P., Blatt, M., and Scheichl, R. (2012). Algebraic multigrid for discontinuous galerkin discretizations of heterogeneous elliptic problems. *Numerical Linear Algebra with Applications*, 19(2):367–388.

Bastian, P. and Engwer, C. (2009). An unfitted finite element method using discontinuous Galerkin. *Int. J. Numer. Methods Eng.*, 79(12):1557–1576.

Bastian, P., Heimann, F., and Marnach, S. (2010). Generic implementation of finite element methods in the distributed and unified numerics environment (dune). *Kybernetika*, 46(2):294–315.

Bauer, M., Pursiainen, S., Vorwerk, J., Köstler, H., and Wolters, C. H. (2015). Comparison study for whitney (raviart–thomas)-type source models in finite-element-method-based eeg forward modeling. *IEEE Transactions on Biomedical Engineering*, 62(11):2648–2656.

Bentley, J. L. (1975). Multidimensional binary search trees used for associative searching. *Communications of the ACM*, 18(9):509–517.

Bertrand, O., Thévenet, M., and Perrin, F. (1991). 3d finite element method in brain electrical activity studies. In Nenonen, J., Rajala, H., and Katila, T., editors, *Biomagnetic Localization and 3D Modeling*, Report of the Department of Technical Physics, page 154–171. Helsinki University of Technology.

Blatt, M. (2010). *A parallel algebraic multigrid method for elliptic problems with highly discontinuous coefficients*. PhD thesis.

Blatt, M. and Bastian, P. (2006). The iterative solver template library. In *International Workshop on Applied Parallel Computing*, pages 666–675. Springer.

Braess, D. (2007). *Finite elements: Theory, fast solvers, and applications in solid mechanics*. Cambridge University Press.

Brenner, S. and Scott, R. (2007). *The mathematical theory of finite element methods*, volume 15. Springer Science & Business Media.

Brown, P. J. and Faigle, C. T. (1997). A robust efficient algorithm for point location in triangulations. Technical report, University of Cambridge, Computer Laboratory.

Buchner, H., Fuchs, M., Wischmann, H.-A., Dössel, O., Ludwig, I., Knepper, A., and Berg, P. (1994). Source analysis of median nerve and finger stimulated somatosensory evoked potentials: multichannel simultaneous recording of electric and magnetic fields combined with 3d-mr tomography. *Brain topography*, 6(4):299–310.

Burman, E. (2010). Ghost penalty. *Comptes Rendus Mathematique*, 348(21-22):1217–1220.

Burman, E., Claus, S., Hansbo, P., Larson, M. G., and Massing, A. (2015). CutFEM: Discretizing geometry and partial differential equations. *International Journal for Numerical Methods in Engineering*, 104(7):472–501.

Burman, E. and Hansbo, P. (2012). Fictitious domain finite element methods using cut elements: Ii. a stabilized nitsche method. *Applied Numerical Mathematics*, 62(4):328–341.

Burman, E., Hansbo, P., Larson, M. G., and Massing, A. (2017). A cut discontinuous galerkin method for the laplace–beltrami operator. *IMA Journal of Numerical Analysis*, 37(1):138–169.

Chernyaev, E. V. (1995). Marching cubes 33: Construction of topologically correct isosurfaces. Technical report, CERN.

Cook, M. J. and Koles, Z. J. (2006). A high-resolution anisotropic finite-volume head model for eeg source analysis. In *Engineering in Medicine and Biology Society, 2006. EMBS'06. 28th Annual International Conference of the IEEE*, pages 4536–4539. IEEE.

Dannhauer, M., Lanfer, B., Wolters, C. H., and Knösche, T. R. (2011). Modeling of the human skull in EEG source analysis. *Human brain mapping*, 32(9):1383–1399.

De Munck, J. and Peters, M. J. (1993). A fast method to compute the potential in the multisphere model. *IEEE Trans. Biomed. Eng*, 40(11):1166–1174.

De Munck, J., Wolters, C. H., and Clerc, M. (2012). Eeg and meg: forward modeling. *Handbook of neural activity measurement*, 19:192–248.

Di Pietro, D. A. and Ern, A. (2011). *Mathematical aspects of discontinuous Galerkin methods*, volume 69. Springer Science & Business Media.

Drechsler, F., Wolters, C. H., Dierkes, T., Si, H., and Grasedyck, L. (2009). A full subtraction approach for finite element method based source analysis using constrained Delaunay tetrahedralisation. *NeuroImage*, 46(4):1055–1065.

Engwer, C. (2009). *An Unfitted Discontinuous Galerkin Scheme for Micro-scale Simulations and Numerical Upscaling*. PhD thesis, Heidelberg University.

Engwer, C. and Heimann, F. (2012). Dune-udg: A cut-cell framework for unfitted discontinuous galerkin methods. In *Advances in DUNE*, pages 89–100. Springer.

Engwer, C., Johannsen, K., and Nüßing, A. (2016). Algebraic multigrid for discontinuous galerkin methods using local transformations. In *Domain Decomposition Methods in Science and Engineering XXII*, pages 177–185. Springer.

Engwer, C. and Nüßing, A. (2017). Geometric reconstruction of implicitly defined surfaces and domains with topological guarantees. *ACM Transactions on Mathematical Software (TOMS)*, 44(2):14.

Engwer, C., Vorwerk, J., Ludewig, J., and Wolters, C. H. (2017). A discontinuous galerkin method to solve the EEG forward problem using the subtraction approach. *SIAM Journal on Scientific Computing*, 39(1):B138–B164.

Engwer, C. and Westerheide, S. (2014). Heterogeneous coupling for implicitly described domains. In *Domain Decomposition Methods in Science and Engineering XXI*, pages 809–817. Springer.

Epshteyn, Y. and Rivière, B. (2007). Estimation of penalty parameters for symmetric interior penalty galerkin methods. *Journal of Computational and Applied Mathematics*, 206(2):843–872.

Forster, O. (2008). *Differentialrechnung im $\mathbb{R}^n$, gewöhnliche Differentialgleichungen*. Vieweg+Teubner|GWV Fachverlage GmbH.

Freudenthal, H. (1942). Simplizialzerlegungen von beschränkter Flachheit. *Annals of Mathematics*, 43:580–582.

Friedlander, F. G. and Joshi, M. S. (1998). *Introduction to the Theory of Distributions*. Cambridge University Press.

Gençer, N. G. and Acar, C. E. (2004). Sensitivity of eeg and meg measurements to tissue conductivity. *Physics in Medicine & Biology*, 49(5):701.

Georgoulis, E. H., Hall, E., and Houston, P. (2007). Discontinuous galerkin methods for advection-diffusion-reaction problems on anisotropically refined meshes. *SIAM Journal on Scientific Computing*, 30(1):246–271.

Gramfort, A., Luessi, M., Larson, E., Engemann, D. A., Strohmeier, D., Brodbeck, C., Goj, R., Jas, M., Brooks, T., Parkkonen, L., et al. (2013). Meg and eeg data analysis with mne-python. *Frontiers in neuroscience*, 7:267.

Gramfort, A., Papadopoulo, T., Olivi, E., and Clerc, M. (2011). Forward field computation with openmeeg. *Computational intelligence and neuroscience*, 2011.

Gräser, C. and Sander, O. (2009). The dune-subgrid module and some applications. *Computing*, 86(4):269.

Grüne, F. (2014). Validierung von FEM-Ansätzen höherer Ordnung für das EEG-Vorwärtsproblem. Master's thesis, Fachbereich Mathematik und Informatik, Westfälische Wilhelms-Universität Münster, Germany.

Gueziec, A. and Hummel, R. (1995). Exploiting triangulated surface extraction using tetrahedral decomposition. *Visualization and Computer Graphics, IEEE Transactions on*, 1(4):328–342.

Gürkan, C. and Massing, A. (2018). A stabilized cut discontinuous galerkin framework: I. elliptic boundary value and interface problems. *arXiv preprint arXiv:1803.06635*.

Hämäläinen, M., Hari, R., Ilmoniemi, R. J., Knuutila, J., and Lounasmaa, O. V. (1993). Magnetoencephalography—theory, instrumentation, and applications to noninvasive studies of the working human brain. *Reviews of modern Physics*, 65(2):413.

Hansbo, A. and Hansbo, P. (2002). An unfitted finite element method, based on nitsche's method, for elliptic interface problems. *Computer methods in applied mechanics and engineering*, 191(47-48):5537–5552.

Heimann, F., Engwer, C., Ippisch, O., and Bastian, P. (2013). An unfitted interior penalty discontinuous galerkin method for incompressible navier–stokes two-phase flow. *International Journal for Numerical Methods in Fluids*, 71(3):269–293.

Johannsen, K. (2006). Multigrid methods for nonsymmetric interior penalty discontinuous galerkin methods. *ICES Report*, pages 05–23.

Kwon, J.-H., Kim, J. S., Kang, D.-W., Bae, K.-S., and Kwon, S. U. (2006). The thickness and texture of temporal bone in brain ct predict acoustic window failure of transcranial doppler. *Journal of Neuroimaging*, 16(4):347–352.

Lehrenfeld, C. (2016). High order unfitted finite element methods on level set domains using isoparametric mappings. *Computer Methods in Applied Mechanics and Engineering*, 300:716–733.

Lew, S., Wolters, C., Dierkes, T., Röer, C., and MacLeod, R. (2009). Accuracy and run-time comparison for different potential approaches and iterative solvers in finite element method based eeg source analysis. *Applied Numerical Mathematics*, 59(8):1970–1988.

Lewiner, T., Lopes, H., Vieira, A. W., and Tavares, G. (2003). Efficient implementation of marching cubes' cases with topological guarantees. *Journal of Graphics Tools: JGT*, 8(2):1–15.

Li, G., Nie, J., Wang, L., Shi, F., Gilmore, J. H., Lin, W., and Shen, D. (2014). Measuring the dynamic longitudinal cortex development in infants by reconstruction of temporally consistent cortical surfaces. *Neuroimage*, 90:266–279.

Lorensen, W. and Cline, H. (1987). Marching cubes: A high resolution 3D surface construction algorithm. *Computer Graphics*, 21(4):163–169.

Medani, T., Lautru, D., Schwartz, D., Ren, Z., and Sou, G. (2015). Fem method for the eeg forward problem and improvement based on modification of the saint venant's method. *Progress In Electromagnetics Research*, 153:11–22.

Min, C. and Gibou, F. (2007). Geometric integration over irregular domains with application to level-set methods. *Journal of Computational Physics*, 226(2):1432 – 1443.

Montes-Restrepo, V., van Mierlo, P., Strobbe, G., Staelens, S., Vandenberghe, S., and Hallez, H. (2014). Influence of skull modeling approaches on eeg source localization. *Brain topography*, 27(1):95–111.

Mosher, J. C., Leahy, R. M., and Lewis, P. S. (1999). Eeg and meg: forward solutions for inverse methods. *IEEE Transactions on Biomedical Engineering*, 46(3):245–259.

Müller, B., Kummer, F., and Oberlack, M. (2013). Highly accurate surface and volume integration on implicit domains by means of moment-fitting. *International Journal for Numerical Methods in Engineering*, 96(8):512–528.

Nitsche, J. (1971). Über ein variationsprinzip zur lösung von dirichlet-problemen bei verwendung von teilräumen, die keinen randbedingungen unterworfen sind. In *Abhandlungen aus dem mathematischen Seminar der Universität Hamburg*, volume 36, pages 9–15. Springer.

Nüßing, A. (2013). Algebraic multigrid for discontinuous galerkin methods. Master's thesis, Westfälische Wilhelms-Universität Münster.

Nüßing, A., Wolters, C. H., Brinck, H., and Engwer, C. (2016). The unfitted discontinuous galerkin method for solving the eeg forward problem. *IEEE Transactions on Biomedical Engineering*, 63(12):2564–2575.

Oostenveld, R., Fries, P., Maris, E., and Schoffelen, J.-M. (2011). Fieldtrip: open source software for advanced analysis of meg, eeg, and invasive electrophysiological data. *Computational intelligence and neuroscience*, 2011:1.

Oostenveld, R. and Oostendorp, T. F. (2002). Validating the boundary element method for forward and inverse eeg computations in the presence of a hole in the skull. *Human brain mapping*, 17(3):179–192.

Oostenveld, R. and Praamstra, P. (2001). The five percent electrode system for high-resolution eeg and erp measurements. *Clinical neurophysiology*, 112(4):713–719.

Osher, S. and Sethian, J. A. (1988). Fronts propagating with curvature-dependent speed: algorithms based on hamilton-jacobi formulations. *Journal of computational physics*, 79(1):12–49.

Piastra, M. C., Nüßing, A., Vorwerk, J., Bornfleth, H., Oostenveld, R., Engwer, C., and Wolters, C. H. (2018). The discontinuous galerkin finite element method for solving the meg and the combined meg/eeg forward problem. *Frontiers in Neuroscience*, 12:30.

Pursiainen, S., Agsten, B., Wagner, S., and Wolters, C. H. (2018). Advanced boundary electrode modeling for tes and parallel tes/eeg. *IEEE Transactions on Neural Systems and Rehabilitation Engineering*, 26(1):37–44.

Pursiainen, S., Lucka, F., and Wolters, C. (2012). Complete electrode model in eeg: relationship and differences to the point electrode model. *Physics in Medicine & Biology*, 57(4):999.

Pursiainen, S., Sorrentino, A., Campi, C., and Piana, M. (2011). Forward simulation and inverse dipole localization with the lowest order raviart—thomas elements for electroencephalography. *Inverse Problems*, 27(4):045003.

Pursiainen, S., Vorwerk, J., and Wolters, C. H. (2016). Electroencephalography (eeg) forward modeling via h (div) finite element sources with focal interpolation. *Physics in Medicine & Biology*, 61(24):8502.

Quarteroni, A., Sacco, R., and Saleri, F. (2010). *Numerical mathematics*, volume 37. Springer Science & Business Media.

Rice, J. K., Rorden, C., Little, J. S., and Parra, L. C. (2013). Subject position affects eeg magnitudes. *NeuroImage*, 64:476–484.

Roche-Labarbe, N., Aarabi, A., Kongolo, G., Gondry-Jouet, C., Dümpelmann, M., Grebe, R., and Wallois, F. (2008). High-resolution electroencephalography and source localization in neonates. *Human brain mapping*, 29(2):167–176.

Ruge, J. W. and Stüben, K. (1987). Algebraic multigrid. In *Multigrid methods*, pages 73–130. SIAM.

Schimpf, P. H., Ramon, C., and Haueisen, J. (2002). Dipole models for the eeg and meg. *IEEE Transactions on Biomedical Engineering*, 49(5):409–418.

Si, H. (2015). Tetgen, a delaunay-based quality tetrahedral mesh generator. *ACM Transactions on Mathematical Software (TOMS)*, 41(2):11.

Sonntag, H., Vorwerk, J., Wolters, C. H., Grasedyck, L., Haueisen, J., and Maeß, B. (2013). Leakage effect in hexagonal fem meshes of the eeg forward problem. In *International Conference on Basic and Clinical Multimodal Imaging (BaCI)*, volume 102.

Stenroos, M. and Sarvas, J. (2012). Bioelectromagnetic forward problem: isolated source approach revis (it) ed. *Physics in Medicine & Biology*, 57(11):3517.

Sudhakar, Y. and Wall, W. A. (2013). Quadrature schemes for arbitrary convex/concave volumes and integration of weak form in enriched partition of unity methods. *Computer Methods in Applied Mechanics and Engineering*, 258:39–54.

Tadel, F., Baillet, S., Mosher, J. C., Pantazis, D., and Leahy, R. M. (2011). Brainstorm: a user-friendly application for meg/eeg analysis. *Computational intelligence and neuroscience*, 2011:8.

Taubin, G. (1995). A signal processing approach to fair surface design. In *Proceedings of the 22nd annual conference on Computer graphics and interactive techniques*, pages 351–358. ACM.

Vallaghé, S. and Papadopoulo, T. (2010). A trilinear immersed finite element method for solving the electroencephalography forward problem. *SIAM Journal on Scientific Computing*, 32(4):2379–2394.

Vallaghé, S., Papadopoulo, T., and Clerc, M. (2008). The adjoint method for general eeg and meg sensor-based lead field equations. *Physics in Medicine & Biology*, 54(1):135.

Van Uitert, R., Weinstein, D., Johnson, C., and Zhukov, L. (2001). Finite elenent eeg and meg simulations for realistic head models: Quadratic vs. linear approximations. *Biomedizinische Technik/Biomedical Engineering*, 46(s2):32–34.

Vatta, F., Meneghini, F., Esposito, F., Mininel, S., and Di Salle, F. (2009). Solving the forward problem in eeg source analysis by spherical and fdm head modeling: a comparative analysis-biomed 2009. *Biomedical sciences instrumentation*, 45:382–388.

Vese, L. A. and Chan, T. F. (2002). A multiphase level set framework for image segmentation using the mumford and shah model. *International journal of computer vision*, 50(3):271–293.

Vorwerk, J. (2011). Comparison of numerical approaches to the eeg forward problem. Master's thesis, Westfälische Wilhelms-Universität Münster.

Vorwerk, J. (2016). *New Finite Element Methods to Solve the EEG/MEG Forward Problem*. PhD thesis, University of Münster.

Vorwerk, J., Cho, J.-H., Rampp, S., Hamer, H., Knösche, T. R., and Wolters, C. H. (2014). A guideline for head volume conductor modeling in eeg and meg. *NeuroImage*, 100:590–607.

Vorwerk, J., Clerc, M., Burger, M., and Wolters, C. (2012). Comparison of boundary element and finite element approaches to the eeg forward problem. *Biomedical Engineering/Biomedizinische Technik*, 57(SI-1 Track-O):795–798.

Vorwerk, J., Engwer, C., Pursiainen, S., and Wolters, C. H. (2017). A mixed finite element method to solve the eeg forward problem. *IEEE transactions on medical imaging*, 36(4):930–941.

Vorwerk, J., Oostenveld, R., Piastra, M. C., Magyari, L., and Wolters, C. H. (2018). The fieldtrip-simbio pipeline for eeg forward solutions. *BioMedical Engineering OnLine*, 17(1):37.

Weinstein, D., Zhukov, L., and Johnson, C. (2000). Lead-field bases for electroencephalography source imaging. *Annals of biomedical engineering*, 28(9):1059–1065.

Wendel, K., Narra, N. G., Hannula, M., Kauppinen, P., and Malmivuo, J. (2008). The influence of csf on eeg sensitivity distributions of multilayered head models. *IEEE Transactions on Biomedical Engineering*, 55(4):1454–1456.

Whitaker, R. T. (2000). Reducing aliasing artifacts in iso-surfaces of binary volumes. In *Proceedings of the 2000 IEEE symposium on Volume visualization*, pages 23–32. ACM.

Wolters, C., Köstler, H., Möller, C., Härdtlein, J., Grasedyck, L., and Hackbusch, W. (2007a). Numerical Mathematics of the Subtraction Method for the Modeling of a Current Dipole in EEG Source Reconstruction Using Finite Element Head Models. *SIAM Journal on Scientific Computing*, 30(1):24–45.

Wolters, C. H., Anwander, A., Berti, G., and Hartmann, U. (2007b). Geometry-adapted hexahedral meshes improve accuracy of finite-element-method-based EEG source analysis. *IEEE Transactions on Biomedical Engineering*, 54(8):1446–1453.

Wolters, C. H., Grasedyck, L., and Hackbusch, W. (2004). Efficient computation of lead field bases and influence matrix for the fem-based eeg and meg inverse problem. *Inverse problems*, 20(4):1099.

Wolters, C. H., Kuhn, M., Anwander, A., and Reitzinger, S. (2002). A parallel algebraic multigrid solver for finite element method based source localization in the human brain. *Computing and visualization in science*, 5(3):165–177.

Xu, J. (1992). Iterative methods by space decomposition and subspace correction. *SIAM review*, 34(4):581–613.

Zhang, Y., Zhu, S., and He, B. (2004). A second-order finite element algorithm for solving the three-dimensional eeg forward problem. *Physics in Medicine & Biology*, 49(13):2975.